

**THE UNIVERSITY OF ADELAIDE**

**NUMERICAL INVESTIGATION OF  
WIND INPUT AND SPECTRAL DISSIPATION  
IN EVOLUTION OF WIND WAVES**

**KAKHA TSAGARELI**

Submitted in fulfillment of the requirements for the degree of

**DOCTOR OF PHILOSOPHY**

November 2008

Faculty of Engineering, Computer and Mathematical Sciences

---

School of Civil, Environmental and Mining Engineering



# Table of Contents

---

Table of Contents .....	i
List of Symbols .....	iv
List of Equations .....	x
List of Figures .....	xviii
Abstract .....	xxix
Statement of Originality .....	xxxii
Acknowledgements .....	xxxiii
CHAPTER 1 INTRODUCTION .....	1
1.1 PROBLEM STATEMENT .....	1
1.2 RESEARCH BACKGROUND .....	5
1.3 RESEARCH OBJECTIVES .....	6
1.4 APPROACH TO THE STUDY .....	7
1.5 LAYOUT AND CONTENTS OF THESIS .....	9
CHAPTER 2 BACKGROUND .....	10
2.1 OCEAN WAVES .....	10
2.2 THE WAVE SPECTRUM .....	11
2.2.1 Shape of the Frequency Spectra .....	12
2.2.2 Directional Spectrum .....	17
2.2.3 Wave Steepness .....	19
2.3 MODELLING WAVE EVOLUTION .....	20
2.3.1 Radiative Transfer Equation .....	22
2.3.2 Source Functions .....	23
2.3.2.1 Wind Input .....	23

2.3.2.2	Wave Dissipation.....	29
2.3.2.3	Nonlinear Wave-Wave Interaction.....	32
2.3.3	Wave Growth Relationships.....	36
2.3.4	Observational Data .....	38
2.4	METHODOLOGY FOR ASSESSMENT OF SPECTRAL SHAPE.....	39
CHAPTER 3    NUMERICAL MODEL.....		41
3.1	THE SPECTRAL GRID.....	41
3.2	INITIAL SPECTRUM.....	44
3.3	SOURCE TERMS IN WAVETIME-1.....	44
3.4	NUMERICAL SCHEME .....	45
3.4.1	Optimal Time Step.....	45
3.5	VALIDATION OF THE MODEL.....	47
3.5.1	Verification of $S_{nl}$ Source Term.....	47
3.5.2	Preparation of Experimental Data .....	48
3.5.3	Verification of Growth Curves .....	49
CHAPTER 4    METHODS AND RESULTS.....		52
4.1	THE NEW WIND INPUT SOURCE FUNCTION.....	53
4.1.1	Preliminary Computations .....	54
4.1.1.1	Growth Rate.....	55
4.1.1.2	Wind Input Source Function .....	62
4.1.2	Validating the Wind Input Source Term .....	68
4.1.2.1	Stresses during Wind-Wave Interaction.....	68
4.1.2.2	A New Approach for the Correction of $S_{in}$ .....	72
4.1.3	Results.....	83
4.1.3.1	High Frequency Tail.....	87
4.1.3.2	Wave Steepness .....	90
4.1.1	Computations of $S_{in}$ for the Combi Spectra.....	92
4.1.2	Conclusions.....	106

4.2	THE NEW SPECTRAL DISSIPATION SOURCE FUNCTION .....	107
4.2.1	Threshold Spectrum $F_T(f)$ .....	109
4.2.2	Determination of Coefficients $a$ and $b$ .....	114
4.2.3	Directional spreading.....	139
4.2.4	Comparing to the Experimental Data .....	143
4.2.4.1	Comparing to Melville and Matusov (2002).....	145
4.2.4.2	Comparing to Gemmrich (2005) .....	153
4.2.5	Conclusions.....	156
4.3	MODELLING SPECTRAL EVOLUTION .....	159
4.3.1	Model Setup.....	159
4.3.1.1	Initial Conditions .....	160
4.3.1.2	Output Parameters .....	160
4.3.2	Self-Correcting Wave Model.....	161
4.3.3	Validation Strategy .....	162
4.3.4	Results.....	165
4.3.4.1	Results for the Unconstrained $S_{ds}(f)$ .....	165
4.3.4.2	Results for the Constrained $S_{ds}(f)$ .....	166
4.3.5	Conclusions.....	191
CHAPTER 5 CONCLUSIONS AND RECOMMENDATIONS .....		196
5.1	THE WIND INPUT SOURCE FUNCTION $S_{IN}$ .....	196
5.2	THE WAVE DISSIPATION SOURCE FUNCTION $S_{DS}$ .....	198
5.3	MODEL PERFORMANCE .....	202
5.4	THE WAVE SPECTRUM.....	204
5.5	WAVE STEEPNESS .....	204
BIBLIOGRAPHY .....		206

# List of Symbols

---

<b>Symbol</b>	<b>Quantity</b>	<b>SI Unit</b>
$a$	coefficient of the inherent breaking term	-
$a_{et}, a_{ft}$	exponents of time-limited growth curves	-
$a_{ex}, a_{fx}$	exponents of fetch-limited growth curves	-
$a_{exp}$	experimental value for the coefficient $a$	-
$a_w$	wave amplitude	m
$A$	directional spectral width of wave spectrum	m
$A_{et}, A_{ft}$	relational coefficients of time-limited growth curves	-
$A_{ex}, A_{fx}$	relational coefficients of fetch-limited growth curves	-
$b$	coefficient of the forced breaking term	-
$b_{br}$	coefficient reflecting the strength of the wave breaking	-
$b_{G05}$	coefficient of the wave breaking by Gemmrich (2006)	-
$b_{MM02}$	coefficient of the wave breaking by Melville and Matusov (2002)	-
$B$	spectral saturation	-
$B_n$	spectral saturation normalized directionally	-
$B_{nT}$	normalized threshold spectral saturation	-
$c$	wave phase speed	$\text{m s}^{-1}$
$c_g$	group velocity	$\text{m s}^{-1}$
$c_p$	phase speed of components at the spectral peak	$\text{m s}^{-1}$
$d$	water depth	m
$C_D$	atmospheric drag coefficient	-

<b>Symbol</b>	<b>Quantity</b>	<b>SI Unit</b>
$C_V$	viscous drag coefficient	-
$D$	integral of dissipation source function	-
$D(f, \theta)$	directional spreading function	$\text{m}^2 \text{s}$
$D_n$	normalized directional spreading function	$\text{m}^2 \text{s}$
$E$	total wave energy	$\text{m}^2$
$f$	frequency 1 / T	$\text{s}^{-1}$
$f_{max}, f_{cut}$	maximum (cut) frequency of spectral scale	$\text{s}^{-1}$
$f_p$	frequency of spectral peak	$\text{s}^{-1}$
$f_T$	transition frequency	$\text{s}^{-1}$
$F(f)$	one-dimensional wave frequency spectrum	$\text{m}^2 \text{s}$
$F(f, \theta)$	directional frequency spectrum	$\text{m}^2 \text{s}$
$F_{max}$	maximum of wave spectrum	$\text{m}^2 \text{s}$
$F_T$	threshold spectrum for the dissipation source function	$\text{m}^2 \text{s}$
$\Delta F_p$	residual between the wave spectrum and the threshold spectrum	$\text{m}^2 \text{s}$
$\Phi(k)$	wavenumber spectrum integrated in directional space	$\text{m}^3 \text{rad}^{-1}$
$g$	gravitational acceleration	$\text{ms}^{-2}$
$G$	sheltering coefficient	-
$G_q$	quadruplet nonlinear interaction coupling coefficient	-
$H$	significant wave height	$\text{m}$
$j_{v2k}$	transformation Jacobian	-
$k$	wave number	$\text{rad m}^{-1}$
$k_p$	wave number of spectral peak	$\text{rad m}^{-1}$
$K(f, \theta)$	directional spreading function	-

<b>Symbol</b>	<b>Quantity</b>	<b>SI Unit</b>
$L(f)$	correction function for wind input source function	-
$M(f)$	wind momentum input spectrum	-
$MSS$	mean spectral slope	-
$n$	exponent of the wave spectrum	-
$N(\mathbf{k})$	action density	$\text{m}^2\text{rad}^{-1}$
$p$	pressure of the air exerted on the water surface	-
$p(f, U_{10} / c_p)$	trough parameter of bimodal directional function	-
$Q(\omega)$	quadrature wave spectrum	-
$Q(s)$	normalization factor for directional spreading	-
$R$	dissipation rate	-
$s$	directional spreading exponent	-
$s_p$	directional spreading exponent at the peak frequency	-
$S_{ds}$	dissipation source term	$\text{m}^2$
$S_{in}$	atmospheric input source term	$\text{m}^2$
$S_{nl}$	quadruplet nonlinear interaction source term	$\text{m}^2$
$S_{tot}$	total source term	$\text{m}^2$
$S_1, S_2, S_{11}, S_{12}$	partial integrals of source function	$\text{m}^2$
$t$	time	s
$T$	wave period	s
$T(f)$	saturation transformer	-
$T_1$	inherent breaking term for dissipation function	$\text{m}^2$
$T_2$	forced breaking term for dissipation function	$\text{m}^2$

<b>Symbol</b>	<b>Quantity</b>	<b>SI Unit</b>
$u^*$	friction velocity	$\text{ms}^{-1}$
$U_{10}$	wind speed measured at a height of 10m	$\text{ms}^{-1}$
$U_h$	wind speed measured at a height $h$	$\text{ms}^{-1}$
$U_{L/2}$	wind speed measured at a height of $L/2$	$\text{ms}^{-1}$
$U_{10} / c_p$	inverse wave age	-
$x$	horizontal length co-ordinate	m
$x$	fetch length over which the wind blows	m
$X$	correction factor for the wind input source function	-
$V$	bimodal directional spreading function	-
$W$	integral of wind input source function	-
$W_1, W_2$	partial integrals of wind input source function	-
$\alpha$	JONSWAP Phillips parameter	-
$\alpha_{BY}$	scale parameter of wind direction slice of the wavenumber spectrum from Banner and Young (1994)	-
$\beta$	spectrum scale parameter by Donelan et al. (1985)	-
$\gamma$	growth rate parameter	-
$\gamma_D$	peak enhancement factor by Donelan et al. (1985)	-
$\gamma_J$	JONSWAP peak enhancement factor	-
$\delta$	wave steepness	-
$\eta(x,t)$	water surface elevation	m
$\eta$	correction rate	-
$\eta_o$	lower boundary value of the correction rate	-
$\lambda$	wave length	m

<b>Symbol</b>	<b>Quantity</b>	<b>SI Unit</b>
$\lambda(k)$	lobe-ratio	-
$A(v)$	the average length of breaking crests per unit area per unit speed interval	m
$\mu$	slope exponent of wind source function	-
$v$	non-dimensional peak frequency	-
$v_c$	the crest propagation speed	m/s
$\zeta$	similarity parameter of the spectral energy level	-
$\pi$	pi constant	-
$\rho_a$	density of air	kg/m <sup>3</sup>
$\rho_w$	density of water	kg/m <sup>3</sup>
$\sigma$	spectral peak width parameter	-
$\sigma^2$	variance or total energy of the wave record	m
$\varepsilon$	non-dimensional energy	-
$\chi$	non-dimensional fetch	-
$\phi$	wave phase	rad
$\omega$	angular frequency	s <sup>-1</sup>
$\tau$	total wind stress	-
$\tau_t$	turbulent stress	-
$\tau_w$	wave-induced stress	-
$\tau_v$	viscous stress	-
$\zeta$	non-dimensional duration	-
$\theta$	wave direction	rad
$\theta_m$	mean wave direction	rad

<b>Symbol</b>	<b>Quantity</b>	<b>SI Unit</b>
$\theta_{max}$	direction of the spectral peak	rad
$\theta_w$	wind direction	rad
$\theta_H$	directional spectral width by Hwang et al. (2000)	rad
$\bar{\theta}$	mean spectral width	rad
$\Delta\theta_f$	total increment of the peak angle along the frequency scale	rad
$\Delta\theta_{ucp}$	total increment during the wave evolution	rad

# List of Equations

---

$$\eta(\mathbf{k}, \omega, \mathbf{x}, t) = a \cdot \sin(\mathbf{kx} - \omega t) \dots\dots\dots(\text{Eq. 2-1}) \dots\dots\dots 10$$

$$\eta(t) = \sum_{i=1}^N a_i \cdot \sin(\omega_i t + \phi_i) \dots\dots\dots(\text{Eq. 2-2}) \dots\dots\dots 11$$

$$F(k) = \frac{cc}{2\pi\omega} g F(f, \theta) \dots\dots\dots(\text{Eq. 2-3}) \dots\dots\dots 12$$

$$F(f, \theta) = \alpha \frac{g^2}{(2\pi)^4} f^{-5} \exp\left[-\frac{5}{4}\left(\frac{f}{f_p}\right)^{-4}\right] \cdot \gamma_J \exp\left[\frac{-(f-f_p)^2}{2\sigma^2 f_p^2}\right] \dots\dots\dots(\text{Eq. 2-4}) \dots\dots\dots 14$$

$$F(f, \theta) = \beta \frac{g^2}{(2\pi)^4} f_p^{-1} f^{-4} \exp\left[-\left(\frac{f}{f_p}\right)^{-4}\right] \cdot \gamma_D \exp\left[\frac{-(f-f_p)^2}{2\sigma^2 f_p^2}\right] \dots\dots\dots(\text{Eq. 2-5}) \dots\dots\dots 15$$

$$\beta = 0.0165v^{0.55} \dots\dots\dots(\text{Eq. 2-6}) \dots\dots\dots 15$$

$$\gamma_D = \begin{cases} 6.489 + 61 \log v & v \geq 0.159 \\ 1.7 & v < 0.159 \end{cases} \dots\dots\dots(\text{Eq. 2-7}) \dots\dots\dots 15$$

$$\sigma = 0.08 + 1.29 \times 10^{-3} v^{-3} \dots\dots\dots(\text{Eq. 2-8}) \dots\dots\dots 15$$

$$f_T \sim \frac{2.5}{\pi} \frac{g}{U_{10}} \dots\dots\dots(\text{Eq. 2-9}) \dots\dots\dots 16$$

$$F(f, \theta) = F(f) \cdot D(f, \theta) \dots\dots\dots(\text{Eq. 2-10}) \dots\dots\dots 17$$

$$\int D(f, \theta) = 1 \dots\dots\dots(\text{Eq. 2-11}) \dots\dots\dots 17$$

$$D(f, \theta) = Q(s) \cos^{2s} \left\{ \frac{\theta - \theta_m(f)}{2} \right\} \dots\dots\dots(\text{Eq. 2-12}) \dots\dots\dots 17$$

$$s = \begin{cases} s_p \left( \frac{f}{f_p} \right)^5, & f < f_p \\ s_p \left( \frac{f}{f_p} \right)^{-2.5}, & f \geq f_p \end{cases} \dots\dots\dots(\text{Eq. 2-13}) \dots\dots\dots 17$$

$$s_p = 11.5 \left( \frac{U_{10}}{c_p} \right)^{-2.5} \dots\dots\dots(\text{Eq. 2-14}) \dots\dots\dots 17$$

$$A(f)^{-1} = \int_{-\pi}^{\pi} D_n(f, \theta) d\theta \dots\dots\dots(\text{Eq. 2-15}) \dots\dots\dots 18$$

$$D_n(f, \theta_{\max}) = 1 \dots\dots\dots(\text{Eq. 2-16}) \dots\dots\dots 18$$

$$MSS = \iint k^4 \Phi(k, \theta) \frac{1}{k} dk d\theta = \int k^4 \Phi(k) d(\ln k) \dots\dots\dots(\text{Eq. 2-17}) \dots\dots\dots 19$$

$$B = \omega^5 E(\omega) / 2g^2 = (2\pi)^4 f^5 F(f) / 2g^2 \dots\dots\dots(\text{Eq. 2-18}) \dots\dots\dots 19$$

$$B_n(\omega) = \frac{\omega^5 E(\omega)}{2g^2} A(\omega) \dots\dots\dots(\text{Eq. 2-19}) \dots\dots\dots 20$$

$$\frac{\partial F}{\partial t} + c_g \times \nabla F = S_{tot} \dots\dots\dots(\text{Eq. 2-20}) \dots\dots\dots 22$$

$$S_{tot} = S_{in} + S_{ds} + S_{nl} \dots\dots\dots(\text{Eq. 2-21}) \dots\dots\dots 23$$

$$\gamma = \left( \frac{1}{\omega E} \right) \frac{\partial E}{\partial t} \dots\dots\dots(\text{Eq. 2-22}) \dots\dots\dots 23$$

$$\frac{\partial E(\omega)}{\partial t} = S_{in}(\omega) = \frac{1}{\rho_w g} \overline{p(x,t) \frac{\partial \eta(x,t)}{\partial t}} \dots\dots\dots(\text{Eq. 2-23}) \dots\dots\dots 24$$

$$S_{in}(f) = 2\pi \rho_a / \rho_w f \gamma(f) F(f) \dots\dots\dots(\text{Eq. 2-24}) \dots\dots\dots 24$$

$$\gamma = G \sqrt{B_n} \cdot \left[ \frac{U_{10}}{c} - 1 \right]^2 \dots\dots\dots(\text{Eq. 2-25}) \dots\dots\dots 26$$

$$G = 2.8 - 1.0 \cdot (1 + \tanh(10 \cdot \sqrt{B_n} \cdot \left[ \frac{U_{10}}{c} - 1 \right]^2 - 11)) \dots\dots\dots(\text{Eq. 2-26}) \dots\dots\dots 26$$

$$\tau = \tau_t + \tau_w + \tau_v \dots\dots\dots(\text{Eq. 2-27}) \dots\dots\dots 27$$

$$\tau = \rho_a C_d U_{10}^2 \dots\dots\dots(\text{Eq. 2-28}) \dots\dots\dots 28$$

$$S_{ds}(f) = a \cdot \underbrace{f \cdot A(f) \cdot (F(f) - F_T(f))}_{T_1(f)} + b \underbrace{\int_{f_p}^{f_{cut}} A(f) \cdot (F(f) - F_T(f)) df}_{T_2(f)} \dots\dots\dots(\text{Eq. 2-29}) \dots\dots\dots 31$$

$$\begin{cases} \mathbf{k}_1 + \mathbf{k}_2 = \mathbf{k}_3 + \mathbf{k}_4 \\ \omega_1 + \omega_2 = \omega_3 + \omega_4 \end{cases} \dots\dots\dots(\text{Eq. 2-30}) \dots\dots\dots 32$$

$$\frac{\partial N_1}{\partial t} = \iiint G_q(\mathbf{k}_1, \mathbf{k}_2, \mathbf{k}_3, \mathbf{k}_4) \delta(\mathbf{k}_1 + \mathbf{k}_2 - \mathbf{k}_3 - \mathbf{k}_4) \delta(\omega_1 + \omega_2 - \omega_3 - \omega_4) \times [N_1 N_3 (N_4 - N_2) + N_2 N_4 (N_3 - N_1)] d\mathbf{k}_2 d\mathbf{k}_3 d\mathbf{k}_4 \dots\dots\dots(\text{Eq. 2-31}) \dots\dots\dots 33$$

$$\varepsilon = \frac{\sigma^2 g^2}{U_h^4} \dots\dots\dots(\text{Eq. 2-32}) \dots\dots\dots 36$$

$$\mathbf{v} = \frac{f_p U_h}{g} \dots\dots\dots(\text{Eq. 2-33}) \dots\dots\dots 36$$

$$\chi = \frac{gx}{U_h^2} \dots\dots\dots(\text{Eq. 2-34}) \dots\dots\dots 36$$

$$\zeta = \frac{gt}{U_h} \dots\dots\dots(\text{Eq. 2-35}) \dots\dots\dots 36$$

$$\begin{aligned} \varepsilon &= A_{et} \cdot \zeta^{a_{\zeta t}} \\ \mathbf{v} &= A_{f\zeta} \cdot \zeta^{a_{\zeta f}} \end{aligned} \dots\dots\dots(\text{Eq. 2-36}) \dots\dots\dots 37$$

$$\begin{aligned} \varepsilon &= A_{ex} \cdot \chi^{a_{\chi ex}} \\ \mathbf{v} &= A_{f\chi} \cdot \chi^{a_{\chi f}} \end{aligned} \dots\dots\dots(\text{Eq. 2-37}) \dots\dots\dots 37$$

$$\begin{aligned} \mathbf{v} &= 2.40 \cdot \chi^{-0.275} \\ \varepsilon &= 8.3 \cdot 10^{-6} \cdot \mathbf{v}^{-3.01} \end{aligned} \dots\dots\dots(\text{Eq. 2-38}) \dots\dots\dots 38$$

$$\alpha = \begin{cases} 8.03 \cdot 10^{-2} \cdot \mathbf{v}^{1.24}, & \mathbf{v} \leq 0.23 \\ 13.2 \cdot 10^{-3}, & \mathbf{v} > 0.23 \end{cases} \dots\dots\dots(\text{Eq. 2-39}) \dots\dots\dots 38$$

$$\gamma_J \approx 7.6 \cdot \mathbf{v} \dots\dots\dots(\text{Eq. 2-40}) \dots\dots\dots 38$$

$$\frac{\partial F}{\partial t} = S_{tot} \dots\dots\dots(\text{Eq. 3-1}) \dots\dots\dots 45$$

$$F_{j+1} = F_j + \Delta F = F_j + S_{tot} \cdot \Delta t \dots\dots\dots(\text{Eq. 3-2}) \dots\dots\dots 45$$

$$A_{ft} = A_{fx} \frac{1}{a_{fx} + 1} \left[ \frac{R \cdot (a_{fx} + 1)}{2\pi} \right]^{a_{ft}}, \quad a_{ft} = \frac{a_{fx}}{a_{fx} + 1}$$

$$A_{et} = A_{ex} \left[ \frac{R \cdot (a_{fx} + 1)}{2\pi A_{fx}} \right]^{a_{et}}, \quad a_{et} = \frac{a_{ex}}{a_{fx} + 1} \dots\dots\dots(\text{Eq. 3-3}) \dots\dots\dots 48$$

$$v = 10.74 \cdot \zeta^{-0.38}$$

$$\varepsilon = 6.54 \cdot 10^{-9} \cdot \zeta^{1.14} \dots\dots\dots(\text{Eq. 3-4}) \dots\dots\dots 49$$

$$\tau_w = \tau - \tau_v \dots\dots\dots(\text{Eq. 4-1}) \dots\dots\dots 68$$

$$\tau_w' = \int M(f) df \dots\dots\dots(\text{Eq. 4-2}) \dots\dots\dots 68$$

$$M(f) = \rho_w g \frac{S_{in}(f)}{c(f)} \dots\dots\dots(\text{Eq. 4-3}) \dots\dots\dots 69$$

$$\tau_w' = \rho_w g \int \frac{S_{in}(f)}{c(f)} df \dots\dots\dots(\text{Eq. 4-4}) \dots\dots\dots 69$$

$$\tau_w' = \tau_w \dots\dots\dots(\text{Eq. 4-5}) \dots\dots\dots 69$$

$$\tau_w = \rho_a U_{10}^2 (C_D - C_V) \dots\dots\dots(\text{Eq. 4-6}) \dots\dots\dots 70$$

$$C_V = -5 \cdot 10^{-5} U_{10} + 1.1 \cdot 10^{-3} \dots\dots\dots(\text{Eq. 4-7}) \dots\dots\dots 70$$

$$C_D = [0.78 + 0.475 \cdot f(\delta) \cdot U_{10}] \times 10^{-3} \dots\dots\dots(\text{Eq. 4-8}) \dots\dots\dots 70$$

$$f(\delta) = 0.85^B A^{1/2} \delta^{-B} \dots\dots\dots(\text{Eq. 4-9}) \dots\dots\dots 70$$

$$\tau_w' = \int_{f_{min}}^{f_0} M(f) df + \int_{f_0}^{f_{max}} M(f) df \dots\dots\dots(\text{Eq. 4-10}) \dots\dots\dots 73$$

$$S_1 = \int_{f_{min}}^{f_0} M(f) df \quad \text{and} \quad S_2 = \int_{f_0}^{f_{max}} M(f) df \dots\dots\dots(\text{Eq. 4-11}) \dots\dots\dots 73$$

$$\begin{cases} \tau_w = S_1 + X \cdot S_2 \\ \tau'_w = S_1 + S_2 \end{cases} \dots\dots\dots(\text{Eq. 4-12}) \dots\dots\dots 73$$

$$X = 1 + \frac{\tau_w - \tau'_w}{S_2} \dots\dots\dots(\text{Eq. 4-13}) \dots\dots\dots 73$$

$$1 + \frac{\tau_w - \tau'_w}{S_2} > 0 \dots\dots\dots(\text{Eq. 4-14}) \dots\dots\dots 76$$

$$S_2 > \tau'_w - \tau_w \dots\dots\dots(\text{Eq. 4-15}) \dots\dots\dots 76$$

$$S_1 < \tau_w \dots\dots\dots(\text{Eq. 4-16}) \dots\dots\dots 76$$

$$L(f) = \exp\left(\frac{f_0 - f}{f} \cdot \eta\right) \dots\dots\dots(\text{Eq. 4-17}) \dots\dots\dots 79$$

$$\int_{f_0}^{f_{\max}} L(f)M(f)df = X \int_{f_0}^{f_{\max}} M(f)df \dots\dots\dots(\text{Eq. 4-18}) \dots\dots\dots 79$$

$$\int_{f_0}^{f_{\max}} L(f)M(f)df = L(f_i) \int_{f_0}^{f_{\max}} M(f)df \dots\dots\dots(\text{Eq. 4-19}) \dots\dots\dots 81$$

$$\begin{cases} L(f_0) = 1 \\ L(f_i) = X \end{cases} \dots\dots\dots(\text{Eq. 4-20}) \dots\dots\dots 81$$

$$\exp\left(\frac{f_0 - f_i}{f_i} \eta\right) = X \dots\dots\dots(\text{Eq. 4-21}) \dots\dots\dots 81$$

$$\eta = \frac{f_i \ln X}{f_0 - f_i} \dots\dots\dots(\text{Eq. 4-22}) \dots\dots\dots 81$$

$$\begin{cases} F(f, \theta) = \beta \frac{g^2}{(2\pi)^4} f_p^{-1} f^{-4} \exp\left[-\left(\frac{f}{f_p}\right)^{-4}\right] \cdot \gamma_D \exp\left[\frac{-(f-f_p)^2}{2\sigma^2 f_p^2}\right] & f \leq f_T \\ F(f, \theta) = \beta \frac{g^2}{(2\pi)^4} f_T f_p^{-1} f^{-5} \exp\left[-\left(\frac{f}{f_p}\right)^{-4}\right] \cdot \gamma_D \exp\left[\frac{-(f-f_p)^2}{2\sigma^2 f_p^2}\right] & f > f_T \end{cases} \dots\dots\dots(\text{Eq. 4-23}) \dots\dots\dots 89$$

$$T(f) = (2\pi)^4 f_p^{n+5} f^{-n} F(f) / 2g^2 \dots\dots\dots(\text{Eq. 4-24}) \dots\dots\dots 90$$

$$T(f) = \left(\frac{f_p}{f}\right)^{n+5} B(f) = \left(\frac{f_p}{f}\right)^{n+5} A^{-1}(f) B_n(f) \quad \text{.....(Eq. 4-25) ..... 90}$$

$$F_T(f) = 2g^2 (2\pi)^{-4} f_p^{-(n+5)} f^n T_T(f) \quad \text{.....(Eq. 4-26) ..... 110}$$

$$F_T(f) = 2g^2 (2\pi)^{-4} f^{-5} A^{-1}(f) B_{nT}(f) \quad \text{.....(Eq. 4-27) ..... 110}$$

$$\Delta F_p \leq 0 \quad \text{.....(Eq. 4-28) ..... 111}$$

$$R = \frac{\int S_{ds}(f) df}{\int S_{in}(f) df} \quad \text{.....(Eq. 4-29) ..... 116}$$

$$R_{linear} = \begin{cases} -0.12 U_{10}/c_p + 1.52, & 4.5 < U_{10}/c_p \leq 5.8 \\ 0.0031 U_{10}/c_p + 0.96, & 1.5 < U_{10}/c_p \leq 4.5 \\ -0.052 U_{10}/c_p + 1.043, & 0.83 < U_{10}/c_p \leq 1.5 \\ 1, & U_{10}/c_p = 0.83 \end{cases} \quad \text{.....(Eq. 4-30) ..... 116}$$

$$R_{smooth} = \begin{cases} 0.97 - 0.07 \times (1 + \tanh[3(U_{10}/c_p - 5.2)]), & 2 < U_{10}/c_p \leq 5.8 \\ 0.97 + 0.015 \times (1 - \tanh[5(U_{10}/c_p - 1.1)]), & 0.9 < U_{10}/c_p \leq 2 \\ 1, & 0.83 \leq U_{10}/c_p \leq 0.9 \end{cases} \quad \text{(Eq. 4-31) ..... 118}$$

$$\int S_{ds}(f) df = R \int S_{in}(f) df \quad \text{.....(Eq. 4-32) ..... 118}$$

$$W = \int S_{in}(f) df, \quad W_1 = \int_{f_{min}}^{f_p} S_{in}(f) df, \quad W_2 = \int_{f_p}^{f_{cut}} S_{in}(f) df \quad \text{..... 119}$$

$$D = \int S_{ds}(f) df, \quad S_1 = \int T_1(f) df, \quad S_2 = \int T_2(f) df \quad \text{.....(Eq. 4-33) ..... 119}$$

$$S_{11} = \int_{f_{min}}^{f_p} T_1(f) df, \quad S_{12} = \int_{f_p}^{f_{cut}} T_1(f) df \quad \text{..... 119}$$

$$S_{ds}(f) = a_0 \cdot T_1(f) \quad \text{.....(Eq. 4-34) ..... 119}$$

$$\int_{f_{min}}^{f_p} a_0 \cdot T_1(f) df = R \int_{f_{min}}^{f_p} S_{in}(f) df \quad \text{.....(Eq. 4-35) ..... 121}$$

$$a_0 = \frac{RW_1}{S_{11}} = \frac{R \int_{f_{\min}}^{f_p} S_{in}(f) df}{\int_{f_{\min}}^{f_p} f \cdot A(f) \cdot (F(f) - F_T(f)) df} \dots\dots\dots(\text{Eq. 4-36}) \dots\dots\dots 121$$

$$\begin{cases} D = RW \\ D = a_0 S_1 + b_0 S_2 \end{cases} \dots\dots\dots(\text{Eq. 4-37}) \dots\dots\dots 123$$

$$b_0 = \frac{RW - a_0 S_1}{S_2} \dots\dots\dots(\text{Eq. 4-38}) \dots\dots\dots 123$$

$$Z(f) = \left( \frac{f}{f_p} \right)^\mu \dots\dots\dots(\text{Eq. 4-39}) \dots\dots\dots 127$$

$$b = b_0 \cdot Z(f) \dots\dots\dots(\text{Eq. 4-40}) \dots\dots\dots 127$$

$$b = \frac{RW - a_0 S_1}{S_{02}} \dots\dots\dots(\text{Eq. 4-41}) \dots\dots\dots 127$$

$$b = \frac{RW}{S_{02}} \dots\dots\dots(\text{Eq. 4-42}) \dots\dots\dots 128$$

$$RW - a S_1 > 0 \dots\dots\dots(\text{Eq. 4-43}) \dots\dots\dots 132$$

$$a < \frac{RW_2}{S_{12}} \dots\dots\dots(\text{Eq. 4-44}) \dots\dots\dots 132$$

$$a = \begin{cases} a_0, & f \leq f_p \\ a_0 \cdot Z(f), & f > f_p \end{cases} \dots\dots\dots(\text{Eq. 4-45}) \dots\dots\dots 133$$

$$V(\theta, f, U_{10}/c_p) = \begin{cases} V_1(\theta, f, U_{10}/c_p) = A(f) \cdot \exp(-p(\theta + \theta_p)^2), & \theta < 0 \\ V_2(\theta, f, U_{10}/c_p) = A(f) \cdot \exp(-p(\theta - \theta_p)^2), & \theta \geq 0 \end{cases} \dots\dots\dots(\text{Eq. 4-46}) \dots\dots\dots 140$$

$$\begin{cases} \theta_p(f) = \theta_p(f_p) + \Delta\theta_f \frac{(f - f_s)}{(f_{cut} - f_s)} \\ \theta_p(U_{10}/c_p) = \theta_p(f_p) + \Delta\theta_{ucp} \frac{(5.7 - U_{10}/c_p)}{(5.7 - 0.83)} \end{cases} \dots\dots\dots(\text{Eq. 4-47}) \dots\dots\dots 140$$

$$S_{br}(v) = b_{br} \rho_w g^{-1} v^5 \Lambda(v) \dots\dots\dots(\text{Eq. 4-48}) \dots\dots\dots 144$$

$$\Lambda_m(v) = b_{br}^{-1} \rho_w^{-1} g v^{-5} S_{ds}(v) \dots\dots\dots(\text{Eq. 4-49}) \dots\dots\dots 144$$

$$b_{br} = \frac{g}{\rho_w} \frac{S_{ds}(v_p)}{v^5 \Lambda(v_p)} \dots\dots\dots(\text{Eq. 4-50}) \dots\dots\dots 145$$

$$\Lambda_{MM02}(v) = \Lambda(v)(10/U_{10})^3 = 3.3 \times 10^{-4} e^{-0.64v} \dots\dots\dots(\text{Eq. 4-51}) \dots\dots\dots 145$$

$$[b_{br}] = \frac{\left[ \frac{m}{s^2} \right] \left[ \frac{kg}{m^3} \frac{m}{s^2} m^2 \frac{m}{s \cdot rad} \right]}{\left[ \frac{kg}{m^3} \right] \left[ \frac{m}{s} \right]^5 \left[ \frac{1}{rad} \right]} = [1] \dots\dots\dots(\text{Eq. 4-52}) \dots\dots\dots 155$$

$$b_{alt} = \frac{g}{\rho_w} \frac{S_{ds}(f)(10/U_{10})^3}{v^5 \Lambda_{MM02}(v)} \dots\dots\dots(\text{Eq. 4-53}) \dots\dots\dots 155$$

# List of Figures

---

- Figure 2.1** Definition diagram to represent linear wave theory. Here,  $\lambda$  is wavelength,  $d$  - the water depth,  $H$  - the wave height,  $a$  - the amplitude and S. W. L. - represents the stationary water level. The wave profile ( $\eta(x, t)$ ) is assumed to be a function of distance ( $x$ ) and time ( $t$ ) (Young, 1999). 13
- Figure 2.2** Frequency-direction energy density spectrum with the peak frequency  $f_p = 0.3\text{Hz}$  and wind direction at  $0^\circ$ . 13
- Figure 2.3** Comparison of wave energy density spectra according to results of JONSWAP experiments (solid lines) and Donelan et al. (1985) (dashed lines) at different stages of wave development with the magnitudes of peak enhancement:  $\gamma_J = \{7, 5, 3.3, 2, 1\}$  at wind  $U_{10} = 10$  m/s. 16
- Figure 2.4** Comparison of the spectral saturation,  $B(f)$ , computed for the JONSWAP (bold lines) and Donelan (lines with dots) energy density spectra at different stages of wave development with the magnitudes of peak enhancement:  $\gamma_J = \{7, 3.3, 1\}$  at wind  $U_{10} = 10$  m/s. 21
- Figure 2.5** Comparison of the spectral saturation  $B_n(f)$  normalised by the spreading angle  $\theta_w(f)$ , for the JONSWAP (bold lines) and Donelan (lines with dots) energy density spectra at different stages of wave development with the magnitudes of peak enhancement:  $\gamma_J = \{7, 3.3, 1\}$  at wind  $U_{10} = 10$  m/s 21
- Figure 2.6** Example of quadruplet wavenumber vectors, which satisfy the resonance condition 35
- Figure 2.7** The so-called *figure of eight* diagram showing the interaction space for a given value  $\mathbf{k} = \mathbf{k}_1 + \mathbf{k}_2 = \mathbf{k}_3 + \mathbf{k}_4$  (Young, 1999). 35
- Figure 3.1** Comparing the significant wave height  $H_S$  as a function of the duration of the model runs with different time steps  $\Delta t$  and wind speed  $U_{10} = 0$  m/s. 50
- Figure 3.2** Growth curves of the model runs for the different wind speeds  $U_{10} = 7\text{m/s}$  (line with dots),  $10\text{m/s}$  (bold line),  $15\text{m/s}$  (line with crosses) and  $20\text{m/s}$  (line with asterisks). The graph shows the growth of non-dimensional energy  $\varepsilon$  as a function of non-dimensional frequency  $\nu$ . The model results are compared with the experimental data of Babanin and Soloviev (1998) (plane line) with 5% approximation limits (dashed lines).  $\varepsilon_{PM} = 3.64 \cdot 10^{-3}$  and  $\nu_{PM} = 0.13$  are the magnitudes of Pierson-Moskowitz limit, are also shown with bold lines. 50

- Figure 3.3** Growth curves of the model run CL1P0.5A20W10. The subplot (a) shows the curve of non-dimensional frequency  $\nu$  as a function of non-dimensional time  $\zeta$ ; and subplot (b) shows the growth of non-dimensional energy  $\varepsilon$  as a function of non-dimensional time  $\zeta$ . The model results are compared with the experimental data of Kahma (1981) (dashed line), Donelan et al. (1985) (dash-dotted line) and, Babanin and Soloviev (1998) (plane line). The magnitudes of Pierson-Moskowitz limit are shown as  $\varepsilon_{PM}$ ,  $\nu_{PM}$ , and  $\zeta_{PM}$ . 51
- Figure 4.1** Comparison of growth rates,  $\gamma(f)$ , according to Donelan et al. (2006) at different stages of wave development with  $U_{10} / c_p = \{5.8$  (bold lines),  $2.7$  (dashed bold lines),  $0.83$  (solid lines with dots)} at the wind speed  $U_{10} = 10$  m/s for the JONSWAP spectra (subplot [a]) and for the Donelan spectra (subplot [b]); the growth rates according to Donelan (1999) (solid lines) and Hsiao and Shemdin (1983) (dashed lines) are also shown. 58
- Figure 4.2** Comparison of growth rate according to Donelan et al. (2006) (bold line for the JONSWAP spectrum and solid line with dots for the Donelan spectrum), Donelan (1999) (solid line) and Hsiao and Shemdin (1983) (dashed line) for the average developed waves with  $U_{10} / c_p = 2.7$ , peak frequency,  $f_p = 0.43$ Hz and wind speed  $U_{10} = 10$  m/s. 59
- Figure 4.3** Comparison of the growth rates of peak frequency waves for the JONSWAP spectra (subplot [a]) and for the Donelan spectra (subplot [b]) as functions of the inverse wave age, for different wind speeds  $U_{10} = \{7\text{m/s}, 10\text{m/s}, 15\text{m/s}$  and  $20\text{m/s}\}$  and wind dependent drag coefficient,  $C_D(U_{10})$ . The growth rates are according to Donelan et al. (2006) (lines with markings: circles, dots, crosses and asterisks correspondingly to  $7\text{m/s}$ ,  $10\text{m/s}$ ,  $15\text{m/s}$  and  $20\text{m/s}$ ), Donelan (1999) (different type lines: solid, dashed, dash-dotted and dotted corresponding to  $U_{10} = \{7\text{m/s}, 10\text{m/s}, 15\text{m/s}$  and  $20\text{m/s}\}$ ) and Hsiao and Shemdin (1983) (bold line). 60
- Figure 4.4** Comparison of growth rate values at the peak frequencies according to Donelan et al. (2006) for the JONSWAP spectra (line with dots) and for the Donelan spectra (line with asterisks) at different stages of wave development at wind speed  $U_{10} = 10$  m/s; growth rates by Donelan (1999) (dashed bold line) and Hsiao and Shemdin (1983) (bold line) are also shown. 61
- Figure 4.5** Comparison of the wind source function according to Donelan et al. (2006) (a) Donelan (1999) (b) and Hsiao and Shemdin (c) (solid lines) for the JONSWAP spectra at different stages of wave development with  $U_{10} / c_p = \{5.8$  (plain lines),  $2.7$  (lines with crosses),  $0.83$  (lines with dots)} for the wind speed  $U_{10} = 10$  m/s. 63
- Figure 4.6** Comparison of wind source function according to Donelan et al. (2006) (solid line with dots), Donelan (1999) (solid line with crosses) and Hsiao and Shemdin (solid line) for the JONSWAP spectrum for the inverse wave age  $U_{10} / c_p = 2.7$ , the peak frequency  $f_p = 0.43$ Hz and wind speed  $U_{10} = 10$  m/s. 64

- Figure 4.7** Comparison of wind source function according to Donelan et al. (2006) (a), Donelan (1999) (b) and Hsiao and Shemdin (c) (solid lines) for the Donelan spectra at different stages of wave development with the inverse wave age  $U_{10} / c_p = \{5.8$  (plain lines),  $2.7$  (lines with crosses),  $0.83$  (lines with dots) $\}$  at wind  $U_{10} = 10$  m/s. 66
- Figure 4.8** Comparison of wind source function according to Donelan et al. (2006) (solid line with dots), Donelan (1999) (solid line with crosses) and Hsiao and Shemdin (solid line) for the Donelan spectrum for the inverse wave age  $U_{10}/c_p = 2.7$  ( $f_p = 0.43$ Hz) and the wind speed  $U_{10} = 10$  m/s. 67
- Figure 4.9** Comparison of wind source function according to Donelan et al. (2006) computed for the JONSWAP spectra (solid line) and for the Donelan spectra (solid line with dots) at different stages of wave development  $U_{10}/c_p = \{5.8, 2.7, 0.83\}$  for wind  $U_{10} = 10$  m/s. 67
- Figure 4.10** Comparison of wave-induced stresses  $\tau'_w$  computed for wind source functions according to Donelan et al. (2006) (solid line with dots), Donelan (1999) (solid line with asterisks) Hsiao and Shemdin (1983) (solid line with crosses) and Snyder (1981) (solid line with circles) for the JONSWAP spectra with wave-induced stress  $\tau_w$  from the stress balance (Eq. 4-1) [bold line for  $C_D(U_{10})$  and bold dashed line for  $C_D(U_{10}/c_p)$ ]. 74
- Figure 4.11** Comparison of wave-induced stresses  $\tau'_w$  computed for wind source functions according to Donelan et al. (2006) (solid line with dots), Donelan (1999) (solid line with asterisks) Hsiao and Shemdin (1983) (solid line with crosses) and Snyder (1981) (solid line with circles) for the Donelan spectra with wave-induced stress  $\tau_w$  from the stress balance (Eq. 4-1) (bold line for  $C_D(U_{10})$  and bold dashed line for  $C_D(U_{10}/c_p)$ ). 74
- Figure 4.12** Ratio of the wave-induced stress,  $\tau_w$  (Eq. 4-6), to the wave-induced stress,  $\tau'_w$  (Eq. 4-4) computed for the wind input source function according to Donelan et al. (2006) for the JONSWAP spectra at different stages of wave development at wind speed,  $U_{10} = 10$  m/s, for both type of drag coefficients  $C_D$ . 75
- Figure 4.13** Ratio of wave-induced stress,  $\tau_w$  (Eq. 4-6) to the wave-induced stress,  $\tau'_w$  (Eq. 4-4) computed for the wind input source function according to Donelan et al. (2006) for the Donelan spectra at different stages of wave development at wind speed,  $U_{10} = 10$  m/s, for both type of drag coefficient  $C_D$ . 75
- Figure 4.14** Correcting coefficient  $X$  (Eq. 4-13) for stress correction of the wind input source function according to Donelan et al. (2006) computed for the JONSWAP spectra, for both type of drag coefficient  $C_D$  and wind speed,  $U_{10} = 10$  m/s. 78
- Figure 4.15** Correcting coefficient  $X$  (Eq. 4-13) for stress correction of the wind input source function according to Donelan et al. (2006) computed for the Donelan (1985) spectra, for both type of drag coefficient  $C_D$  and wind speed,  $U_{10} = 10$  m/s. 78
- Figure 4.16** Comparison of wind source function according to Donelan et al. (2006) before and after applying the coefficient  $X$  for the JONSWAP (solid line and line with dots, respectively) and Donelan (dashed line and line with crosses, respectively) spectra, with spectral parameter,  $\gamma_s = 3.3$ , at wind  $U_{10} = 10$  m/s. 79

- Figure 4.17** Comparison of wind source function according to Donelan et al. (2006) before and after applying stress correction function  $L(f)$  (Eq. 4-17). Computations were performed for the JONSWAP (solid line and line with dots, respectively) and Donelan (dashed line) spectra for the average developed waves with  $U_{10}/c_p = 2.7$  and the wind speed  $U_{10} = 10$  m/s. 82
- Figure 4.18** Comparison of wind source function according to Donelan et al. (2006) before and after applying stress correction function  $L(f)$  (Eq. 4-17). Computations were performed for the JONSWAP (solid line and line with dots respectively) and Donelan (dashed line and line with crosses, respectively) spectra for the average developed waves with  $U_{10}/c_p = 2.7$  and the wind speed  $U_{10} = 10$  m/s. 85
- Figure 4.19** Comparison of growth rate spectra before and after applying stress correction function  $L(f)$  (Eq. 4-17). Computations were performed for the JONSWAP spectrum for the average developed waves with  $U_{10}/c_p = 2.7$  and the wind speed  $U_{10} = 10$  m/s. 85
- Figure 4.20** Comparison of growth rate spectra before and after applying stress correction function  $L(f)$  (Eq. 4-17). Computations were performed for the Donelan spectrum for the average developed waves with  $U_{10}/c_p = 2.7$  and the wind speed  $U_{10} = 10$  m/s. 86
- Figure 4.21** Wind source function according to Donelan et al. (2006) computed with applying stress correction function  $L(f)$  (Eq. 4-17). Computations were performed for the JONSWAP spectra at different stages of wave development with  $U_{10}/c_p = \{5.8$  (plain lines),  $4.5$  (line with circles),  $2.7$  (lines with crosses),  $0.83$  (lines with dots)} for the wind speed  $U_{10} = 10$  m/s. 86
- Figure 4.22** Wind source function according to Donelan et al. (2006) computed with applying stress correction function  $L(f)$  (Eq. 4-17). Computations were performed for the Donelan (1985) spectra at different stages of wave development with inverse wave age  $U_{10}/c_p = \{5.8$  (plain lines),  $2.7$  (lines with crosses),  $0.83$  (lines with dots)} for the wind speed  $U_{10} = 10$  m/s. 88
- Figure 4.23** Comparing the parameter,  $\eta$  of the stress correction function  $L(f)$  (Eq. 4-17) computed for wind source function according to Donelan et al. (2006) for the JONSWAP spectra for  $C_D(U_{10})$  (line with dots) and for  $C_D(U_{10}/c_p)$  (line with asterisks). 88
- Figure 4.24** Comparing the parameter,  $\eta$  of stress correction function  $L(f)$  (Eq. 4-17) computed for wind source function according to Donelan et al. (2006) for the Donelan (1985) spectra for  $C_D(U_{10})$  (line with dots) and for  $C_D(U_{10}/c_p)$  (line with asterisks). 91
- Figure 4.25** Combi spectrum for the average developed waves with  $U_{10}/c_p = 2.7$  and the wind speed  $U_{10} = 10$  m/s. JONSWAP and Donelan's spectra are also shown (solid line for the JONSWAP spectrum and dashed line for the Donelan spectrum). 91

- Figure 4.26** Comparison of the saturation transformer,  $T(f)$  (Eq. 4-24) for the JONSWAP (solid lines) and Donelan (lines with dots) energy density spectra at different stages of wave development with inverse wave age  $U_{10} / c_p = \{5.8$  (plain lines),  $2.7$  (lines with crosses),  $0.83$  (lines with dots) $\}$  for the wind speed  $U_{10} = 10$  m/s. 93
- Figure 4.27** Comparison of the saturation transformer,  $T(f)$  (Eq. 4-24) with  $n = -5$  for the Combi energy density spectra at different stages of wave development with inverse wave age  $U_{10} / c_p = \{5.8$  (plain line),  $2.7$  (line with crosses),  $0.83$  (line with dots) $\}$  for the wind speed  $U_{10} = 10$  m/s. 93
- Figure 4.28** Comparison of wave induced stresses  $\tau_w$  computed for wind source function according to Donelan et al. (2006) for the Combi spectra using  $T(f)$  (line with dots) with wave induced stress computed from total wind stress by formula (Eq. 4-6) (bold line for  $C_D(U_{10})$  and dashed bold line for  $C_D(U_{10}/c_p)$ ). 96
- Figure 4.29** Comparison of wave-induced stresses computed for the Combi spectra using  $T(f)$  (line with asterisks), for the JONSWAP (line with dots) and Donelan (line with crosses) spectra using  $B(f)$  relative to the wave induced stress computed from total wind stress by formula (Eq. 4-6) (bold line for  $C_D(U_{10})$  and dashed bold line for  $C_D(U_{10}/c_p)$ ). 96
- Figure 4.30** Comparing correcting coefficient  $X$  (Eq. 4-13) for stress correction of the wind input source function according to Donelan et al. (2006) computed for the Combi spectra using  $T(f)$  (solid line with asterisks), for  $C_D(U_{10})$  (line with dots) and  $C_D(U_{10}/c_p)$  (line with asterisks) for wind speed  $U_{10} = 10$  m/s. 97
- Figure 4.31** Comparison of corrected with  $L(f)$  (4.17) wind source function according to Donelan et al. (2006) computed for different type of energy density spectra. Computations were performed for the JONSWAP (solid line), Donelan (line with crosses) and Combi (line with dots) spectra for the average developed waves with inverse wave age  $U_{10}/c_p = 2.7$  and the wind speed  $U_{10} = 10$  m/s. 97
- Figure 4.32** Wind source function according to Donelan et al. (2006) computed with applying stress correction  $L(f)$  (Eq. 4-17) for  $C_D(U_{10})$ . Computations were performed for the Combi spectra at different stages of wave development with  $U_{10} / c_p = \{5.8$  (plain line),  $4.5$  (line with circles),  $2.7$  (line with crosses),  $0.83$  (line with dots) $\}$  for the wind speed  $U_{10} = 10$  m/s. 98
- Figure 4.33** Wind source function according to Donelan et al. (2006) computed with applying of stress correction  $L(f)$  (Eq. 4-17) for  $C_D(U_{10}/c_p)$ . Computations were performed for the Combi spectra at different stages of wave development with  $U_{10} / c_p = \{5.8$  (plain line),  $4.5$  (line with circles),  $2.7$  (line with crosses),  $0.83$  (line with dots) $\}$  for the wind speed  $U_{10} = 10$  m/s. 98
- Figure 4.34** Comparing the correction rate parameter,  $\eta$  of the stress correction function  $L(f)$  (Eq. 4-17) computed for wind source functions according to different authors for the Combi spectra and  $C_D(U_{10})$ . 100
- Figure 4.35** Comparing the correction rate parameter,  $\eta$  of stress correction function  $L(f)$  (Eq. 4-17) computed for wind source function according to Donelan et al. (2006) for the Combi for  $C_D(U_{10})$  (line with dots) and for  $C_D(U_{10}/c_p)$  (line with asterisks). 100

- Figure 4.36** Comparing the correction rate parameter,  $\eta$  of stress correction function  $L(f)$  (Eq. 4-17) computed for wind source functions according to different authors for the Combi spectra and  $C_D(U_{10}/c_p)$ . 103
- Figure 4.37** Comparison of wind source function according to Donelan et al. (2006) after stress correction with  $L(f)$  from (Eq. 4-17) for the Combi spectrum for the average developed waves with the inverse wave age  $U_{10}/c_p = 2.7$ , at different winds  $U_{10} = \{7 \text{ m/s}, 10 \text{ m/s}, 20 \text{ m/s and } 30 \text{ m/s}\}$  for  $C_D(U_{10})$ . 103
- Figure 4.38** Comparison of wind source function according to Donelan et al. (2006) after stress correction with  $L(f)$  from (Eq. 4-17) for the Combi spectrum for the average developed waves with the inverse wave age  $U_{10}/c_p = 2.7$ , at different winds  $U_{10} = \{7 \text{ m/s}, 10 \text{ m/s}, 20 \text{ m/s and } 30 \text{ m/s}\}$  for  $C_D(U_{10}/c_p)$ . 104
- Figure 4.39** Comparison of the wind source function according to Donelan et al. (2006) after stress correction with  $L(f)$  from (Eq. 4-17) for  $C_D(U_{10}/c_p)$  (bold line), with the wind input source functions of Donelan (1999) (line with crosses) and Hsiao and Shemdin (solid line) for the Combi spectrum for the average developed waves with the inverse wave age  $U_{10}/c_p = 2.7$ , at different winds  $U_{10} = \{7 \text{ m/s}, 10 \text{ m/s}, 20 \text{ m/s and } 30 \text{ m/s}\}$ . 104
- Figure 4.40** Comparison of corrected wind source functions for  $C_D(U_{10}/c_p)$ : Donelan et al. (2006) (bold line), Donelan (1999) (line with crosses) and Hsiao and Shemdin (solid line) for the Combi spectrum for the average developed waves with the inverse wave age  $U_{10}/c_p = 2.7$ , at different winds  $U_{10} = \{7 \text{ m/s}, 10 \text{ m/s}, 20 \text{ m/s and } 30 \text{ m/s}\}$ . 105
- Figure 4.41** The threshold spectrum  $F_T(f)$  computed for the Combi spectrum of the fully developed waves ( $f_p = 0.13\text{Hz}$ ) with the inverse wave age  $U_{10}/c_p = 0.83$ , for the wind speed  $U_{10} = 10 \text{ m/s}$ . The shaded area is showing dissipating part of the wave energy spectrum. 113
- Figure 4.42** Ratio of the dissipating wave energy to the spectral energy density as a function of the relative frequency computed for the spectral saturation threshold value  $\sqrt{B_{nT}}(f) = 0.035$ . The computations were performed for the Combi spectrum of the fully developed waves ( $f_p = 0.13\text{Hz}$ ) with  $U_{10}/c_p = 0.83$  for the wind speed  $U_{10} = 10 \text{ m/s}$ . 113
- Figure 4.43** The spectral dissipation function  $S_{ds}(f)$  (Eq. 2-29) (bold line) with the two terms  $T_1(f)$  (line with dots) and  $T_2(f)$  (line with asterisks) with coefficients  $a = b = 0.0065$ . The computations were performed for the Combi spectrum of the average-developed waves ( $f_p = 0.13\text{Hz}$ ) with  $U_{10}/c_p = 0.27$  for the wind speed  $U_{10} = 10 \text{ m/s}$ . 117
- Figure 4.44** Figure 6 from Donelan (1998) showing the fraction of momentum (dashed line) and of energy (plain line) from the wind is delivered to the surface waters. 117
- Figure 4.45** Two parameterisation forms of the dissipation rate:  $R_{linear}$  (Eq. 4-30) and  $R_{smooth}$  (Eq. 4-31). The computations were performed for the Combi spectra at the different stages of the wave development for the wind speed  $U_{10} = 10 \text{ m/s}$ . 120

- Figure 4.46** Schematic illustration of the notations (4.2-8) for the computations of coefficients  $a$  and  $b$  of the spectral dissipation function  $S_{ds}(f)$  (bold line) with its two phase terms  $T_1(f)$  (dashed line) and  $T_2(f)$  (solid line). The wind input source function  $S_{in}(f)$  (line with dots) is also shown. 120
- Figure 4.47** Comparison of integral values of the wind input source function  $S_{in}(f)$  (bold line) with the wave-wave nonlinear interaction source term  $S_{nl}(f)$  (plain line) for long-scale spectral components. Integration was performed in the range  $[f_{min}, f_p]$ . 122
- Figure 4.48** Coefficients  $a_0$  (Eq. 4-36) (line with asterisks) and  $b_0$  (Eq. 4-38) (line with dots) as the functions of the wind forcing parameter  $U_{10} / c_p$  computed for the Combi spectra at the different stages of the wave development for the wind speed  $U_{10} = 10$  m/s. The experimental coefficient  $a_{exp} = 0.0065$  (bold line) is shown. 125
- Figure 4.49** The spectral dissipation function  $S_{ds}(f)$  (line with dots) with coefficients  $a_0$  (Eq. 4-2-11) and  $b_0$  (Eq. 4-2-13). The corresponding wind input source functions  $S_{in}(f)$  (plain line) is also shown. Computations were performed for the Combi spectrum of the average-developed waves with wind forcing  $U_{10} / c_p = 2.7$  for the wind speed  $U_{10} = 10$  m/s. 125
- Figure 4.50** Coefficients  $a_0$  (Eq. 4-36) (line with asterisks) and  $b_0$  before (Eq. 4.38) (dashed line) and after the correction in the high frequency spectral tail (Eq. 4-41) (line with dots) of the wave dissipation source term computed for the Combi spectra at different stages of the wave development for the wind speed  $U_{10} = 10$  m/s. The experimental coefficient  $a_x = 0.0065$  (bold line) is also shown. 129
- Figure 4.51** Results of computations of coefficients  $a_0$  (bold line in all subplots) and  $b$  (Eq. 4-41) for the JONSWAP spectra (subplot [a]), the Donelan (1985) spectra (subplot [b]) and the Combi spectra (subplot [c]), at different stages of the wave development at different wind speeds  $U_{10} = \{7\text{m/s (plain line), } 10\text{m/s (line with dots), } 15\text{m/s (line with asterisks), } 20\text{m/s (line with circles) and } 30\text{m/s (line with crosses)}\}$ . The experimental coefficient  $a_{exp} = 0.0065$  (bold dashed line) is shown. 130
- Figure 4.52** Results of computations of the coefficients  $a$  (Eq. 4-45) (bold line in all subplots) and  $b$  (Eq. 4-41) after the correction with the function  $Z(f)$  (Eq. 4-39) for the JONSWAP spectra (subplot [a]), the Donelan (1985) spectra (subplot [b]) and the Combi spectra (subplot [c]), at different stages of the wave development at different wind speeds  $U_{10} = \{7\text{m/s (dashed line), } 10\text{m/s (line with dots), } 15\text{m/s (line with asterisks), } 20\text{m/s (line with circles) and } 30\text{m/s (line with crosses)}\}$ . The experimental coefficient  $a_{exp} = 0.0065$  (bold dashed line) is shown. 136
- Figure 4.53** Coefficients  $a$  (Eq. 4-45) and  $b$  (Eq. 4-41) after the applied correction using the exponential function  $Z(f)$  (Eq. 4-39). Coefficient  $b$  before the correction is also shown as  $b_{orig}$  (dashed line). Computations were performed for the Combi spectra at different stages of the wave development for the wind speed  $U_{10} = 10$  m/s The experimental coefficient  $a_x = 0.0065$  (bold dashed line) is also shown. 137

- Figure 4.54** The spectral dissipation source function  $S_{ds}(f)$  (Eq. 2-29) computed with coefficients  $a$  (Eq. 4-45) and  $b$  (Eq. 4-41). The corresponding wind input source functions  $S_{in}(f)$  are also shown. Computations were performed for the Combi spectra at different stages of the wave development with the wind forcing conditions:  $U_{10} / c_p = \{5.7$  (bold line),  $2.7$  (bold line with crosses),  $0.83$  (bold line with dots) $\}$ , for the wind speed  $U_{10} = 10$  m/s. 137
- Figure 4.55** Dissipation source term  $S_{ds}(f)$  (Eq. 2-3-10) computed with coefficients  $a$  (Eq. 4-2-20) and  $b$  (Eq. 4-2-16) for the Combi spectra of the average-developed waves ( $U_{10} / c_p = 2.7$ ) for the different wind speeds  $U_{10} = \{7$  m/s (plain line),  $10$  m/s (bold line),  $15$  m/s (line with dots),  $20$  m/s (line with crosses) and  $30$  m/s (line with circles) $\}$  and wind forcing parameter,  $U_{10} / c_p = 2.7$ . 138
- Figure 4.56** Coefficient  $a$  (Eq. 4-45) (continuous lines) and  $b$  (Eq. 4-41) (dashed lines) computed for different values of the threshold steepness  $\sqrt{B_{nT}(f)}$  as a function of the wind forcing parameter  $U_{10} / c_p$ . Computations were performed for the Combi spectra at different stage of the wave development for the wind speed  $U_{10} = 10$  m/s. 138
- Figure 4.57** Directional spreading function  $V(f, \theta_p)$  (Eq. 4-46) with different values of the parameters  $\theta_p$  and  $p$ . 142
- Figure 4.58** Two-dimensional dissipation spectrum  $S_{ds}(f, \theta)$  with the bimodal directional spreading  $V(f, \theta_p)$  (Eq. 4-46) ( $\theta_p = 20^\circ$ ,  $p = 1$  and  $\Delta\theta_f = 10^\circ$  with  $f_s = 3f_p$ ) computed for the Combi spectrum of the average-developed waves with the inverse wave age  $U_{10} / c_p = 2.7$  for the wind speed  $U_{10} = 10$  m/s. 142
- Figure 4.59** The wavenumber Combi spectrum similar to the wavenumber spectrum observed by Melville and Matusov (2002) for well developed waves with wind forcing  $U_{10} / c_p = 1.3$  and wind speed  $U_{10} = 13.6$  m/s. Transition from  $k^{-5/2}$  slope to a  $k^{-3}$ . 148
- Figure 4.60** Comparing the average length of the breaking crests spectra  $A_m(k)(10 / U_{10})^3$ , computed by (Eq. 4-49) using  $b_{br} = 0.001$ , with the observed  $A_{MM02}(k)$  (Melville and Matusov, 2002). The computations were performed for the Combi spectrum for the mature waves with wind forcing  $U_{10} / c_p = 1.3$  and the wind speed  $U_{10} = 10$  m/s. 148
- Figure 4.61** Comparing a new dissipation function  $S_{ds}(k)$  (Eq. 2-29) with the dissipation due to the wave breaking  $S_{br}(k)$  (Eq. 4-48) (Melville and Matusov, 2002) using different values of coefficient  $b_{br} = \{2 \times 10^{-5}$  (dashed line),  $1 \times 10^{-3}$  (plain line) and  $8.5 \times 10^{-3}$  (bold line) $\}$ . Computations were performed for the Combi spectra of the well-developed waves with wind forcing  $U_{10} / c_p = 1.3$  and for the wind speeds  $U_{10} = \{7.2$  m/s (line with dots),  $9.8$  m/s (line with crosses),  $13.6$  m/s (line with asterisks) $\}$ . The computed dissipation functions  $S_{ds}(f)$  (Eq. 2-29) are weighted by the term  $(10 / U_{10})^3$ . 150

- Figure 4.62** Coefficient  $b_{br}$  (Eq. 4-50) as a function of the wind forcing parameter  $U_{10} / c_p$  computed at the spectral peak of the Combi spectra at different stages of the wave development for the different wind speeds:  $U_{10} = \{7.2\text{m/s (plain line), 9.8m/s (line with dots), 13.6m/s (line with asterisks), 15m/s (line with circles), 20m/s (line with crosses) and 30m/s (line with diamonds)}\}$ . 150
- Figure 4.63** Comparing the wave spectral dissipation source functions  $S_{ds}(f)$  computed for the Combi spectra at different stages of the wave development with the wind forcing conditions:  $U_{10} / c_p = \{5.7$  (plain line), 4.5 (line with circles) 2.7 (line with crosses), 1.6 (line with dots) and 0.83 (line with asterisks)}, for the wind speed  $U_{10} = 10$  m/s. The dissipation functions are weighted by the term  $(10 / U_{10})^3$ . 152
- Figure 4.64** Comparing the wave spectral dissipation source functions  $S_{ds}(f)$  (2-29) computed for the Combi spectrum of the mature waves with the wind forcing parameter:  $U_{10} / c_p = 1.6$  for the different wind speeds  $U_{10} = \{7.2\text{m/s (plain line), 9.8m/s (line with crosses), 13.6m/s (line with dots), 20m/s (line with asterisks) and 30m/s (line with circles)}\}$ . The computed dissipation functions are weighted by the term  $(10 / U_{10})^3$ . 152
- Figure 4.65** Comparing the results of computations of  $A_m(v_p)$  computed for the Combi spectra of the waves with wind forcing  $U_{10} / c_p = 1.2$  and 0.98, for the wind speed  $U_{10} = 12$  m/s to the corresponding wave breaking data according to Gemmrich (2005) ( $A_{G05}(v_p)$ ) and model computations by Banner et al. (2006) ( $A_{B07}(v_p)$ ). 154
- Figure 4.66** Comparing coefficient  $b_{br}$  (Eq. 4-40) with coefficient  $b_{alt}$  for (Eq. 4-54) computed for the Combi spectra at different stages of the wave development for the wind speed  $U_{10} = 10$  m/s. The experimental values  $b_{MM02}$  for (Melville and Matusov, 2002) and  $b_{G06}$  for (Gemmrich, 2006) are also shown. 156
- Figure 4.67** Split-balance scheme integrated with the self-correcting routine of the wave model WAVETIME-1. 163
- Figure 4.68** The integral of  $S_{tot}$  as function of the inverse wave age produced by the model during the run UP0.5A20W10. 167
- Figure 4.69** Coefficient  $a$  and  $b$  during the model run UP0.5A20W10. 167
- Figure 4.70** Growth curves of the model run CL1P0.5A20W10. The subplot (a) shows the growth of non-dimensional energy  $\varepsilon$  as a function of non-dimensional frequency  $\nu$ ; and subplot (b) shows the growth of non-dimensional energy  $\varepsilon$  as a function of the inverse wave age  $U_{10} / c_p$ . The model results are compared with the experimental data of Babanin and Soloviev (1998) (plain line) with 10% approximation limits (dashed lines). The  $\varepsilon_{PM} = 3.64 * 10^{-3}$  and  $\nu_{PM} = 0.13$ , the magnitudes of the Pierson-Moskowitz limit are also shown. 169

- Figure 4.71** Growth curves of the model run CL1P0.5A20W10. The subplot (a) shows the growth of non-dimensional frequency  $\nu$  as a function of non-dimensional time  $\zeta$ ; and subplot (b) shows the growth of non-dimensional energy  $\varepsilon$  as a function of non-dimensional time  $\zeta$ . The model results are compared with the experimental data of Kahma (1981) (dashed line), Donelan et al. (1985) (dash-dotted line) and, Babanin and Soloviev (1998) (plane line). The magnitudes of Pierson-Moskowitz limit are also shown as  $\varepsilon_{PM}$ ,  $\nu_{PM}$ , and  $\zeta_{PM}$ . 170
- Figure 4.72** Comparing the growth curves computed for the different wind speeds  $U_{10} = 7\text{m/s}$ ,  $10\text{m/s}$ ,  $15\text{m/s}$  and  $20\text{m/s}$ . with the experimental data of Babanin and Soloviev (1998) (plain line) with 10% approximation limits (dashed lines). The magnitude of energy for the Pierson-Moskowitz limit is also shown as  $\varepsilon_{PM}$ . 171
- Figure 4.73** Values of  $\alpha$  during the model run CL1P0.5A20W10. The results of computations are compared with the experimental values obtained by different studies. 173
- Figure 4.74** Values of nondimensional spectral parameters  $\alpha_{BY}$  (subplot [a]) and  $n$  (subplot [b]) for wind direction slice of the wavenumber spectra as functions of the inverse wave age  $U_{10} / c_p$  for the model run CL1P0.5A20W10. The parameters  $\alpha_{BY}$  and  $n$  were computed by means of the least square method for the model data in the high-frequency range  $f > 2.5f_p$ . The model results (lines with dots) are compared to the results of Banner and Young (1994) (bold lines). 174
- Figure 4.75** The similarity parameter  $\zeta$  as a function of the inverse wave age  $U_{10} / c_p$  computed from the results of the model run CL1P0.5A20W10. 175
- Figure 4.76** Directional spreading function of the wave spectrum at the average stage of wave development ( $U_{10} / c_p = 2.7$ ) from the model run CL1P0.5A20W10. The computations were performed for the directional spectral slices at the frequencies  $f_p$ ,  $2f_p$  and  $3f_p$ . An angle  $\theta = 0$  corresponds to the wind direction. 177
- Figure 4.77** Directional spreading function of the wave spectrum at the average stage of wave development ( $U_{10} / c_p = 2.7$ ) from the model run CL1P0.5A20W10. The computations were performed for the directional spectral slices at the frequencies  $f_p$ ,  $0.9f_p$ ,  $0.8f_p$  and  $0.7f_p$ . An angle  $\theta = 0$  corresponds to the wind direction. 177
- Figure 4.78** The sidelobe ratio  $\lambda$  at the frequencies  $2f_p$  and  $3f_p$  as a function of inverse wave age  $U_{10} / c_p$  during the model run CL1P0.5A10W10. 178
- Figure 4.79** Comparisons of the model results for the directional spreading parameter  $A$  with the experimental data of Babanin and Soloviev (1998). The computations were performed for the directional spectral slices at the frequencies  $f_p$ ,  $2f_p$  and  $3f_p$ . 179
- Figure 4.80** Comparisons of the directional spreading parameter  $A$  computed for different wind speeds  $U_{10} = 10$  (bold lines),  $20$  (plain lines) m/s. The computations were performed for the directional spectral slices at the frequencies  $f_p$  (plain line),  $2f_p$  (dashed lines) and  $3f_p$  (lines with crosses). 180

- Figure 4.81** Comparison of the correction rates  $\eta$  as functions of the inverse wave age  $U_{10} / c_p$  computed for the model run CP0.5A20W10 (shown as WT-1) and for the MATLAB modeled wave evolution for the wind speed  $U_{10} = 10\text{m/s}$ . 181
- Figure 4.82** Comparisons of the correction rate  $\eta$  as a function of the inverse wave age  $U_{10} / c_p$  computed for model runs with various wind speeds  $U_{10} = 7\text{m/s}$ ,  $10\text{m/s}$ ,  $15\text{m/s}$  and  $20\text{m/s}$ . 183
- Figure 4.83** Coefficients  $a$  and  $b$  of the new dissipation source term  $S_{ds}(f)$  as functions of the inverse wave age  $U_{10} / c_p$  for the model run CP0.5A20W10 (assigned as WT-1) in the both subplots (a) and (b). The experimental value of  $a_{exp} = b_{exp} = 0.0065$  is shown in both subplots. The coefficients  $a$  and  $b$  from the model run CP0.5A20W10 are compared with coefficients of the dissipation source term computed from the MATLAB pseudo-evolution of the Combi spectra for the wind speed  $U_{10} = 10\text{m/s}$  (assigned by MATLAB). 184
- Figure 4.84** Coefficients  $a$  and  $b$  as functions of the inverse wave age  $U_{10} / c_p$  computed for the model runs for different wind speeds  $U_{10} = 7\text{m/s}$  (plain line),  $10\text{m/s}$  (bold line),  $15\text{m/s}$  (line with dots) and  $20\text{m/s}$  (line with asterisk). 186
- Figure 4.85** Slope exponent  $\mu$  computed for both source terms  $S_{in}(f)$  (line with dots) and  $S_{ds}(f)$  (line with asterisk) as a function of the inverse wave age  $U_{10} / c_p$  for the model runs with different wind speeds  $U_{10} = 7\text{m/s}$ ,  $10\text{m/s}$ ,  $15\text{m/s}$  and  $20\text{m/s}$  shown in the subplots (a), (b), (c) and (d), respectively. 188
- Figure 4.86** Coefficient  $b_{br}$  as a function of the inverse wave age  $U_{10} / c_p$  computed from the model run CP0.5A20W10 (assigned as WT-1) (bold line). The model results were compared with the experimental values  $b_{MM02} = 8.5 \times 10^{-3}$  (Melville and Matusov, 2002) (plain line) and  $b_{G05} = 2 \times 10^{-5}$  (Gemmrich, 2006) (dashed line) and the results of pseudo-evolution performed in MATLAB (line with dots). 190
- Figure 4.87** The coefficient  $b_{br}$  as a function of the inverse wave age  $U_{10} / c_p$  computed for the model runs with different wind speed  $U_{10} = 7\text{m/s}$ ,  $10\text{m/s}$ ,  $15\text{m/s}$  and  $20\text{m/s}$ . 190
- Figure 4.88** Comparison of the dissipation source function produced by model run CP0.5A20W10 for dominant waves with inverse wave age  $U_{10} / c_p = 1.55$  with the dissipation function computed by Melville and Matusov (2002) on the basis of their experimental data. 191

# Abstract

---

The present study comprised an intensive investigation of the two newly proposed parameterisation forms for the wind input source term  $S_{in}$  (Donelan et al., 2006) and the wave dissipation source term  $S_{ds}$  (Young and Babanin, 2006) proposed on the basis of the recent experimental findings at Lake George, New South Wales, Australia in 1997-2000. The main objective of this study was to obtain advanced spectral forms for the wind input source function  $S_{in}$  and wave spectral dissipation source function  $S_{ds}$ , which satisfy important physical constraints.

A new approach was developed to achieve the objectives of this study, within the strong physical framework. This approach resulted in a new balance scheme between the energy source terms in the wave model, mentioned before as the split balance scheme (Badulin, 2006). The wave-induced stress was defined as the main physical constraint for a new wave model including recently suggested source functions for the wind input and wave dissipation source terms. Within this approach, a new methodology was developed for correction of the wind input source function  $S_{in}$ . Another important physical constraint was the consistency between the wave dissipation and the wind energy input to the waves. The new parameter, the dissipation rate,  $R$ , was introduced in this study, as the ratio of the wave dissipation energy to the wind input energy. The parameterisation form of the dissipation rate is presented as a function of the inverse wave age  $U_{10} / c_p$ . Some aspects of wave spectral modelling regarding the shape of the wave spectrum and spectral saturation were revised.

The two-phase behaviour of the spectral dissipation function was investigated in terms of the functional dependency of the coefficients  $a$  for the inherent wave breaking term and  $b$  for the forced dissipation term. The present study found that the both coefficients have functional dependence on the inverse wave age  $U_{10} / c_p$  and the spectral frequency. Based on the experimental data by Young and Babanin (2006), a new directional spreading function of bimodal shape was developed for the wave dissipation source term.

The performance of the new spectral functions of the wind input  $S_{in}(f)$  and the wave dissipation  $S_{ds}(f)$  source terms was assessed using a new third-generation two-dimensional

research wave model WAVETIME-1. The model incorporating the corrected source functions was able to reproduce the existing experimental data.

# Statement of Originality

---

I hereby state that this thesis contains no material which has been accepted for the award of any other degree or diploma in any University or other tertiary institution. To the best of my knowledge and belief, the thesis contains no material previously published or written by another person, except where stated.

I give consent for this thesis to be available for photocopying and loan purposes after depositing in The University of Adelaide library.

The experiments reported in this work were performed by myself and any assistance received from others is acknowledged. To my knowledge, there are no intellectual property issues or conflicts of interest with other persons or organizations with respect to the data presented in this thesis.

**Kakha Tsagareli**

November 2008

# Acknowledgements

---

I would like to thank my supervisors, Prof. Ian Young, Dr. Alex Babanin and Dr. David Walker for giving me the opportunity to work with them, their encouragement and continued support throughout my project. Thank you for being such awesome supervisors, who helped me enjoy the new experience of being a postgraduate student and getting me through all the difficulties that I experienced at some points of my study. Thank you especially for the meticulous proofreading of my work. It was a pleasure to work with you, develop and discover myself in a new field.

I would like to particularly thank Dr. Gerbrant van Vledder of Alkyon Hydraulic Consultancy and Research (Emelood, the Netherlands), for providing his great help and support regarding a new wave model WAVETIME-1.

My very special thanks to Dr. Eric Rogers, who unconditionally contributed his time and provided valuable comments to this study.

My special thanks to Dr. Joseph Davis for his faithful support, warm friendship and responsive heart. I am grateful to Dr. Joseph Davis for valuable discussions and his provision of a number of useful MATLAB routines. It was great honour to share an office with Dr. Joseph Davis while I was undertaking this study. I would like to express my gratitude to Dr. Aaron Zecchin for his friendship and very useful discussions. My special thanks to Dr. Matthew Gibbs for his assistance and friendship.

My very special thanks to Barbara Brougham for her editorial service.

I appreciate very much all the assistance offered to me and friendship of the people of the School of Civil and Environmental Engineering. In particular, a very special thanks to Stephen Carr, for his endless support; for Deanne Keable for her enormous assistance with my conference travel and other administrative routines. Thank you all for your enormous assistance, co-operation and encouragement in all aspects related to my work. I am very grateful to The University of Adelaide for the scholarship granted to me during my postgraduate candidature.

Ultimately and with much love, I would like to acknowledge and thank my family for their enormous support, encouragement, love and care throughout my postgraduate work, especially my wife Victoria who helped me with proofreading the draft manuscript and made valuable linguistic comments to the thesis.

# CHAPTER 1 INTRODUCTION

---

## 1.1 PROBLEM STATEMENT

In the field of coastal and ocean engineering, wave prediction is one of the most important activities, and ranks with shipping, coastal structure design, shoreline stability and near-shore flood estimation in terms of importance when considering human interaction with the sea. The main goal of wind wave prediction is to predict the wind wave field in the time-space domain and its effect on the environment (Young, 1999).

A new era in oceanography began in 1947 when Sverdrup and Munk (1947) first offered a theory of the evolution of wind generated waves for the prediction of the sea state on the basis of observational data. Since then, a large number of theoretical and observational studies have resulted in a broad understanding of the physical processes involved in the development of the sea state. These studies have led to the construction of complex numerical models for wave forecasting.

Wave models can be divided into two general classes: phase resolving and phase averaging models:

- The phase resolving models predict the amplitude and phase of individual waves either in time or frequency domain.
- The phase averaging models predict average quantities including the wave energy spectrum (i.e. a superposition of sinusoidal waves of different frequencies with random phase and travelling in different directions) or its integral properties (e.g. the significant wave height  $H_s$ , the period of dominant waves  $T_p$  etc.).

Neither of these two general classes is superior as both are applicable to different tasks in wave modelling. The phase resolving models are computationally expensive in terms of time and resources as they predict the sea elevation in the time-space domain. On the other hand, the phase averaging model (or spectral model) is the more efficient due to the spectral wave energy distribution containing sufficient information about the wave field to determine the most important parameters. The spectral models are widely used for global and regional wave forecasts. The present study was undertaken with regard to the latter: spectral wave modelling.

Most spectral wave models are based on the numerical solution of the energy balance equation, the so-called *radiative transfer equation* (hereafter RTE). This equation has been commonly adopted to represent the temporal and spatial evolution of the wave energy spectrum as a result of the physical processes involved in wave development. In deep water, it is generally accepted that wind wave growth is a result of three physical processes including atmospheric input from the wind to the waves  $S_{in}$ ; wave dissipation (breaking, turbulence and viscosity)  $S_{ds}$ , and nonlinear energy transfer between the waves  $S_{nl}$ . The physical processes are represented via spectral parametric functions, the source terms. Among the source terms, the wind input  $S_{in}$  and the wave dissipation  $S_{ds}$  were the focus for the present study.

The previously conducted observational and analytical studies developed various theories of wind wave interaction (Jeffreys 1925, Miles 1957, Janssen 1991) and different parameterisation forms for the wind input source term  $S_{in}$ . Some of these forms were developed on the basis of observational data (Snyder et al., 1981; Hsiao and Shemdin, 1983; and Donelan 1999), whereas other forms were developed as a result of direct modeling of the air-sea boundary layer (Gent and Taylor 1976; Makin and Chalikov 1979; Al Zanaidi and Hui, 1984; Chalikov and Makin 1991; Chalikov and Belevich 1993). However, no fully consistent and conclusive theory of wind wave interactions exists as yet. Suggested theories need further development and meticulous empirical validation due to their inconsistency. Moreover, together with the existing limitations of observational techniques, the complexity of the wind wave interaction mechanisms creates further difficulties for experimental validation.

On the other hand, existing observational data do not provide the necessary accuracy and comprehension either. Measured wave growth rates differ by an order of magnitude and the parameterisations result in estimates that can differ by more than 100% (Donelan et al., 2006). Suggested parameterisation forms, used in wave models, were defined for light and moderate winds and their use in strong wind conditions is uncertain.

Yet, these parameterisation forms are widely used in contemporary wave models. Examples are the WAM (WAMDI, 1988; Komen et al., 1994) and SWAN (Booij et al., 1996) models. Furthermore, these parameterisation forms do not reflect the physical processes recently revealed by recent experimental studies, such as Donelan et al. (2006), which are the effect of:

- 1) wave steepness on wind energy transfer from non-separated wind flow to the waves
- 2) full separation of the wind flow and the waves

There is presently a need to develop an advanced parameterisation form of  $S_{in}$  on the basis of a physical framework, applicable to the wide range of environmental conditions common in operational wave modelling. The major difficulty with such an investigation is that the two mechanisms driving wave formation, i.e. wind input and wave dissipation, are inseparable, making investigations of these source terms extremely complex.

The physical processes of wave dissipation have always been poorly understood and suggested parameterisation forms for the dissipation source term have always been loosely based on physics and used as a residual tuning lever for wave models (Babanin et al., 2007; Babanin and van der Westhuysen, 2007; Cavaleri et al., 2007). Most contemporary wave models compute dissipation rates using these parametric functions. The WAM model (WAMDI, 1988; Komen et al., 1994) uses a parametric function for the dissipation source term based on the assumption that wave breaking is the week-in-the-mean process, depending quasi-linearly on the wave spectrum (Hasselmann, 1974). Banner and Young (1994) showed that in the WAM cycle 3 model, the dissipation function (Hasselmann, 1974) could not reproduce the detailed observational data and an alternate function was required. The first attempt to advance the performance of the wave dissipation source term was made in the WAVEWATCH model by accommodating the two-phase behavioral dissipation source function based on the theory of Tolman and Chalikov (1996).

Recently, the following new features of wave dissipation processes were experimentally discovered and described in the literature:

1. the threshold behavior of wave breaking (Banner et al., 2000; Babanin et al., 2001; Banner et al. 2002)
2. the cumulative effect of wave dissipation at smaller scales (Donelan, 2001; Babanin and Young, 2005; Young and Babanin, 2006)
3. quasisingular behavior of dissipation in the middle wavelength range (Hwang and Wang, 2004b)
4. two-phase behavior of the dissipation (Babanin and Young, 2005, Manasseh et al., 2006)

5. alteration of wave breaking/dissipation at strong wind forcing (Babanin and Young, 2005)
6. downshift of wave energy due to breaking (Donelan and Pierson, 1987; Waseda and Tulin, 1999; and Babanin et al., 2008).

Based on the new findings, Van der Westhuysen et al. (2007), in SWAN model simulations, incorporated threshold limitations and a wind-forcing dependence for the dissipation function. It was demonstrated that the altered dissipation source term yields improved agreement with fetch- and depth-limited growth curves in complex conditions, such a mixed sea and swell (Van der Westhuysen et al. 2007). Incorporation of the new dissipation features is more complex than a mere replacing of one dissipation term with another. For instance, if a cumulative integral is added to the breaking dissipation term, then local-in-wavenumber-space balance can no longer be satisfied and reformulations and readjustments of the wind input function, and perhaps of the entire model, are required. To the best of my knowledge, no study has tried to incorporate the cumulative effect of wave dissipation for small-scale waves.

On the whole, it must be acknowledged, therefore, that most wave models do not reflect the correct physics and do not describe the reality of wave processes. Recently observed features of wave dissipation need to be accommodated in modern dissipation terms. Without incorporating these features, the models cannot properly forecast complex or nonstandard natural phenomena. Currently, the development of an advanced parameterisation form for the dissipation source term, accommodating the new features of wave dissipation, is the barest necessity in operational wave modelling.

In general, the present state of competing and often contradictory theories of wind wave coupling and wave dissipation require the development of a conclusive and consistent wave model incorporating the newly recognised features of wave processes.

The present study investigated two newly proposed parameterisation forms for the wind input source term (Donelan et al., 2006) and the wave dissipation source term (Young and Babanin, 2006). Furthermore, a new approach was developed to achieve the objectives of this study within a strong physical framework. Moreover, this study made an attempt to address some of the existing issues in wave modelling regarding the shape of the wave spectrum and spectral saturation.

## 1.2 RESEARCH BACKGROUND

Partly to address the issues raised in wave modelling a field experiment – the Australian Shallow Water Experiment (AUSWEX) – was undertaken at Lake George, New South Wales, Australia from 1997-2000 in order to study wind wave coupling and wave breaking processes. A comprehensive description of the experiment and relevant technique, developed during this study has been given in Young et al. (2005). This study was distinct from previous field studies because it was the first attempt to measure the pressure growth term on waves in shallow water. The depth limiting effect on the wave propagation phase speed made it possible to study a wide range of wind forcing conditions ( $U_{10}/c_p$ ) including very strongly forced waves, with  $U_{10}/c_p = 5.1 - 7.6$  and  $U_{10}/c$  ranging up to 11.2, with varying wave steepness.

This study revealed previously unrecognised features of wind wave interaction, finding the following:

- Wind flow separation from the water surface during very strong winds reduces wind energy transfer to the waves.
- Wave growth rates depend on wave steepness.

Furthermore, this study resulted in a new parameterisation form for wind input source term  $S_{in}$  employing these new features (Donelan et al., 2006). The Lake George conditions, however, were only those of strong wind forcing and, thus, the results were obtained under limited air-sea conditions. Therefore, further numerical investigation and verification of the new wind input function was required to develop an advance parameterisation form for the wind input source term, which will be designed to work in the entire range of wave generation by wind: from light and moderate to very strong winds; from young waves to mature seas. At the same time, AUSWEX brought new insight into wave dissipation processes and their relationship to wind wave interactions. One of the advantages of the techniques developed during AUSWEX was a simultaneous estimation of the dissipation source function in situ and in finite depth conditions. AUSWEX brought to light important features of wave dissipation processes such as the:

- Threshold behavior of wave breaking (Banner et al., 2000; Babanin et al., 2001; Banner et al. 2002)
- Cumulative effect of wave dissipation at smaller scales (Donelan, 2001; Babanin and Young, 2005; Young and Babanin, 2006)
- Two-phase behavior of the dissipation (Babanin and Young, 2005)
- Alteration of wave breaking/dissipation at strong wind forcing (Babanin and Young, 2005)
- Bimodal directional properties of the dissipation, in terms that higher dissipation rates were found at oblique angles than in the main wave propagation direction (Babanin and Young, 2005).

Most of these features were accommodated in a two-term parameterisation form for the dissipation source term (Young and Babanin, 2006). However, the behavior of the parameters of this complex function in a wide range of air-sea conditions was not explored. Therefore, further intensive investigation and verification of the suggested form were required to obtain an advanced dissipation function applicable to a wide range of air-sea conditions. Moreover, it was essential to determine whether the new spectral dissipation function was able to reconcile computed breaking rates with the results of other observations (e.g. Melville and Matusov, 2002; Hwang and Wang, 2004b; and Gemmrich, 2005).

The outcomes of the AUSWEX study required further intensive numerical elaboration of the suggested new parameterisation forms for the wind input and the wave dissipation. Consequently, the development of advanced forms of  $S_m$  and  $S_{ds}$  and the proper specification of their parameter values depend on further numerical modeling and fine tuning. The present study was undertaken to carry out a compound numerical investigation of both source functions to adapt them for operational wave modeling.

### 1.3 RESEARCH OBJECTIVES

The overall objective of the present research was to develop advanced parameterisation forms of wind input and wave dissipation source terms by means of numerical experiments in order to:

- Establish a greater understanding of the physics of wind wave interaction and wave breaking provided by AUSWEX (Young et al. 2005, Donelan et al., 2006, and, Young and Babanin 2006)
- Establish a strong physical framework
- Develop a new parameterisation form for the directional spreading of the dissipation source term accommodating the new features of directional properties of wave dissipation found in the AUSWEX study
- Develop a numerical model that incorporates the advanced functions of the wind input and dissipation source terms and is able to reproduce the existing experimental data
- Ensure that the parametric functions are applicable to a wide range of air-sea conditions.

## 1.4 APPROACH TO THE STUDY

The investigation of a novel source function from the Radiative Transfer Equation (RTE) was a complex task involving the concurrent investigation of two new source functions  $S_{in}$  and  $S_{ds}$  interrelating with one another. Moreover, it was required that these functions comply with a number of physical constraints that determined the physical framework of the model.

The traditional approach to testing source functions employed in the RTE was established by Komen et al. (1984) and with some variations has persisted for more than 30 years. This approach emphasizes the implementation of a new function in a wave model and the comparison of the outcomes with known experimental results.

These outcomes present a time-space development of integral, spectral and directional properties of the wave field. The development of these wave properties has been extensively investigated, well understood, described and parameterised. However, the physics of the source terms  $S_{in}$  and particularly  $S_{ds}$  needs further extensive investigation. Therefore, attention to the traditional approach has focused on reproducing the already known wave growth curves and some spectral features (e.g. Banner and Young, 1994). The ability of a model to replicate these curves serves as a validation measure for the source terms.

The validation criteria, however, are subject to potentially serious shortcomings. The wind input term represents the positive flux of the energy into the wave system; whereas the dissipation term relates to the negative flux. Together, they can balance each other and produce correct growth curves while individually being physically inconsistent. An additional disadvantage of the traditional approach is that it is impossible to investigate and verify the source terms separately. Any change to any of the source terms within a full spectral model requires extensive testing, which is computationally expensive, particularly if the exact nonlinear term is included. Moreover, alterations to one term often lead to compensative tuning of other source functions which smear the physics of the original update. Therefore, the traditional approach has required revision, which was supplied by the current study.

This current research developed a new method to overcome the above-mentioned difficulties through a physical framework of wind wave processes involved in the air-sea interface. The approach was based on physical constraints suggested by Donelan (WISE-2004, Reading, England). The first constraint was that the wind input source term had to correspond to the total wind stress exerted on the water surface. Based on this constraint, behaviour of a new wind-input function could be investigated and tuned separately. The second constraint related to the dissipation source term, in particular to the relationship between its integral value and the integral of the wind input source term. The ratio of these two integrals as a function of the wave development stage was obtained experimentally (e.g. Donelan, 1998). Therefore, the dissipation term could be studied and tuned individually. This approach provided insight into operational wave modelling in terms of the coupling of the wind input and the wave dissipation source terms in the RTE.

The current study was conducted using a new research wave model WAVETIME-1 (Van Vledder, 2004). The approach of this study was three-fold:

1. The validation and verification of the new model WAVETIME-1
2. Investigation of new parameterisation forms of  $S_{in}$  and  $S_{ds}$  source terms
3. Comprehensive test of the performance of the new forms of  $S_{in}$  and  $S_{ds}$  developed on the basis of the method suggested by Banner and Young (1994)

One of the advantages of the approach developed in the course of this study is that it is applicable to a wide range of research activities in operational wave modelling.

## **1.5 LAYOUT AND CONTENTS OF THESIS**

This thesis is structured to provide a logical progression through the work that has been completed. The contents of this thesis are:

**Chapter 2** presents the existing literature review in regard to wave modelling and its major concepts relevant to this work

**Chapter 3** provides a description of a numerical model selected for this study

**Chapter 4** outlines the approach and the major results of the study. This chapter consists of three main sections:

**Section 4.1** outlines the investigation of the wind input source function

**Section 4.2** outlines the investigation of the wave dissipation source function

**Section 4.3** outlines the test results of performance of corrected forms of the wind input the wave dissipation source terms in the numerical model

**Chapter 5** presents the major conclusions drawn from the research and highlights recommendations for the future work.

## CHAPTER 2 BACKGROUND

---

### 2.1 OCEAN WAVES

Ocean surface waves are mechanical waves that propagate along the air-water interface. Due to the restoring force provided by gravity, they are often referred to as surface gravity waves. As the wind blows, pressure and friction forces perturb the equilibrium of the ocean surface resulting in its displacement (see Figure 2.1). These forces transfer energy from the air to the water, forming waves. In the case of monochromatic linear plane waves in deep water, particles near the surface move in circular paths, making ocean surface waves a combination of longitudinal (back and forth) and transverse (up and down) wave motions. When waves propagate in shallow water, (where the depth is less than half the wavelength) the particle trajectories are compressed into ellipses.

The displacement of the water surface can be described mathematically by the Navier-Stokes equations for a two-layer fluid. The direct solution of this equation is not practical for the case of wind-wave generation as the sea surface is represented by waves with various shapes and scales. Therefore, to solve this equation a number of simplifications need to be assumed:

1. The water is of uniform depth, and the waves propagate without deformation:  
( $d, \lambda = \text{const}$ )
2. The effects of viscosity, turbulence and surface tension are neglected.
3. The ratio of air-water densities is very small.
4. Waves have small amplitude-wavelength ratios.
5. Wave motion is irrotational, and is mainly under the influence of gravity.

These limitations form the basis of *linear wave theory* (Airy, 1845) (hereafter LWT). Solving the equation with consideration of the free surface boundary conditions, the displacement associated with the arbitrary wave component with angular frequency  $\omega = 2\pi / T = 2\pi f$  and wavenumber  $k = 2\pi / \lambda$  can be described by the sinusoidal function periodic in both space (wave length  $\lambda$ ) and time (period  $T$ ):

$$\eta(\mathbf{k}, \omega; \mathbf{x}, t) = a \cdot \sin(\mathbf{kx} - \omega t) \quad (\text{Eq. 2-1})$$

According to (Eq. 2-1), the water surface varies in a sinusoidal manner. In nature, however, there are cases where the simplifying assumptions of LWT cannot be applied. In these cases, there is a need to use a nonlinear or *finite amplitude wave theory* (hereafter FAWT). According to this theory, the wave has an influence on its own properties. Therefore, the wave properties become functions of wave amplitude. In contrast to LWT, FAWT predicts a small net fluid transport in the direction of wave propagation. Furthermore, FAWT can predict steep waves with peaked crests and flat troughs, which are important in shallow water applications. However, FAWT still has limitations in terms of the prediction of waves with variable height, period and propagation direction.

## 2.2 THE WAVE SPECTRUM

Wind wave prediction involves the determination of sea surface conditions at a given location and time. Therefore, it is necessary to describe the sea surface in terms of a numerical model. In nature, the sea surface appears as a chaotic wavy surface which can be represented by a collection of waves with varying heights, periods and wavelengths. In many areas of physics, such a surface can be mathematically represented by a spectral or Fourier model. According to the Fourier model, the water surface elevation can be represented by a linear superposition of sinusoidal forms (spectral components) with varying frequencies, amplitudes and phases. The magnitude and distribution of these components vary with both time and space. Under this approximation the water surface elevation can be defined by the equation:

$$\eta(t) = \sum_{i=1}^N a_i \cdot \sin(\omega_i t + \phi_i) \quad (\text{Eq. 2-2})$$

where  $a_i$ ,  $\omega_i$  and  $\phi_i$  are the amplitude, angular frequency and phase of the  $i$ -th component in the summation.

On the other hand, the energy of the wave relates to the wave amplitude squared (Dean and Dalrymple, 1991). On this basis, for a given state of water surface there is a certain distribution of the wave energy between the wave components. Therefore, the sea surface can be identified by the distribution of wave energy with respect to the frequency and direction (or wavenumber) of all wave components. This energy distribution is called the *wave energy spectrum*. It is expressed either in frequency-direction ( $F(f, \theta)$ ) or wavenumber space ( $F(\mathbf{k})$  or  $F(k, \theta)$ ), where  $f$ ,  $\theta$  and  $\mathbf{k}$  are the frequency, direction of wave propagation and the wavenumber.

The wavenumber spectrum relates to the frequency-direction spectrum through the following equation:

$$F(k) = \frac{cc_g}{2\pi\omega} F(f, \theta) \quad (\text{Eq. 2-3})$$

where  $c$  is the wave phase speed and  $c_g$  is the wave group velocity, which is  $c/2$  in deep water conditions.

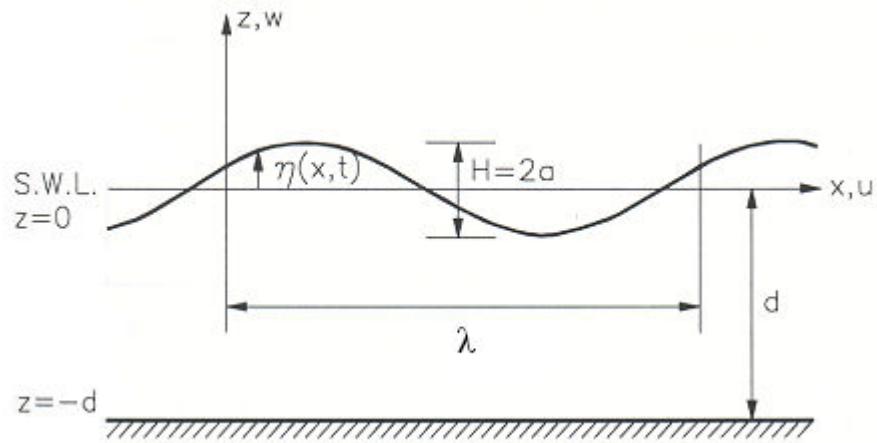
The existing experimental data show that most wave spectra have specific attributes, which include the maximum energy ( $F_{max}$ ) and the corresponding frequency, the so-called peak frequency ( $f_p$ ). This characteristic of the wave spectrum shows that at a given location and time the waves with peak frequency are dominating all other spectral components. These waves are called the *dominant waves*.

Figure 2.2 shows a typical wave spectrum in the frequency-direction domains. The spectral peak indicates that waves with the peak frequency (dominant waves) mostly propagate in the wind direction placed at  $0^0$ . The wave spectrum shows that most of the spectral energy is carried by the dominant waves.

Various statistical approaches can be used to determine a wind-wave field. These include parametric predictions in terms of integral properties, such as significant wave height and peak period (Kahma et al. 1981; Dobson et al. 1989) and more sophisticated techniques defining a full wave spectrum, based on approaches such as those of Donelan et al. (1985) and Babanin and Soloviev (1998). In both studies, the wave spectra were obtained by means of arrays of wave probes. Donelan et al. (1985) found that the frequency spectrum in the rear face is inversely proportional to the fourth power of the frequency  $f$ . Babanin and Soloviev (1998) described a transformation of the wind wave spectrum, which has the fifth power of the frequency  $f$ . The discussions regarding the form of the wave spectrum are still ongoing.

### 2.2.1 SHAPE OF THE FREQUENCY SPECTRA

The state of the ocean surface is described by the mean distribution of wave energy, which is represented by the energy density spectrum. The equilibrium shape of the wave spectrum is determined by processes occurring in the medium. In deep water, the most significant processes are: wave-wave interactions, energy input from the wind and wave dissipation.



**Figure 2.1** Definition diagram to represent linear wave theory. Here,  $\lambda$  is wavelength,  $d$  - the water depth,  $H$  - the wave height,  $a$  - the amplitude and S. W. L. - represents the stationary water level. The wave profile ( $\eta(x, t)$ ) is assumed to be a function of distance ( $x$ ) and time ( $t$ ) (Young (1999)).

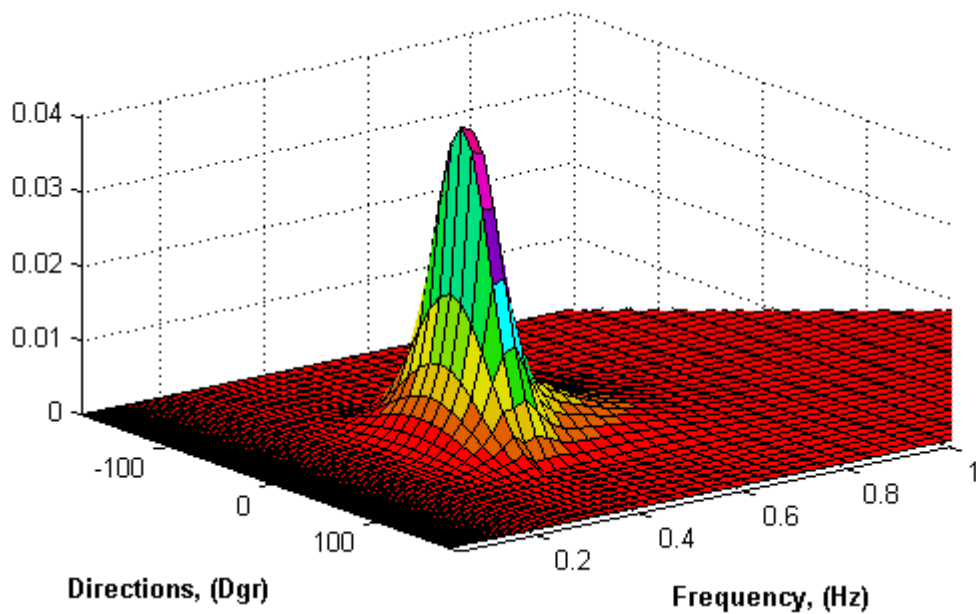


**Figure 2.2** Frequency-direction energy density spectrum with the peak frequency  $f_p = 0.3\text{Hz}$  and wind direction at  $0^\circ$ .

From a theoretical background, considerable agreement has been achieved regarding the equilibrium shape of wave spectra. On the other hand, the large collection of experimental datasets is inconsistent and discrepant. The main point of all arguments is the power-law dependence of energy density on frequency. The experimental data show that there is no common value for power-law dependence of energy density on frequency for short scale waves. The issues regarding the form of the wave spectrum require thorough revision.

Wave spectral shape can be divided into three main sub-ranges: the dominant-wave range  $[0.7f_p, 1.3f_p]$ , equilibrium range  $[1.5f_p, 3f_p]$  and high frequency range  $[3f_p, f_c]$ . In each sub-range, the source terms are balanced differently, thereby determining a certain spectral shape. The pioneering work of Phillips (Phillips, 1958) on the equilibrium range of wave spectral shape proposes that the spectral form is mainly determined by the wave breaking at frequencies above the peak frequency. Nonlinear wave interactions were not considered in that model. Phillips (1958) proposed a  $f^{-5}$  power-law relationship for the equilibrium range.

The  $f^{-5}$  power-law relationship was verified by the JONSWAP experiment (Hasselmann et al., 1973), which resulted in wave spectrum (hereafter the JONSWAP spectrum) of developing waves, the so-called JONSWAP spectrum:

$$F(f, \theta) = \alpha \frac{g^2}{(2\pi)^4} f^{-5} \exp\left[-\frac{5}{4}\left(\frac{f}{f_p}\right)^{-4}\right] \gamma_J \exp\left[\frac{-(f-f_p)^2}{2\sigma^2 f_p^2}\right] \quad (\text{Eq. 2-4})$$

where  $\alpha$ ,  $\sigma$  and  $\gamma_J$  are spectral shape parameters.

The main body of the JONSWAP spectrum (Eq. 2-4) is represented by the Pierson-Moskowitz (PM) frequency spectrum (Pierson and Moskowitz 1964), which is the observational verification of Kitaigorodskii's hypothesis (Kitaigorodskii 1962) for fully developed waves. The main shortcoming of the JONSWAP spectrum is that it never transforms into the PM spectrum within the framework of this model, although the JONSWAP data approach fully developed situations. To overcome this deficiency, Hasselmann et al. (1973) refer to the rapid change, which takes place when waves approach the full development stage. However, there is no observational support of such phenomena.

Over thirty years ago, Toba (1973) proposed a spectral form  $f^{-4}$  which was an alternative to that of Phillips (1958). The field experiments of Kawai et al. (1977), Mitsuyasu et al. (1980), Kahma (1981), Forristall (1981) and Donelan et al. (1985) supported this spectral form. The theoretical works of Kitaigorodskii (1983) and Phillips (1985) also supported

the  $f^{-4}$  power-law relationship. Later, Battjes (1987) reanalysed the JONSWAP data and found a better correlation with the  $f^{-4}$  than the  $f^{-5}$  form. Liu (1989) analysed wave spectra from Great Lakes experimental datasets and found that most values of the exponents in frequency dependence were clustered in the range 3.5 and 5.5. Banner (1990) showed that the  $f^{-4}$  power-law relationship for equilibrium range was determined by the dependence of directional spreading of wave spectra on  $f / f_p$ . Theoretical and observational background strongly support the  $f^{-4}$  power-law relationship, rather than  $f^{-5}$ . On this basis, Donelan et al. (1985) proposed a modification to the JONSWAP spectral form:

$$F(f, \theta) = \beta \frac{g^2}{(2\pi)^4} f_p^{-1} f^{-4} \exp\left[-\left(\frac{f}{f_p}\right)^{-4}\right] \cdot \gamma_D \exp\left[\frac{-(f-f_p)^2}{2\sigma^2 f_p^2}\right] \quad (\text{Eq. 2-5})$$

where  $\beta$ ,  $\sigma$  and  $\gamma_D$  are spectral shape parameters analogous to JONSWAP spectral parameters with different wave-age dependences.

Donelan et al. (1985) represented these parameters as:

$$\beta = 0.0165\nu^{0.55} \quad (\text{Eq. 2-6})$$

$$\gamma_D = \begin{cases} 6.489 + 61 \log \nu & \nu \geq 0.159 \\ 1.7 & \nu < 0.159 \end{cases} \quad (\text{Eq. 2-7})$$

$$\sigma = 0.08 + 1.29 \times 10^{-3} \nu^{-3} \quad (\text{Eq. 2-8})$$

where  $\nu$  is the non-dimensional peak frequency. The wave spectrum represented by the parameterisation form (Eq. 2-5) in this thesis will be referred as the Donelan spectrum.

Figure 2.3 compares the JONSWAP (Hasselmann et al., 1973) and Donelan spectra (Donelan et al., 1985) at different stages of wave development, where  $\gamma_J$  is the peak enhancement (Eq. 2-4) and  $U_{10}$  is the wind speed at standard 10m height. The difference between the spectral magnitudes of the compared spectra is shown.

Inconsistency becomes visible for wave spectral components in the high frequency range. The analysis of source term balance is complicated by additional phenomena like Doppler shifting of high frequency waves by longer wavelength waves, wind drift currents and ambient currents. Furthermore, the measurement techniques for the high frequency scale are limited because of the significant noisiness of the wave records and operational complications that arise when using thinner wave probe wires in oceanic conditions.

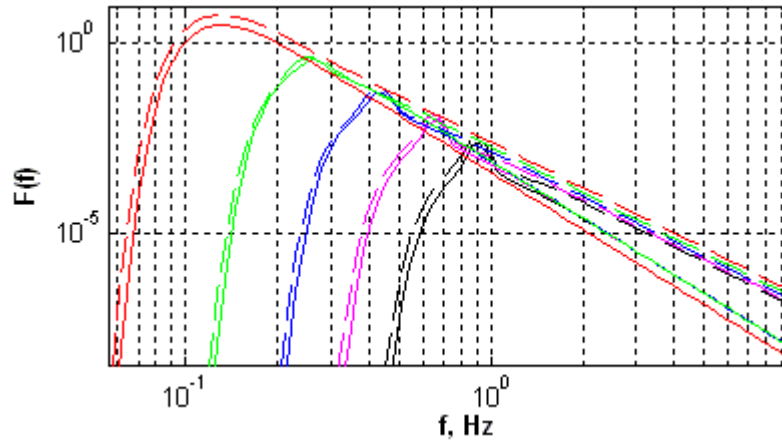


**Figure 2.3** Comparison of wave energy density spectra according to results of JONSWAP experiments (solid lines) and Donelan et al. (1985) (dashed lines) at different stages of wave development with the magnitudes of peak enhancement:  $\gamma_j = \{7, 5, 3.3, 2, 1\}$  at wind  $U_{10} = 10$  m/s.

There have been relatively few studies of the high frequency spectral range due to observational limitations. The results of Mitsuyasu (1977) and Stolte (1984) are, however, close to the results of Donelan et al. (1985), confirming  $f^{-4}$  power-law relationship. On the other hand, anomalous frequency spectra have been reported from the experimental datasets of Forristall (1981), Kahma (1981), Kahma and Calkoen (1992) and Babanin and Soloviev (1998). These authors have found that wave spectra behave as  $f^{-4}$  just above the spectral peak in the equilibrium range and behave as  $f^{-5}$  power-law relationship above a transition frequency  $f_T \sim 3f_p$ , which is introduced as:

$$f_T \sim \frac{2.5}{\pi} \frac{g}{U_{10}} \quad (\text{Eq. 2-9})$$

Kitaigorodskii (1983) predicted this transition on a theoretical basis. Kahma and Calkoen (1992) assume that the transition from the  $f^{-4}$  to  $f^{-5}$  power-law relationship is derived from directional effects, specifically the Doppler shift induced by currents and the orbital velocities of waves with frequencies near the peak frequency. Summarizing this discussion, it is likely that there is no universal value of power-law exponent for wave spectra (Young, 1999).

### 2.2.2 DIRECTIONAL SPECTRUM

In nature, the sea surface is represented by waves with varying heights, periods, wavelengths and propagation directions. The propagation direction of a wave is specified in terms of the angle  $\theta$  between the wave propagation direction and the wind direction. The directional spectrum defines the distribution of wave energy, along with the propagation directions of the spectral components. The directional spectrum is one of the important characteristics used for validating existing wave models. The directional distribution of spectral energy  $D(f, \theta)$  is determined as the cross-section of the directional frequency spectrum  $F(f, \theta)$ :

$$F(f, \theta) = F(f) \cdot D(f, \theta) \quad (\text{Eq. 2-10})$$

where  $F(f)$  is a one-dimensional frequency spectrum.

The directional spreading function  $D(f, \theta)$  must satisfy the condition:

$$\int D(f, \theta) d\theta = 1 \quad (\text{Eq. 2-11})$$

Based on the observational data, Longuet-Higgins et al. (1963) represent the directional spreading function in the form:

$$D(f, \theta) = Q(s) \cos^{2s} \left\{ \frac{\theta - \theta_m(f)}{2} \right\} \quad (\text{Eq. 2-12})$$

where  $Q(s)$  is a normalisation factor required to satisfy the condition (Eq. 2-11) and  $\theta_m$  is the mean wave direction at frequency  $f$ . The parameter  $s$  has been parameterised as a function of the relative frequency by Mitsuyasu et al. (1975) on the basis of their field data:

$$s = \begin{cases} s_p \left( \frac{f}{f_p} \right)^5, & f < f_p \\ s_p \left( \frac{f}{f_p} \right)^{-2.5}, & f \geq f_p \end{cases} \quad (\text{Eq. 2-13})$$

where  $s_p$  is the value of  $s$  at the peak frequency  $f_p$  presented in the following form:

$$s_p = 11.5 \left( \frac{U_{10}}{c_p} \right)^{-2.5} \quad (\text{Eq. 2-14})$$

where  $c_p$  is the phase speed of the dominant waves and  $U_{10}$  is the wind speed at a reference height of 10 m.

Experimental observations have shown that in the absence of currents the maximum energy belongs to the dominant waves propagating in the wind direction. However, in the high frequency range of the wave spectrum, maximum energy belongs to the waves propagating at oblique angles relative to the wind direction. Therefore, the chosen unimodal shape at peak frequency is transformed into a bimodal shape in the high frequency spectral range. Furthermore, bimodality can be observed for long waves with frequencies less than the peak frequency.

For the identification of the directional wave spectrum, Babanin and Soloviev (1998) have introduced the directional spectral width  $A(f)$  as the spectral spreading function, presented as:

$$A(f)^{-1} = \int_{-\pi}^{\pi} D_n(f, \theta) d\theta \quad (\text{Eq. 2-15})$$

where  $D_n(f, \theta)$  is the distribution of wave spectral energy at the frequency  $f$  along direction  $\theta$ , normalized by its maximal value at this frequency:

$$D_n(f, \theta_{\max}) = 1 \quad (\text{Eq. 2-16})$$

The Black Sea experiment (Babanin and Soloviev, 1998) resulted in a clearer understanding of the behaviour of the directional wave spectrum during wave development. The study makes a number of points:

1. The width of  $D_n(f_p, \theta)$  in general decreases with wave development.
2. The directional spectrum broadens towards short scale waves in the range of high frequencies ( $f > f_p$ ) independently of the stage of wave development.
3. The broadening of  $D_n(f_p, \theta)$  to lower frequencies ( $f < f_p$ ) depends on the stage of wave development.
4. The narrowest directional spectrum was observed for the dominant waves independently of the stage of wave development.

These findings have formed a strong framework for validation of wave models. The present study used these results (Babanin and Soloviev, 1998) for validation of the wave model.

### 2.2.3 WAVE STEEPNESS

Wave steepness is one of the important factors which determine the physics of wind-wave interactions. One of the outcomes of the Lake George experiment (Donelan et al. 2006) has been an appreciation of the dependence of growth rates on wave steepness which is described in terms of azimuth-integrated spectral saturation  $B_n(\omega)$ .

The spectral saturation is a non-dimensional representation of the wave steepness in spectral form. Phillips (1984) introduced the spectral saturation density as  $B(k) = k^4 \Phi(k)$ , where  $\Phi(k)$ , the wavenumber spectrum, is integrated in directional space. The idea of a saturation level in the spectral range of short gravity waves assumes a magnitude where  $B(k)$  is a constant and independent of  $k/k_p$ . Phillips (1984) found that  $B(k)$  correlates to the mean square slope:

$$MSS = \iint k^4 \Phi(k, \theta) \frac{1}{k} dk d\theta = \int k^4 \Phi(k) d(\ln k) \quad (\text{Eq. 2-17})$$

where  $d(\ln k)$  is the fractional bandwidth.

Using the linear-gravity wave dispersion relationship ( $\omega^2 = gk \tanh(kd)$ ), the azimuth-integrated spectral saturation can be represented in terms of the frequency energy-density spectrum  $E(\omega)$ :

$$B = \omega^5 E(\omega) / 2g^2 = (2\pi)^4 f^5 F(f) / 2g^2 \quad (\text{Eq. 2-18})$$

where  $\omega = 2\pi f$  is the angular frequency. The spectral shape of  $B(f)$  is determined by the form of wave spectrum  $F(f)$ .

Figure 2.4 shows the results of computations of spectral saturation  $B(f)$  for the energy spectra JONSWAP and Donelan (1985). It shows that the spectral saturation  $B(f)$  for Donelan spectra has no saturation level compared to the JONSWAP spectra. This behaviour of  $B(f)$  is determined by the term  $f^5 F(f)$ .

The term  $f^5 F(f)$  for Donelan spectra is proportional to frequency  $f$ , whereas for the JONSWAP spectrum this term reaches its saturation level. This fact significantly affects the results of computations for the  $S_{in}$  source function by Donelan et al. (2006), taking into consideration the dependence of the growth rate on spectral saturation.

The significant differences at high frequency spectral components create significant inconsistencies in stress computations for the JONSWAP and Donelan spectra, even if

they correspond to the same state of the sea surface. The qualitative dependence of  $B(f)$  on the spectral shape has a quantitative effect on the computation of the new wind input source function (Donelan et al., 2006), which includes spectral saturation  $B(f)$ , and it is necessary to reduce this effect for consistent computation.

Banner et al. (2002) have introduced a normalized saturation  $B_n(f)$  per unit spreading angle to reduce the increase in spectral saturation for high frequency waves. The suggestion was based on the fact that spectral directional widths broaden towards high frequencies. To remove the effect of different spreading widths at different frequencies, Banner et al. (2002) normalize  $B(f)$  by the local angular spreading width  $\theta_w(f)$ , obtained by Hwang et al. (2000):

$$B_n(f) = B(f) / \theta_w(f).$$

In Donelan et al. (2006), the authors use the normalized spectral saturation that includes the directional integral parameter  $A(f)$  from the experimental study on the Black Sea (Babanin and Soloviev 1998) as an analogue of the spectral width  $\theta_w(f)$ . According to Donelan et al. (2006), the azimuth-integrated spectral saturation is represented in a form:

$$B_n(\omega) = \frac{\omega^5 E(\omega)}{2g^2} A(\omega) \quad (\text{Eq. 2-19})$$

where  $A(\omega)$  is the directional spectral width (Babanin and Soloviev, 1998).

The results of computations of the spectral saturation  $B_n(f)$  using  $A(f)$  for different types of wave spectra are shown in Figure 2.5. According to Figure 2.5, the differences of  $B_n(f)$  at high frequencies computed for the Donelan and JONSWAP spectra are still significant to perform consistent computations of the new wind input source term (Donelan et al., 2006). Therefore, the parameterisation form of the spectral saturation requires revision in terms to reduce the effect of the spectral shape on computations of the new wind input source term (Donelan et al., 2006).

## 2.3 MODELLING WAVE EVOLUTION

To predict a sea surface at the given space and time, it is required to resort to a mathematical model which can describe the development of the wavefield as a result of the physical processes contributing to this development. This section introduces the basic concepts of wave modelling.

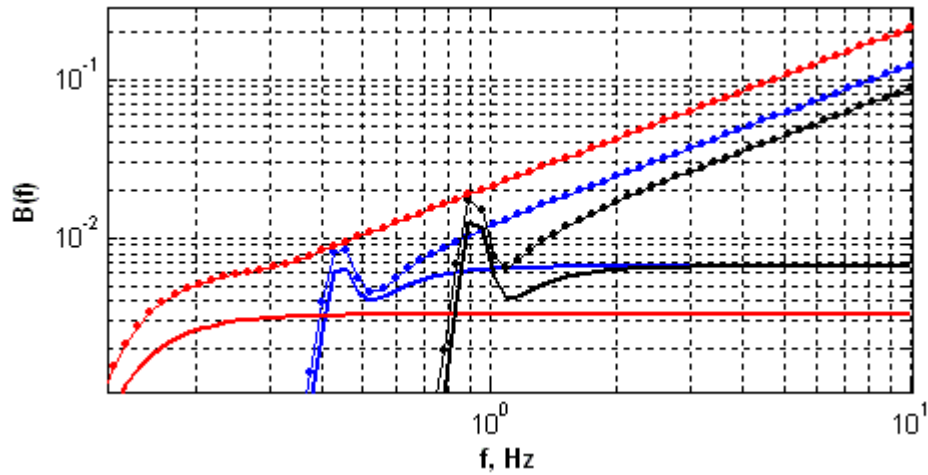


**Figure 2.4** Comparison of the spectral saturation,  $B(f)$ , computed for the JONSWAP (bold lines) and Donelan (lines with dots) energy density spectra at different stages of wave development with the magnitudes of peak enhancement:  $\gamma_J = \{7, 3.3, 1\}$  at wind  $U_{10} = 10$  m/s.

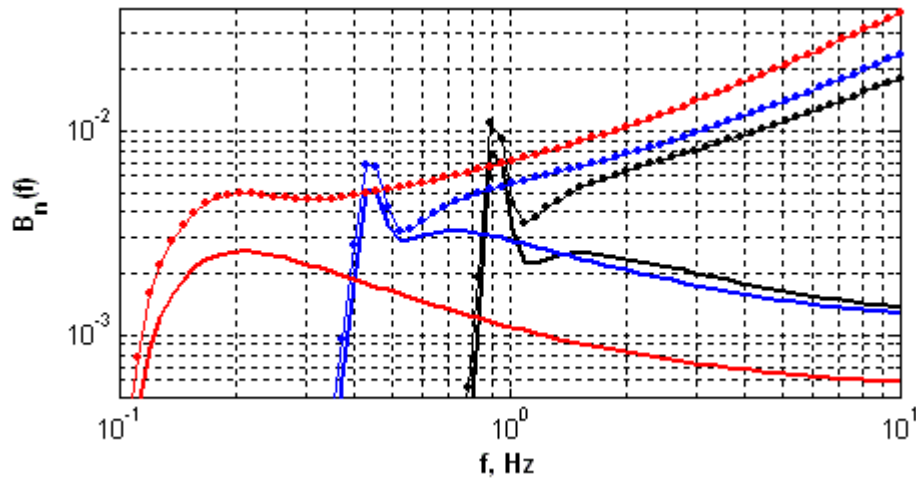


**Figure 2.5** Comparison of the spectral saturation  $B_n(f)$  normalised by the spreading angle  $\theta_w(f)$ , for the JONSWAP (bold lines) and Donelan (lines with dots) energy density spectra at different stages of wave development with the magnitudes of peak enhancement:  $\gamma_J = \{7, 3.3, 1\}$  at wind  $U_{10} = 10$  m/s

### 2.3.1 RADIATIVE TRANSFER EQUATION

Under the influence of physical processes, as waves propagate in time-spatial space, they change their properties, which is referred to as wave evolution (Young, 1999). Respectively, the shape of the wave spectrum corresponding to the sea-state undergoes transformation. The mathematical description of the changing wave field in the time-space domain in response to environmental perturbation, is based on the major energy fluxes involved in the process.

In the absence of currents, the evolution of the wave spectrum in deep water can be described by the *radiative transfer equation* (Gelci et al., 1957; Hasselmann, 1960; Phillips, 1977 and Komen et al. 1994), presented by the form:

$$\frac{\partial F}{\partial t} + c_g \times \nabla F = S_{tot} \quad (\text{Eq. 2-20})$$

where  $F = F(\mathbf{k}, f, x, t)$  is the wave spectrum.

The radiative transfer equation (Eq. 2-20) is the governing equation in operational wave modelling. The left hand side of Equation 2-20 describes the evolution of the wave spectrum, components of which are advected at their respective group velocity  $c_g$ . The total source term  $S_{tot}$  represents all energy fluxes contributing to wind wave evolution. In the case of a non-homogenous medium, when the currents or depth interaction processes are significant, the conservation of wave energy no longer exists. In these cases, a more general form of radiative transfer equation should be used in terms of wave action  $N = F(k, \theta) / \omega$  (Komen et al., 1994).

The derivative operator  $\frac{d}{dt} = \frac{\partial}{\partial t} + c_g \cdot \nabla$  in Equation 2-20 represents two idealised cases of wind wave evolution: duration-limited growth ( $\frac{\partial}{\partial t}$ ) and fetch-limited growth ( $c_g \cdot \nabla$ ). Fetch-limited growth refers to a case when a wind of constant speed and direction blows over deep water perpendicular to a long and straight coastline. It is assumed that if the wind blows a sufficiently long time the wave field will reach a steady state (independent of time). In these circumstances, wave growth is a function of the distance (fetch,  $x$ ) from the shoreline.

Duration-limited growth relates to the development of a wave field from initially calm water. It is assumed that a wind of constant speed and direction blows over spatially homogeneous deep water. In this case, the wave growth becomes a function of the duration of time,  $t$ , that the wind blows.

### 2.3.2 SOURCE FUNCTIONS

The total source term  $S_{tot}$  can be represented as the algebraic sum of a number of physical processes (source terms) contributing to the evolution of wind waves:

$$S_{tot} = S_{in} + S_{ds} + S_{nl} \quad (\text{Eq. 2-21})$$

where  $S_{in}$  - represents the atmospheric input from the wind;

$S_{ds}$  - is the dissipation due to white capping and other processes  
(e.g. turbulent viscosity)

$S_{nl}$  - is the nonlinear interactions between the spectral components.

These source terms do not exhaust all physical processes that may contribute to wind wave evolution in deep water conditions. However, it is generally assumed that these three source terms represent the dominant driving mechanisms in the evolution of wind waves. Each of the source terms is represented by a spectral parametric function.

#### 2.3.2.1 Wind Input

Air-sea interaction is one of the dominant processes resulting in a change in the statistical properties of a wind-driven water surface, a change referred to as *wave evolution*. The energy and momentum fluxes across the air-water boundary layer determine the intensity of wave evolution. Therefore, precise modelling of the air-sea interaction plays a significant role in wave forecasting.

As the wind blows upon young and average-developed waves, wave energy increases in time-spatial space. Miles in 1957 defined the temporal growth rate  $\gamma$  to describe the wave energy increase:

$$\gamma = \left( \frac{1}{\omega E} \right) \frac{\partial E}{\partial t} \quad (\text{Eq. 2-22})$$

The growth rate parameter  $\gamma$  determines the magnitude of increment of wave energy relative to the wave energy. The growth rate can be directly measured during wave observations.

It is well known that most of the momentum fluxes from wind to waves are caused by the component of pressure correlating with the wave slope (see Young 1999; Donelan 1999; Donelan et al. 2006):

$$\frac{\partial E(\omega)}{\partial t} = S_{in}(\omega) = \frac{1}{\rho_w g} \overline{p(x,t) \frac{\partial \eta(x,t)}{\partial t}} \quad (\text{Eq. 2-23})$$

Where  $E(\omega)$  is the one-dimensional energy spectrum in angular frequency scale;  
 $S_{in}(\omega)$  is the corresponding one-dimensional wind input source function;  
 $p(x,t)$  is the pressure exerted by the air on the water surface;  
 $\eta(x,t) = a \cos(kx - \omega t)$  is the surface elevation of amplitude  $a$  at distance  $x$   
time  $t$  and  $k$  is the wavenumber.

The overbar indicates an average in time. Most wave observation data are represented as simultaneous records of pressure and surface elevation. These records can be translated in

Fourier space giving the quadrature spectrum,  $Q(\omega) = \frac{1}{\omega} \overline{p \frac{\partial \eta}{\partial t}}$ . The quadrature spectrum

can be used to determine the nondimensional growth rate  $\gamma(\omega) = \frac{Q(\omega)}{\rho_a g E(\omega)}$  (see Donelan

et al., 2006). Substituting the quadrature spectrum  $Q(\omega)$  from the later equation for  $\gamma(\omega)$  in the (Eq. 2-23) and converting to the frequency scale ( $S_{in}(f) = 2\pi S_{in}(\omega)$ ), the wind input source term becomes the following form:

$$S_{in}(f) = 2\pi \rho_a / \rho_w f \gamma(f) F(f) \quad (\text{Eq. 2-24})$$

where  $\rho_a$  is the density of air and  $\rho_w$  is the density of water.

Equation 2-24 shows a direct relationship between the wind input source function  $S_{in}$  and the growth rate  $\gamma$ . In field observations, oceanographers measure the growth rate  $\gamma$  to determine the energy input from the wind to the waves,  $S_{in}(f)$ . Thus, the growth rate  $\gamma$  has significant impact on wave prediction in wave modelling. However, existing observational data for the growth rate are contradictory and obscure.

Almost a hundred years of human attempts to understand and describe the processes of energy and momentum input from wind to waves has resulted in a number of theories, which are still inconsistent and fail to correspond with the observed nature of waves. Every experiment revealing a new phenomenon of air-sea interaction requires revision of the existing theories until a new conclusive and consistent model is developed. The originality of environmental conditions and complexity of wave measurements create difficulties when comparing experimental data from different wave experiments and inhibit understanding of the physical mechanisms of air-sea interaction. Therefore, development of a consistent theory is complicated.

Suggested parameterisations of the wind input spectral function  $S_{in}$  have been defined for some particular environmental conditions, but their application generally is questionable. For example, the parameterisations presently used in wave modelling (3G-WAM, SWAN, WAVEWATCH-III) were defined for light and moderate winds and their use in strong wind conditions is unjustified. Furthermore, they do not reflect all the physical processes observed in the recent experiment by Donelan et al. (2006) at Lake George, New South Wales, Australia in 1997-2000, which revealed new mechanisms of wind-wave interaction and resulted in a new approach to parameterisation for the wind input source function in terms of the properties of the wind profile and the wave field. The Lake George experiment was the first attempt to measure the pressure growth term on waves in shallow water. The depth limiting effect on the wave propagation phase speed made it possible to study a wide range of wind forcing conditions ( $U_{10} / c_p$ ). The study revealed the following new features of wind-wave interaction.

1. Wind flow separates from the water surface when the wind is very strong, which reduces wind energy transfer to the waves.
2. Wave growth rates depend on the steepness of the wave.

**Flow Separation** was described by Jeffreys (1925) in his *sheltering theory*, where he explained the mechanism of an energy transfer from the wind to the waves. Jeffreys (1925) assumed that the energy transfer is caused by form drag associated with flow separation, which is occurred on the leeward side of wave crests. However, the sheltering theory fell into disrepute after the experiments of Stanton (1932), Motzfeld (1937) and Thijsse (1951) found the sheltering effect too small to support the measured wave growth rates. As a result, this feature was not included in parameterisation forms for

the wind input source term. Suggested parameterisation forms demonstrated a gradual increase in wave growth rates towards higher frequencies.

Only half a century later, the Lake George experiment found that flow separation occurs at wave spectral components higher than some threshold wave components, resulting in reduction of wind energy input for these wave components. It was defined that the full separation of the flow over a steep wave crest to mean that the streamlines detach from the flow at the steep crest and do not reattach until well up the windward face of the preceding wave towards its crest.

**Wave Growth Rates** depend on wave steepness. Previously, based on the potential theory for gravity waves, growth rate was considered a non-dependent parameter of wave steepness. However, the Lake George experiment showed that both the phase shift and the normalized induced pressure amplitude are related to the wave steepness and approach their potential flow values only when  $ak \rightarrow 0$ . The experiment at Lake George resulted in the dependency of the wave growth rate in the form:

$$\gamma = G\sqrt{B_n} \cdot \left[ \frac{U_{10}}{c} - 1 \right]^2 \quad (\text{Eq. 2-25})$$

where  $\gamma$  is the growth rate,  $B_n$  is the normalised spectral saturation (Eq. 2-19) used as spectral analogue of wave steepness and  $G$  is the sheltering coefficient accounting for the effect of the flow separation on wave growth:

$$G = 2.8 - 1.0 \cdot (1 + \tanh(10 \cdot \sqrt{B_n} \cdot \left[ \frac{U_{10}}{c} - 1 \right]^2 - 11)) \quad (\text{Eq. 2-26})$$

The function (Eq. 2-26) is a smoothed analogue of the Heaviside function used for the representation of the flow separation effect. Thus, the Lake George experiment resulted in a new parameterisation form for the wind input source term  $S_{in}$  employing these new features (Donelan et al., 2006). The results of the Lake George experiment show that previously suggested wind-wave coupling theories need thorough revision and experimental confirmation due to present inconsistencies.

**Wind Stress** is one of the important characteristics of the wind-wave interaction and helps determine the strength of this interaction. Wind stress is the drag or tangential force per unit area exerted on the water surface by the adjacent layer of the airflow. The production of waves on water surface is a manifestation of the wind stress.

The positive flux of energy through the air-sea interface is a result of stress variations exerted on the water surface by the wind. Therefore, wind stress determines the exchange of momentum between the atmosphere and the water surface.

Significant stresses arise within the boundary layer because of the strong shear of the wind between the slowly moving air near the water surface (critical layer from Miles 1957) and the more rapidly moving air in the layer above due to the turbulent nature of the airflow in this area. Within the air-sea boundary layer, the total wind stress can be represented by three components: 1) the turbulent stress, 2) the wave-induced stress, and 3) the viscous or tangential stress:

$$\tau = \tau_t + \tau_w + \tau_v \quad (\text{Eq. 2-27})$$

where  $\tau$  is the total wind stress  
 $\tau_t$  is the turbulent stress  
 $\tau_w$  is the wave-induced stress and  
 $\tau_v$  is the viscous stress.

The atmospheric turbulent momentum flux decreases to zero at the surface where the turbulence vanishes. Therefore, at the surface the total wind stress is a combination of the wave-induced stress  $\tau_w$  applying to the ocean waves and the viscous stress  $\tau_v$  affecting the ocean currents directly.

Wind stress depends on the geometry of the air-sea boundary layer. In light winds, the sea surface is calm and aerodynamically smooth. Wind stresses exerted on the sea's surface are, therefore, small. In strong winds, the sea surface is aerodynamically rough and the wind stresses are large. Thus, surface roughness determines the wind drag force over the sea surface characterised by the drag coefficient.

The drag coefficient over the sea is an important quantity in both meteorology and oceanography since it relates the wind speed to the drag. The drag generates ocean waves, drives the ocean currents and sets the scale of the atmospheric turbulence, which transfers water vapour and heat from the ocean to the atmosphere to provide the energy for clouds and weather systems.

The drag coefficient of the sea surface depends on the wave field and on the turbulent structure of the flow in the air and the water. Existing knowledge of complicated fluid mechanics is not sufficient for the theoretical calculation of the drag coefficient.

The coefficient is mostly independent of the fetch and depends more on the short waves and ripples rather than on large waves.

It has been generally accepted that the drag coefficient increases with the wind speed. However, continued observations from Donelan et al. (2004) have indicated that the drag coefficient approaches a limiting value in strong winds.

The relationship of wind stress to the drag coefficient can be expressed in the form:

$$\tau = \rho_a C_d U_{10}^2 \quad (\text{Eq. 2-28})$$

where  $\rho_a$  is the density of air  
 $U_{10}$  is the wind speed measured at 10m height and  
 $C_D$  is the drag coefficient.

According to (Eq. 2-28), the total wind stress is determined by the wind speed  $U_{10}$  and drag coefficient  $C_D$  characterising the state of air-sea boundary layer.

**Wind-Wave Coupling.** The profile of the air-sea boundary layer plays a key role in the interaction between wind and sea surface. Janssen (1991) has shown that momentum fluxes are determined not only by wind speed but by the wave spectrum. Air and water form a coupled system (Young, 1999). The momentum flux from wind to wave significantly depends on the profile of the air-sea interface, which includes the near surface atmospheric boundary layer and near surface water boundary layer. The profile of the water surface is defined by surface roughness,  $z_0$ . The presence of high frequency waves modulated on the longer waves results in the enhancement of surface roughness  $z_0$ . The growth of surface roughness  $z_0$  results in an increase of airflow roughness (coupling effect) increasing the height of the critical layer from Mile's theory (Janssen, 1991). Hence, the high frequency components of the wave spectrum influence the roughness of the air-sea boundary layer, thus increasing the height of the critical layer.

On the other hand, a study by Pushkarev et al. (2002) shows the importance of the state of the high frequency spectral components in the process of energy dissipation during wave development. The authors define the high frequency range as an effective sink of wave energy. Furthermore, Janssen (1991) notes that most of the wave-induced stress is carried by high frequency waves, which rapidly respond to a change of wind direction. According to Janssen, most of the energy fluxes from the wind to the waves occur at these scales

of the wave spectrum. Therefore, the shape of the wave spectrum, especially the level of the high frequency spectral tail, has a significant influence on air-sea interaction.

According to Donelan et al. (2006), the wind input source function  $S_{in}$  is nonlinearly dependent on the wave spectrum. As seen from the definition of the wind input energy term  $S_{in}$  (Eq. 2-23), it is a function of wave energy density and the fractional growth rate  $\gamma$ . The latter, in turn, is dependent on wave steepness, which Donelan et al. (2006) describe by the spectral saturation  $B_n$  (Eq. 2-18) and which also depends on the wave spectrum. Therefore, the shape of the wave spectrum defines the shape of the wind input spectral function and consequently the amount of energy transferred from the wind to the waves. The difference between the spectral levels in the high frequency range (see Figure 2.4) determines the difference in energy transfer rates from the wind to the short scale waves. Therefore, wind stresses computed for these spectra are expected to be different.

### 2.3.2.2 Wave Dissipation

As waves grow under the influence of the wind they tend to break as steepness increases, and dissipate energy through various mechanisms. The appearance of ‘white caps’ is one of the indications of this dissipative process. White capping has generally been regarded as the dominant dissipative mechanism in a wave field at moderate and higher wind speeds, simply because other dissipative processes, such as molecular viscosity and turbulence, appear to be inadequate to remove the energy which is known to be imparted to the waves by the wind (Hasselmann, 1974). This process of gravitational breaking is transient and initiated when waves become unstable.

A number of approaches have been suggested to model energy dissipation due to a wave breaking. Two of these approaches, the *pressure pulse model* (Hasselmann, 1974) and the *quasi-saturated model* (Phillips 1985, Donelan and Pierson 1987), treat dissipation as a quasi-linear function of the wave spectrum. The *probability model* (Yuan et al., 1986), on the other hand, considers dissipation to be exponentially dependent on the wave spectrum.

The *pressure pulse* or *quasi-saturated* models are deterministic (Young, 1999). Observations of waves, however, indicate that white-capping is highly variable. There can be two waves, which for all practical purposes appear identical with the same height, period and steepness. One will break and the other will not (Young, 1999). Thus, Yuan et al. (1986) suggest that white-capping be regarded as a stochastic process, where each wave is assigned a probability of white-capping defined by a *probability model*.

Early attempts to compute the energy losses due to wave dissipation have been loosely based on physics. Suggested parameterisation forms were developed based on the consideration of the dissipation's source term as a residual tuning term for wave models in order to reproduce the existing observational data. The review work of Banner and Young (1994) regarding the performance of the dissipation source term demonstrate the limitations of the tested parametric function. Babanin and Van der Westhuysen (2007) have demonstrated that such an approach is no longer satisfactory.

Over the past decade, new features of wave dissipation processes have been discovered experimentally, which have brought new insights in wave modelling. The experimental study at Lake George obtained valuable experimental data of wave dissipation processes in terms of breaking probability (Banner et al., 2000; Babanin et al., 2001; Babanin and Young, 2005, Young and Babanin, 2006). In a series of recent papers these researchers have suggested that wave dissipation is a result of hydrodynamic effects associated with nonlinear ocean wave groups (Banner et al., 2000; Banner et al., 2002). Based on these physical considerations, Banner and Babanin and their colleagues have been able to describe the probability of breaking as a function of environmental conditions, which include properties of the local wind and wave field, shear current and bottom interaction (Banner et al., 2000; Babanin et al., 2001).

The breaking probability was determined using the average number of breaking waves passing a fixed point per wave period (Banner et al., 2000). The researchers observed that waves breaking in deep water are driven primarily by nonlinear hydrodynamic processes associated with wave groups. Secondary influences on breaking waves include the wind drift layer (critical layer), shear current and wind forcing (Banner et al., 2000; Babanin et al., 2001). In addition, analysis of data from the Lake George investigation revealed the existence of a threshold of a predominantly hydrodynamic parameter, significant wave steepness, below which breaking does not occur (Banner et al., 2000; Babanin et al., 2001 and Banner et al., 2002). The data showed a rapid increase of breaking probability above this threshold for a broad range of wave conditions.

On the basis of the recent experimental observations at Lake George (Banner et al, 2000 and Babanin et al, 2001), the authors showed that the breaking of waves depends on the excess of the steepness of the waves above the threshold steepness at some particular spectral scale. The value of the threshold steepness plays a significant role in determining the spectral level of the threshold spectrum. The observed values for threshold steepness were reported to be

in the range of  $\sqrt{B_{nT}}(f) = [0.0223, 0.0254]$  by Babanin and Young (2005) on the basis of wave breaking data from Lake George. According to Young and Babanin (2006) no wave breaking was observed for waves having a lower value of steepness than the threshold steepness. Translating this into spectral terms, the threshold wave spectrum  $F_T(f)$  represents the state of the sea where no wave breaking occurs. Subsequently, the wave energy dissipation is determined by the magnitude of the spectral exceedance of the wave spectrum over the threshold spectrum,  $\Delta F = F(f) - F_T(f)$ . Hence, the spectral level of the threshold spectrum determines the magnitude of the residual spectrum  $\Delta F$ .

Another feature of the wave dissipation process revealed in the Lake George experiment is the fact that the breaking of long waves affects the breaking of short waves (Babanin and Young, 2005; Young and Babanin, 2006). This feature has never been included in previously suggested parameterization forms for the dissipation source term.

The results of the study at Lake George have shown that wave breaking exhibits two-phase behaviour (Babanin and Young, 2005) and can be represented in a parametric form as follows:

$$S_{ds}(f) = a \cdot \underbrace{f \cdot A(f) \cdot (F(f) - F_T(f))}_{T_1(f)} + b \underbrace{\int_{f_p}^{f_{cut}} A(f) \cdot (F(f) - F_T(f)) df}_{T_2(f)} \quad (\text{Eq. 2-29})$$

where  $F(f)$  - is the wave spectrum  
 $F_T(f)$  - is the threshold spectrum  
 $A(f)$  - is the directional spreading width  
 $a$  and  $b$  - are coefficients for inherent wave breaking term,  $T_1(f)$  and cumulative or forced wave breaking term,  $T_2(f)$ , respectively.

According to Equation 2-29, the wave dissipation source function includes two terms accounting for two types of wave dissipation processes. The main source of the wave energy loss is the wave breaking known as the white-capping. It was found that waves are prone to break if their steepness exceeds the threshold steepness (Banner et al. 2000 and Babanin et al. 2001). This type of wave breaking is termed inherent wave breaking and represented by the first term  $T_1(f)$  (Eq. 2-29).

In addition, wave energy can dissipate due to turbulent viscosity, which plays a significant role in small scale waves. It is believed that turbulent viscosity dissipation is minimal

for dominant waves and significant for short scale waves, where the induced dissipation phenomenon was observed by Manasseh et al. (2005) and Young and Babanin (2006).

At the same time, small scale waves tend to break due to the breaking of longer scale waves (Young and Babanin, 2006). Both types of wave energy dissipation are induced by the breaking of the dominant waves and referred to as forced dissipation, represented by the second term  $T2(f)$  (Eq. 2-29). One of the origins of induced dissipation can be enhanced turbulent viscosity due to the breaking of the dominant waves (Young and Babanin, 2006).

A series of recent observations were conducted in order to estimate dissipation rates in terms of the average length of breaking crests per unit area per unit speed interval  $A(v)$ , as introduced by Phillips (1985). Field measurements of Phillips et al. (2001), Melville and Matusov (2002), Hwang and Wang (2004b) and Gemmrich (2005) have enriched the existing knowledge of wave dissipation processes with valuable facts and observational data. The FAIRS experiment (Gemmrich, 2005) showed that the dissipation rates are highest for intermediate-scale waves, which is consistent with earlier observations of Hwang and Wang (2004b).

However, most experimental data relating to wave dissipation are still discrepant and inconclusive. The reasons for the discrepancies are not clear yet and require further experimental investigation. In the present study, an attempt was made to reconcile the computation results with the existing observational data.

### 2.3.2.3 *Nonlinear Wave-Wave Interaction*

The JONSWAP (Hasselmann, 1973) experiments showed the important role in the evolution of wind waves played by nonlinear wave-wave interactions, which result in a transfer of energy between the spectral components (Phillips, 1980). A theoretical investigation of the nonlinear interaction processes has been performed by Hasselmann and Hasselmann (1981) and Young and Van Vledder (1993). In deep water the nonlinear energy transfer involves the interaction within a group of four waves, which is called a quadruplet. These waves can exchange energy if they satisfy the following resonance conditions:

$$\begin{cases} \mathbf{k}_1 + \mathbf{k}_2 = \mathbf{k}_3 + \mathbf{k}_4 \\ \omega_1 + \omega_2 = \omega_3 + \omega_4 \end{cases} \quad (\text{Eq. 2-30})$$

where  $\mathbf{k}_j$  is the wavenumber vector and  $\omega_j$  is the angular frequency ( $j = 1, \dots, 4$ )

Figure 2.6 provides an example of quadruplet wavenumber vectors which satisfy the resonance condition (Eq. 2-30).

The mathematical representation of the nonlinear interactions in the wind wave spectrum was first formulated and studied by Hasselmann (1962) and Zakharov (1968) independently. It was assumed that waves are weakly nonlinear. The equation determining the rate of change of action density at  $\mathbf{k}_l$  is written as the kinetic equation of the form:

$$\frac{\partial N_1}{\partial t} = \iiint G_q(\mathbf{k}_1, \mathbf{k}_2, \mathbf{k}_3, \mathbf{k}_4) \delta(\mathbf{k}_1 + \mathbf{k}_2 - \mathbf{k}_3 - \mathbf{k}_4) \delta(\omega_1 + \omega_2 - \omega_3 - \omega_4) \times [N_1 N_3 (N_4 - N_2) + N_2 N_4 (N_3 - N_1)] d\mathbf{k}_2 d\mathbf{k}_3 d\mathbf{k}_4 \quad (\text{Eq. 2-31})$$

where  $N_j = N(\mathbf{k}_j)$  is the action density at wavenumber  $\mathbf{k}_j$ ,  
 $G$  is a complex interaction matrix defining the strength of the interaction  
 $\delta(\mathbf{k}_j)$  and  $\delta(\omega_j)$  are the Dirac delta functions describing the resonance conditions of the interaction

The integral is known as the Boltzmann integral for wind waves. The most important property of the kinetic equation (Eq. 2-31) is the conservation of the following three integral quantities during wind wave development:

The total wave action	$\int N(\mathbf{k}) d\mathbf{k}$
The total energy	$\int \frac{\omega N(\mathbf{k})}{4\pi^2 g} d\mathbf{k}$
The total momentum	$\int \mathbf{k} N(\mathbf{k}) d\mathbf{k}$

The existence of these integrals of motion for the kinetic equation was first proved by Hasselmann (1963).

For the solution of the Boltzmann integral numerous techniques have been proposed. All these techniques have the same major goal: to improve computational speed and to provide better understanding of the physical processes occurring during nonlinear wave-wave interactions (Young, 1999). Hasselmann (1963b) proposed the visualization of the interaction space, the so-called *figure of eight*, which significantly helped to explain the existing issue. Hasselmann and Hasselmann (1981, 1985b) proposed a symmetric

integration technique, which reduced the effective computational time by a factor of four. Figure 2.7 shows the so-called *figure of eight* diagram showing the interaction space for a given value  $\mathbf{k} = \mathbf{k}_1 + \mathbf{k}_2 = \mathbf{k}_3 + \mathbf{k}_4$  (Young (1999)).

Additional increases of computational speed by up to a factor of 100 have been made by reducing the number of quadruplets, which are an insignificant contribution to the Boltzmann integral (Young, 1999). Increasing the computational speed enabled the development of the first spectral model with a full solution for  $S_{nl}$  – EXACT-NL (Hasselmann and Hasselmann, 1985a). This model provided a one-dimensional solution for the energy balance equation.

For two-dimensional wave prediction models various techniques for the parameterisation of  $S_{nl}$  have been proposed. These methods have proved relatively simple and computationally efficient (Barnett, 1968; Ewing, 1971; Hasselmann et al., 1985a; Young, 1988a). Hasselmann (1985a) proposed *the discrete interaction approximation* (DIA) to the Boltzmann integral.

The DIA uses a small number of quadruplets which all have the same configuration. However, Van Vledder et al. (2000) and Van Vledder and Bottema (2002) have shown that some limitations of the DIA method compare to the EXACT-NL solution of the Boltzmann integral in terms of precise representation of the nonlinear transfer rate. Furthermore, the DIA pumps too much energy to higher frequencies from the spectral region near the spectral peak (Van Vledder et al., 2000, and Van Vledder and Bottema, 2002). Therefore, the EXACT-NL solution is the more preferable method for use in wave modeling.

Lin and Huang (1998) proposed a solution based on the Hamiltonian approach of Zakharov (1968), which enables development of a two-dimensional model. Webb (1978) rewrote Hasselmann's equation (Eq. 2-31) using some analytical transformations to eliminate the  $\delta$ -functions. One of the advantages of Webb's method is that the equations and structure of the computational method are equal, both for deep and shallow water. This considerably simplifies the computations and the implementation in operational wave models.

Webb's (1978) method was extended and implemented in a discrete spectral model by Tracy and Resio (1982) and Resio and Perrie (1991). They proposed a numeric technique which makes integration of the Boltzmann integral simpler and more efficient by the utilization of a geometrically spaced polar grid over the spectral region.

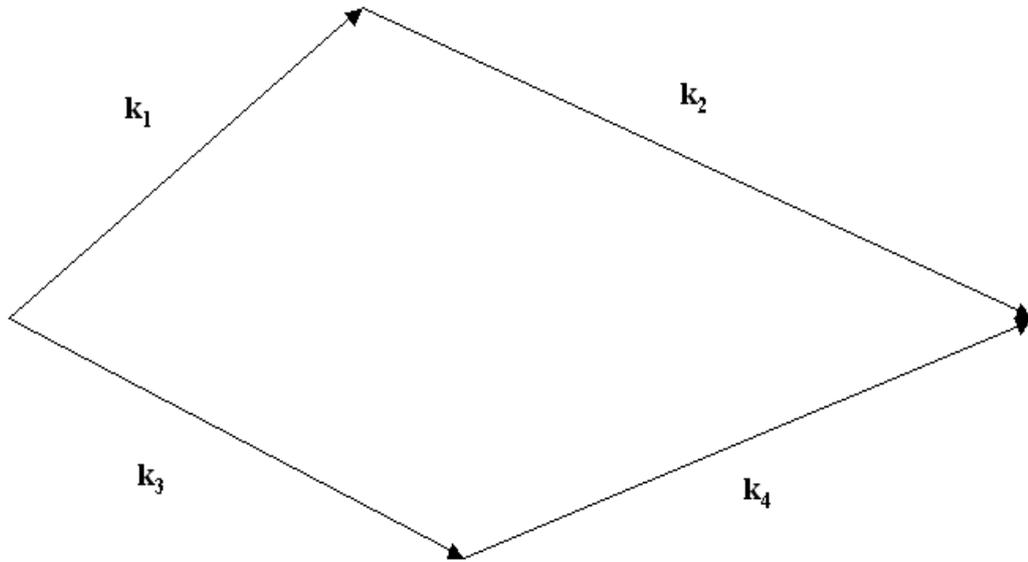


**Figure 2.6** Example of quadruplet wavenumber vectors, which satisfy the resonance condition

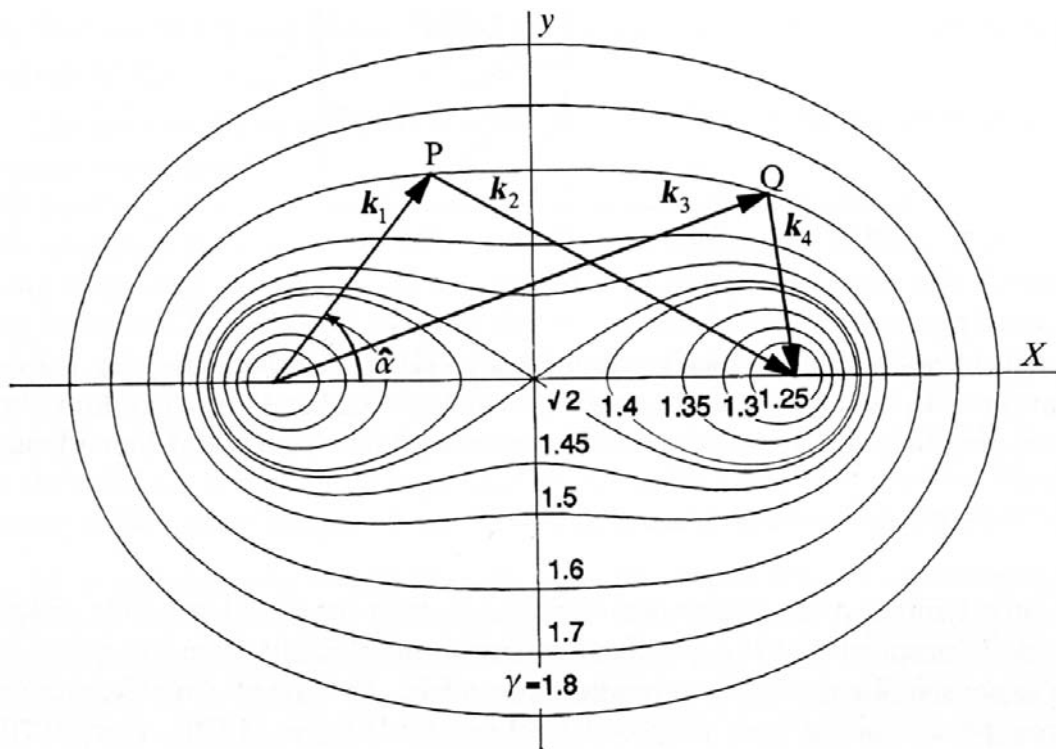


**Figure 2.7** The so-called *figure of eight* diagram showing the interaction space for a given value  $k = k_1 + k_2 = k_3 + k_4$  [Young (1999)].

Tracy and Resio (1982) demonstrated that different parts of the integration space are related via scaling laws, thus making computations of the nonlinear transfer rate more efficient in timescale by an order of magnitude. This method is generally known as the WRT method for the computation of the nonlinear transfer rate in a discrete wave spectrum.

Resio and Perrie (1991) and Young and Van Vledder (1993) presented further applications of this method. Resio et al. (2001) developed a shallow water version of Webb's method. To improve the original WRT method, Van Vledder (2005) completely rewrote it to make it available as a subroutine for implementation in any third generation wave model. The WRT method has been implemented in various third generation wave prediction models, such as WaveWatch III (Tolman, 1999), SWAN (Booij et al., 2004), CREST (Ardhuin et al., 2001), PROWAM (Monbalieu et al., 1999) and WAVETIME-1 (Van Vledder, Alkyon, 2002, personal communication). The latter wave model was used in the present study.

### 2.3.3 WAVE GROWTH RELATIONSHIPS

In oceanography, it is generally accepted that wave growth can be expressed in the form of non-dimensional growth curves. Based on dimensional analysis, Sverdrup and Munk (1947) and Kitaigorodskii (1962, 1970) suggested that five quantities, including the total energy or variance of the water surface elevation  $\sigma^2$ , fetch  $x$ , peak frequency  $f_p$ , the wind speed  $U_h$  at a reference height  $h$  and duration  $t$  for which the wind blows, can be grouped in non-dimensional forms:

$$\varepsilon = \frac{\sigma^2 g^2}{U_h^4} \quad (\text{Eq. 2-32})$$

$$\nu = \frac{f_p U_h}{g} \quad (\text{Eq. 2-33})$$

$$\chi = \frac{gx}{U_h^2} \quad (\text{Eq. 2-34})$$

$$\zeta = \frac{gt}{U_h} \quad (\text{Eq. 2-35})$$

where  $\varepsilon$  is non-dimensional energy,  $\nu$  is non-dimensional frequency,  $\chi$  is non-dimensional fetch and  $\zeta$  is non-dimensional duration.

Accordingly, the duration- and fetch-limited growth can be expressed in the following relational forms, respectively:

$$\begin{aligned}\varepsilon &= A_{et} \cdot \zeta^{a_{ft}} \\ \nu &= A_{ft} \cdot \zeta^{a_{ft}}\end{aligned}\quad (\text{Eq. 2-36})$$

$$\begin{aligned}\varepsilon &= A_{ex} \cdot \chi^{a_{ex}} \\ \nu &= A_{fx} \cdot \chi^{a_{fx}}\end{aligned}\quad (\text{Eq. 2-37})$$

where  $A_{et}$ ,  $A_{ft}$ ,  $A_{ex}$ ,  $A_{fx}$  are relational coefficients and  $a_{et}$ ,  $a_{ft}$ ,  $a_{ex}$ ,  $a_{fx}$  are exponents of time-limited and fetch-limited growth curves, respectively.

Under steady wind forcing, the development of waves follows the duration- and fetch-limited growth laws. These growth functions are used extensively to obtain sea-state information when only limited observations of environmental variables are available. Validation and verification of wave models also employ experimentally obtained data of duration- and fetch-limited wave growth for benchmark tests.

It worth mentioning some issues regarding duration-limited growth arising in wave studies. Most field and laboratory wave observations have obtained fetch-limited evolution data. At the same time, experimental data of duration-limited growth are rare and do not cover a wide range of the wave development stage (Hwang and Wang, 2004a).

On the other hand, most analytical solutions for wind waves are given in time rather than fetch domain. Numerical modelling of wave development is also often performed in temporal evolution mode. As a result, theorists and modellers have to rely on fetch-limited evolution data, converting them into duration-limited conditions on the basis of some assumptions (Hwang and Wang, 2004a). Therefore, conversion equations of simple power-law fetch-limited growth functions to duration-limited growth functions have been proposed by Bretschneider (1952a,b) and Mitsuyasu and Rikiishi (1978). Recent work of Hwang and Wang (2004a) provide strong support for the relation of space–time conversion of the fetch-limited growth functions to duration-limited growth functions. Based on the method of Hwang and Wang (2004a), the advanced formula for the conversion of fetch-limited growth functions to duration-limited growth functions is suggested by the present study.

### 2.3.4 OBSERVATIONAL DATA

Currently a large number of wave observations result in huge amounts of accumulated experimental wave data without providing the necessary accuracy or insight into wave growth. Still, there is a large scattering in measured wave growth rates and the parameterisations result in a broad range of values for estimated parameters.

One of the most significant studies resulting in accurate wave data was the Black Sea experiment of Babanin and Soloviev (1998). This experiment investigated wave development at a wide range of wind speeds using a wire resistance wave gauge. Based on the experimental data, the researchers determined dependencies of non-dimensional frequency and wave energy from the fetch:

$$\begin{aligned} \nu &= 2.40 \cdot \chi^{-0.275} \\ \varepsilon &= 8.3 \cdot 10^{-6} \cdot \nu^{-3.01} \end{aligned} \quad (\text{Eq. 2-38})$$

The growth curves obtained in this study show good agreement with the experimental dependencies observed by other authors including Kahma (1981), Donelan et al. (1985), Dobson et al. (1989) and Donelan et al. (1992).

On the basis of the obtained data, Babanin and Soloviev (1998) described a transformation of the wind wave spectrum with the wave development in terms of the JONSWAP spectrum shape parameters including  $\alpha$  and  $\gamma_J$ . The authors found that the spectral shape parameters  $\alpha$  and  $\gamma_J$  are functions of non-dimensional frequency:

$$\alpha = \begin{cases} 8.03 \cdot 10^{-2} \cdot \nu^{1.24}, & \nu \leq 0.23 \\ 13.2 \cdot 10^{-3}, & \nu > 0.23 \end{cases} \quad (\text{Eq. 2-39})$$

$$\gamma_J \approx 7.6 \cdot \nu \quad (\text{Eq. 2-40})$$

According to Equation 2-38, the equilibrium interval level  $\alpha$  remains constant for the first stage of wave development. For developed waves, the level  $\alpha$  decreases.

Furthermore, Babanin and Soloviev (1998) showed a variability of directional spectrum with wave development. According to their data, the researchers determined the relationship between the width of the directional distribution  $A$  and the wave development parameters: the wind-forcing  $U_{10}/c_p$  and the relative frequency  $f/f_p$ :

$$A = \begin{cases} \left[ 1.18 \cdot \left( \frac{U_{10}}{c_p} \right)^{-0.5} + (2\pi)^{-1} \right] \cdot \left[ 2.05 \cdot \left( \frac{f}{f_p} \right)^{\exp(1.39 \frac{U_{10}}{c_p})} - 1.05 \right] & f < 0.95 f_p \\ 1.18 \cdot \left( \frac{U_{10}}{c_p} \right)^{-0.5} + (2\pi)^{-1}, & f = 0.95 f_p \\ 1.12 \cdot \left( \frac{U_{10}}{c_p} \right)^{-0.5} \left( \frac{f}{f_p} \right)^{-0.95} + (2\pi)^{-1}, & f \geq 0.95 f_p \end{cases} \quad (\text{Eq. 2-41})$$

It was shown that broadening of the directional width at higher frequencies depends only on the relative frequency  $f/f_p$ , while at the peak frequency the directional width is determined only by  $U_{10}/c_p$ . The behaviour of the directional width at frequencies lower than peak frequency is strongly dependent on both  $U_{10}/c_p$  and  $f/f_p$ . The narrowest directional spectra are on average observed at  $0.95 f_p$ . The above-mentioned relationships were used for validation of computational results in the present study. The results of comparisons will be shown later in Section 4.3.

## 2.4 METHODOLOGY FOR ASSESSMENT OF SPECTRAL SHAPE

In wave modelling, prediction of wave fields requires the determination of the wave spectrum at a given time and space. In order to verify the results of a wave model, the resulting wave spectrum must be assessed in terms of its spectral shape in both the frequency and directional domain. One of the most comprehensive methods for assessment of spectral shapes was suggested by Banner and Young (1994). According to this method, a number of integral spectral parameters were accepted as diagnostic features for comparison between model results and observations. These features include:

- the evolution of non-dimensional energy,  $\varepsilon$ , and peak frequency,  $\nu$ , with non-dimensional fetch  $\chi$  or duration  $\zeta$ .
- the spectral shape parameters  $\alpha_{BY}$  and  $n$  are diagnostic for the behaviour of the wind direction slice of the wavenumber spectrum:

$$F(k, \theta_w) = \alpha_{BY} u_*^{-2(n+4)} g^{(n+4)} k^n$$

- the directional spreading of the spectrum  $D(\theta, k)$  from

$$F(k) = F(k, \theta_w) D(\theta, k)$$

- the ratio of the maximum of wave spectrum to the magnitudes of wind direction slice wavenumber spectrum, hereafter the lobe-ratio:

$\lambda(k) = F_{max}(k, \theta) / F(k, \theta_w)$  as a diagnostic parameter for bimodality of the directional shape of wave spectrum. Hence, a value  $\lambda = 1$  indicates a unimodal directional spread.

- the mean spectral width,  $\bar{\theta}(k) = \frac{\int_0^{\pi/2} F(k, \theta) \theta d\theta}{\int_0^{\pi/2} F(k, \theta) d\theta}$ , for identification of the directional distribution of wave spectrum

- the similarity parameter  $\zeta$  for diagnostic of the spectral energy level in the high frequency range computed as the ratio of wind direction energy at a given wavenumber and wave age to that predicted by Banner (1990):

$$\zeta = \frac{F(k = 0.5cpm, \theta_w)}{F_{B90}(k = 0.5cpm, \theta_w)}$$

The suggested diagnostics were used as a basis for validation technique developed in the present study.

## CHAPTER 3      NUMERICAL MODEL

---

The investigation of the spectral functions of the wind input  $S_{in}$  and the wave dissipation  $S_{ds}$  source terms was performed using a new third generation, one dimensional research wave model WAVETIME-1 developed by Van Vledder (Alkyon, 2002, personal communication). The model WAVETIME-1 was developed in FORTRAN-90. It includes the EXACT-NL model (Hasselmann and Hasselmann, 1985a) using the WRT method (Webb, 1978; Tracy and Resio, 1982) for computations of the nonlinear wave interactions incorporated by Van Vledder (2002).

WAVETIME-1 essentially solves the radiative transfer equation (Eq. 2-20) (Gelci et al., 1957; Hasselmann, 1960; Phillips, 1977 and Komen et al. 1994) either for fetch-limited or duration-limited conditions. For the present study, however, only duration-limited conditions were considered based on the preliminary test results of the model, which is still in the development stage.

One of the advantages of this model is modular design, which enables further development of the model for research purposes. The model operates in one of four different modes:

1. source mode – computations of the source terms for the given spectrum
2. time mode – computations of duration-limited growth
3. fetch mode – computations of fetch-limited growth
4. grid mode – computations of wave propagation on a spatial grid

The model is able to perform computations in different numerical schemes (e.g. explicit or implicit).

### 3.1      THE SPECTRAL GRID

WAVETIME-1 can perform computations for different types of frequency-direction grids. It generates a frequency grid on the basis of specified data including minimum frequency,  $f_{min}$ , maximum frequency,  $f_{max}$ , and number of frequency points,  $nfr$ . In terms of the frequency distribution, the model can specify two types of frequency grids, either linear or geometric spacing.

For the first type, frequency points are evenly distributed along the chosen bandwidth. For a geometric grid the following frequency is defined as  $f_{i+1} = \delta f_i$  where  $\delta > 1$  is the spacing factor. In terms of the directional grid, the model is able to generate a polar grid either over the full circle or in a sector with two specified directions. Furthermore, computations can be performed for a single direction. Selection of the appropriate spectral grid predetermines the numerical stability of the wave model.

In the present study, the single spatial grid point version of the WAVETIME-1 model was used for the numerical experiments. Selection of the optimal spectral grid was based on the accuracy of the computation of the nonlinear transfer rate to satisfy the conservation laws for action, energy and momentum. Van Vledder (2005) showed that for deep water the minimum frequency should at most be equal to half the peak frequency ( $f_{min} \leq 0.5f_p$ ). The maximum frequency should be taken sufficiently high to achieve the optimal accuracy in computations using the WRT method. The selection of the maximum frequency is related to the cut-off effects near the upper boundary of the frequency grid (Van Vledder, 2005). Accurate computation of the nonlinear transfer rate in a certain spectral bin requires consideration of all interactions with higher and lower frequencies. For the frequency bins near the maximum discrete frequency, a number of interactions with frequencies higher than the maximum frequency is omitted resulting in inaccuracy of the computations of the nonlinear rate, called the cut-off effect. In the recent study, Van Vledder (2005) showed that the cut-off effects affect the nonlinear transfer rate for the upper 20% of the frequency bandwidth and vanish when  $f_{cut} > 6f_p$ .

For time-efficient computations of the WRT method, selection of the frequency grid spacing is very important. In operational wave modeling, it is convenient to use a geometric spacing of wave numbers in discrete spectral models, in which  $k_{n+1} = \delta k_n$  with  $\delta > 1$ . Such spacing provides a higher spectral resolution near the peak frequency and less resolution in the high frequency range of the wave spectrum. The geometric spaced grid allows the use of scaling laws in computations of the WRT method for deep water conditions. According to Resio and Perrie (1991), this scaling technique speeds up the computation of the nonlinear transfer rate by an order of magnitude compared to integration on regular spaced grids. The geometric spacing of the frequencies is widely used in spectral wave models, including WAM, WaveWatch, TOMAWAC and SWAN.

On this basis, the directional frequency spectrum  $F(f, \theta)$  was discretised into a polar grid with 36 angular bands evenly distributed over a full circle and 80 frequencies within the bandwidth limited by the lower frequency  $f_{min} = 0.02$  Hz and the upper frequency

$f_{cut} = 4.5\text{Hz}$ . The geometric spacing of the discrete frequencies was selected as  $f_n = 1.05f_{n-1}$  giving a frequency resolution of 5% for the frequency spectral grid. Such a spectral grid has a higher frequency resolution than computational grids widely used in current wave modeling practice (i.e. 10%).

The selected frequency bandwidth allowed accurate computations to be performed from the very young stages of wave development up to full development for a wide range of wind speeds  $U_{10} \leq 30$  m/s. The computational grid remained the same throughout the model computations. It is worth mentioning that this bandwidth of the frequency scale does not cover the range of short scale waves, where their contribution to total wave-induced stress is important.

The accuracy of the computations of wave-induced stress has a significant impact on the outcome results of the model. It is desirable that the frequency bandwidth computations of the new spectral functions of the wind input and wave dissipation source terms be lengthened up to  $f_{max} = 10\text{Hz}$ . On the other hand, in operational wave modeling, according to Banner and Young (1994), the frequency bandwidth for spectral computations is limited by the validity of the nonlinear interaction term  $S_{nl}$  in terms of the ratio of the root-mean square wave height  $H_{rms}$  to the shortest wave wavelength  $\lambda_{cut}$ . The computations are valid if  $H_{rms} / \lambda_{cut} < O(1)$ . The mentioned value for the maximum frequency,  $f_{max} = 10\text{Hz}$ , is out of the range for valid computation. Therefore, a new approach was developed to overcome this issue.

Using the new approach, the computations for the wind input and dissipation source terms were performed on a spectral grid formed by combining the main spectral grid with an extensional grid as the continuation of the main spectral grid up to the maximum frequency,  $f_{max} = 10\text{Hz}$ . On the other hand, the wave spectrum used in computations of the wind input and dissipation source terms was defined only on the main spectral grid. It became apparent, however, that the wave spectrum also needed to be expanded up to the maximum frequency of  $f_{max} = 10\text{Hz}$ . To extend the wave spectrum, a three-point extrapolation was applied to the wave spectrum by attaching a spectral tail with a slope  $f^{-5}$ . This type of extrapolation was selected to keep the numerical fluctuations low, particularly for the spectral magnitudes near the cut frequency  $f_{cut}$ .

## 3.2 INITIAL SPECTRUM

At the initial stage, the model computed the wave spectrum either from the spectral data file or by means of spectral parameters given in the input file. Using the spectral parameters, the model was able to compute different types of frequency spectra, including JONSWAP (Hasselmann et al., 1973) and Donelan (1985). On the basis of a given frequency spectrum, the model produces a directional spectrum by multiplying the frequency spectrum with a specified directional spreading function  $D(f, \theta)$ . The model was able to generate different types of spreading functions, including  $\cos^n \theta$ ,  $\cos^{2n} \theta / 2$  and the function of Babanin and Soloviev (1998). The latter was used in the present research.

## 3.3 SOURCE TERMS IN WAVETIME-1

The WAVETIME-1 model is applicable either for deep or shallow water conditions. Therefore, the model also includes computations of the source terms, which are considered significant in shallow water conditions (bottom friction, near-shore wave breaking and triad wave-wave nonlinear interactions). However, the present study considered only the deep water case and discussion about finite depth source terms was out of the scope of this study.

Initially, for computations of energy input from the wind to the waves, the model included the parameterisation form proposed by Komen et al. (1984), which was based on the earlier proposal of Snyder et al. (1981). Later in the present study this function was changed to the new parametric function of Donelan et al. (2006).

In addition, initial computations of wave dissipation used the parameterisation form introduced by Komen et al. (1984) based on the theory of Hasselmann (1974). Later in the present study this function was replaced by the new form of wave dissipation (Young and Babanin, 2006).

The WAVETIME-1 model included an improved WRT method (Van Vledder, 2005) - the full solution of the Boltzmann integral (Eq. 2-30) for computation of the nonlinear transfer within the wave spectrum. The improved technique was adopted by Van Vledder (2005) for computations in finite depth conditions. This representation of wave-wave nonlinear interactions was used as the nonlinear source term in the present study.

### 3.4 NUMERICAL SCHEME

The WAVETIME-1 model solves the RTE (Eq. 2-20) for either fetch or duration limited growth. In the present study, only duration-limited growth was considered, thus (Eq. 2-20) yields:

$$\frac{\partial F}{\partial t} = S_{tot} \quad (\text{Eq. 3-1})$$

where  $S_{tot}$  represents the summation of all contributing source terms, including the wind input  $S_{in}$ , the wave dissipation  $S_{ds}$  and the nonlinear energy transfer between the waves  $S_{nl}$ .

The simplified energy balance equation (Eq. 3-1) was solved with the explicit first order finite difference scheme:

$$F_{j+1} = F_j + \Delta F = F_j + S_{tot} \cdot \Delta t \quad (\text{Eq. 3-2})$$

where  $F_j$  is the spectral energy at the time step  $j$   
 $F_{j+1}$  is the spectral energy at the following next step  
 $\Delta F$  is the change of the spectral energy and  
 $\Delta t$  is the time interval when the change occurred.

For the present study optimal magnitude of the time step ( $\Delta t = 35s$ ) was selected on the basis of intensive numerical tests to achieve the numerical stability of the model. The selection analysis for the time step will be discussed in more detail in the following subsection 3.4.1.

#### 3.4.1 OPTIMAL TIME STEP

Accuracy of the model predictions, using the duration-limited integration scheme, significantly depends on the time step of this scheme. In this case, the energy balance equation can be represented in the form of Equation 3-1. In the present study, the computations were performed using a simple explicit integration scheme ( $\Delta F = S_{tot}\Delta t$ , see Equation 3-2). The model with the large time step performs time-efficient computations. However, the results of this computational scheme can be inaccurate, since the selection of an optimal time step in wave modelling strongly influences the computational results of the model. The length of the time step must correspond to the optimal energy interaction between the source terms, particularly with wave-wave nonlinear interactions.

The time step very much dependent on energy redistribution in the short-scale range of wave spectrum and requires precise tuning, in order to avoid the accumulation of energy in the high-frequency range.

To achieve stability in the computations, the model WAVETIME-1 includes a limitation (a so-called ‘limiter’) for the energy increment  $\Delta F$ , which restricts the change of energy density  $\Delta F$  per time step for each spectral bin to a fraction ( $\sim 10\%$ ) of the Pierson-Moskowitz level. The discrete time step  $\Delta t$  can influence numerical errors in two ways. First, numerical distortions can be increased by increasing the time step. Second, the limitation of the change to the spectral density per time step will take place more often as the magnitude of the time step increases (Tolman, 1992). Therefore, the time step must be reasonably small to avoid numerical instabilities.

The rough estimation of the optimal time step can be made based on the value of cut frequency  $f_{cut}$  selected for the spectral grid. The time step must be small comparably small to the periods of the upper spectral components. According to this estimation the time step for the selected spectral grid with  $f_{cut} = 4.5$  Hz may be in a range  $\Delta t = [20s - 40s]$

On the other hand to achieve reasonable accuracy in the model computations, a number of numerical experiments were conducted to determine an optimal time step for duration-limited wave evolution in the WAVETIME-1 model. The determination of the optimal time step was based on one of the important properties of the kinetic equation, which describes wave-wave nonlinear interactions, and the conservation of the total energy of the spectral components.

Therefore, from the source terms, only nonlinear energy transfer between the waves was considered. Other processes, like wind energy input and wave dissipation were excluded.

In this case, since the significant wave height  $H_s = 4 \sqrt{\int_{\theta} \int_{f} F(f, \theta) df d\theta}$  relates to the total energy of the waves, this parameter was expected to remain constant during wave development. Therefore, the significant wave height was selected as the main criterion for determination of the optimal time step.

The series of the above-mentioned numerical experiments was carried out with different discrete time steps,  $\Delta t = [1s, 10s, 20s, 30s, 40s, 50s, 60s]$ . Some of the results of the computations are presented in Figure 3.1. As illustrated, the significant wave height computed for the model run with the time step  $\Delta t = 35s$  was most close to its initial value. Based on these results, it was decided that the optimal time step was  $\Delta t = 35s$ .

### 3.5 VALIDATION OF THE MODEL

Prior to the investigation of the new parameterisation forms for the wind input and wave dissipation source terms, WAVETIME-1 (Van Vledder, Alkyon, 2002, personal communication) underwent intensive testing and validation of all its active components. The main focus was on the two major outcomes of the model:

- computations of the nonlinear source term  $S_{nl}$  spectra in terms of spectral integral and the spectral shape at different stages of wave development
- consistency of the model results in relation to the experimental growth curves obtained by Babanin and Soloviev (1998).

#### 3.5.1 VERIFICATION OF $S_{NL}$ SOURCE TERM

In the present study, three source terms ( $S_{in}$ ,  $S_{ds}$  and  $S_{nl}$ ) were considered as major driving mechanisms involved in wind wave development. As a prerequisite to the investigation of the wind input and wave dissipation source terms, the model computations of the nonlinear source term had to be assessed in order to ensure correct performance in subsequent numerical experiments. Therefore, the model computations of the nonlinear source term  $S_{nl}$  were verified prior to the major part of the investigation.

Nonlinear energy transfer between waves represents a conservative redistribution of spectral energy between the spectral components. This property of the kinetic equation is represented by the conservation of the total energy. Therefore, one of the criteria for verification of nonlinear source term computations is the condition:  $\int S_{nl}(f)df = 0$ . The results of computations of the nonlinear source term for different wave spectra showed that the integral value was close to zero.

Another criterion of the  $S_{nl}$  spectrum relates to its spectral shape in terms of the translocation of positive and negative lobes of the  $S_{nl}$  spectrum. The numerical tests were performed according to the method introduced by Hasselmann and Hasselmann (1981). The results were compared with the results of Hasselmann and Hasselmann (1981) and Lavrenov (1998). It is worth noting that computations of the nonlinear source term are sensitive to a number of factors relating to the spectral grid and the wave spectrum. Therefore, these comparisons can be considered qualitatively rather than quantitatively in terms of the general behaviour of  $S_{nl}$  spectra. Results of comparisons have shown that the

nonlinear energy transfer rates computed in WAVETIME-1 agree with the results of Hasselmann and Hasselmann (1981) and Lavrenov (1998).

### 3.5.2 PREPARATION OF EXPERIMENTAL DATA

Most wave observations obtain data related to fetch-limited wave growth. The most accurate data have been obtained from the Black Sea experiment (Babanin and Soloviev, 1998). Therefore, the results from the Black Sea were selected for validation of the WAVETIME-1 model in the present study.

In the present study, the WAVETIME-1 model performed computations in the time domain. Therefore, to compare the model results, the experimental fetch-limited data were converted into the time domain through the conversion of equations of simple power-law fetch-limited growth functions to duration-limited growth functions. The equations were derived on the basis of the method used in Hwang and Wang (2004a) and can be presented in the following forms:

$$A_{ft} = A_{fx} \frac{1}{a_{fx} + 1} \left[ \frac{R \cdot (a_{fx} + 1)}{2\pi} \right]^{a_{ft}}, \quad a_{ft} = \frac{a_{fx}}{a_{fx} + 1} \quad (\text{Eq. 3-3})$$

$$A_{et} = A_{ex} \left[ \frac{R \cdot (a_{fx} + 1)}{2\pi A_{fx}} \right]^{a_{et}}, \quad a_{et} = \frac{a_{ex}}{a_{fx} + 1}$$

where  $A_{et}$ ,  $A_{ft}$ ,  $A_{ex}$ ,  $A_{fx}$  are relational coefficients and  $a_{et}$ ,  $a_{ft}$ ,  $a_{ex}$ ,  $a_{fx}$  are exponents of time-limited and fetch-limited growth curves (Eq. 2-35 and 2-36), respectively. These parameters were assigned similarly to Hwang and Wang (2004a) in order to make these equations comparable. The coefficient  $R$  is the ratio  $c_{gx}/c_p$ , where  $c_{gx}$  is the downwind component of the wave group velocity and  $c_p$  is the phase speed of the wave spectral peak component. It was shown that for a monochromatic wave train,  $R = 0.5$  (Hwang and Wang, 2004a). However, for the wind waves,  $R = 0.4$  (Yefimov and Babanin, 1991). The conversion equation for the coefficient  $A_{ft}$  for non-dimensional frequency is different than that presented in Hwang and Wang (2004a).

The fetch-limited growth curves (Eq. 2-37) obtained by Babanin and Soloviev (1998) were converted into the time domain using Equation 3-3. After the conversion the experimental dependencies (Eq. 2-37) were transformed into the form:

$$\begin{aligned} \nu &= 10.74 \cdot \zeta^{-0.38} \\ \varepsilon &= 6.54 \cdot 10^{-9} \cdot \zeta^{1.14} \end{aligned} \quad (\text{Eq. 3-4})$$

The validation of the WAVETIME-1 model was performed using the growth curves from Equation 3-4. The results of the comparisons are presented in the following section.

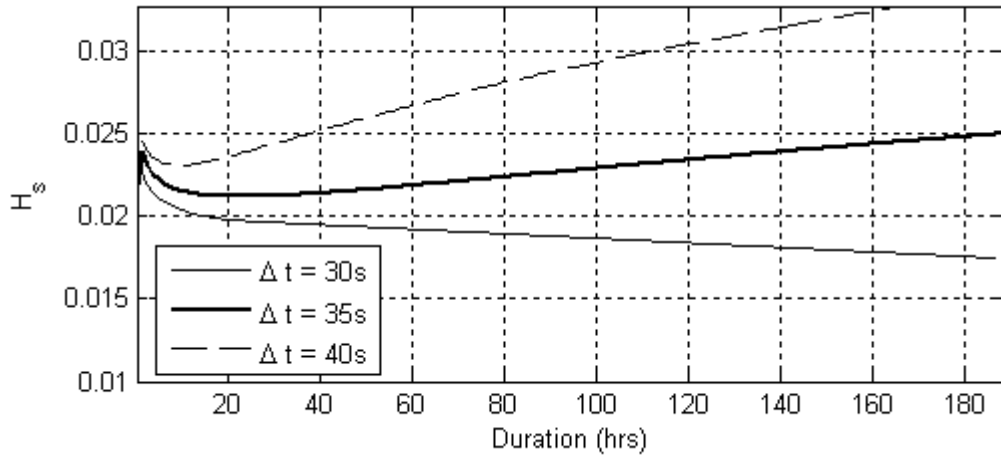
### 3.5.3 VERIFICATION OF GROWTH CURVES

In wave modelling, the main objective for verification of the model performance is to reproduce the existing observational data. In most numerical investigations, the validation strategy consists of a series of experiments for tuning the model for the best performance. In the present study, the results of model computations were tested against the observational data from the Black Sea experiments (Babanin and Soloviev, 1998) in terms of non-dimensional energy, frequency and duration. The main purpose of these comparisons was to determine whether the WAVETIME-1 model was able to reproduce the existing experimental data.

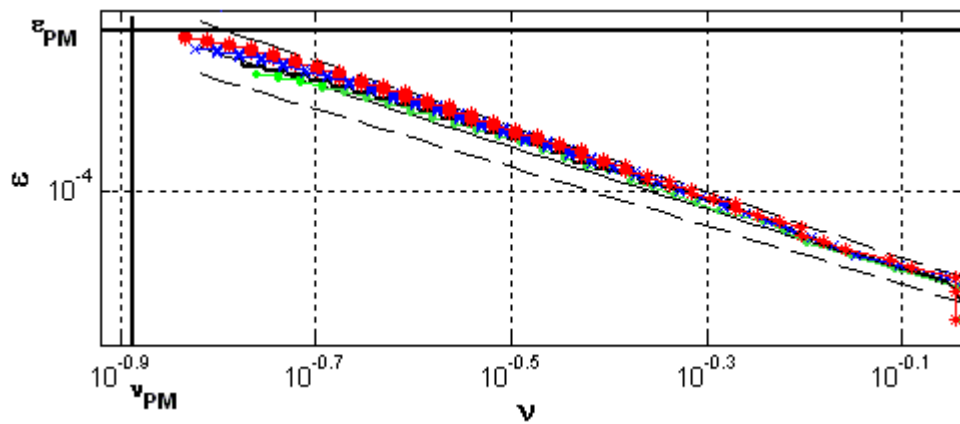
Figure 3.2 compares the growth curves (non-dimensional energy as a function of non-dimensional frequency,  $\varepsilon(\nu)$ ) of wave development under different wind speeds  $U_{10} = 7, 10, 15$  and  $20\text{m/s}$  with the experimental data of Babanin and Soloviev (1998). This comparison shows agreement within the 5% approximation range between the model results and the observations of Babanin and Soloviev (1998) for all selected wind speeds. As wave development approaches to the full development stage, the wave growth is slowing down. This trend is shown by the gradual change of the slope of the growth curve towards the lower frequencies, which is consistent with the wave observations.

Figure 3.3 presents the curves of the non-dimensional frequency  $\nu$  and non-dimensional energy  $\varepsilon$  as functions of the non-dimensional time  $\zeta$  demonstrated in subplot (a) and subplot (b), respectively. The model results were compared with the experimental data of Kahma (1981) (dashed line), Donelan et al. (1985) (dash-dotted line) and, Babanin and Soloviev (1998) (plane line). The magnitudes of Pierson-Moskowitz limit are shown as  $\varepsilon_{PM}$ ,  $\nu_{PM}$ , and  $\zeta_{PM}$ .

As waves approach their full-development stage, the energy growth is reduced, shown as the flattening transition of the slopes of the curves close to the Pierson-Moskowitz limit  $\varepsilon_{PM}$  (see Figure 3.3b). Correspondingly, the peak frequency transition towards the Pierson-Moskowitz limit  $\nu_{PM}$  is slowing down (see Figure 3.3a).



**Figure 3.1** Comparing the significant wave height  $H_s$  as a function of the duration of the model runs with different time steps  $\Delta t$  and wind speed  $U_{10} = 0$  m/s.



**Figure 3.2** Growth curves of the model runs for the different wind speeds  $U_{10} = 7$  m/s (line with dots), 10 m/s (bold line), 15 m/s (line with crosses) and 20 m/s (line with asterisks). The graph shows the growth of non-dimensional energy  $\varepsilon$  as a function of non-dimensional frequency  $\nu$ . The model results are compared with the experimental data of Babanin and Soloviev (1998) (plane line) with 5% approximation limits (dashed lines).  $\varepsilon_{PM} = 3.64 \cdot 10^{-3}$  and  $\nu_{PM} = 0.13$  are the magnitudes of Pierson-Moskowitz limit, are also shown with bold lines.

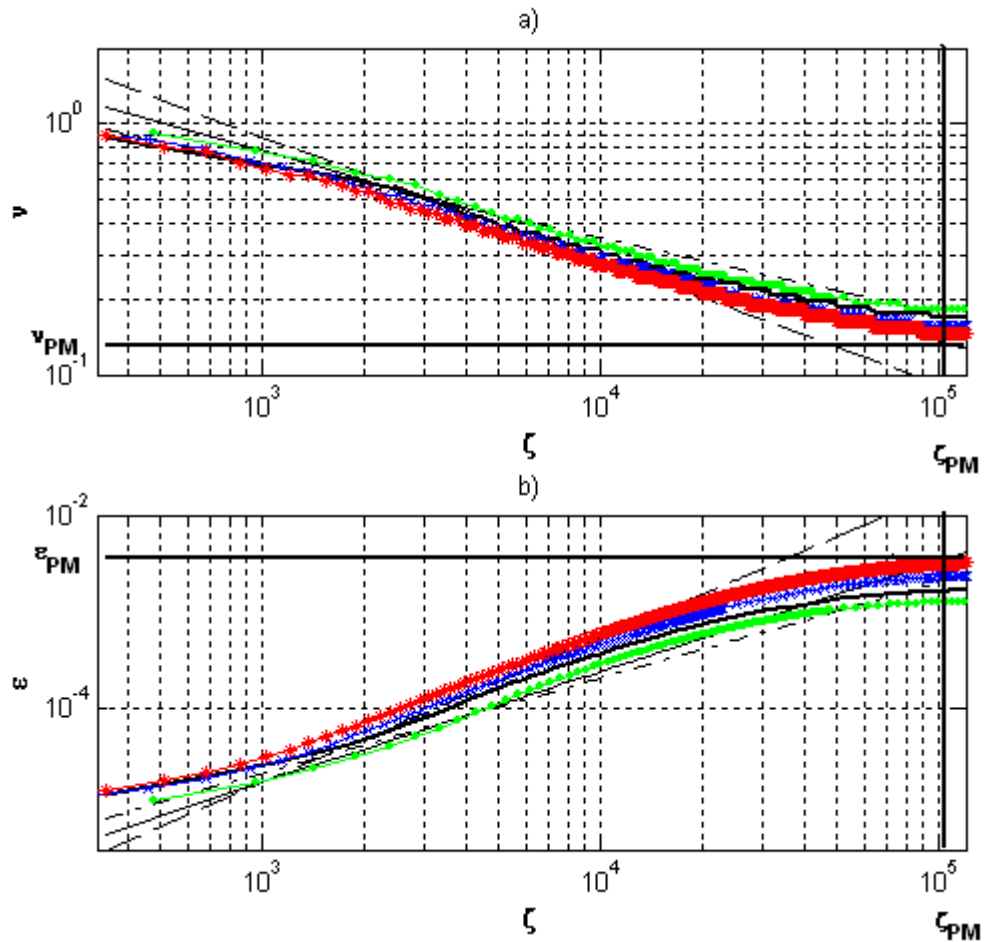


**Figure 3.3** Growth curves of the model run CL1P0.5A20W10. The subplot (a) shows the curve of non-dimensional frequency  $\nu$  as a function of non-dimensional time  $\zeta$ ; and subplot (b) shows the growth of non-dimensional energy  $\varepsilon$  as a function of non-dimensional time  $\zeta$ . The model results are compared with the experimental data of Kahma (1981) (dashed line), Donelan et al. (1985) (dash-dotted line) and, Babanin and Soloviev (1998) (plane line). The magnitudes of Pierson-Moskowitz limit are shown as  $\varepsilon_{PM}$ ,  $\nu_{PM}$ , and  $\zeta_{PM}$ .

The results showed that the model WAVETIME-1 was able to reproduce the experimental growth curves obtained by Babanin and Soloviev (1998). Thus, the model WAVETIME-1 was operational for the investigation of the new source functions mentioned earlier.

## CHAPTER 4 METHODS AND RESULTS

---

The development of advanced parameterisation forms for the wind input  $S_{in}$  and the wave dissipation  $S_{ds}$  source terms was based on a thorough investigation of the recently suggested source functions of Donelan et al. (2006) and Young and Babanin (2006), respectively. The present study was concentrated on the physical constraints of the air-sea processes involved in wave development. The investigation of two interrelational source terms for wind input and wave dissipation was a complex task. The major issue related to the concurrent presence of these two driving mechanisms. This study attempted to address this issue with a new approach, which enabled the above-mentioned difficulties to be overcome within the physical framework of the wind-wave processes involved in the air-sea interface.

The new approach of the present work was based on two main physical constraints suggested by Donelan (WISE-2004, Reading, England). The first constraint is the correspondence between the energy transferred from the wind to the waves and the total wind stress exerted on the water surface. Behavior of a new wind input function was investigated and tuned separately by using this constraint.

The second constraint relates to the dissipation source term, in particular, to the relationship between its integral value and the integral of the wind input source term. Donelan (1998) experimentally obtained the ratio of these two integrals as a function of non-dimensional fetch. Therefore, the dissipation source term can be studied and tuned in terms of this ratio. This approach resulted in a new understanding of operational wave modelling in terms of the coupling of the wind input and the wave dissipation source terms in the radiative transfer equation.

Chapter 4 reports on the methods and results of the current study in three main sections:

**Section 4.1** describes how the new wind input source function suggested by Donelan et al. (2006) was investigated and what conclusions were drawn from the investigation. This section describes how, as originally suggested by Donelan et al. (2006), wind input parameterisation form  $S_{in}$  corresponds to the wind stress exerted on the sea surface. It was shown, that originally suggested by Donelan et al. (2006) wind input source function corresponds to larger values of the wind stress than it was expected from stress-balance

computations. To overcome that inconsistency, a new method was developed to correct the  $S_{in}$  source function within the physical framework.

**Section 4.2** describes the investigation of the wave dissipation source function recently suggested by Young and Babanin (2006). This section introduces a new method for determining the dissipation energy based on the interrelationship between the  $S_{in}$  and  $S_{ds}$ .

**Section 4.3** describes the investigation of the performance of the new source functions  $S_{in}$  and  $S_{ds}$  using the wave model WAVETIME-1. This section outlines the results of the assessment technique developed on the basis of methods suggested by Banner and Young (1994).

## 4.1 THE NEW WIND INPUT SOURCE FUNCTION

As was discussed in Chapter 2, the positive flux of energy from wind to waves is the main source driving the growth of wind-waves. In its turn, the positive flux of energy is a result of stress variations exerted on the water surface by the wind. Wind stress determines the strength of wind-wave interactions and, consequently, the amount of energy transferred to the waves. Therefore, wind stress is the main physical characteristic used to describe wind-wave interactions.

In the present study, wind stress was selected as the main physical quantity for the investigation of the parameterisation form recently suggested by Donelan et al. (2006). During the investigation, it was found that a number of previously suggested parameterisation forms (Snyder, 1981; Hsiao and Shemdin, 1983; Donelan, 1999) for wind input source terms were not consistent with this physical constraint.

The present study developed a unique method for correcting the wind input source function suggested by Donelan et al. (2006). The proposed method represents a dynamic self-correction routine and is applicable to any parameterisation form of the wind input source term. The new method can be widely implemented in different wave models.

This study revealed that the results of computations of the wind input source function (Donelan et al., 2006) for the different parameterisation forms of wave spectra (Hasselmann et al., 1973; Donelan et al., 1985) differ significantly. Therefore, the issue regarding the wave spectral shape was revised and a new alternative parameterisation form of wave spectrum, Combi spectra, (described later in this chapter) is suggested.

This work proposes an alternative spectral form for wave steepness, the saturation transformer  $T(f)$ . The advantage of  $T(f)$  is the presence of the saturation level for most parameterisation forms of wave spectra (JONSWAP and Donelan 1985). The parameterisation form of the saturation transformer will be described further when wave steepness is discussed in the results Section 4.1.3.

Section 4.1 contains four subsections:

- 4.1.1 presents the results of preliminary computations of growth rate and wind input source function suggested by Donelan et al. (2006) and demonstrates the physical inconsistency of the proposed original parameterisation form (Donelan et al. 2006) to wave-induced stress
- 4.1.2 describes the main approach and the new method developed during this study to correct the new wind input source function developed by Donelan et al. (2006)
- 4.1.3 revises aspects of wave modelling in relation to the wave spectral shape and spectral representation of wave steepness; introduces two new parameterisation forms: 1) an alternative wave spectral shape and 2) an alternative parameterisation form for the spectral steepness
- 4.1.4 presents the results of computations of the wind input source term for the suggested spectral forms of the energy density spectrum and wave steepness using the new methodology based on physical constraints.

The section concludes with a discussion of the results of the present work and further recommendations for the future studies.

#### **4.1.1 PRELIMINARY COMPUTATIONS**

In the present study, initial computations of the growth rate and the wind input source term, as given by Donelan et al. (2006), were performed for different wind speeds and for different stages of wave development. These computations were important to understand peculiarities of behaviour of newly proposed wind input source function (Donelan et al., 2006). The results described here are based on computations performed for forcing wind speeds  $U_{10} = \{7\text{m/s}, 10\text{ m/s}, 15\text{ m/s and } 20\text{ m/s}\}$ . For each magnitude of wind speed, the computations were performed for young, average and fully-developed waves with wind forcing conditions  $U_{10} / c_p = \{5.8, 2.7\text{ and } 0.82\}$ , respectively. The corresponding spectral peak enhancement parameter  $\gamma_s$  takes magnitudes  $\gamma_s = \{7, 3.3\text{ and } 1\}$ , respectively.

The results obtained for the selected wind speeds showed behaviour similar to the wind input source function. Based on that fact, in the present work it was decided to show the results of computations only for the wind speed  $U_{10} = 10$  m/s. In addition, computations were performed for two different types of wave spectra, JONSWAP (Hasselmann et al., 1976) and Donelan (Donelan, 1985), taking into consideration the significance of the wind-wave coupling effect on the energy exchange processes between the wind and the waves.

The spectral parameters of the wave spectra at different stages of wave development were determined as functions of the wind forcing parameter,  $U_{10} / c_p$ . The relationships (Eq. 2-39) and (Eq. 2-40) from the Black Sea experiments reported by Babanin and Soloviev (1998) were used for the shape parameters of the JONSWAP spectra. For the Donelan spectra, the relationships (Eq. 2-6), (Eq. 2-7) and (Eq. 2-6) from the measurements taken at Lake Ontario (Donelan, 1985) were used. All computations were performed using the wide range of wave scales within the gravity wave range. Therefore, a discrete frequency spectral grid was defined between the lower and upper limits:  $f_{min} = 0.05\text{Hz}$  and  $f_{cut} = 10\text{Hz}$ , respectively. The selection of the upper frequency took into account the maximal contribution of the small-scale spectral components, which play a significant role in wind-wave interactions. The background for the selection of the spectral grid was discussed in detail in Section 3.1.

#### 4.1.1.1 Growth Rate

The Lake George experiment found new features which revolutionized earlier conceptualisations of the behaviour of the growth rate  $\gamma$  during wave development (Donelan et al. 2006), and resulted in a new parameterisation form for the growth rate  $\gamma$  that included the newly discovered features. However, at that time the new parameterisation function was only partially investigated.

The present study examined the parameterisation form suggested by Donelan et al. (2006) for growth rate. The results of computations of the growth rate  $\gamma$ , and the wind input source function  $S_{in}$  were compared to the results of Hsiao and Shemdin (1983) and Donelan (1999). The selection of these two parameterisation forms for  $\gamma$  was based on their extreme low and high magnitudes compared to other suggested forms.

Figure 4.1 shows comparisons of the  $\gamma$  spectra according to Donelan et al. (2006) with the growth rates suggested by Donelan (1999) and Hsiao and Shemdin (1983) at the different stages of wave development corresponding to the JONSWAP spectra (subplot [a]) and the Donelan spectra (subplot [b]). According to these researchers, all three  $\gamma(f)$  have a

quadratic dependency on frequency. However, the spectral shape of  $\gamma(f)$  suggested by Donelan et al. (2006) is significantly different from previously suggested forms due to the well-defined peaks for young and average-developed waves.

The spectral shape of  $\gamma(f)$  (Donelan et al., 2006) is determined by its dependence on the spectral saturation  $B_n(f)$  (see Eq. 2-24), which includes the wave spectrum  $F(f)$  (Eq. 2-19). Thus,  $\gamma(f)$  is a function of wave spectral magnitudes  $F(f)$ . Furthermore, Figure 4.1 (subplots [a] and [b]) shows the dependence of  $\gamma(f)$  on wind forcing conditions during wave development. Figure 4.1 (subplot [a]) shows that the spectral magnitudes of  $\gamma$ , according to Donelan et al. (2006), in the high frequency range are less than of those previously suggested by Donelan (1999) and Hsiao and Shemdin (1983). This fact is determined by the flow separation effect revealed in the results of the Lake George experiment (Donelan et al., 2006). Moreover, the computational results of  $\gamma$  (Donelan et al., 2006) for the Donelan spectra, as shown in Figure 4.1 (subplot [b]), are greater than the corresponding computations for the JONSWAP spectra, (Figure 4.1, subplot [a]).

The peculiarities of the  $\gamma(f)$  spectrum (Donelan et al., 2006) are the results of the dependence of the growth rate (Donelan et al., 2006) on the wave spectrum through spectral saturation  $B_n$  (see Eq. 2-10). In Figure 4.1  $\gamma(f)$  has a step-wise form in the range of short waves. This step is determined by the dependence of  $\gamma(f)$  on the type of wind flow described by the airflow separation parameter  $G$  in the sheltering coefficient (Eq. 2-26).

According to Equation 2-26, the airflow separation function  $G$  is the smoothed analogue of the Heaviside unit step function. One of the attributes of the  $G$  function is a threshold frequency, above which the spectral components sustain the full separation phenomenon revealed in the Lake George experiments. The energy fluxes from the wind to the short waves are reduced due to the airflow separation over these waves. Therefore, in this range of frequencies the growth rate has lower spectral magnitudes forming the visible step of the spectral shape. This threshold frequency, above which the flow separation takes place, changes during wave development.

Figure 4.1 also shows that the threshold frequency varies depending on the type of wave spectra. This behaviour of the threshold frequency is determined by the dependence of the spectral parameters on the wind forcing parameter

This is due to the presence of the spectral saturation  $B_n$  in the *tanh*-function in the airflow separation function  $G$  (see Equation 2-26). The threshold frequency determines the distribution of momentum fluxes in non-separated and full separated wavelength scales.

This feature was taken into account during the computation of wave-induced stresses in the present study.

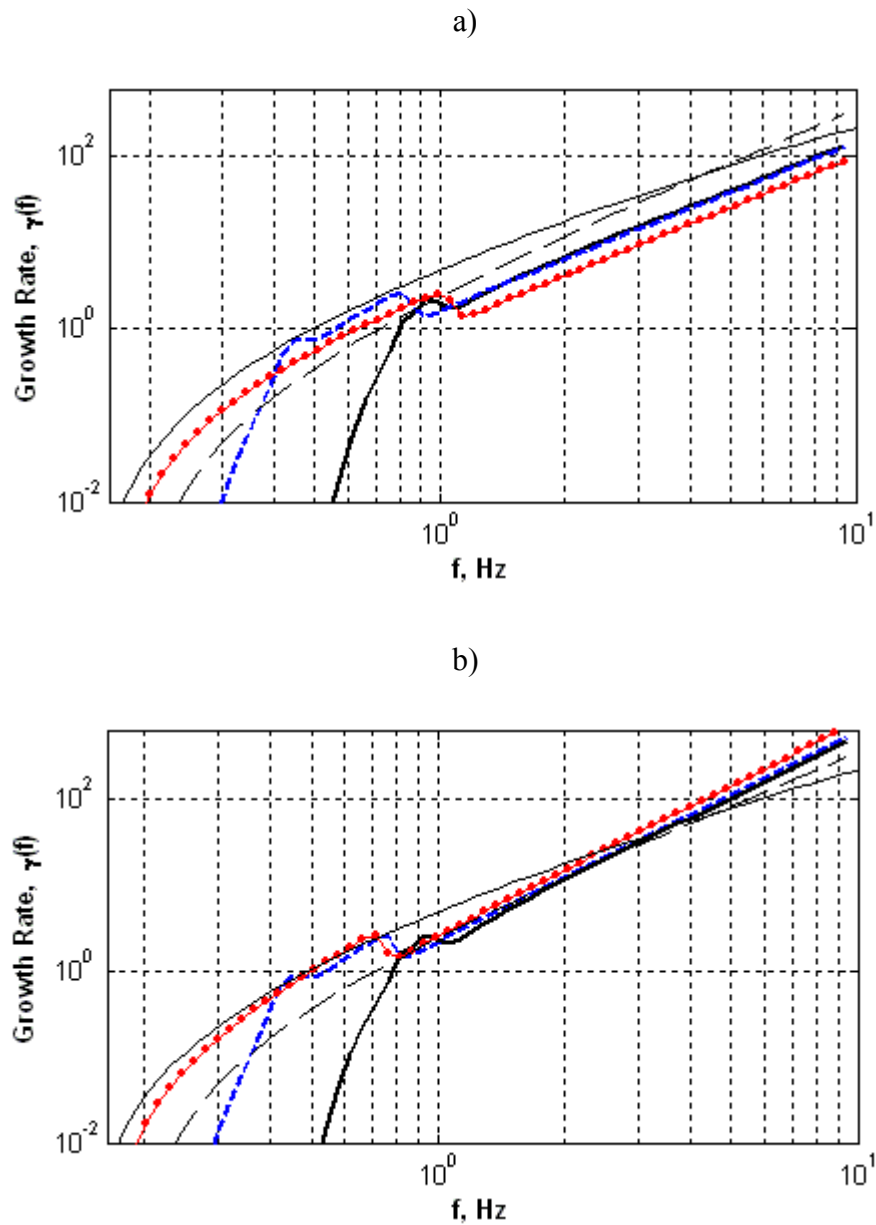
Figure 4.2 represents a comparison of  $\gamma(f)$  spectra for average-developed waves with  $U_{10} / c_p = 2.7$  computed for the JONSWAP and Donelan spectra, respectively. The difference between  $\gamma(f)$  spectra, which is determined by the wave spectral shapes of the JONSWAP and Donelan spectra, is significant in the high frequency range.

This divergence predetermined the selection of the high frequency range because it was at these frequencies that the correction of the wind input source function  $S_{in}$  could be applied. The most experimental wave measurements were performed for the range of frequencies close to the peak frequency  $[0.7f_p, 1.3f_p]$ . Furthermore, previously suggested parameterisation forms represent the results of extrapolations to the high frequency range. Therefore, the high frequency range can be considered an acceptable domain for adjustments in numerical studies of wave processes. In the present study, the wind input source function  $S_{in}$  suggested by Donelan et al. (2006) was investigated and tuned in the range of high frequency spectral components.

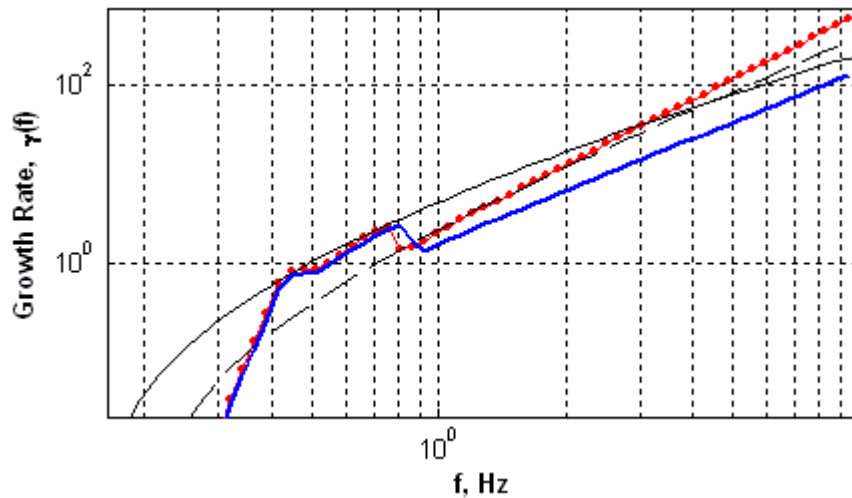
Figure 4.3 provides a comparison of the magnitudes of growth rates computed for peak frequencies  $\gamma(f_p)$  during wave development for various wind speeds. The results of computations for different wind speeds show that the magnitudes of growth rate  $\gamma(f_p)$  (Donelan et al., 2006) are the same as those registered for corresponding wind forcing conditions. The step-form behaviour in the range of  $U_{10} / c_p = [4.5, 5]$  is the result of the transition of the dominant waves with fully separated wind flow to waves with non-separated flow.

Figure 4.3 shows that the growth rates according to Donelan (1999) are different for different wind speeds. The growth rates according to Donelan (1999) are dependent on  $U_{\lambda/2} / c_p$ , where  $U_{\lambda/2}$  is the wind at a reference height of a half-wavelength. During wave development with changing peak frequency, wind  $U_{\lambda/2}$  varies, while  $U_{10}$  is constant. Thus, the wind forcing parameter  $U_{\lambda/2} / c_p$  has a different dependence on  $f_p$  than it does on  $U_{10} / c_p$ . Therefore, the growth rates for dominant waves according to Donelan (1999) have altered magnitudes for different wind speeds  $U_{10}$  for the same wind forcing conditions. This peculiarity determines the results presented in Figure 4.3.

According to Hsiao and Shemdin (1983) the growth rates of dominant waves are independent of wind speed. The magnitudes of all the growth rates according to the researchers noted here are consistent for fully-developed waves with  $U_{10} / c_p$  up to 1.5.



**Figure 4.1** Comparison of growth rates,  $\gamma(f)$ , according to Donelan et al. (2006) at different stages of wave development with  $U_{10} / c_p = \{5.8$  (bold lines),  $2.7$  (dashed bold lines),  $0.83$  (solid lines with dots)} at the wind speed  $U_{10} = 10$  m/s for the JONSWAP spectra (subplot [a]) and for the Donelan spectra (subplot [b]); the growth rates according to Donelan (1999) (solid lines) and Hsiao and Shemdin (1983) (dashed lines) are also shown.



**Figure 4.2** Comparison of growth rate according to Donelan et al. (2006) (bold line for the JONSWAP spectrum and solid line with dots for the Donelan spectrum), Donelan (1999) (solid line) and Hsiao and Shemdin (1983) (dashed line) for the average developed waves with  $U_{10} / c_p = 2.7$ , peak frequency,  $f_p = 0.43\text{Hz}$  and wind speed  $U_{10} = 10\text{ m/s}$ .

In the case of very young waves with  $U_{10}/c_p > 5$ ,  $\gamma$  as postulated by Donelan et al. (2006) is closer to the results of Hsiao and Shemdin (1983) because of the dependence of the growth rate (Donelan et al. 2006) on the type of wind flow over the waves. The full-separation phenomenon observed in the Lake George experiment for young waves resulted in low values for the growth rate  $\gamma$ . In the range of average-developed waves  $U_{10}/c_p = [2.5, 3.5]$ , the results of Donelan et al. (2006) and Donelan (1999) are close in average. This range of wind forcing conditions corresponds to non-separated wind flow, giving high values of growth rate.

As illustrated in Figure 4.3, the most intensive growth of waves can be observed for the range of wind forcing  $U_{10}/c_p = [4, 4.5]$ . At this stage of wave development, the dominant waves obtain the best hydrodynamic properties (steepness and velocity) and the non-separated wind flow transfers maximum energy to the waves. Furthermore, at this stage, the dominant waves are most strongly dragged by the wind. Therefore, the growth rate of the peak waves almost doubles, as shown in Figure 4.3.

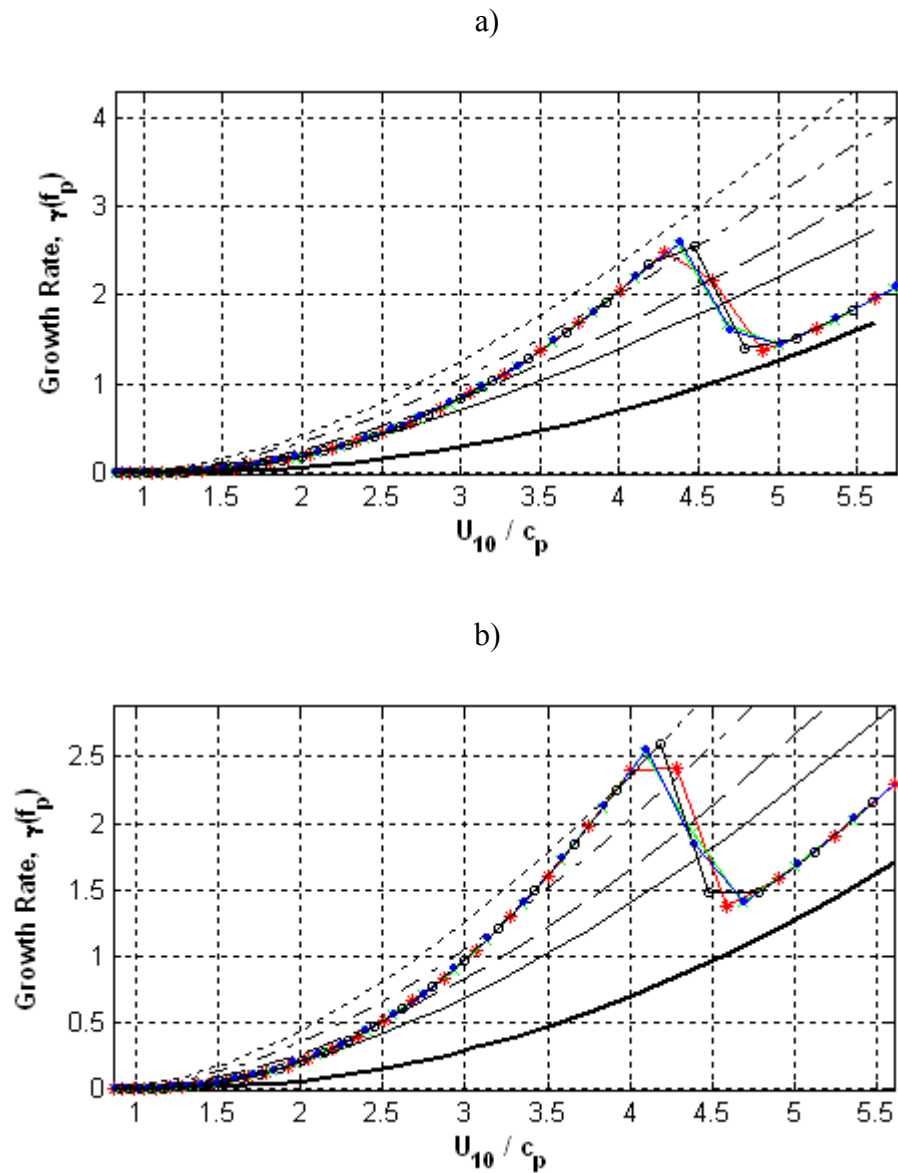


**Figure 4.3** Comparison of the growth rates of peak frequency waves for the JONSWAP spectra (subplot [a]) and for the Donelan spectra (subplot [b]) as functions of the inverse wave age, for different wind speeds  $U_{10} = \{7\text{m/s}, 10\text{m/s}, 15\text{m/s}$  and  $20\text{m/s}\}$  and wind dependent drag coefficient,  $C_D(U_{10})$ . The growth rates are according to Donelan et al. (2006) (lines with markings: circles, dots, crosses and asterisks correspondingly to  $7\text{m/s}$ ,  $10\text{m/s}$ ,  $15\text{m/s}$  and  $20\text{m/s}$ ), Donelan (1999) (different type lines: solid, dashed, dash-dotted and dotted corresponding to  $U_{10} = \{7\text{m/s}, 10\text{m/s}, 15\text{m/s}$  and  $20\text{m/s}\}$ ) and Hsiao and Shemdin (1983) (bold line).

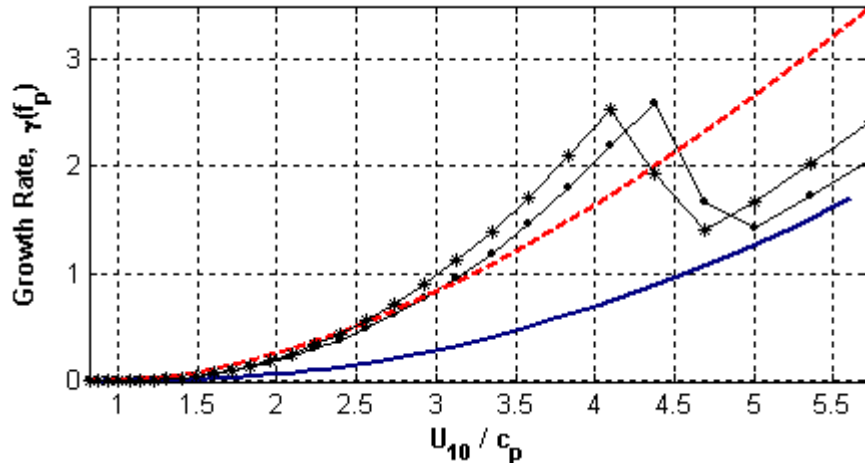


**Figure 4.4** Comparison of growth rate values at the peak frequencies according to Donelan et al. (2006) for the JONSWAP spectra (line with dots) and for the Donelan spectra (line with asterisks) at different stages of wave development at wind speed  $U_{10} = 10$  m/s; growth rates by Donelan (1999) (dashed bold line) and Hsiao and Shemdin (1983) (bold line) are also shown.

Figure 4.4 provides a comparison of the growth rates of peak frequency waves produced by the Donelan et al. (2006) parameterisation for different types of wave spectra for wind speed  $U_{10} = 10$  m/s. The result of this comparison shows that spectral shape does not significantly affect the growth rates of dominant waves.

The main difference between the JONSWAP and Donelan (1985) spectra is in the high frequency range and they are almost similar at the peak. The parameterisations of Donelan (1999) and Hsiao and Shemdin (1983) are also shown. The difference within 20% is most sensitive for young waves. This difference is predetermined by the different behaviour of the spectral shape parameters with wind forcing  $U_{10} / c_p$ . Figure 4.4 shows that for  $U_{10} / c_p = [4, 4.5]$  the growth rates according to Donelan et al. (2006) are higher than the results of growth rates observed by other researchers. The present study demonstrates how this fact affects the spectral development and the shape of the growth curves of wind-wave evolution.

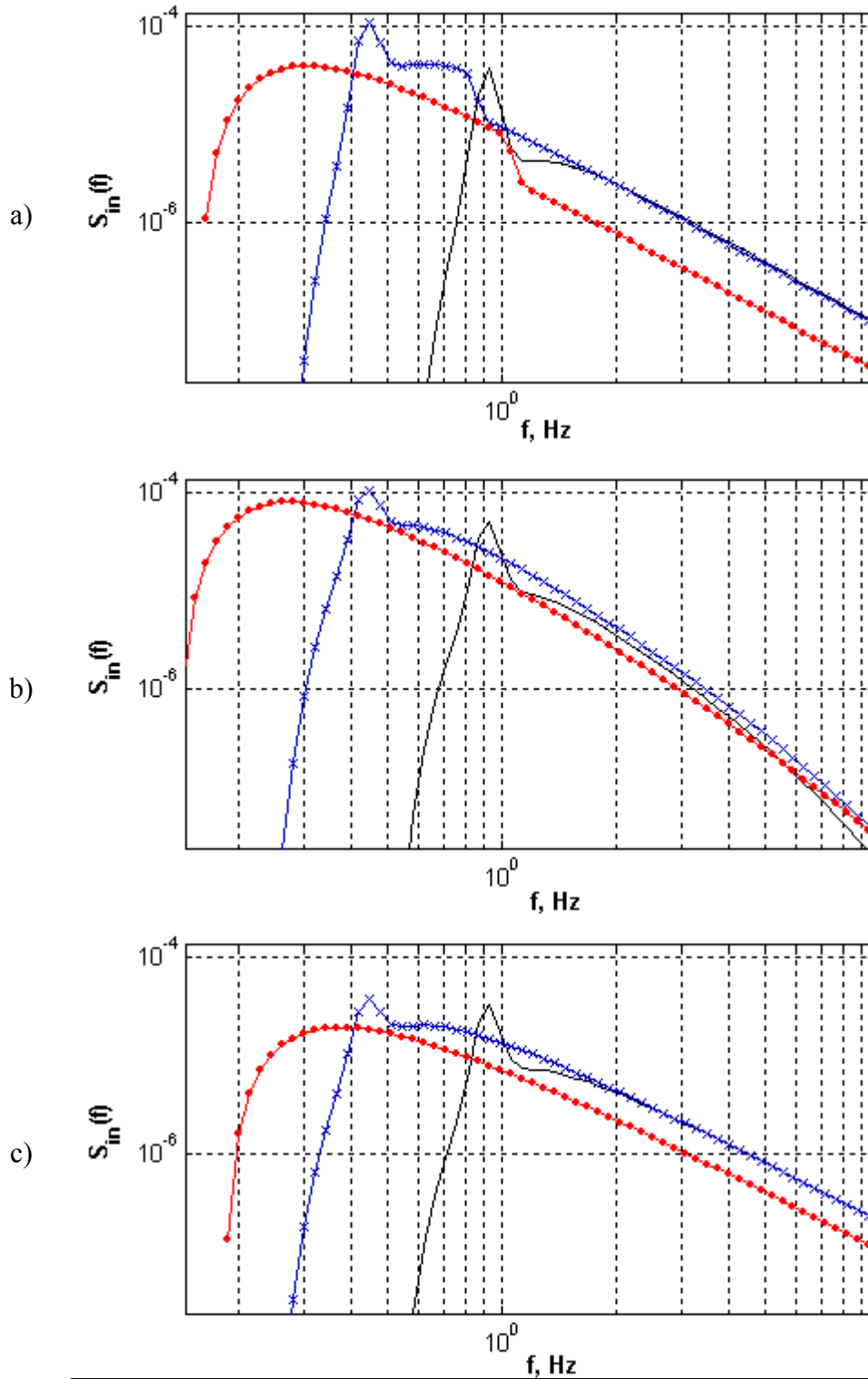
Considering the shallow water conditions in Lake George, certain corrections were necessary when considering the growth rate (Donelan et al., 2006) for deep water conditions. The peculiarities of the behaviour of growth rate  $\gamma$  predetermine the performance of the wind input source function (Donelan et al., 2006), which is discussed in the following section.

#### 4.1.1.2 Wind Input Source Function

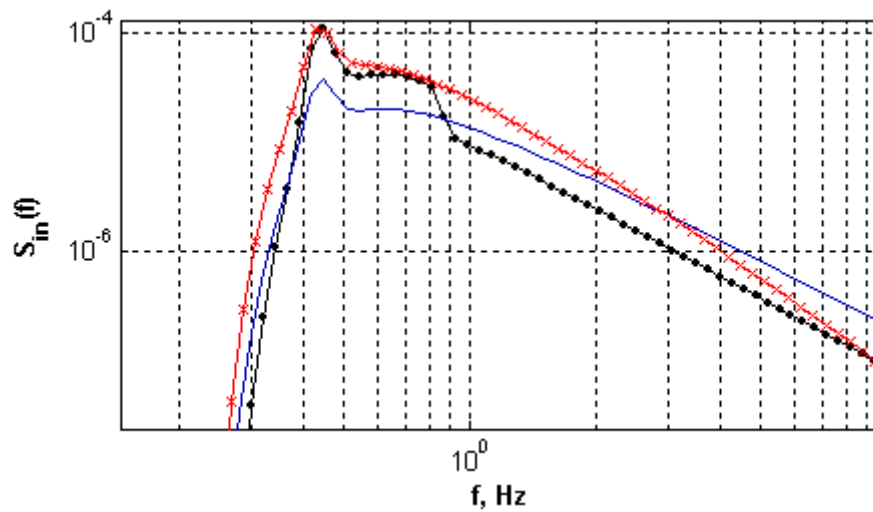
In this section, the results of the computations of the wind energy input source function  $S_{in}$  (Donelan et al., 2006) are analysed and compared to the results of other researchers. Wind-wave interactions result in energy input from wind to waves described by the wind input source term  $S_{in}$ . According to Donelan et al. (2006) the wind input source function is nonlinearly dependent on the wave spectrum. As discussed in Section 2.2, the nonlinear dependence of  $S_{in}$  on the wave spectrum is determined by the newly observed features of growth rate  $\gamma$  revealed in the Lake George experiment. This dependence has considerable importance when calculating to correct the  $S_{in}$  source function in relation to the physical constraints considered in this study.

Figure 4.5 represents the results of computations of  $S_{in}$  for the JONSWAP spectrum according to Donelan et al. (2006) (subplot [a]), Donelan (1999) (subplot [b]) and Hsiao and Shemdin (1983) (subplot c) at different stages of wave development. The high frequency range, where airflow separation is represented, shows a distinct step, which is evident in subplot (a).

Taking into account the influence of the shape of the wave spectrum on the energy input from wind to waves, computations of the wind input source function (Donelan et al., 2006) were performed for different types of wave spectra and results were compared to the results of other researchers. Figure 4.6 compares the computational results of  $S_{in}$  according to Donelan et al. (2006), Donelan (1999) and, Hsiao and Shemdin (1983) for average-developed waves at  $U_{10}/c_p = 2.7$ . The spectral magnitudes of Donelan et al. (2006) and Donelan (1999) almost coincide at the peak, whereas for frequencies higher than the peak frequency  $f_p$ , where the effect of flow separation is dominant, the spectral magnitudes of  $S_{in}$  by Donelan et al. (2006) are significantly less than previously suggested.



**Figure 4.5** Comparison of the wind source function according to Donelan et al. (2006) (a) Donelan (1999) (b) and Hsiao and Shemdin (c) (solid lines) for the JONSWAP spectra at different stages of wave development with  $U_{10}/c_p = \{5.8$  (plain lines),  $2.7$  (lines with crosses),  $0.83$  (lines with dots) $\}$  for the wind speed  $U_{10} = 10$  m/s.



**Figure 4.6** Comparison of wind source function according to Donelan et al (2006) (solid line with dots), Donelan (1999) (solid line with crosses) and Hsiao and Shemdin (solid line) for the JONSWAP spectrum for the inverse wave age  $U_{10} / c_p = 2.7$ , the peak frequency  $f_p = 0.43\text{Hz}$  and wind speed  $U_{10} = 10\text{ m/s}$ .

The slope of the high frequency spectral tail of the wind input spectral form by Donelan et al. (2006) is similar to the wind input parameterisation form suggested by Hsiao and Shemdin (1983) for all stages of wave development. However, the wind input source function of Donelan (1999) has a different slope from the spectral tail compared to others. This difference is determined by the dependence of the growth rate  $\gamma$  of Donelan (1999) on the wind speed  $U_{\lambda/2}$  at the height of  $\lambda/2$  above the sea surface, where  $\lambda$  is the wavelength. According to these observations, the wind speed  $U_{\lambda/2}$  is changing along the frequency scale due to changes in the reference height  $\lambda/2$ . Therefore, the parameterisation form of Donelan et al. (1999) has a distinguishing high frequency spectral tail.

Similar computations were performed for the Donelan spectra. Figure 4.7 and Figure 4.8 show the results of these computations. The results show similar relative location of the spectral magnitudes of the wind input source functions around the peak frequency. However, for frequencies higher than  $f = 2.5\text{Hz}$ , the wind input spectrum identified by Donelan et al. (2006) has the highest magnitudes despite the effects of flow separation.

This behaviour is determined by the dependence of the growth rate  $\gamma$  (Donelan et al., 2006) on the spectral saturation  $B_n$ , which behaves differently for different wave spectral shapes.

In the case of the Donelan wave spectrum, the spectral saturation  $B_n$  is dependent on frequency as the basis of its definition. Therefore, for the Donelan spectrum the slope of the spectral tail of the wind source function (Donelan et al. 2006) is altered compared to the computations for the JONSWAP spectrum. This issue will be discussed in results of section 4.1.3 in the context of the high frequency tail.

Figure 4.7 shows the computations of the wind input source term  $S_{in}$  according to Donelan et al. (2006) performed for the JONSWAP and Donelan spectra at different stages of wave development. The results show a huge difference between the spectral magnitudes in the high frequency region, with up to  $10^2$  times difference.

Comparing the situation with the growth rate (see Figure 4.2), the difference in the magnitudes of  $S_{in}$  for the small scales of spectral components in Figure 4.9 is considerably larger. This difference is determined by the nonlinear dependence of  $S_{in}$  on the wave spectrum as was mentioned before.

On the other hand, differences in  $S_{in}$  computed for the JONSWAP and Donelan spectra make questionable the credibility of one of these spectral forms in the high frequency range. Figure 4.9 shows a significant difference between the momentum fluxes computed for the JONSWAP and Donelan spectra for the same state of the water surface in the high frequency range. This fact determines that numerical investigations are applicable in the high frequency range, and the latter was selected as an operational frequency domain for the present study. Furthermore, the attempt was made to reconcile existing differences between the JONSWAP and Donelan spectra by introducing a new parameterisation form for the wave spectrum.

Taking into consideration the technical limitations of wave measurements for the high frequency scale components, the following suggestions were employed:

- A correction of the wind input source function is applicable in the range of high frequency waves.
- The suggested wave spectral form is to be validated for its credibility for further use in wave modelling. The validation is required to be based on the physical constraints and the experimental data from various studies.

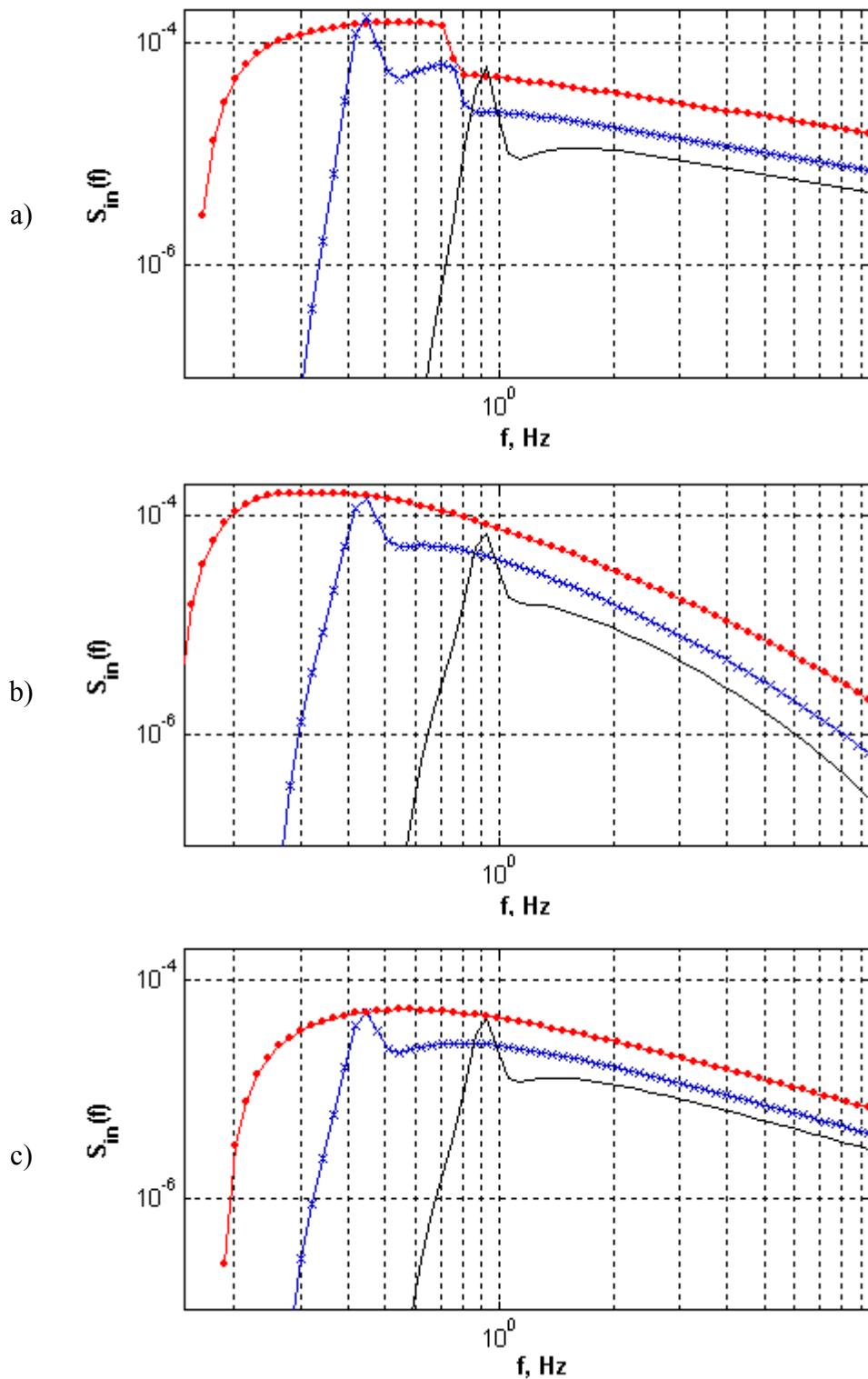


**Figure 4.7** Comparison of wind source function according to Donelan et al. (2006) (a), Donelan (1999) (b) and Hsiao and Shemdin (c) (solid lines) for the Donelan spectra at different stages of wave development with the inverse wave age  $U_{10}/c_p = \{5.8$  (plain lines),  $2.7$  (lines with crosses),  $0.83$  (lines with dots) $\}$  at wind  $U_{10} = 10$  m/s..

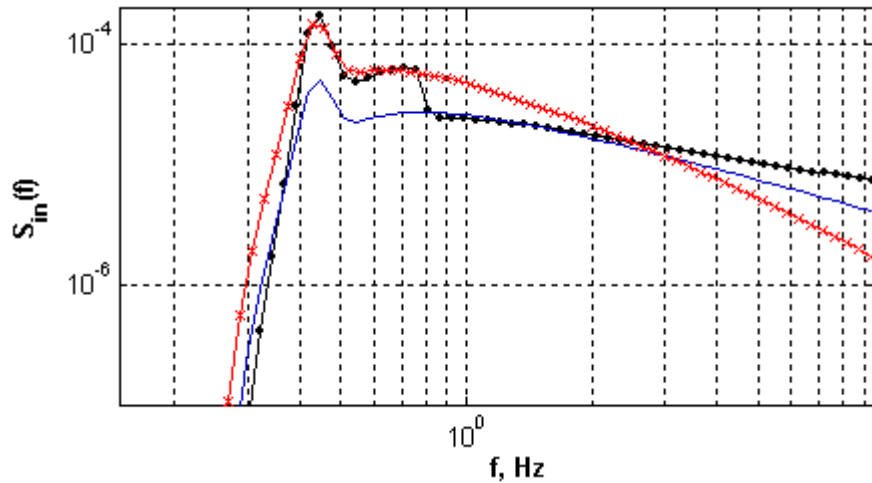


**Figure 4.8** Comparison of wind source function according to Donelan et al. (2006) (solid line with dots), Donelan (1999) (solid line with crosses) and Hsiao and Shemdin (solid line) for the Donelan spectrum for the inverse wave age  $U_{10}/c_p = 2.7$  ( $f_p = 0.43\text{Hz}$ ) and the wind speed  $U_{10} = 10\text{ m/s}$ .

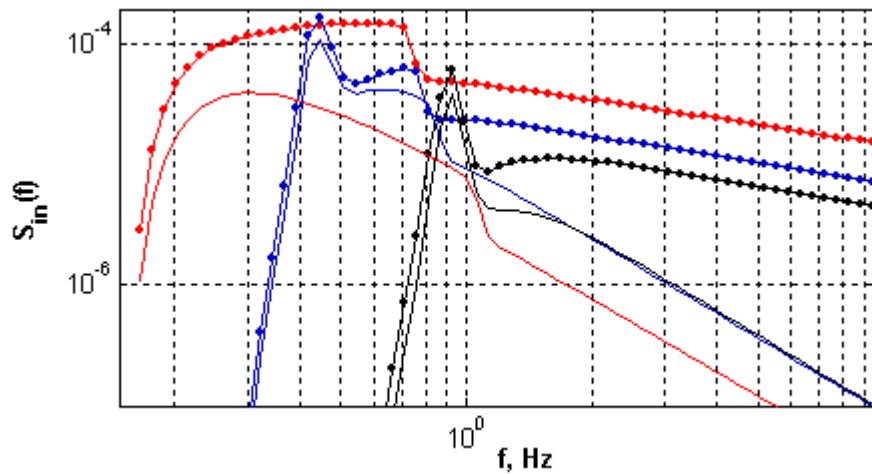


**Figure 4.9** Comparison of wind source function according to Donelan et al. (2006) computed for the JONSWAP spectra (solid line) and for the Donelan spectra (solid line with dots) at different stages of wave development  $U_{10}/c_p = \{5.8, 2.7, 0.83\}$  for wind  $U_{10} = 10\text{ m/s}$ .

In the present study, a new approach was developed based on strong consistency to the physical constraints of wind-wave processes. This approach will be discussed in detail in the following section.

### 4.1.2 VALIDATING THE WIND INPUT SOURCE TERM

One of the main objectives of the present study was to determine an advanced parameterisation form for the wind input source term  $S_{in}$  based on the new understanding of the physics of air-sea interactions provided by Donelan et al. (2006). Furthermore, this parameterisation form must satisfy the physical constraints and reflect wind-wave interaction processes in a wide range of air-sea conditions.

This section describes the physical constraints used as a conceptual basis for this investigation and a new method developed to meet the objectives of the present study. Moreover, this section reviews a number of aspects of wave modelling including the shapes of wave spectra and the spectral saturation.

#### 4.1.2.1 Stresses during Wind-Wave Interaction

The flux of momentum in the wind-wave interaction is the most significant exchange across the air-sea interface. It plays an important role in wind-wave coupling, reflecting the strength of the air-sea interaction. Therefore, in the present study, the flux of momentum was considered as the key boundary parameter for the investigation of the wind input source function.

Among the different types of stresses (see stress balance Equation 2-27) occurring during the air-sea interaction, the wave-induced stress is directly related to the energy exchange between the wind and the waves and is used as an important characteristic for the wind input source term.

$$\tau_w = \tau - \tau_v \quad (\text{Eq. 4-1})$$

where  $\tau_w$  is the wave-induced stress  
 $\tau$  is the total wind stress computed from (2.3-9) and  
 $\tau_v$  is the viscous stress.

On the other hand, the wave-induced stress is determined by the wind momentum input spectrum as:

$$\tau_w' = \int M(f)df \quad (\text{Eq. 4-2})$$

where  $M(f)$  is the wind momentum input spectrum.

In its turn, the wind momentum input spectrum  $M(f)$  is determined by the wind input source function  $S_{in}(f)$  using the following equation:

$$M(f) = \rho_w g \frac{S_{in}(f)}{c(f)} \quad (\text{Eq. 4-3})$$

where  $c(f)$  is the wave phase speed.

Substitution of the momentum flux (Eq. 4-3) into (Eq. 4-2) yields:

$$\tau_w' = \rho_w g \int \frac{S_{in}(f)}{c(f)} df \quad (\text{Eq. 4-4})$$

Hence, the wave-induced stress  $\tau_w'$  computed by Equation 4-4 from experimental data cannot exceed the  $\tau_w$  computed from the balance of stresses at the water surface (Eq. 4-1).

Based on that, the wave-induced stress  $\tau_w$  becomes the main physical constraint for the wind input source term, which must meet the following condition:

$$\tau_w' = \tau_w \quad (\text{Eq. 4-5})$$

The fulfilment of this criterion (Eq. 4-5) determines the credibility of a parameterisation form for the wind input source term  $S_{in}$ . The present study considered this criterion as the main physical framework for the investigation of the parameterisation for the wind input source term.

Wave-induced stress is highly dependent on the upper limit of the integral in Equation 4-4. The contribution of momentum fluxes at short-wave scales plays a significant role in stress estimation. The higher the upper limit of the integral, the more precise is the magnitude of wave-induced stress. Therefore, the upper limit of  $f_{max} = 10\text{Hz}$  was selected for the integral (Eq. 4-4) to achieve computational accuracy in stress analysis.

The partial weights of the wave-induced stress  $\tau_w$  and viscous stress  $\tau_v$  depend on the air-sea conditions (Donelan, 1998; Banner and Peirson, 1998). Banner and Peirson (1998) investigated the relative contribution of the viscous stress, mentioned as the tangential stress, in the total wind stress. The measurements were performed in a laboratory wind-wave flume. However, the researchers extrapolated the laboratory measurement results to open sea conditions. They concluded that the mean viscous stress level persists at an appreciable level and its relative contribution to the wind stress depends on the stage of wave development. The results of their study indicated that for mature wind seas, the relative contribution of the viscous stress decreases as the wind speed increases.

For transient, very young wind seas, the relative contribution of viscous stress is reduced, but is still not negligible (Banner and Peirson, 1998).

The present study included the viscous stress level in the stress analysis according to the results of Banner and Peirson (1998). Substitution of  $\tau$  (Eq. 2-27) and  $\tau_v$  using  $\tau_v = \rho_a C_V U_{10}^2$ , where  $C_V$  is the viscous drag coefficient (Banner and Peirson, 1998), into Equation 4-4, yields:

$$\tau_w = \rho_a U_{10}^2 (C_D - C_V) \quad (\text{Eq. 4-6})$$

Banner and Peirson (1998) showed the qualitative trend of the viscous stress relative to the wind speed. However, the quantitative dependence of the viscous drag on the wind speed was not presented in the empirical formula. In the present study, the data of Banner and Peirson's (1998) Figure 12 were quantified and parameterised as a function of wind speed  $U_{10}$ . In this parameterisation, the viscous drag was represented in the form:

$$C_V = -5 \cdot 10^{-5} U_{10} + 1.1 \cdot 10^{-3} \quad (\text{Eq. 4-7})$$

The present study considered the discrepancy among the drag coefficients  $C_D$  previously proposed by different researchers. A number of experimental studies had resulted in a situation where various researchers were divided in their opinions, and were suggesting that the drag coefficients  $C_D$  could be present as a function of wind speed  $U_{10}$  and also as wind forcing conditions  $U_{10}/c_p$ . Both types of drag coefficient  $C_D$  were taken into consideration in the present study.

Drawing from the experimental results of Garratt (1977), the drag coefficient was used for the wind dependent drag coefficient  $C_D(U_{10})$ . The wave-age dependent drag coefficient  $C_D(U_{10}/c_p)$  was computed according to the formula proposed by Guan and Xie (2004) corresponding to the recent results reported by Drennan et al. (2003). The results of this current study were obtained using five field data sets for pure wind sea conditions.

According to Guan and Xie (2004) the general parameterisation of the wave age dependent drag coefficient can be represented by:

$$C_D = [0.78 + 0.475 \cdot f(\delta) \cdot U_{10}] \times 10^{-3} \quad (\text{Eq. 4-8})$$

where

$$f(\delta) = 0.85^B A^{1/2} \delta^{-B} \quad (\text{Eq. 4-9})$$

where  $\delta = H\omega_p^2 / g$  - is the wave steepness

$H$  - is the significant wave height

$\omega_p$  - is the radian peak frequency

$A = 1.7$  and  $B = -1.7$  are the parameters determining the correspondence of  $C_D$  (Eq. 4-12) to the results of Drennan et al. (2003).

The results of computations of wave-induced stress  $\tau'_w$  using Equation 4-4 were compared to the magnitudes of wave induced stress  $\tau_w$  estimated with the use of Equation 4-6 for both type of drag coefficient  $C_D$ . The computations were performed for the JONSWAP and Donelan spectra at different stages of wave development and are illustrated in Figure 4.10 and Figure 4.11, respectively.

Figure 4.10 shows the results of computations of wave-induced stress  $\tau'_w$  using parameterisation forms of the wind input source term  $S_{in}$  according to different researchers. All parameterisations, except those of Snyder (1981) and Donelan et al. (2006) for young waves, give larger values of wave-induced stress than expected from the stress balance equation (Eq. 4-6). This means that all these parameterisation forms, as they were originally proposed, require further elaboration and validation, particularly at high frequencies and for young waves. Wave-induced stress increases with wave development until the inverse wave age reaches  $U_{10}/c_p = 1.5$ , whereupon a decreasing trend is clearly shown. The kink shown in Figure 4.10 is the result of applying the wave age dependence suggested by Babanin and Soloviev (1998) to the JONSWAP spectral shape parameters of energy density spectra. The magnitudes of the stress  $\tau'_w$  computed for  $S_{in}$  by Donelan et al. (2006) is more than two times greater than the expected value of wave induced stress  $\tau_w$  for  $U_{10}/c_p = 1.5$ .

Figure 4.11 shows remarkably larger differences between stresses  $\tau'_w$  and  $\tau_w$  for the Donelan spectra. Furthermore, the stresses  $\tau'_w$  computed for  $S_{in}$  by Donelan et al. (2006) have the largest values, indicating more inconsistency according to the criterion (Eq. 4-5). This fact is predetermined by the nonlinear dependence of  $S_{in}$  (Donelan et al. [2006] on the wave spectrum  $F(f)$ , [see Equation 2-24]).

Summarising the results of comparisons between wave-induced stresses, it was concluded that the wind input source function proposed by Donelan et al. (2006) required certain corrections to be consistent with the wave-induced stress  $\tau_w$  -- the physical constraint chosen for the present study. However, the considerable difference between wave-induced stresses  $\tau'_w$  computed for the JONSWAP and Donelan spectra for the same stage of wave

development makes questionable the credibility of certain types of wave spectra and some aspects of wave modelling. These considerations were taken into account and are discussed later in results Section 4.1.3, when high frequency tails are considered.

#### 4.1.2.2 *A New Approach for the Correction of $S_{in}$*

As discussed in Section 2.3.2 when wind-wave coupling was considered, the wind-wave coupling effect plays a significant role in the determination of momentum fluxes from wind to waves. The wind-wave coupling effect is based on the fact that surface shear stresses are determined by wind speed and the wave spectrum (Janssen, 1991). Under a constant forcing wind, the wave spectrum changes as waves change their physical properties. Therefore, the surface shear stresses change with wave development. On the other hand, the integral of the wind input spectrum  $S_{in}$  must be consistent with the criterion (Eq. 4-5) independent of the wave spectral shape or wave development stage. Therefore, the stress consistence condition (Eq. 4-5) must be checked at every stage of wave development in order to determine whether the wind input source term needs correction.

Correction of the wind input spectrum can be performed by applying a correction coefficient to the wind input spectrum, thus increasing or reducing the integral value in Equation 4-4. For the invariant consistency of  $S_{in}$  to the criterion (Eq. 4-5), the ratio of wave-induced stresses  $\tau_w/\tau'_w$  can be used as the correction coefficient for the wind input spectral magnitudes.

This stress ratio shows the rate of suppression required for a correction of the wind input source term to be consistent to the physical constraint (Eq. 4-5). According to this, the correction represents the scaling of the spectral magnitudes of the wind input source term by the ratio  $\tau_w/\tau'_w$ , which varies with wave development.

Figure 4.12 and Figure 4.13 show the ratio of wave-induced stresses  $\tau_w/\tau'_w$  as a function of wind forcing parameter  $U_{10}/c_p$  for the JONSWAP and Donelan spectra, respectively. These figures show that the shape of wave spectra has a significant influence on the behaviour of the ratio  $\tau_w/\tau'_w$  with wave development. The JONSWAP spectra require less suppression than the Donelan spectra. Initially it was assumed that the correction coefficient  $\tau_w/\tau'_w$  applied to the wind input spectrum over the entire frequency space if the spectral grid were defined. At this stage,  $\tau_w/\tau'_w < 1$  reduces and  $\tau_w/\tau'_w > 1$  increases the spectral magnitudes of the entire  $S_{in}$  spectrum.

However, in Section 4.1.1, when discussing growth rate, it was concluded that the operational frequency domain for the numerical study is the high frequency range. Therefore, the correction coefficient should be determined in the range of frequencies starting from  $f_0 > f_p$ , which is the lower boundary of the operational frequency domain in which the correction can be applied. Because of this, the correction coefficient will be dependent on the choice of  $f_0$  rather than simply the stress ratio  $\tau_w/\tau'_w$ . In that way the defined correction coefficient is named as the correction factor  $X$ . It is desirable that a choice of  $f_0$  does not interfere with the dominant wave scales where the experimental data (Donelan et al. 2006) are measured. The dominant waves are considered within the spectral band of  $0.7 f_p$  and  $1.3 f_p$ . Therefore, the lower frequency  $f_0$  for the operational frequency domain is chosen as  $f_0 = 1.35 f_p$ .

To correct the wind input source term, the correction factor  $X$  must be known. Therefore, the range of integration in Equation 4-2 was split into two ranges,  $[f_{min}, f_0]$  and  $[f_0, f_{cut}]$ , where  $f_{min} = 0.05\text{Hz}$  and  $f_{cut} = 10\text{Hz}$ :

$$\tau'_w = \int_{f_{min}}^{f_0} M(f)df + \int_{f_0}^{f_{cut}} M(f)df \quad (\text{Eq. 4-10})$$

For convenience we assign these two integrals:

$$S_1 = \int_{f_{min}}^{f_0} M(f)df \quad \text{and} \quad S_2 = \int_{f_0}^{f_{cut}} M(f)df \quad (\text{Eq. 4-11})$$

According to the considerations discussed previously, the correction factor  $X$  can be applied to the second interval  $S_2$ . Taking into account Equation 4-5, Equation 4-10 and Equation 4-11, we have:

$$\begin{cases} \tau_w = S_1 + X \cdot S_2 \\ \tau'_w = S_1 + S_2 \end{cases} \quad (\text{Eq. 4-12})$$

Solving this system (Eq. 4-12) for  $X$ , we have:

$$X = 1 + \frac{\tau_w - \tau'_w}{S_2} \quad (\text{Eq. 4-13})$$

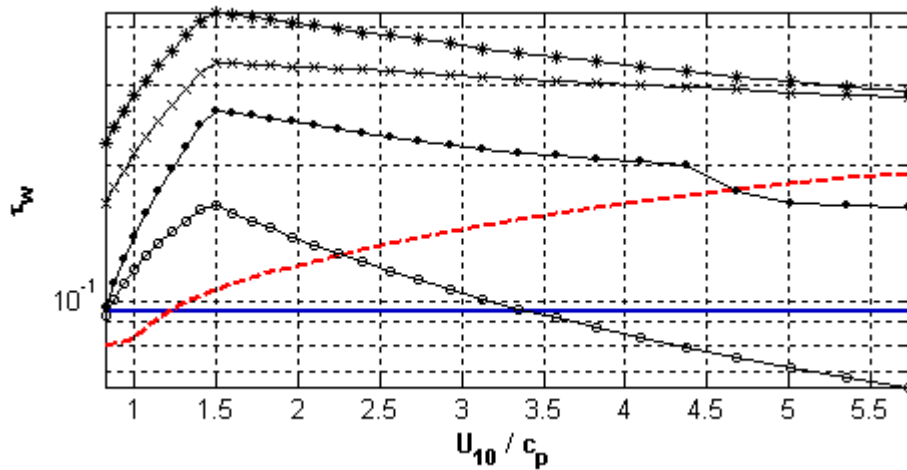


**Figure 4.10** Comparison of wave-induced stresses  $\tau'_w$  computed for wind source functions according to Donelan et al. (2006) (solid line with dots), Donelan (1999) (solid line with asterisks) Hsiao and Shemdin (1983) (solid line with crosses) and Snyder (1981) (solid line with circles) for the JONSWAP spectra with wave-induced stress  $\tau_w$  from the stress balance (Eq. 4-1) [bold line for  $C_D(U_{10})$  and bold dashed line for  $C_D(U_{10}/c_p)$ ].

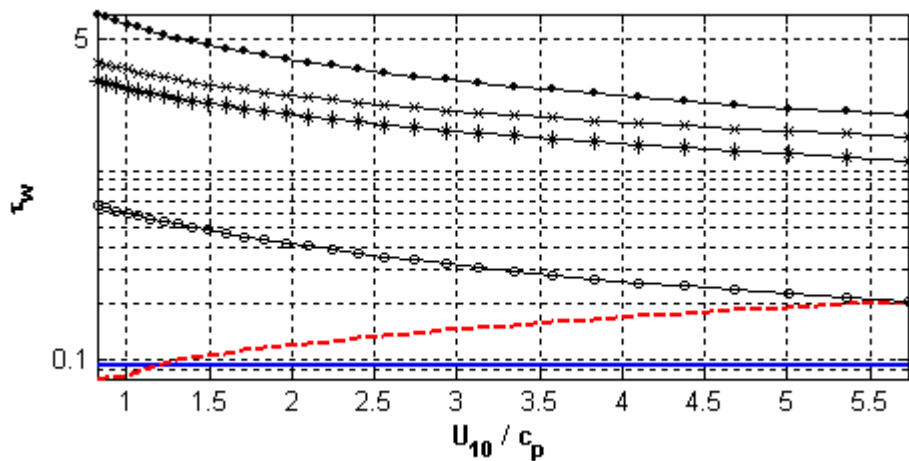


**Figure 4.11** Comparison of wave-induced stresses  $\tau'_w$  computed for wind source functions according to Donelan et al. (2006) (solid line with dots), Donelan (1999) (solid line with asterisks) Hsiao and Shemdin (1983) (solid line with crosses) and Snyder (1981) (solid line with circles) for the Donelan spectra with wave-induced stress  $\tau_w$  from the stress balance (Eq. 4-1) [bold line for  $C_D(U_{10})$  and bold dashed line for  $C_D(U_{10}/c_p)$ ].

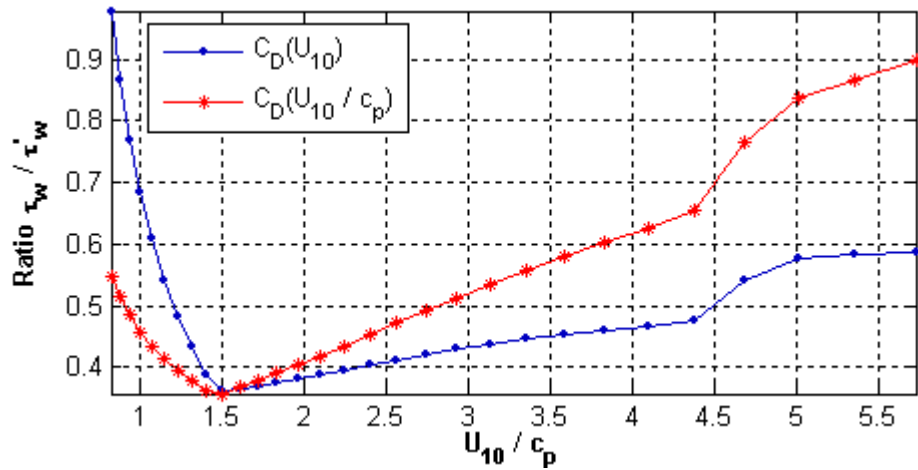


**Figure 4.12** Ratio of the wave-induced stress,  $\tau_w$  (Eq. 4-6), to the wave-induced stress,  $\tau'_w$  (Eq. 4-4) computed for the wind input source function according to Donelan et al. (2006) for the JONSWAP spectra at different stages of wave development at wind speed,  $U_{10} = 10$  m/s, for both type of drag coefficients  $C_D$ .

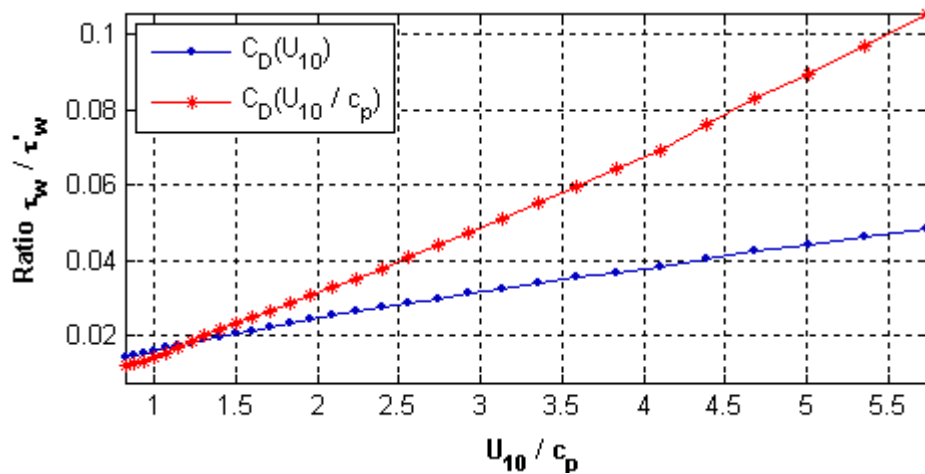


**Figure 4.13** Ratio of wave-induced stress,  $\tau_w$  (Eq. 4-6) to the wave-induced stress,  $\tau'_w$  (Eq. 4-4) computed for the wind input source function according to Donelan et al. (2006) for the Donelan spectra at different stages of wave development at wind speed,  $U_{10} = 10$  m/s, for both type of drag coefficient  $C_D$ .

The difference between the stresses  $\tau_w$  and  $\tau'_w$  in Equation 4-13 determines the increase ( $X > 1$ ) or reduction ( $X < 1$ ) of  $S_{in}$  spectral magnitudes. However, it is possible for  $X$  to have negative values, but a case with negative  $X$  cannot be admitted because the wind input source term then becomes contrary to its definition and describes the negative flux of energy for high frequency waves. This situation would contradict the experimental observations and alter the physical meaning of the wind input source term. To compute the correction factor  $X$ , additional considerations were therefore taken into account.

The boundary conditions were determined where  $X$  was positive. From Equation 4-13 we have:

$$1 + \frac{\tau_w - \tau'_w}{S_2} > 0 \quad (\text{Eq. 4-14})$$

The condition (Eq. 4-14) can be modified into the form:

$$S_2 > \tau'_w - \tau_w \quad (\text{Eq. 4-15})$$

Taking into account that  $S_2 = \tau'_w - S_1$ . Substituting for  $S_2$  we have:

$$S_1 < \tau_w \quad (\text{Eq. 4-16})$$

In most cases of wave development the condition (Eq. 4-16) is true. However, for reliable results, to have the condition (Eq. 4-16) true for all cases, a correction was required to readjust the operational frequency domain in order to apply the correction factor  $X$ . The integral  $S_1$  depends on the choice of the starting frequency  $f_0$ . Therefore, the limitation (Eq. 4-16) was translated into the limiting condition for the choice of the starting frequency  $f_0$ . For cases when  $X < 0$  the starting frequency  $f_0$  instead of  $1.35 f_p$  was chosen as the closest frequency to  $1.35 f_p$  for which the condition (Eq. 4-16) is still true.

Figure 4.14 and Figure 4.15 show the correction factor  $X$  as a function of the wind forcing parameter  $U_{10} / c_p$  computed for the JONSWAP and Donelan spectra, respectively. These figures show that there are different magnitudes and behaviours of the function  $X(U_{10} / c_p)$  for different types of spectra. The effect of flow separation is clearly seen in both figures as a step in the range of the wind forcing parameter  $U_{10} / c_p = [4, 5]$ . Furthermore, most suppression is required in the spectral range of non-separated wind flow for wind forcing  $U_{10} / c_p < 4$ .

Figure 4.16 shows a comparison of the wind input source terms computed for the JONSWAP and Donelan spectra before and after correction by means of the correction factor  $X$ . As the result of applying  $X$  to the wind input source functions computed for the JONSWAP and Donelan wave spectra, the wind input source functions after correction have a sensible jump at the frequency  $f_0$ . Figure 4.16 shows that this jump in magnitude of the wind input spectrum is greater for the Donelan wave spectrum than for the JONSWAP spectrum, because of the required rate of suppression. However, in nature, sudden changes of air pressure over a wavy surface can hardly be observed and the probability of such a state in a wind-wave system is very low, especially for the spectral components close to the dominant waves. Therefore, it was decided to have a smooth transition at the frequency  $f_0$ .

As shown, for a smooth transition at the frequency  $f_0$ , the correction factor  $X$  cannot be a function of only the wind forcing parameter  $U_{10}/c_p$ . The physical consistency of the wind input source term requires that  $X$  must be a function of frequency, too,  $X(f, U_{10}/c_p)$ .

Accordingly, for each stage of wave development with certain wind forcing  $U_{10}/c_p$  there is a corresponding function  $X(f)$ . In the present study, this function was termed  $L(f)$  the correction function to differentiate it from the correction factor  $X(U_{10}/c_p)$  which was used later in the correction routine for the wind input source term.

The selection of a correction function was based on its meeting the specific requirements:

- The correction function  $L(f)$  must be a monotonic continuous function.
- $L(f)$  must have smooth transition at the frequency  $f_0$ :  $L(f_0) = 1$ .
- The wave induced stress  $\tau'_w$ , computed for  $L(f)S_{in}(f)$  must be consistent with  $\tau_w$ .
- The magnitudes of  $L(f)S_{in}(f)$  for very small scale waves must be comparable to the spectral magnitudes of the wave spectral dissipation function  $S_{ds}$ . Otherwise, the dissipation will prevail at high frequency spectral components, which can cause singularities during wave development.

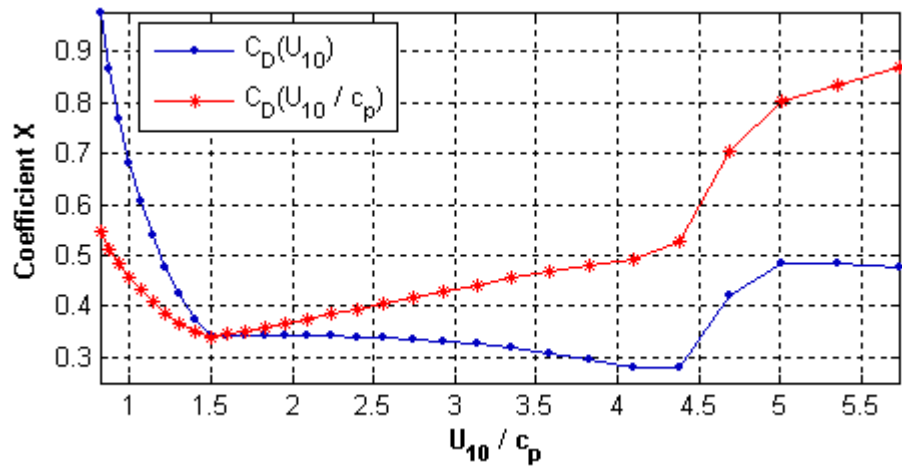


**Figure 4.14** Correction factor  $X$  (Eq. 4-13) for stress correction of the wind input source function according to Donelan et al. (2006) computed for the JONSWAP spectra, for both type of drag coefficient  $C_D$  and wind speed,  $U_{10} = 10$  m/s.

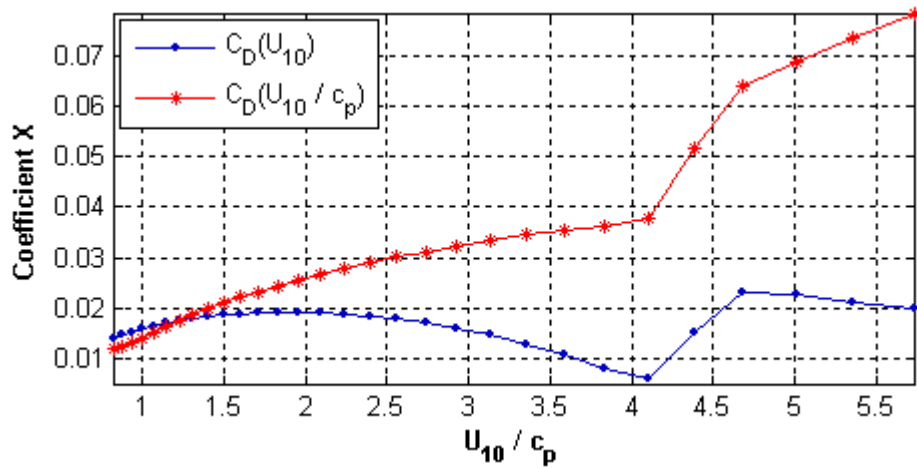


**Figure 4.15** Correction factor  $X$  (Eq. 4-13) for stress correction of the wind input source function according to Donelan et al. (2006) computed for the Donelan (1985) spectra, for both type of drag coefficient  $C_D$  and wind speed,  $U_{10} = 10$  m/s.

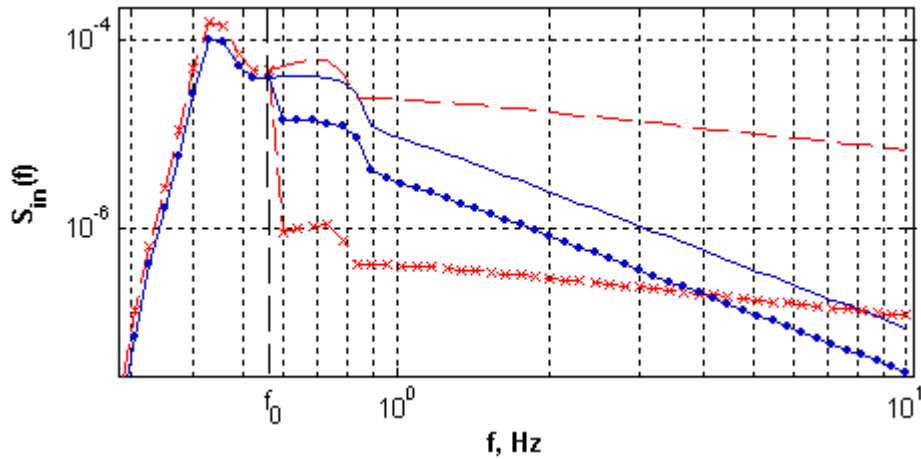


**Figure 4.16** Comparison of wind source function according to Donelan et al. (2006) before and after applying the coefficient  $X$  for the JONSWAP (solid line and line with dots, respectively) and Donelan (dashed line and line with crosses, respectively) spectra, with spectral parameter,  $\gamma_s = 3.3$ , at wind  $U_{10} = 10$  m/s.

After a series of attempts to find the best suitable function, which satisfied the requirements outlined above, the following function was selected:

$$L(f) = \exp\left(\frac{f_0 - f}{f} \cdot \eta\right) \quad (\text{Eq. 4-17})$$

where  $\eta$  is a correction rate which is computed from the stress correspondence condition (Eq. 4-15). This parameter determines the slope of the wind input spectral tail in the range of frequencies  $f > f_0$  and depends on wind forcing conditions  $U_{10}/c_p$ .

Hence the stress corresponding condition (Eq. 4-15) can be written in terms of the correction function  $L(f)$  and the correction factor  $X$ :

$$\int_{f_0}^{f_{\max}} L(f)M(f)df = X \int_{f_0}^{f_{\max}} M(f)df \quad (\text{Eq. 4-18})$$

The physical correction of the wind input function, therefore, lies in the determination of the  $L(f)$  function when the condition (Eq. 4-18) is true. In its turn, the correction function  $L(f)$  is uniquely determined by the correction rate  $\eta$ . Therefore, determining the correction function  $L(f)$  comes down to the picking the magnitude of  $\eta$  when the condition (Eq. 4-16) is true.

This scheme was implemented as part of the routine in the operational wave model. Different values were assigned to  $\eta$  by iteration through the range of chosen values and checking the feasibility of condition (Eq. 4-16). The selection of the correct value for  $\eta$  was based on the criterion considering the case when the difference

$\Delta I = \left( X \int_{f_0}^{f_{\max}} M(f)df - \int_{f_0}^{f_{\max}} L(f)M(f)df \right)^2$  takes its minimum value. The precision of this criterion

is dependent on the starting boundary value of the range and the number of iterations which determine the number of values in this range. For a fast search for the correct value of  $\eta$ , the dynamic adjustment scheme was implemented in the wave model. The negative values of  $\eta$  correspond to an expansion of the integral of the wind input source function, while positive  $\eta$  values correspond to suppression.

Using this scheme, the first boundary value  $\eta_o = -1$  and iteration step  $\Delta\eta_o = 1$  were set up. The selection of this value for  $\eta_o$  was determined by the aim to encompass both cases: expansion and suppression of the integral of  $S_{in}$ . The next  $\eta_i$  value following  $\eta_o$  was  $\eta_i = \eta_o + i\Delta\eta_o$ . The number of iterations was selected as 1000. Whenever the difference  $\Delta I$  changes an order (becoming less), the iteration step is dynamically changing to  $0.1\Delta\eta_o$ , thus increasing the resolution of the numerical scheme. The acceptable precision was set as the order of 0.01 and when achieved the iteration ceased.

However, despite of simplicity of this method it has one drawback. This drawback lies in the fact that the boundary value  $\eta_o$  is set up by guess. Moreover,  $\eta_o$  is dependent on wind speed and wind forcing conditions and requires careful estimation for each case. If the value of  $\eta_o$  is too low or too high the precision of this scheme becomes lower. Therefore, another better scheme was developed for determination of correction rate  $\eta$ .

The alternative scheme includes a self-determination routine for the first boundary value of  $\eta$  for the given frequency domain of  $L(f)$ . According to the mean value theorem, if  $L(f)$  and  $M(f)$  are differentiable and continuous in the range  $[f_0, f_{\max}]$ , there is at least one point  $f_i$  between  $f_0$  and  $f_{\max}$  such that:

$$\int_{f_0}^{f_{\max}} L(f)M(f)df = L(f_i) \int_{f_0}^{f_{\max}} M(f)df \quad (\text{Eq. 4-19})$$

Figure 4.17 shows the graphical representation of this theorem for computation of the correction rate  $\eta$ .

Taking into account the right hand side of Equation 4-19, we have:

$$\begin{cases} L(f_0) = 1 \\ L(f_i) = X \end{cases} \quad (\text{Eq. 4-20})$$

Substituting  $L(f)$  in the lower equation in Equation 4-20 by Equation 4-17 for frequency  $f_i$ , we have:

$$\exp\left(\frac{f_0 - f_i}{f_i} \eta\right) = X \quad (\text{Eq. 4-21})$$

Solving Equation 4-21 relative to  $\eta$  we have:

$$\eta = \frac{f_i \ln X}{f_0 - f_i} \quad (\text{Eq. 4-22})$$

The formula (Eq. 4-22) represents an implicit solution for  $\eta$  because of the uncertainty of  $f_i$ . The correction rate  $\eta$  (Eq. 4-22) can be determined by iteration through the range of frequencies  $[f_0, f_{\max}]$  and checking each frequency in order to establish that it meets the condition expressed by Equation 4-19. In this range of frequencies there is only one frequency  $f_i$ , which satisfies the condition (Eq. 4-19). To prove this, assume that we have multiple frequencies  $f_i$  which satisfy Equation 4-19. According to Equation 4-17, each frequency  $f_i$  uniquely determines the correction function  $L_i(f)$ .

Thus the corresponding correction rates  $\eta_i$  depend on frequencies  $f_i$  (Eq. 4-22) and the function  $\eta_i(f_i)$  decreases with increasing  $f_i$ . Hence, the corresponding integral

$\int_{f_0}^{f_{\max}} L_i(f)M(f)df$  increases with increasing  $f_i$  and reaches the maximal value when  $f_i = f_{\max}$ .

Considering this integral as a monotonic function of  $f_i$ , there is only a single frequency  $f_i$  that can satisfy the condition (Eq. 4-22). For each stage of wave development, therefore, there can be found a single value of  $\eta$  which satisfies the condition expressed by Equation 4-19.

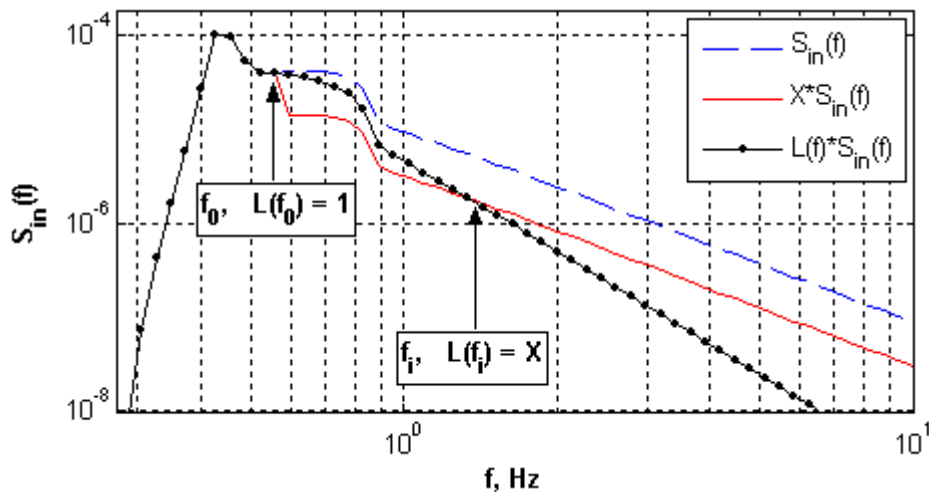


**Figure 4.17** Comparison of wind source function according to Donelan et al. (2006) before and after applying stress correction function  $L(f)$  (Eq. 4-17). Computations were performed for the JONSWAP (solid line and line with dots, respectively) and Donelan (dashed line) spectra for the average developed waves with  $U_{10} / c_p = 2.7$  and the wind speed  $U_{10} = 10$  m/s.

According to this routine, the computation of  $\eta$  depends on the resolution of the frequency scale. For low frequency resolution the accuracy of the numerical computation is low. This fact impedes the accuracy of model computations. Therefore, in the present study, the independent frequency grid for the correcting routine computations was implemented in the wave model. In order to do this, the range of frequencies  $[f_0, f_{max}]$  was divided into a certain number of small equal intervals with frequency resolution independent from the spectral grid of the wave model.

The number of these intervals was chosen by the following optimum criteria:

- the optimal accuracy of computations
- the optimal computational time.

Optimal accuracy is the accuracy of computations which cannot be increased by a further increase in the number of frequencies in the range of  $[f_0, f_{max}]$ . Considering accuracy as a function of the number of frequencies, this function reaches saturation for the certain number of frequencies. Optimal computational time means there is no significant time delay during the model computations. In the present study, on the basis of the analysis of a series of numerical experiments, the optimal number of frequencies in the range of  $[f_0, f_{max}]$  was found to be 1000. This number fits well with the optimum criteria and provides great precision for numerical computations. The outlined dynamic self-correction routine was implemented in the wave model WAVETIME-1.

### 4.1.3 RESULTS

The new method developed in the present study for the correction of the wind input source term was implemented using the wave model WAVETIME-1. The results of this approach are discussed in the current section. The new method performed as a dynamic self-correction routine for numerical wave modelling – termed dynamic because the correction routine is applied to the computation of the wind input source term at every stage of wave development. The dynamic correction routine includes computations of wave-induced stress at each stage of wave development and the outcome is a corrected wind input source term.

The correction was applied to the wind input source function suggested by Donelan et al. (2006) and computed for the JONSWAP and Donelan spectra at different stages of wave development. Furthermore, the spectra of the growth rate  $\gamma(f)$ , computed for the JONSWAP and Donelan spectra, were analysed as a result of the applied correction routine.

Figure 4.18 shows the comparison of the wind input source term  $S_{in}$  before and after the correction routine by means of the correction function  $L(f)$  (Eq. 4-17) performed for the JONSWAP and Donelan wave spectra. The corrected wind input source functions computed for the JONSWAP and Donelan spectra do not differ significantly, as shown in Figure 4.16. This relative equality of the spectral magnitudes is determined by the correspondence of the integrals of the corrected wind input source terms computed for both wave spectra, to the wave-induced stress occurring at this stage of wave development.

Furthermore, Figure 4.18 shows that the wind input source functions computed for different wave spectra have different rates of frequency dependence in the high frequency domain.

This can be observed in the difference between the high frequency spectral slopes of the JONSWAP and the Donelan spectra.

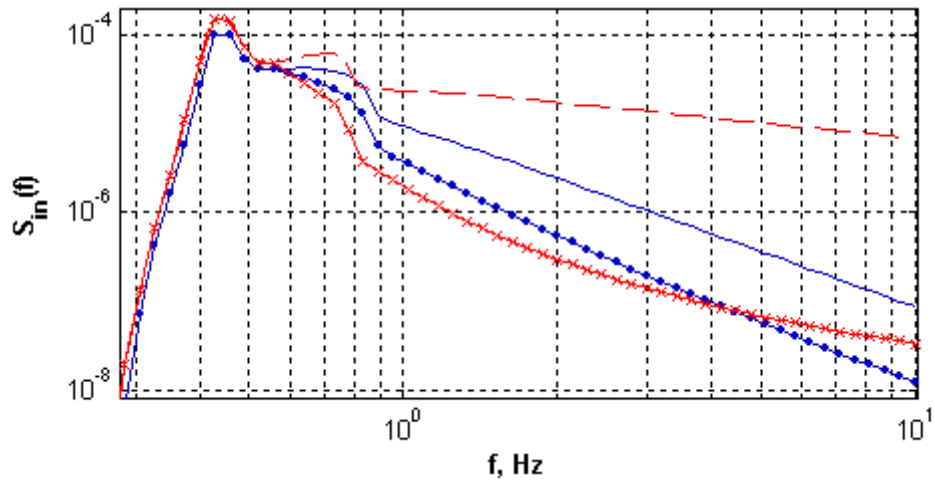
Figure 4.19 shows the growth rate spectra before and after stress correction computed for the JONSWAP wave spectrum of average-developed waves. As shown in this figure, the frequency dependence rates are changed having a reduced spectral slope. Almost similar results were obtained by Chalikov (personal communication). Chalikov, based on numerical simulations of the air-sea interaction, found that the growth rate is a linear function of frequency in the high frequency range.

A similar trend of change of frequency dependence rates was obtained for growth rates computed for the Donelan spectrum. Figure 4.20 shows the comparison of the original and corrected growth rates for average-developed waves.

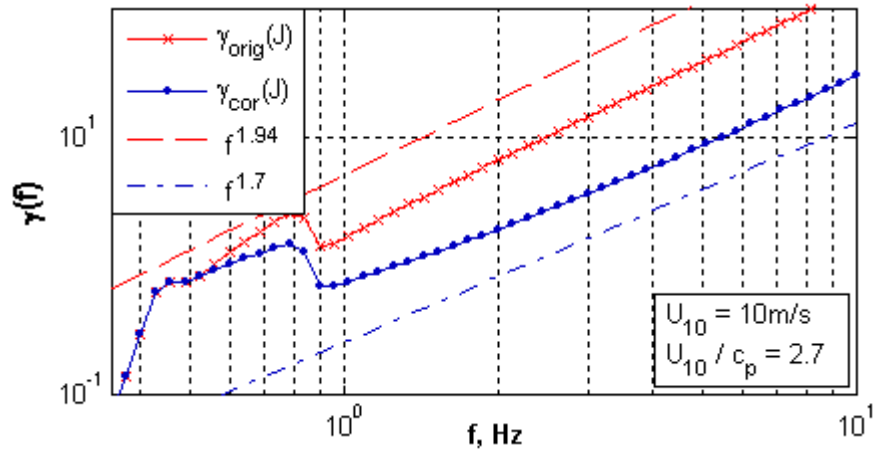
In this case the change of frequency dependence is greater than for the JONSWAP spectrum. After the stress correction, the frequency dependence of  $\gamma$  for the Donelan spectrum comes close to the rate of  $\gamma$  for the JONSWAP spectrum. Therefore, it can be concluded that the stress correction results in a reduction of the frequency dependence rate of the growth rate spectrum.

Figure 4.21 shows the results of the correction of the wind input source functions at different stages of wave development for the JONSWAP spectra. The spectral tails of the wind input spectra have similar slopes, except in the case of the full development stage. For fully-developed waves, the wind input spectrum has a reduced slope. The magnitudes of the wind input spectrum are determined by the magnitudes of the energy density spectrum (the JONSWAP spectrum in this case), which are determined by the spectral parameters. In this study, the Babanin and Soloviev (1998) parameterisations for the spectral shape parameters of the JONSWAP spectrum were used to compute the JONSWAP spectra at different stages of wave development. Therefore, the relative disposition of wind input spectra in Figure 4.21 is not a fundamental result but only a particular case.

The transition from full-separated flow to non-separated during wave development is located in the narrow range of frequencies near  $f_i = 1\text{Hz}$ . Figure 4.21 shows that the energy flux from wind to wave is strongest for average-developed waves with wind forcing  $U_{10}/c_p = 2.7$ .



**Figure 4.18** Comparison of wind source function according to Donelan et al. (2006) before and after applying stress correction function  $L(f)$  (Eq. 4-17). Computations were performed for the JONSWAP (solid line and line with dots, respectively) and Donelan (dashed line and line with crosses, respectively) spectra for the average developed waves with  $U_{10}/c_p = 2.7$  and the wind speed  $U_{10} = 10$  m/s.



**Figure 4.19** Comparison of growth rate spectra before and after applying stress correction function  $L(f)$  (Eq. 4-17). Computations were performed for the JONSWAP spectrum for the average developed waves with  $U_{10}/c_p = 2.7$  and the wind speed  $U_{10} = 10$  m/s.

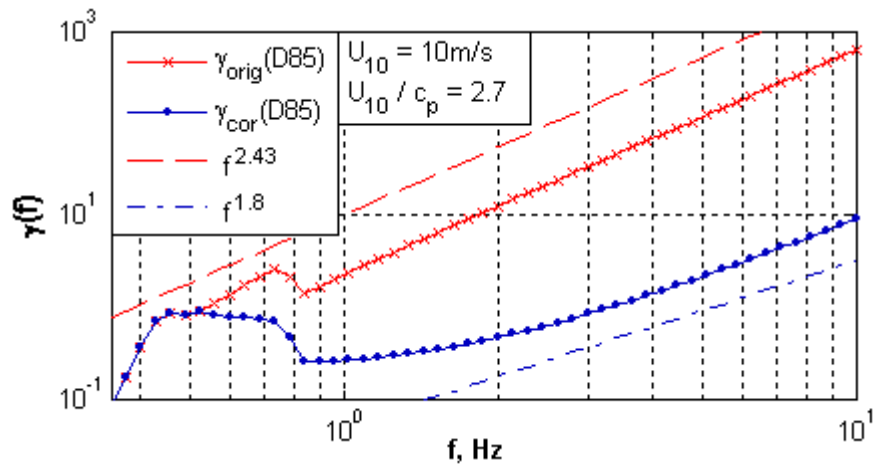


**Figure 4.20** Comparison of growth rate spectra before and after applying stress correction function  $L(f)$  (Eq. 4-17). Computations were performed for the Donelan spectrum for the average developed waves with  $U_{10}/c_p = 2.7$  and the wind speed  $U_{10} = 10$  m/s.

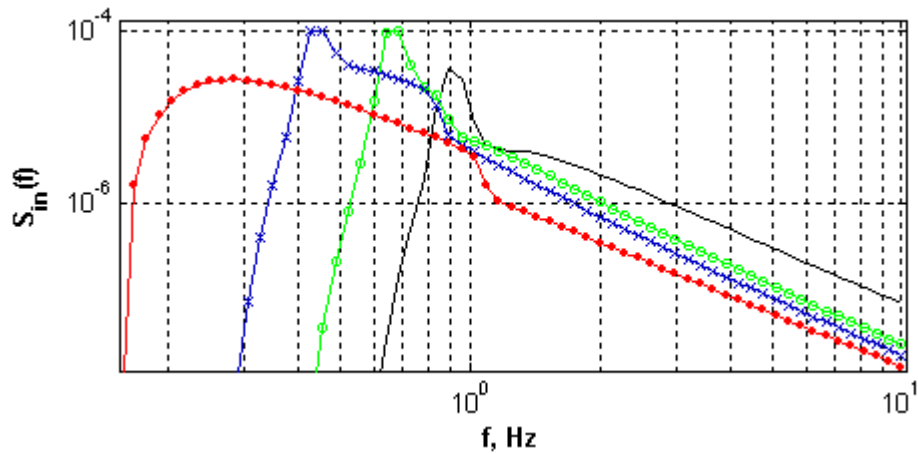


**Figure 4.21** Wind source function according to Donelan et al. (2006) computed with applying stress correction function  $L(f)$  (Eq. 4-17). Computations were performed for the JONSWAP spectra at different stages of wave development with  $U_{10}/c_p = \{5.8$  (plain lines),  $4.5$  (line with circles),  $2.7$  (lines with crosses),  $0.83$  (lines with dots)} for the wind speed  $U_{10} = 10$  m/s.

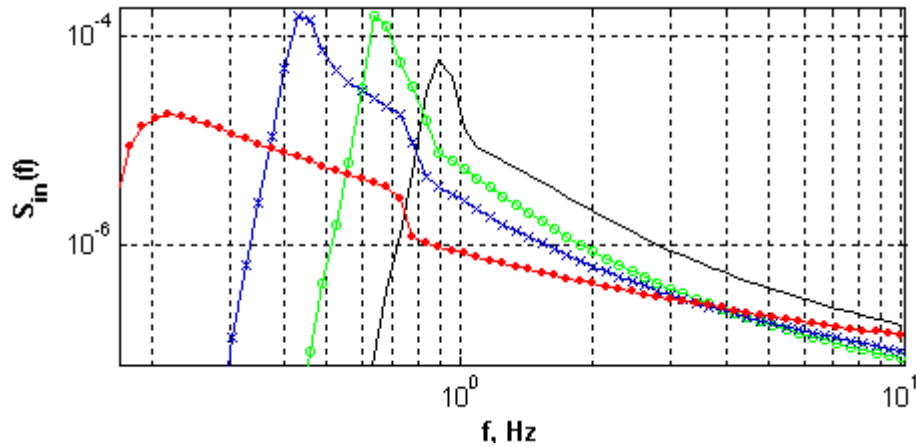
Figure 4.22 shows the corrected wind input spectra computed for the Donelan wave spectra at different stages of wave development for wind speed  $U_{10} = 10$  m/s. In this case the slopes of the spectral tails are different at each stage of wave development. However, at high frequencies ( $f > 3$ Hz) the spectral tails of the wind input spectra are close to each other for all stages of wave development.

Figure 4.23 shows the correction rate  $\eta$  as a function of wind forcing. The function  $\eta(U_{10}/c_p)$  shows the rate of suppression of the wind input spectrum which is the result of the stress correction at different stages of wave development. The results of computations shown in Figure 4.23 were obtained for the JONSWAP spectra at different stages of wave development. As shown, the behaviour of this function depends on the type of drag coefficient selected for the computations of wave-induced stress (Eq. 4-6). For waves with  $U_{10}/c_p > 1.6$  the suppression is higher using  $C_D(U_{10})$  and has a generally decreasing trend. The opposite behaviour for  $\eta$  is obtained for  $C_D(U_{10}/c_p)$ . For the drag coefficient  $C_D(U_{10}/c_p)$  the maximal suppression of wind input function happened at  $U_{10}/c_p = 1.6$  (well developed waves), while for  $C_D(U_{10})$  it was at  $U_{10}/c_p = 4.1$  (young waves). For both type of drag coefficient there is a jump at  $U_{10}/c_p = 4.5$ , which corresponds to the transition of wind flow from fully-separated to non-separated.

Different correction rates  $\eta$  are obtained for the Donelan spectra at different stages of wave development, which are shown in Figure 4.24. The figure shows the significant influence of the type of drag coefficient used on the correction rates  $\eta$ . Furthermore, the values of  $\eta$  (i.e. required suppression) are much greater compared to the case of the JONSWAP spectrum. For  $C_D(U_{10}/c_p)$ , the correction rate remains almost constant during the wave development if we do not consider the step when the wind flow is changing from fully-separated to non-separated.

#### 4.1.3.1 High Frequency Tail

The present study shows more evidence supporting the existence of composite wave spectra with the transition from  $f^{-4}$  to  $f^{-5}$  dependence. This evidence is strongly based on the physical constraints considered in this study. The results of computations of wave-induced stress,  $\tau'_w$  (Eq. 4-4), using the wind input source term from Lake George (Donelan et al. 2006) for  $f^{-4}$  wave spectra (Donelan 1985) show a large excess over the total wind stresses  $\tau$  exerted on the waves (see Figure 4.11).



**Figure 4.22** Wind source function according to Donelan et al. (2006) computed with applying stress correction function  $L(f)$  (Eq. 4-17). Computations were performed for the Donelan (1985) spectra at different stages of wave development with inverse wave age  $U_{10}/c_p = \{5.8$  (plain lines),  $2.7$  (lines with crosses),  $0.83$  (lines with dots)} for the wind speed  $U_{10} = 10$  m/s.

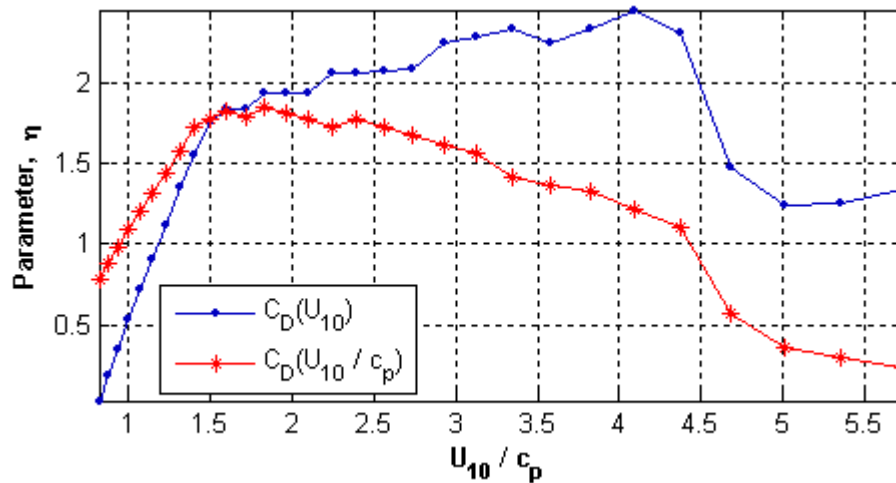


**Figure 4.23** Comparing the parameter,  $\eta$  of the stress correction function  $L(f)$  (Eq. 4-17) computed for wind source function according to Donelan et al. (2006) for the JONSWAP spectra for  $C_D(U_{10})$  (line with dots) and for  $C_D(U_{10}/c_p)$  (line with asterisks).

The shape of the wave spectrum used in these computations has a significant influence on the results because of the nonlinear dependence of the wind input source function on the wave spectrum (see Equations 4-1, 4-2 and 4-3). Moreover, the computations of wave-induced stress  $\tau'_w$  (Eq. 4-4) include integration up to very high frequency scales,  $f_{max} = 10\text{Hz}$ , which increases the importance of the spectral shape. The remarkable difference shown in Figure 4.25 indicates that wave spectra with  $f^{-4}$  dependence should have a transition to  $f^{-5}$  dependence in the high frequency range.

Otherwise, the integral in Equation 4-4 becomes very large and wave-induced stress  $\tau'_w$  significantly exceeds the estimated value for wave-induced stress  $\tau_w$ , which seems inconsistent with the actual processes. This fact unambiguously supports the plausibility of the existence of composite spectra. Therefore, in the present study, composite wave spectra have been taken into consideration and termed the Combi spectra, as it is a combined spectrum.

The Combi spectra were modelled on the wave spectra from Donelan et al. (1985). However, a transition to  $f^{-5}$  dependence was achieved by introducing an additional dimensionless coefficient  $f_T/f$  into Donelan's (1985) spectra for frequencies  $f > f_T$  where  $f_T$  is the transition frequency (Eq. 2-29). The Combi spectrum can be represented in the form:

$$\begin{cases} F(f, \theta) = \beta \frac{g^2}{(2\pi)^4} f_p^{-1} f^{-4} \exp\left[-\left(\frac{f}{f_p}\right)^{-4}\right] \cdot \gamma_D \exp\left[\frac{-(f-f_p)^2}{2\sigma^2 f_p^2}\right] & f \leq f_T \\ F(f, \theta) = \beta \frac{g^2}{(2\pi)^4} f_T f_p^{-1} f^{-5} \exp\left[-\left(\frac{f}{f_p}\right)^{-4}\right] \cdot \gamma_D \exp\left[\frac{-(f-f_p)^2}{2\sigma^2 f_p^2}\right] & f > f_T \end{cases} \quad (\text{Eq. 4-23})$$

According to this model, the wave spectra with  $f^{-5}$  dependence correspond to young waves with wind forcing  $U_{10}/c_p > 5$ . As waves approach the fully-developed state, the part of the spectrum with  $f^{-4}$  dependence enlarges towards lower frequencies.

The Combi spectrum for  $U_{10} = 10$  m/s is shown in Figure 4.25. Similar analysis of wind stress and computations of the wind input source function (Donelan et al. 2006) using the method discussed previously were performed for the Combi spectra in the present study. The results of these computations are discussed in Section 4.2.1.

### 4.1.3.2 Wave Steepness

As it was demonstrated in Section 2.2.3, the shape of the wave spectrum has a significant impact on the magnitudes of the spectral saturation in the high frequency range. These differences in the high frequency spectral components create remarkable inconsistencies in stress computations for the JONSWAP and Donelan spectra, even if they correspond to the same state of the sea surface. To solve this dilemma an alternative parameterisation form for the spectral saturation was devised. The idea consisted of the development of a dimensionless empirical form for the spectral saturation, which would give a saturation level at high frequencies for most types of wave spectra. This alternative form of spectral saturation was represented as:

$$T(f) = (2\pi)^4 f_p^{n+5} f^{-n} F(f) / 2g^2 \quad (\text{Eq. 4-24})$$

where  $n$  is the power-law of the high frequency spectral tail. This alternative function of the spectral saturation was named the saturation transformer  $T(f)$ . The relationship between the saturation transformer  $T(f)$  and the spectral saturation  $B(f)$  can be simply derived from Equations 4-24 and 2-29. The saturation transformer relates to the spectral saturation through the following mathematical expression:

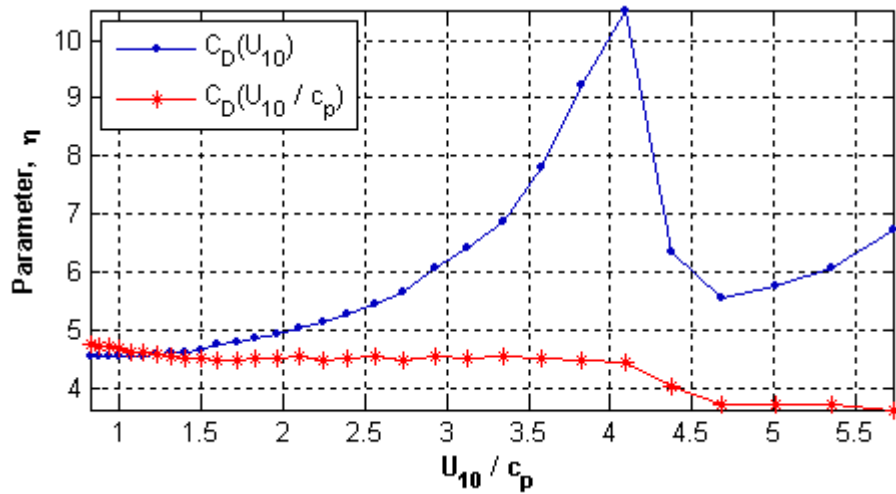
$$T(f) = \left(\frac{f_p}{f}\right)^{n+5} B(f) = \left(\frac{f_p}{f}\right)^{n+5} A^{-1}(f) B_n(f) \quad (\text{Eq. 4-25})$$

According to Equation 4-25, the saturation transformer becomes identical to the spectral saturation when  $n = -5$  (the JONSWAP spectrum). For the Donelan spectrum, when

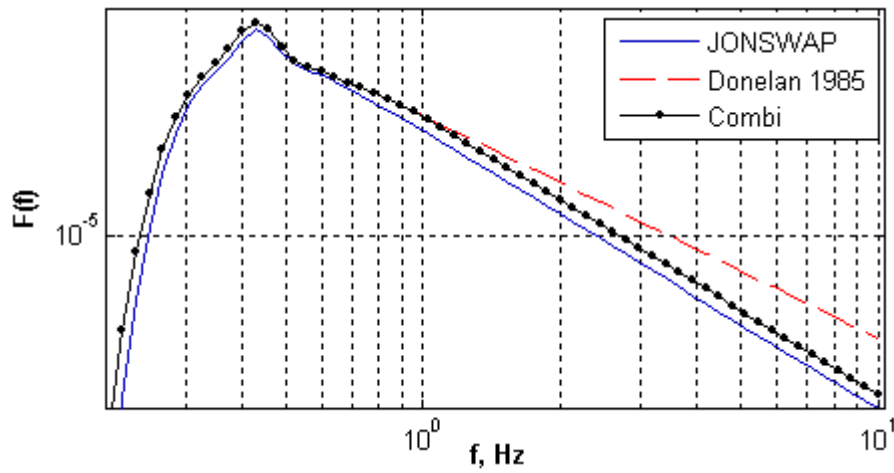
$$n = -4, \text{ the saturation transformer is } T(f) = \left(\frac{f_p}{f}\right) B(f).$$

Figure 4.26 shows the results of computations of the saturation transformer  $T(f)$  according to Equation 4-24 at different stages of wave development. The computations were performed for the JONSWAP and Donelan spectra. The figure shows that for both types of wave spectra the spectral steepness has saturating levels in the range of high frequencies.

In contrast to the spectral saturation  $B(f)$  (see Figures 2.4 and 2.5), Figure 4.26 shows the close spectral magnitudes of  $T(f)$  for both types of wave spectra at every stage of wave development. The use of the saturation transformer  $T(f)$  diminishes the inconsistencies of stress computations for different spectra when using  $B(f)$ .



**Figure 4.24** Comparing the parameter,  $\eta$  of stress correction function  $L(f)$  (Eq. 4-17) computed for wind source function according to Donelan et al. (2006) for the Donelan (1985) spectra for  $C_D(U_{10})$  (line with dots) and for  $C_D(U_{10}/c_p)$  (line with asterisks).



**Figure 4.25** Combi spectrum for the average developed waves with  $U_{10}/c_p = 2.7$  and the wind speed  $U_{10} = 10$  m/s. JONSWAP and Donelan spectra are also shown (solid line for the JONSWAP spectrum and dashed line for the Donelan spectrum).

The term  $f^5 F(f)$  in the formula (Eq. 2-18) of the spectral saturation is represented by the term  $f_p^{n+5} f^{-n} F(f)$  having the same dimensional units as  $f^5 F(f)$ . The spectral saturation  $B(f)$  becomes a particular case of  $T(f)$  when  $n = -5$  (JONSWAP spectrum). The only difference is the dependence of  $T(f)$  on the spectral peak frequency,  $f_p$ . This dependence has strong observational support from the experimental study at Lake George (Babanin et al., 2001). One of the most important findings of that study was the influence of long scale waves on the breaking events of shorter waves (Babanin et al., 2001).

This influence may result in the increase of the steepness of short waves beyond some threshold of steepness which results in the breaking of these waves. The threshold value for wave steepness was found from the experimental studies of Banner et al. (2000) and Babanin et al. (2001). Thus, the dominant waves have an influence on the steepness of shorter waves. This phenomenon was included in the formulation of the saturation transformer.

In the present study, the computations of the saturation transformer were performed for the Combi spectra. Figure 4.27 shows the results of these computations. The saturation level of the high frequency range increases with wave development.

It is worth mentioning that the steepness of the short waves increases as the steepness of the dominant waves decreases with wave development. Furthermore, the transition from  $f^{-4}$  dependence to  $f^{-5}$  in the Combi spectra is clearly shown by the starting frequency of the saturation range, which is the transition frequency  $f_T = 0.78\text{Hz}$  mentioned in Section 2.2.1, Equation 2-9. The following computations of the wind input source function, performed for the Combi spectra, include the saturation transformer  $T(f)$  as a convenient alternative form for the spectral saturation  $B(f)$ .

#### 4.1.1 COMPUTATIONS OF $S_{IN}$ FOR THE COMBI SPECTRA

As discussed earlier, there is much evidence for the existence of the Combi spectra in nature. Moreover, it is believed that wave spectra do not have a universal value for a power-law dependence on wave frequency along the frequency scale. On the other hand, observational limitations in the high frequency range result in inconsistencies in the resulting spectral datasets. Therefore, based on the available evidence (see Section 2.2.1) of the existence of the Combi spectra, computations of the wind input source function (Donelan et al., 2006) were performed for this type of wave spectra.

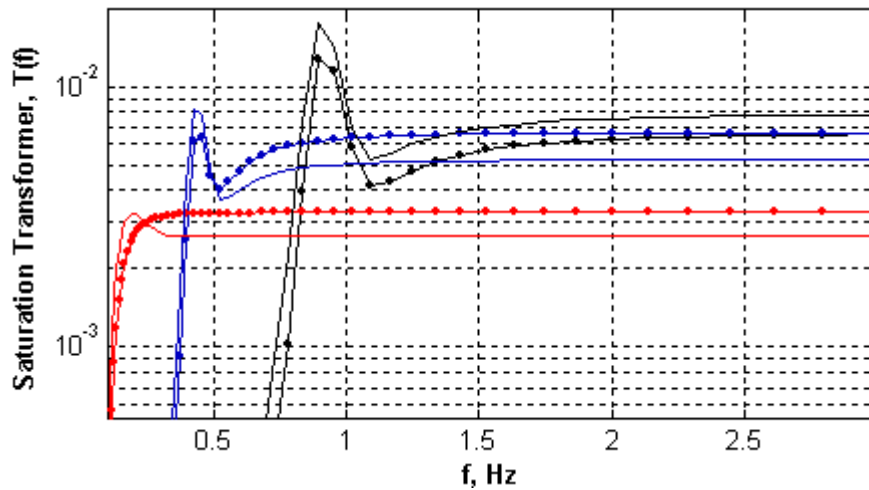


**Figure 4.26** Comparison of the saturation transformer,  $T(f)$  (Eq. 4-24) for the JONSWAP (solid lines) and Donelan (lines with dots) energy density spectra at different stages of wave development with inverse wave age  $U_{10} / c_p = \{5.8, 2.7, 0.83\}$  for the wind speed  $U_{10} = 10$  m/s.

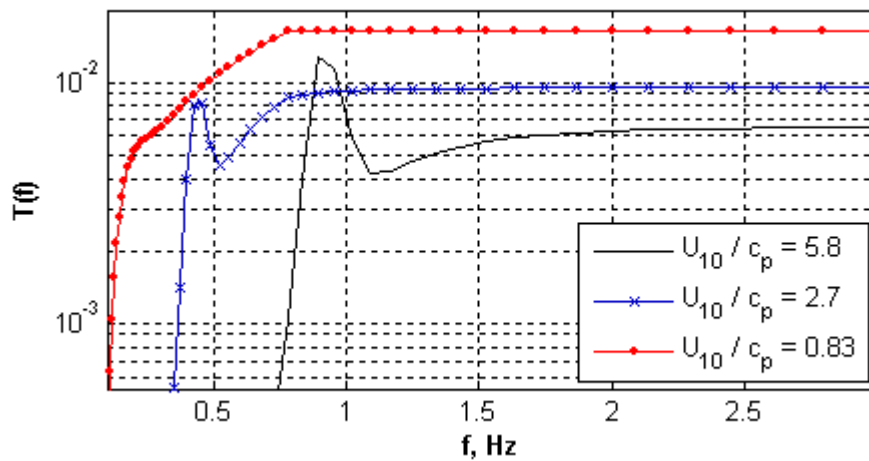


**Figure 4.27** Comparison of the saturation transformer,  $T(f)$  (Eq. 4-24) with  $n = -5$  for the Combi energy density spectra at different stages of wave development with inverse wave age  $U_{10} / c_p = \{5.8$  (plain line),  $2.7$  (line with crosses),  $0.83$  (line with dots) $\}$  for the wind speed  $U_{10} = 10$  m/s.

All computations were performed in accord with the methods developed in the present study for correcting the wind input source function. Furthermore, the saturation transformer  $T(f)$  was included in these computations as an alternative form of spectral saturation  $B(f)$ . Primarily, the wave-induced stress  $\tau'_w$ , computed from the momentum flux according to Equation 4-4 was analysed against the estimating wave-induced stress  $\tau_w$  (Eq. 4-6) for different types of drag dependence on the wave age.

Figure 4.28 shows the increasing trend of wave-induced stress  $\tau'_w$  with the development of waves. This trend is determined by the increasing part of  $f^{-4}$ -dependence in the Combi spectra as waves approach full-development stage. However, in contrast to Figure 4.11, the wave-induced stress computed for the Combi spectra has a lower magnitude than for the Donelan spectra.

Figure 4.29 provides a comparison of wave-induced stresses computed for the Combi spectra using  $T(f)$  and for the JONSWAP and Donelan spectra using  $B(f)$ . The magnitudes of wave-induced stress computed for the Combi spectra are approximately ten times less than wave-induced stresses computed for the Donelan spectra.

For young waves, the wave-induced stresses computed for the Combi and JONSWAP spectra are similar in magnitude. This agreement is determined by the similar high frequency spectral tail rates for both spectra. However, the difference is determined by the different empirical spectral forms of these spectra.

Figure 4.30 shows correction factor  $X$  computed for the Combi spectra at different stages of wave development. For young waves, the values of  $X$  for the Combi spectra have the same order of magnitude as those for the JONSWAP spectra (see Figure 4.14), as demonstrated by the form of the Combi spectrum introduced previously. In the early stages of wave development this form includes a  $f^{-5}$  dependence. The spectral tail of the Combi spectrum is close to that of the JONSWAP for young dominant waves. Therefore, the results of the computations of the correction factor  $X$  are close for the Combi and JONSWAP spectra. In keeping with the method developed during this study, the correction function  $L(f)$  (Eq. 4-17) was determined using the correction factor  $X$  and applied to the wind input source term computed for the Combi spectrum.

The resultant corrected wind input source function  $S_{in}$  is shown in Figure 4.31 together with those computed for the JONSWAP and Donelan spectra. Figure 4.31 shows that all these spectral functions are close in terms of their spectral magnitudes. However, the wind input source function for the Donelan spectrum has different spectral slope in the high frequency

range where  $f > 2\text{Hz}$ . In the range close to the dominant waves the wind input source functions, computed for the Combi and Donelan spectra, coincide.

Figure 4.32 shows a comparison of wind input source terms computed for the Combi spectra at different stages of wave development when the drag coefficient is a function of wind speed only. The different rates of suppression of wind input function at different stages of wave development are clearly shown in Figure 4.32.

This effect is shown as the slope variation of wind input spectral tails. It is remarkable that the spectral magnitudes of the wind input source function for young waves and for fully developed waves have close spectral magnitudes in the high frequency spectral range. This variation of the high frequency spectral slopes is determined by the magnitudes of correction rates  $\eta$  in the correction function  $L$  during wave development.

According to these results, the energy input from the wind to high frequency waves is higher for young, dominant and fully-developed waves than in the middle stages of wave development. At the same time the wind energy input into dominant waves is higher in the middle stages of wave development.

A different picture for the wind input source functions is obtained for the case when the drag coefficient is dependent on the inverse wave age,  $C_D(U_{10} / c_p)$ . As shown in Figure 4.33, the spectral slopes of the wind input source functions in the high frequency range remain almost similar during wave development. The figure shows a decreasing trend of the spectral magnitudes in the high frequency range. According to this, the energy input from wind to high frequency waves does not have such remarkable variation during wave development as was shown in Figure 4.32. The main variation of wind energy input during wave development is obtained in the range of dominant waves.

More recent observational studies have shown an increasing support for a wave age dependent drag coefficient. The results obtained in the present study support this trend as well. Comparison of Figure 4.33 and 4.32 shows the behaviour of the wind input source function at different stages of wave development.

This variation is clearly exposed when considering the correction rate as a function of wind forcing  $\eta(U_{10} / c_p)$ , as shown in Figure 4.34. The correction rate  $\eta$  is a very useful parameter for the estimation of the suppression rate of the wind input source function as a result of the stress correction methodology developed in the present study.

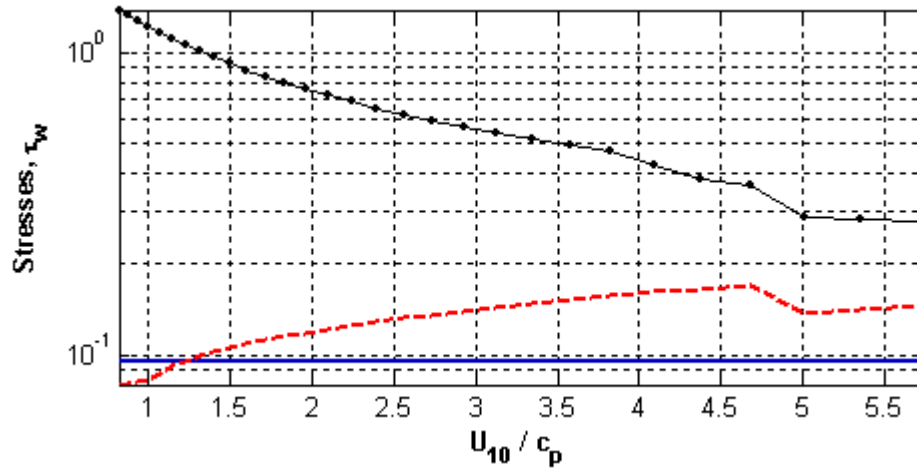


**Figure 4.28** Comparison of wave induced stresses  $\tau_w$  computed for wind source function according to Donelan et al. (2006) for the Combi spectra using  $T(f)$  (line with dots) with wave induced stress computed from total wind stress by formula (Eq. 4-6) (bold line for  $C_D(U_{10})$  and dashed bold line for  $C_D(U_{10}/c_p)$ ).

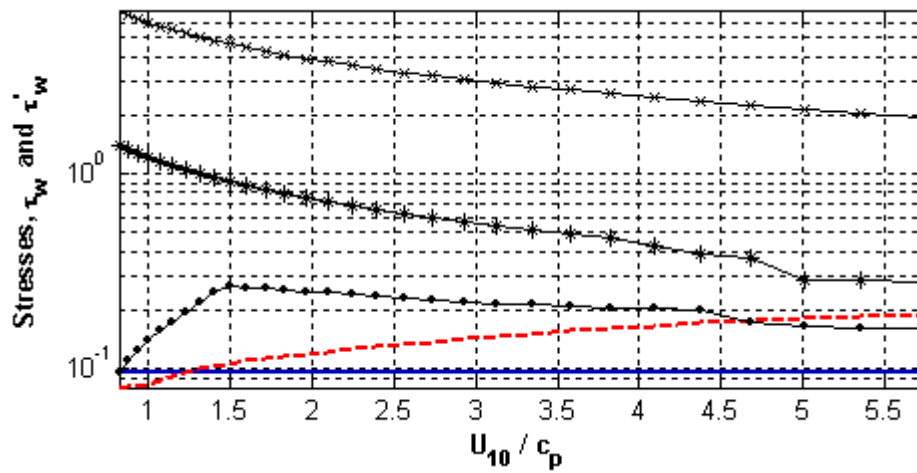


**Figure 4.29** Comparison of wave-induced stresses computed for the Combi spectra using  $T(f)$  (line with asterisks), for the JONSWAP (line with dots) and Donelan (line with crosses) spectra using  $B(f)$  relative to the wave induced stress computed from total wind stress by formula (Eq. 4-6) (bold line for  $C_D(U_{10})$  and dashed bold line for  $C_D(U_{10}/c_p)$ ).

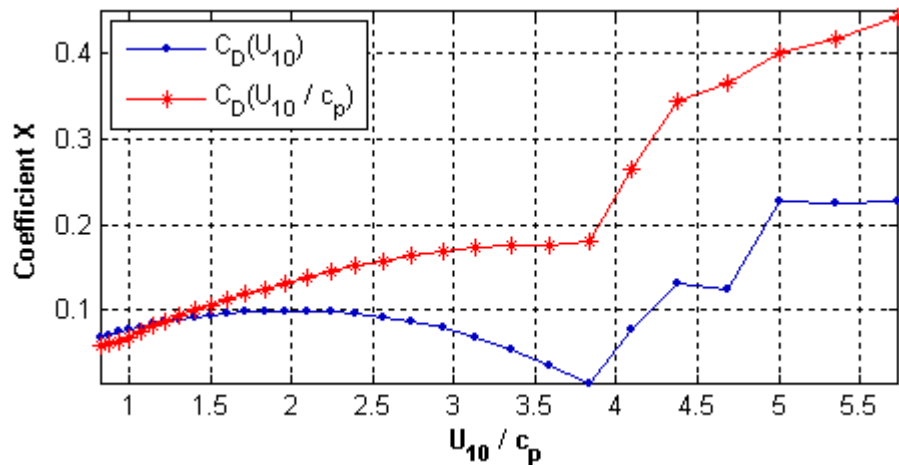


**Figure 4.30** Comparing correcting coefficient  $X$  (Eq. 4-13) for stress correction of the wind input source function according to Donelan et al. (2006) computed for the Combi spectra using  $T(f)$  (solid line with asterisks), for  $C_D(U_{10})$  (line with dots) and  $C_D(U_{10}/c_p)$  (line with asterisks) for wind speed  $U_{10} = 10$  m/s.

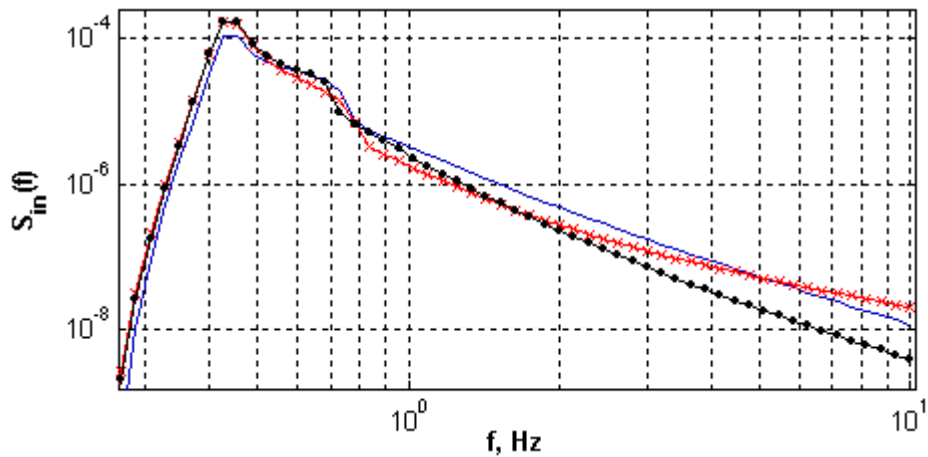


**Figure 4.31** Comparison of corrected with  $L(f)$  (4.17) wind source function according to Donelan et al. (2006) computed for different type of energy density spectra. Computations were performed for the JONSWAP (solid line), Donelan (line with crosses) and Combi (line with dots) spectra for the average developed waves with inverse wave age  $U_{10}/c_p = 2.7$  and the wind speed  $U_{10} = 10$  m/s.

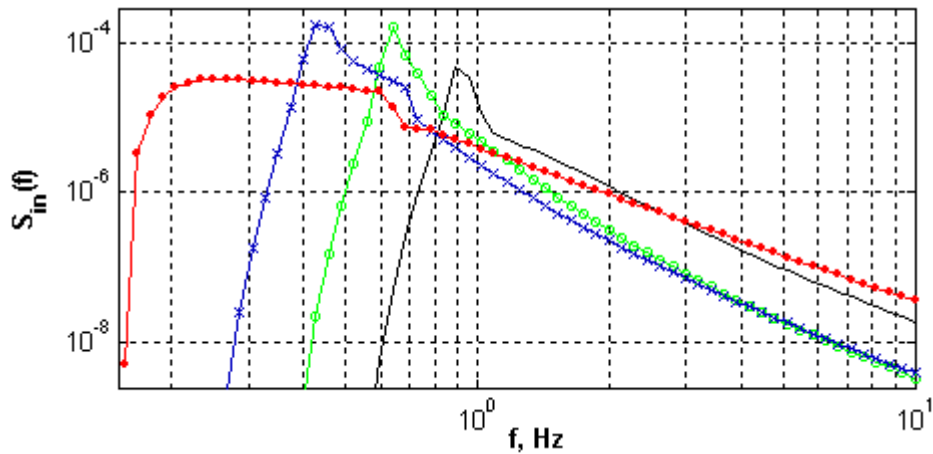


**Figure 4.32** Wind source function according to Donelan et al. (2006) computed with applying stress correction  $L(f)$  (Eq. 4-17) for  $C_D(U_{10})$ . Computations were performed for the Combi spectra at different stages of wave development with  $U_{10} / c_p = \{5.8$  (plain line),  $4.5$  (line with circles),  $2.7$  (line with crosses),  $0.83$  (line with dots)} for the wind speed  $U_{10} = 10$  m/s.

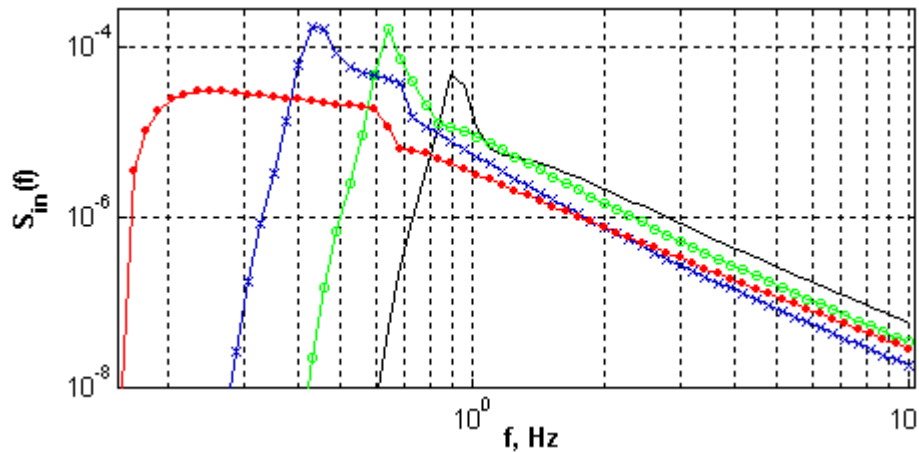


**Figure 4.33** Wind source function according to Donelan et al. (2006) computed with applying of stress correction  $L(f)$  (Eq. 4-17) for  $C_D(U_{10} / c_p)$ . Computations were performed for the Combi spectra at different stages of wave development with  $U_{10} / c_p = \{5.8$  (plain line),  $4.5$  (line with circles),  $2.7$  (line with crosses),  $0.83$  (line with dots)} for the wind speed  $U_{10} = 10$  m/s.

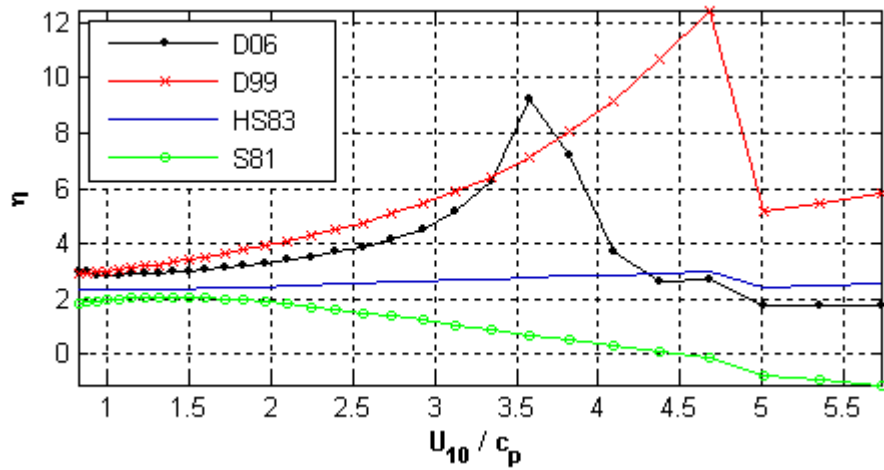
In the case of a wave age dependent drag coefficient,  $\eta$  remains almost constant during the wave development stage (has the same order values). So, the rate of suppression of the wind input spectrum is almost constant.

Figure 4.34 clearly shows in which cases the suppression of the wind input source term is larger. According to the results shown in this figure, in the case of wind dependent drag coefficient  $C_D(U_{10})$  there is a larger suppression of the wind input source function. Moreover, the correction rate for  $C_D(U_{10})$  reaches a maximal value at an inverse wave age  $U_{10} / cp = 3.6$  when the growth rate magnitudes of dominant waves have maximal value corresponding to non-separated wind flow over the dominant waves (see Figure 4.3b). Consequently, the correction rate  $\eta$  is the parameter which describes the suppression rate in the stress correction routine for wind input source function.

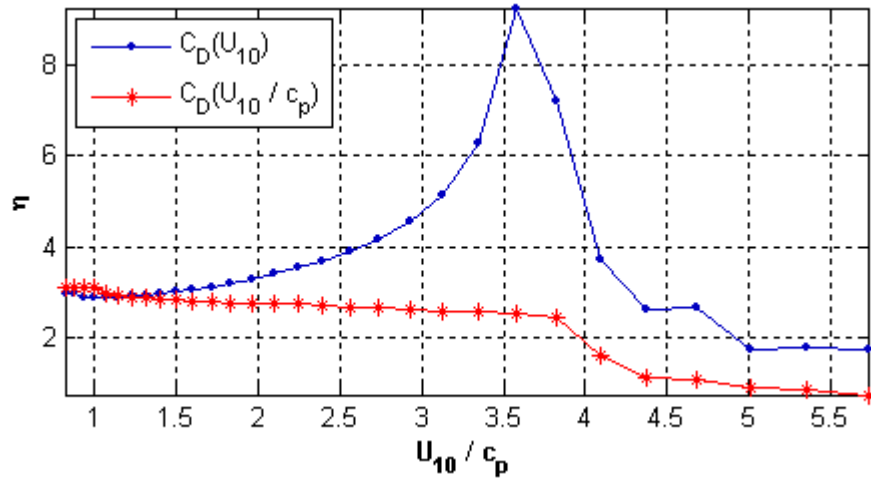
The developed method for correction of the wind input source term by wave-induced stress was applied to other parameterisations of wind input according to Donelan (1999), Hsiao and Shemdin (1983) and Snyder (1981). The mentioned parameterisation forms were computed for the Combi spectra at different stages of wave development. As a result of applying this method, the correction rate  $\eta$  was obtained for each parameterisation form at different stages of wave development. The computations of the correction rate  $\eta$  were performed for both types of wave age dependency of drag coefficient. Comparisons of the obtained values of  $\eta$  clearly show that the suppression rates required for the wind input parameterisation forms correspond to the wind stresses applied to the sea surface. According to the definition of correction rate  $\eta$ , the best correspondence of wind input function to wind stress is when  $\eta = 0$ . This means that neither suppression nor expansion is necessary for the wind input source term to correspond to the wind stress. In cases in which the correction rates  $\eta$  are negative, they correspond to expansion of the wind input source term.

Figure 4.35 shows a comparison of the correction rate  $\eta$  as a function of the inverse wave age for different parameterisation forms of the wind input source term. The figure shows the results corresponding to stress computations with wind dependent drag coefficient  $C_D(U_{10})$ .

The figure represents the suppression rates required for correction of the parameterisation forms. The comparison shows that the suppression rates for well developed waves, where  $U_{10} / cp < 1.5$ , are almost similar for all parameterisation forms. However, for younger waves there is a big difference.



**Figure 4.34** Comparing the correction rate parameter,  $\eta$  of the stress correction function  $L(f)$  (Eq. 4-17) computed for wind source functions according to different authors for the Combi spectra and  $C_D(U_{10})$ .



**Figure 4.35** Comparing the correction rate parameter,  $\eta$  of stress correction function  $L(f)$  (Eq. 4-17) computed for wind source function according to Donelan et al. (2006) for the Combi for  $C_D(U_{10})$  (line with dots) and for  $C_D(U_{10}/c_p)$  (line with asterisks).

This comparison shows that the least suppression is required for the Snyder (1981) parameterisation form, which shows the best correspondence to the wind stresses computed for the Combi spectra at different stages of wave development. The magnitudes of the correction rate  $\eta$  obtained for the wind input source term according to Donelan et al. (2006) are close to the correction rates for the parameterisation of Hsiao and Shemdin (1983) for young waves with  $U_{10}/c_p > 4$  and close to correction rates for the parameterisation of Donelan (1999) for average-developed waves with  $U_{10}/c_p < 3.8$ .

Correction rates,  $\eta$ , for different parameterisation forms of the wind input source term for the case of the wave age dependent drag coefficient  $C_D(U_{10}/c_p)$  are shown in Figure 4.36. In this case, the suppression rates applied to the wind source function according to Donelan et al. (2006) are close to the suppression values required for Donelan (1999) and Hsiao and Shemdin (1983). In the early stages of wave development the suppression rates required for Donelan et al. (2006) are less than for Donelan (1999) and Hsiao and Shemdin (1983). This fact demonstrates that the wind input source term according to Donelan et al. (2006) has a better correspondence to wind stresses occurring on the air-sea boundary for very young waves with  $U_{10}/c_p > 5$ .

Taking into consideration the fact that experimental data from Lake George (Donelan et al., 2006) were obtained in shallow water conditions, where wave spectra are represented mostly by young waves, it is obvious that Donelan et al. (2006) offer the best correspondence of wind input parameterisation for the early stages of wave development.

As the waves are growing, the parameterisation form by Donelan et al. (2006) requires more suppression to correspond to the wind stress. Using the method adopted to correct the wind input source term, the correction is applied to the high frequency spectral range. The parameterisation of the dominant waves is not changed. Further experimental elaboration is, therefore, required in deep water conditions to obtain the best correspondence to the wind stress, wind input parameterisation in light of the new physical phenomena discovered in the Lake George experiments (Donelan et al., 2006).

In both cases of the dependency of the drag coefficient on wave age, the correction rates for Snyder's (1981) parameterisation form have the closest magnitudes to  $\eta = 0$  in comparison to correction rates for the parameterisation forms of other authors. On the basis of these comparisons, the parameterisation according to Snyder (1981) has the best correspondence to wind stress. However, Snyder's (1981) parameterisation form was developed on the basis of experimental data obtained in very light wind speed conditions

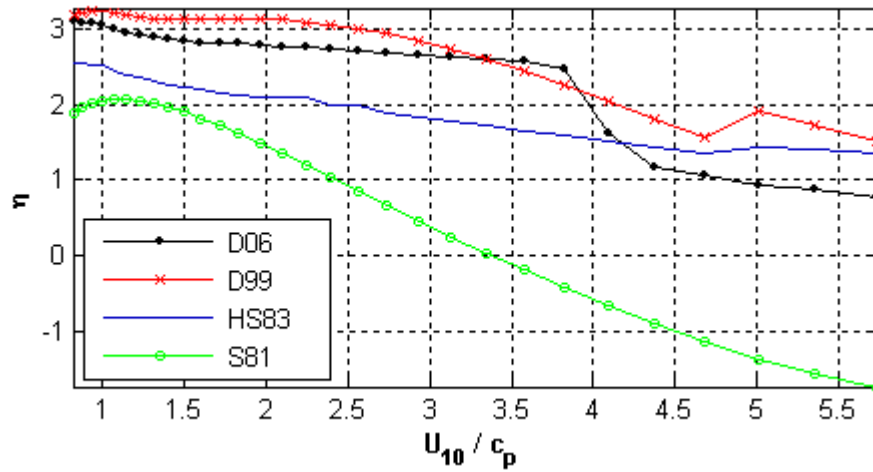
(high viscous stresses) and its applicability for the strong wind seas is questionable. The parameterisation from Lake George (Donelan et al., 2006) has a more advanced physical background than the others. It includes the new physical phenomena revealed in the Lake George experiment (see Section 2.3.2, the discussion of wind input). The preferences of choice in wave modelling should be based on physics rather than the best fitting parameterisation form. Therefore, the parameterisation according to Donelan et al. (2006) with the corrections, using the method developed in the current study, is considered an advanced form of wind input source term.

Figure 4.37 shows the results of computation of the wind input source term according to Donelan et al. (2006) for the Combi spectra of averaged-developed waves for  $U_{10}/c_p = 2.73$  at different wind speeds in the case of wind-dependent drag coefficient  $C_D(U_{10})$ . Figure 4.37 shows the rate of the high frequency spectral tails is changing with the wind speed. For low wind speed  $U_{10} = 7\text{m/s}$  the suppression rate is higher than for the other winds. This fact is determined by the magnitude of the wave-induced stress, which is computed from the total wind stress, allowing for viscous stress. In low winds the contribution of viscosity to the stress balance (Eq. 4-1) is greater than at high wind speeds (Banner and Peirson, 1998). At higher speeds, from  $U_{10} = 20\text{ m/s}$ , the suppression rates are almost similar.

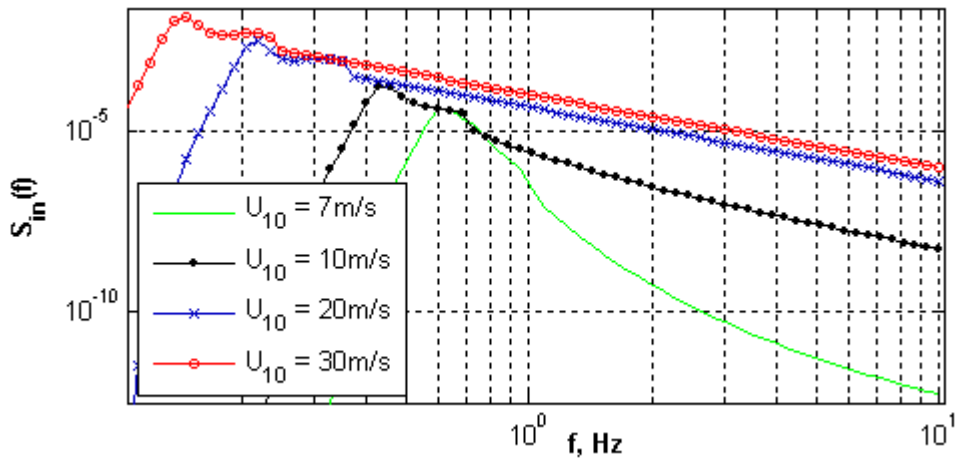
Figure 4.38 shows the results of the computation of the wind input source term according to Donelan et al. (2006) for the Combi spectra of averaged-developed waves for  $U_{10}/c_p = 2.73$  at different wind speeds in the case of a wave age dependent drag coefficient  $C_D(U_{10}/c_p)$ . The figure shows a trend similar to the rate of high frequency spectral tail with growth in association with wind speed. However, the magnitudes of the rate have less variation than the wind dependent drag coefficient.

Figure 4.39 shows the comparison of a corrected wind input source term according to Donelan et al. (2006) with the parameterisation forms of Donelan (1999), Hsiao and Shemdin (1983), and Snyder (1981) for average-developed waves with  $U_{10}/c_p = 2.7$  in wind  $U_{10} = 10\text{ m/s}$ , using the wave age dependent drag coefficient  $C_D(U_{10}/c_p)$ .

It should be mentioned that for dominant waves the spectral magnitudes of all these parameterisation forms, except Hsiao and Shemdin (1983), are close. Moreover, the parameterisation form of Snyder (1981) shows the best agreement to the wind input source function suggested by Donelan et al. (2006).



**Figure 4.36** Comparing the correction rate parameter,  $\eta$  of stress correction function  $L(f)$  (Eq. 4-17) computed for wind source functions according to different authors for the Combi spectra and  $C_D(U_{10}/c_p)$ .



**Figure 4.37** Comparison of wind source function according to Donelan et al. (2006) after stress correction with  $L(f)$  from (Eq. 4-17) for the Combi spectrum for the average developed waves with the inverse wave age  $U_{10}/c_p = 2.7$ , at different winds  $U_{10} = \{7 \text{ m/s}, 10 \text{ m/s}, 20 \text{ m/s}, 30 \text{ m/s}\}$  for  $C_D(U_{10})$

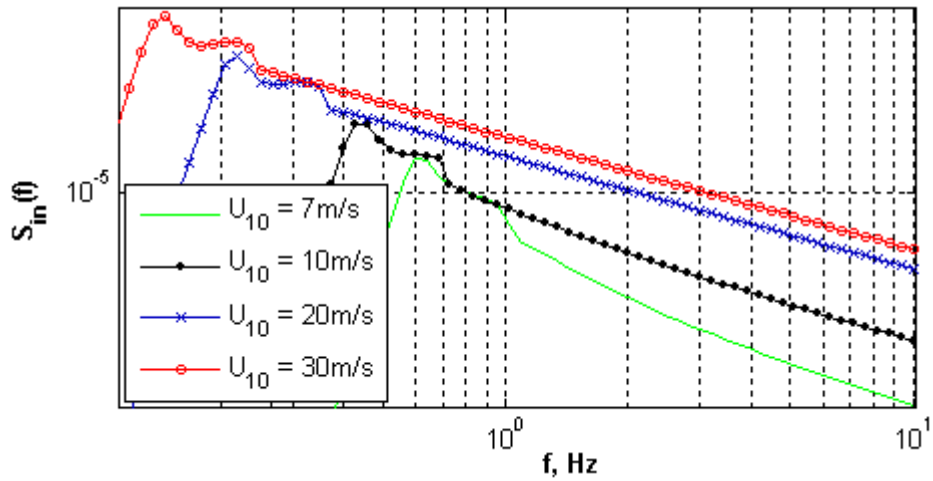


**Figure 4.38** Comparison of wind source function according to Donelan et al. (2006) after stress correction with  $L(f)$  from (Eq. 4-17) for the Combi spectrum for the average developed waves with the inverse wave age  $U_{10}/c_p = 2.7$ , at different winds  $U_{10} = \{7 \text{ m/s}, 10 \text{ m/s}, 20 \text{ m/s}, 30 \text{ m/s}\}$  for  $C_D(U_{10}/c_p)$ .

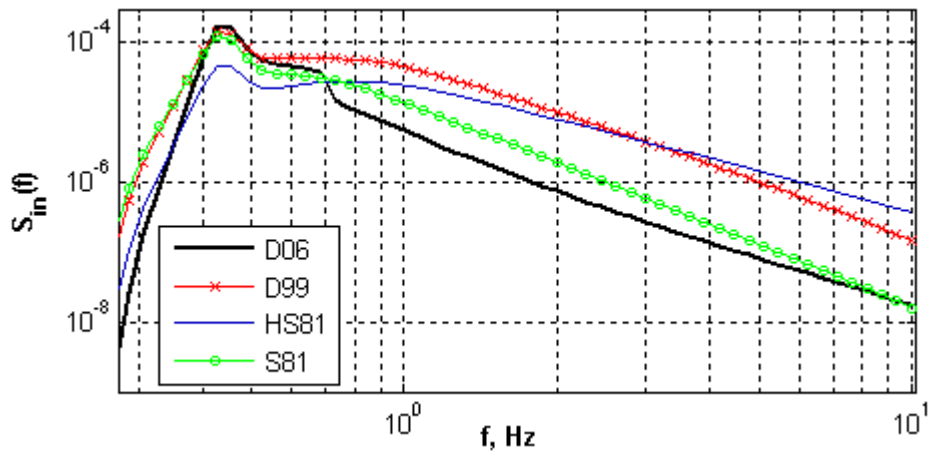


**Figure 4.39** Comparison of the wind source function according to Donelan et al. (2006) after stress correction with  $L(f)$  from (Eq. 4-17) for  $C_D(U_{10})$  (bold line), with the wind input source functions of Donelan (1999) (line with crosses) and Hsiao and Shemdin (solid line) for the Combi spectrum for the average developed waves with the inverse wave age  $U_{10}/c_p = 2.7$ , at different winds  $U_{10} = \{7 \text{ m/s}, 10 \text{ m/s}, 20 \text{ m/s}, 30 \text{ m/s}\}$ .

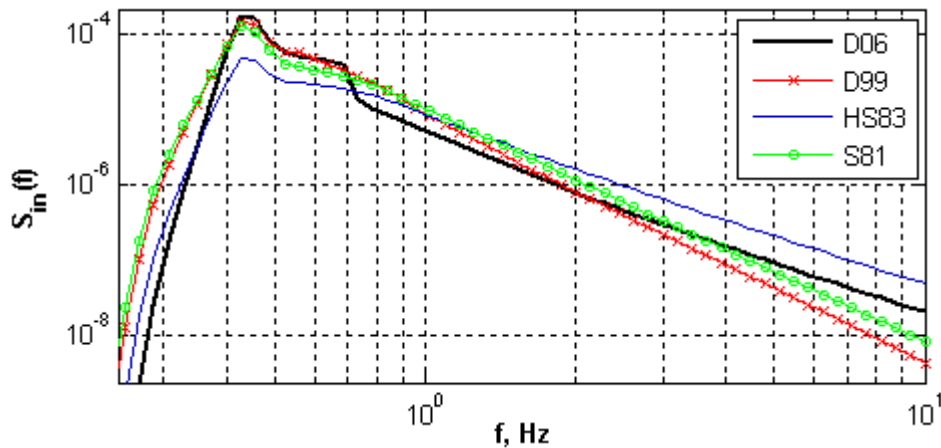


**Figure 4.40** Comparison of corrected wind source functions for  $C_D(U_{10} / c_p)$ : Donelan et al. (2006) (bold line), Donelan (1999) (line with crosses) and Hsiao and Shemdin (solid line) for the Combi spectrum for the average developed waves with the inverse wave age  $U_{10} / c_p = 2.7$ , at different winds  $U_{10} = \{7 \text{ m/s}, 10 \text{ m/s}, 20 \text{ m/s}, 30 \text{ m/s}\}$ .

The distinguishing feature of the spectral shape of Donelan et al.'s (2006) parameterisation is the step-wise jump determined by wind flow separation over the waves, where the growth rates of waves are less than suggested by other authors. The figure clearly shows the remarkable difference in the high frequency spectral tail of Donelan et al.'s (2006) parameterisation form from other researchers. This difference is determined by the new physical phenomena included in the new wind input source function offered by Donelan et al. (2006).

The new correction routine was applied to other parameterisation forms (Donelan, 1999; Hsiao and Shemdin, 1983; and Snyder, 1981). The results of the correction applied to the mentioned parameterisation forms were compared with the corrected wind input source function of Donelan et al. (2006). This comparison is represented in Figure 4.40. As a result of applying the correction routine, the spectral tails all of these source functions are located in a narrower range of spectral magnitudes than is shown in Figure 4.39. However, the slopes of the high frequency spectral tails are different. This difference can predetermine the different performances of these functions in a numerical model.

### 4.1.2 CONCLUSIONS

The behaviour of a suggested new parameterisation form for the wind input source term (Donelan et al., 2006) at different stages of wave development was investigated. The approach of this present study was based on a strong physical framework. One of the important physical constraints for wave models is wave-induced stress, which describes the strength of wind-wave interactions and can be directly measured in wave observations. The present study showed the remarkable inconsistency of previously suggested parameterisation forms for the wind input source term to the physics of wind-wave interactions.

The approach used in the present study, therefore, resulted in the development of a new method for the correction of wind input source functions in spectral wave modelling. The method represents a dynamic self-correction routine that is simple enough for implementation in operational wave modelling. According to this approach, the wave-induced stress is defined as the main physical constraint, which determines the momentum transfer from wind to waves. One of the advantages of the new method is that the correction is applied in the range of high frequency scales, which do not interfere with the range of applicability of the experimental results. Taking into consideration the contribution of very small scale waves in the wind momentum transfer, the upper limit for the frequency scale was set at  $f_{cut} = 10\text{Hz}$ . The suggested correction function  $L(f)$  (Eq. 4-17) allows for a smooth spectral shape transformation of the wind input source function in the wave model to correspond to the physical constraints. The correction rate  $\eta$  (Eq. 4-28) was defined as the parameter describing the suppression rate of the integral (Eq. 4-4), which is required for correction of the wind input source function. The correction methodology is applicable for any parameterisation form of the wind input source term and can be widely used in wave modelling.

The results of correcting the wind input source function (Donelan et al. 2006) show that the growth rate in the high frequency range becomes close to a linear dependency on frequency. Comparing the correction rates  $\eta$  for different wind speeds, it was found that for higher wind speeds less suppression is required for the integral (Eq. 4-4). At the same time, the correction rate is a function of inverse wave age  $U_{10} / c_p$ . It was found that the correction rate is maximal for young waves with  $U_{10} / c_p = [3.5, 4]$ , when wind flow type is changed from fully-separated to non-separated over the waves. The range of wind forcing conditions

where the correction rate  $\eta (U_{10} / c_p)$  is maximal indicates that further experimental observations are required for these types of waves.

Based on the results of the present study, some aspects of wave spectral modelling were revised. In this study a new function, the saturation transformer  $T(f)$ , was suggested as an alternative form for the spectral saturation  $B(f)$ . One of the advantages of this function is that it keeps the saturation level in the high frequency range regardless of which type of frequency spectrum is used, JONSWAP or Donelan's (1985).

The saturation transformer includes the effect of the influence of long scale waves on the steepness of short scale waves. These facts can be considered as an advantage in using this form in spectral wave modelling.

Another issue of spectral modelling regarding the shape of the wave spectrum was revised in the present study. Based on the comparisons of the results of stress computations corresponding to wind input source functions suggested by different authors for different wave spectra, the Combi spectra were suggested as the plausible wave spectra of a sea surface. The Combi spectra can be interpreted as the correction to Donelan et al.'s (1985) spectra. The parameterisation form (Eq. 4-23) of the Combi spectrum, introduced in this study, was suggested for wide application in operational wave modelling.

It can be concluded that the wind input parameterisation form according to Donelan et al. (2006) is an advanced form describing the physical nature of wind-wave interactions and can be widely adopted in different wave models. The performance of the corrected wind input source function (Donelan et al., 2006) in the wave model is discussed in Section 4.3.4.

## 4.2 THE NEW SPECTRAL DISSIPATION SOURCE FUNCTION

This section describes the investigation of the new source function for wave spectral dissipation suggested by Young and Babanin (2006) (Eq. 2-29) and discussed in Section 2.3. The general form for wave spectral dissipation was proposed on the basis of wave observations at Lake George (Young and Babanin, 2006) in a limited range of air-sea conditions. According to Equation 2-29, the wave dissipation source function demonstrates two-phase behaviour along the spectral frequency scale. The main source of wave energy loss is the wave breaking, known as the whitecapping. It was found that waves are prone to break if their steepness exceeds the threshold steepness (Banner et al., 2000 and

Babanin et al., 2001). This type of wave breaking is termed as inherent wave breaking and represented by the first term  $T_1(f)$  (see Equation 2-29). In addition to this, wave energy can dissipate due to turbulent viscosity, which plays a significant role in small scale waves. In addition, small-scale waves tend to break due to the breaking of the longer scale waves (Young and Babanin, 2006). Both types of wave energy dissipation are induced by the breaking of the dominant waves, a situation referred to as forced dissipation, represented by the second term  $T_2(f)$  (see Eq. 2-29).

The main purpose of this investigation was to obtain an advanced spectral form for wave spectral dissipation that could be applied to a wide range of air-sea conditions. There were many uncertainties regarding the magnitudes and functional dependencies of parameters  $a$  and  $b$  (Eq. 2-29) for various wind-sea conditions (Young and Babanin, 2006).

These parameters play an important role in determining the spectral levels of the wave dissipation function. Furthermore, the threshold spectrum  $F_T(f)$  requires precise tuning to allow wave model applications. Moreover, the two-phase behaviour of wave spectral dissipation creates additional complexity in terms of tuning the dissipation source term for the wave models. The present investigation addresses as following a list of matters that arose due to their uncertainty from the experimental studies (Babanin and Young, 2005; and Young and Babanin, 2006):

1. Threshold spectrum  $F_T(f)$
2. Coefficient  $a$  for inherent wave breaking
3. Coefficient  $b$  for cumulative or forced wave breaking
4. Behaviour and functional dependences of coefficients  $a$  and  $b$  in different wind-sea conditions
5. Directional spreading of the spectral dissipation function
6. Comparing to the experimental data

All these issues are addressed in Section 4.2.

The present investigation of the new source function was carried out within the physical framework based on the experimental results of Donelan (1998), Banner et al. (2000) and Young and Babanin (2006). A literature review showed that observational studies related to the wave spectral dissipation source term are very few (Donelan, 2001; Phillips, 2001; Melville and Matusov, 2002; Hwang and Wang, 2004 (2); Babanin and Young, 2005;

Young and Babanin, 2006; Gemmrich and Farmer, 2004; Gemmrich, 2005 and Gemmrich, 2006). The results of two independent studies by Melville and Matusov (2002) and Gemmrich (2005) were selected for comparison with the results of the present research.

All computations of the wave dissipation source function (Young and Babanin 2006) were performed for the Combi spectra in a wide range of air-sea conditions. The selection of the Combi spectra was based on the growing number of facts supporting the credibility of this type of wave spectra (see Section 4.1.3, the discussion of the high energy tail). The Combi spectrum is the most general representation of two different types of wave spectra, JONSWAP (Hasselmann et al., 1976) and Donelan (1985), suggested from experimental observations. A similar approach to that used with the wind input source term was used to select the upper frequency of the spectral scale. Taking into account that small-scale waves play an important role in wave processes, the frequency,  $f_{cut} = 10\text{Hz}$ , was selected as an upper limit for the frequency spectral scale.

#### 4.2.1 THRESHOLD SPECTRUM $F_T(f)$

The concept of the threshold spectrum was introduced by Young and Babanin (2006) on the basis of recent experimental observations (Banner et al., 2000 and Babanin et al., 2001) showing that the breaking of waves depends on the excess steepness of the waves above the threshold steepness at a particular spectral scale. The value of the threshold steepness plays a significant role in the determination of the spectral level of the threshold spectrum.

The observed values for the threshold steepness were reported in the range  $\sqrt{B_{nT}(f)} = [0.0223, 0.0254]$  by Babanin and Young (2005) on the basis of wave breaking data from Lake George. According to Young and Babanin (2006) no wave breaking was observed for waves which had less steepness than the threshold steepness. Translating this into the spectral terms, the threshold wave spectrum  $F_T(f)$  represents the state of the sea where no wave breaking occurs. Subsequently, the wave energy dissipation is determined by the magnitude of the spectral exceedance of the wave spectrum over the threshold spectrum,  $\Delta F = F(f) - F_T(f)$ . Hence, the spectral level of the threshold spectrum determines the magnitude of the residual  $\Delta F$ .

The investigation of the threshold spectrum  $F_T(f)$  was carried out using the newly introduced Combi spectra and the saturation transformer  $T(f)$  (analogue to the spectral saturation) previously discussed in Section 4.1. Babanin and Young (2005) highlighted the fact that the old representation of spectral saturation  $B(f)$  (Phillips, 1984) causes significant scattering of

the breaking probability of the observed waves. The scattering is present since the spectral saturation (Phillips, 1984) is the fifth moment of the wave spectrum, which makes it very sensitive to any variation in the spectral shape, particularly in the high frequency range. Furthermore, Babanin and Young (2005) concluded that spectral saturation is not the most suitable parameter for the quantitative dependence of the breaking rates. Young and Babanin (2006) applied azimuthal normalization to the spectral saturation  $B(f)$  by the local angular spreading width  $A(f)$  (Eq. 2-15) of the directional wave spectrum, thus reducing the variations in the high frequency range. In contrast to that, in the present study, the saturation transformer  $T(f)$  (Eq. 4-24) was proposed as a new alternative form for the spectral saturation  $B(f)$  (see Chapter 4, Section 4.1.3, discussion of wave steepness). The form (Eq. 4-24) is less dependent on the variations of spectral shape in deep-water conditions. Therefore, in the present study, computations of the threshold spectrum  $F_T(f)$  were performed using the saturation transformer  $T(f)$  instead of the spectral saturation  $B(f)$ .

The threshold spectrum  $F_T(f)$  was determined using Equation 4-24. Solving Equation 4-24 relative to  $F(f)$  and assigning it as the threshold spectrum  $F_T(f)$ , the following equation emerges:

$$F_T(f) = 2g^2(2\pi)^{-4} f_p^{-(n+5)} f^n T_T(f) \quad (\text{Eq. 4-26})$$

where  $n$  is the exponent of the high frequency spectral tail and  $T_T(f)$  is the threshold saturation transformer. The threshold spectrum  $F_T(f)$  is mainly determined by the value of the threshold saturation transformer  $T_T(f)$ . Therefore, the value of  $T_T(f)$  which is used for the computations of the threshold spectrum is very important.

Babanin and Young (2005) suggested the following range of threshold values  $\sqrt{B_{nT}(f)} = [0.0223, 0.0254]$  for the directionally normalised spectral saturation. To adapt the experimental values for the computation of the threshold spectrum it was necessary to convert the spectral saturation  $B_{nT}(f)$  into the saturation transformer  $T_T(f)$ . Using Equation 4-25, the corresponding values of the saturation transformer are:

$$\sqrt{T_T(f)} = \left(\frac{f_p}{f}\right)^{\frac{n+5}{2}} A^{-\frac{1}{2}}(f) \sqrt{B_{nT}(f)}. \text{ Substituting } T_T(f) \text{ in Equation 4-26 with the given}$$

expression for the saturation transformer, Equation 4-26 for the threshold spectrum becomes:

$$F_T(f) = 2g^2(2\pi)^{-4} f^{-5} A^{-1}(f) B_{nT}(f) \quad (\text{Eq. 4-27})$$

Equation 4-27 shows that the threshold spectrum  $F_T(f)$  is independent of the spectral slope  $n$  of the wave spectrum. The experimental values of Babanin and Young (2005) for directionally normalised spectral saturation were tested in the wave model computations to satisfy the physical framework of the wave breaking processes occurring during wave development.

The determination of the threshold spectrum  $F_T(f)$  can be used to validate the experimental values for directionally normalised spectral saturation because of their correspondence to the observational findings, which can be used as physical constraints for the modelling of wave dissipation. One of the findings of Young and Babanin (2006) indicates that the breaking probability of fully developed dominant waves ( $U_{10} / c_p \sim 0.83$ ) is significantly small. This fact was used as the physical constraint to determine the correct experimental value for the threshold of the spectral saturation,  $B_{nT}(f)$ . In spectral terms, this physical constraint can be introduced as the residual between the values of the wave spectrum and the threshold spectrum at the spectral peak:  $\Delta F_p = F(f_p) - F_T(f_p)$ . To maintain the consistency of the wave observations for fully developed seas (Young and Babanin, 2006), the following condition must be true:

$$\Delta F_p \leq 0 \quad (\text{Eq. 4-28})$$

The condition (Eq. 4-28) was used as the physical constraint to select an appropriate threshold value for the spectral saturation from the experimental data (Young and Babanin, 2006).

In the present study the threshold spectrum  $F_T(f)$  was computed for the Combi spectra of fully developed dominant waves for various wind speeds  $U_{10} = 7\text{m/s}$ ,  $10\text{ m/s}$ ,  $15\text{ m/s}$  and  $20\text{ m/s}$ . The condition represented by Equation 4-28 was verified for the threshold values of the range  $\sqrt{B_{nT}(f)} = [0.0223, 0.0254]$  (Babanin and Young, 2005) for selected wind speeds. The results showed that the value of the residual  $\Delta F_p$  was greater than 0, indicating the breaking of the dominant waves. The corresponding spectral comparison of the wave spectrum against the threshold spectrum showed the values of  $F(f_p)$  exceeded the values of  $F_T(f_p)$ . Since the magnitudes of threshold spectrum  $F_T(f)$  are directly proportional to the spectral saturation  $B_{nT}(f)$  (see Equation 4- 28), the higher possible values for  $\sqrt{B_{nT}(f)}$  were tested to minimise the residual  $\Delta F_p$  and satisfy the physical constraint (Eq. 4-28). At the same time, the threshold values of  $\sqrt{B_{nT}(f)}$  were carefully selected on the basis of the experimental data from Lake George (Babanin and Young, 2005). The main criterion for

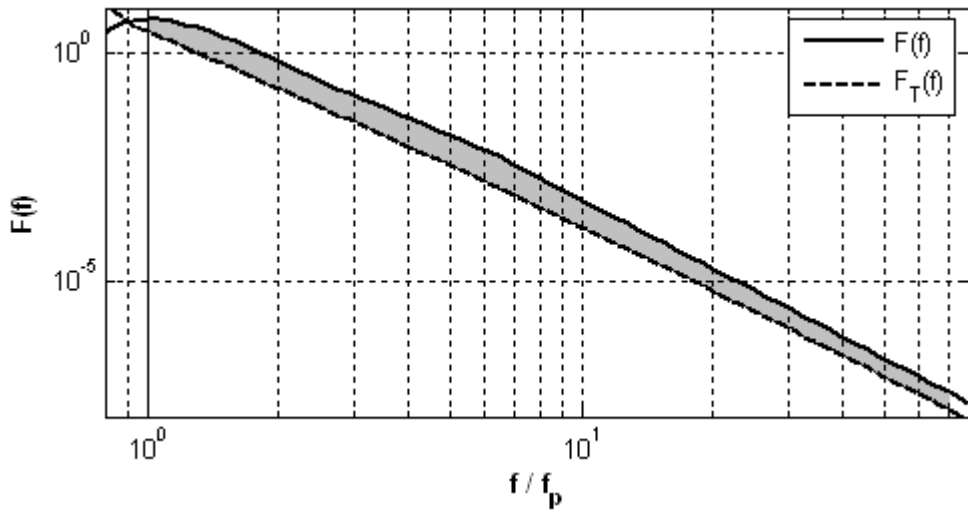
this selection was that the breaking probability must be small enough. After a number of tests, it was determined that the threshold value  $\sqrt{B_{nT}}(f) = 0.035$  was the optimal value when the breaking probability was still small and the residual  $\Delta F_p$  was minimal among the feasible values of  $\sqrt{B_{nT}}(f)$ .

Figure 4.41 shows the relative disposition of the Combi-type energy spectrum of fully developed waves to the threshold spectrum  $F_T(f)$ . The shadowed area of the spectrum relates to the dissipating wave energy. The wave dissipation energy is proportional to the shadowed area of the spectrum above the threshold spectrum  $F_T(f)$ .

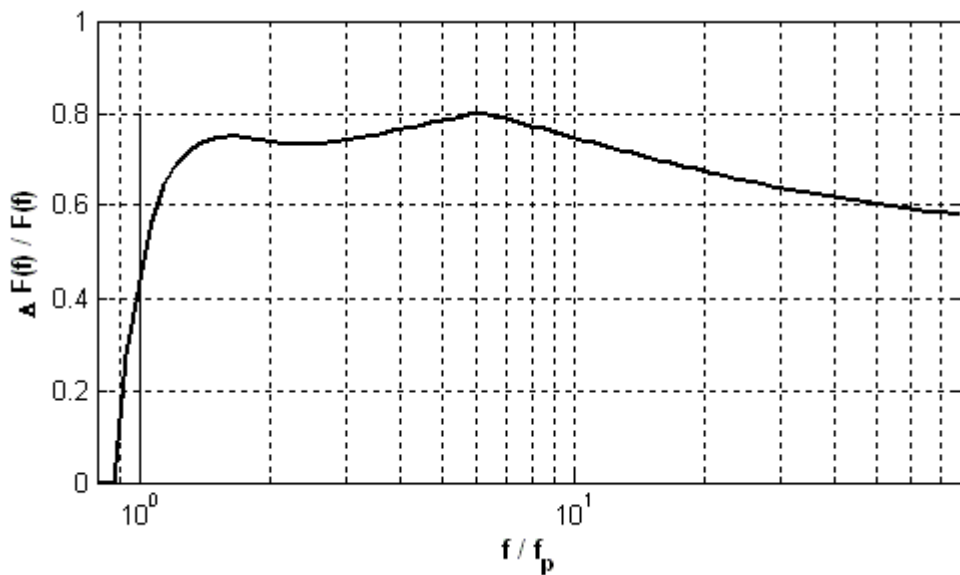
Figure 4.42 shows the ratio of residual  $\Delta F_p$  to the energy density  $F(f)$  for each spectral component. Figure 4.42 demonstrates the distribution of the wave energy dissipation along the frequency scale of the spectrum. Figure 4.412 shows that wave dissipation rates are highest for the intermediate-scale waves. The peak of the graph, for the waves with the relative frequency  $f/f_p \sim 6$ , corresponds to the highest rates of the wave energy dissipation mentioned in the previous paragraph. This fact is in good agreement with the results of existing observational data (Gemrich 2005).

Figure 4.42 shows the non-zero energy loss for the dominant waves ( $f/f_p = 1$ ), an observation that does not correlate well with the experimental findings. However, the choice of the threshold value for the spectral saturation  $\sqrt{B_{nT}}(f) = 0.035$  was firmly based on the experimental data from Lake George (Babanin and Young, 2005). It should be noted that these experimental data were processed for the spectral saturation  $B(f)$  and not for the saturation transformer  $T(f)$  being used for this current study. Furthermore, the scattering of the experimental data can complicate unambiguous identification of the threshold value.

To address the issues that emerged in relation to the breaking of the fully developed dominant waves, a novel approach was developed in the present study. This approach will be discussed further in Section 4.2.2. According to the new approach, the wave spectral dissipation of fully developed dominant waves becomes zero due to specific features developed as part of the present study. Furthermore, in operational wave modelling, the choice of the threshold value  $\sqrt{B_{nT}}(f)$  is a matter of the performance of the spectral dissipation source term in the wave model. This issue will be addressed in Section 4.3.



**Figure 4.41** The threshold spectrum  $F_T(f)$  computed for the Combi spectrum of the fully developed waves ( $f_p = 0.13\text{Hz}$ ) with the inverse wave age  $U_{10} / c_p = 0.83$ , for the wind speed  $U_{10} = 10$  m/s. The shaded area is showing dissipating part of the wave energy spectrum.



**Figure 4.42** Ratio of the dissipating wave energy to the spectral energy density as a function of the relative frequency computed for the spectral saturation threshold value  $\sqrt{B_{nT}(f)} = 0.035$ . The computations were performed for the Combi spectrum of the fully developed waves ( $f_p = 0.13\text{Hz}$ ) with  $U_{10} / c_p = 0.83$  for the wind speed  $U_{10} = 10$  m/s.

### 4.2.2 DETERMINATION OF COEFFICIENTS $a$ AND $b$

The spectral level of the wave dissipation source term is determined by coefficients  $a$  for the inherent wave breaking term and  $b$  for the forced dissipation term (Eq. 2-29). The two-phase behaviour of the wave dissipation source function represented by these two terms (Eq. 2-29) creates additional complexity when trying to determine the correct levels of dissipating wave energy because of the need to ascertain the relative contribution of each of these terms. On the other hand, the magnitudes of coefficients  $a$  and  $b$  should be consistent with the experimental estimation given by Young and Babanin (2006). According to those researchers, the enforced-linear-fit estimation of the single record of the dominant waves ( $U_{10} / c_p = 6.6$ ) shows that  $a_{exp} \approx 0.0065$ . However, coefficients  $a$  and  $b$  are not necessarily constant and may vary according to environmental conditions.

Preliminary computations of the spectral dissipation function (Eq. 2-3-10) were performed for the Combi spectrum of the average-developed waves ( $U_{10} / c_p = 2.7$ ) for the wind speed  $U_{10} = 10$  m/s. Both coefficients  $a$  and  $b$  were assumed to be  $a = b = 0.0065$ . The threshold value for the threshold spectrum was  $\sqrt{B_{nr}(f)} = 0.035$ . The results of these computations are presented in Figure 4.43. The spectra of the inherent breaking term  $T_1(f)$  and the forced dissipation term  $T_2(f)$  are also shown. The spectral shape of the wave dissipation source function is the result of the linear superposition of these two terms  $T_1(f)$  and  $T_2(f)$  (Eq. 2-29). As illustrated in Figure 4.43, long-scale waves up to the size of dominant waves do not experience forced dissipation under the influence of the longer waves and for waves this size  $T_2(f) = 0$ . The contribution of the forced dissipation into the total energy of the wave dissipation increases towards the higher frequencies and reaches a constant magnitude. This transition is present due to the integral of the forced dissipation term  $T_2(f)$  (see Equation 2-29).

Figure 4.43 shows that short waves mostly experience forced dissipation under the influence of longer waves. Coefficients  $a$  and  $b$  determine the spectral level of the wave dissipation source term, as well as the relative contributions of the two different types of wave breaking. Therefore, to achieve the correct level of wave dissipation energy in the wave model, it is necessary to determine the correct values for these coefficients. The investigation of coefficients  $a$  and  $b$  is outlined in this section of Chapter 4.

To address the issues outlined above, it is necessary to estimate the amount of wave energy dissipating during wave development. A novel approach was proposed in the present

research to achieve this estimation. This method of determining wave energy dissipation was based on the fact that wave breaking relates directly to wind energy input into the waves. Hasselmann et al., (1973) using the JONSWAP data as a base, found that 95% of the momentum delivered from wind to waves is transferred locally to underlying currents. On the basis of wave observations, Donelan et al. (1998) reported that from the total momentum transferred from the wind to the waves, the larger fraction is transferred to the underlying water mass either through the viscous drag or through the dissipation of the amplified waves. This fraction was estimated as more than 90% and increases to 100% as the waves approach the full development stage. All these facts support the idea of the dependence of the wave dissipation source function on the wind input source term.

There is no information that tells us about the relationship between the energy transfer from the wind to the waves and the wave dissipation energy along the frequency scale. Measuring the relationship is complicated by the presence of the wave-wave nonlinear interaction source term  $S_{nl}$ . However, even in this case, a solution can be found for the regions of the wave spectrum where the nonlinear term  $S_{nl}$  is negligibly small relative to the wind input source term  $S_{in}$  and the wave dissipation term  $S_{ds}$ . Donelan (2001) showed that for young dominant waves the spectral magnitudes of the nonlinear source term  $S_{nl}$  are close to zero and can be ignored.

On the other hand, the relationship between these two source terms can be defined in terms of the total energy delivered from the wind to the waves and the total energy dissipated in the spectral range of the waves. Since the wave-wave nonlinear interaction source term is conservative in terms of the redistribution of energy between the waves, the contribution of this term into the total energy balance can be ignored. In spectral terms, it means that the integral of the wave dissipation source term along the considered spectral range  $D = \int S_{ds}(f)df$  relates to the integral of the wind input source term  $W = \int S_{in}(f)df$ . Thus, the dissipation energy  $D$  can be determined from the total energy  $W$  transferred from the wind to the waves. However, to achieve this, it is necessary to know the functional relationship between the two integrals  $W$  and  $D$ .

In the present study, the functional relationship between  $W$  and  $D$  was determined on the basis of the existing experimental data observed by Donelan (1998). Figure 4.44 is a replot of Figure 6 from Donelan (1998). Donelan demonstrated the fraction of momentum retained by the waves and the fraction of energy that is delivered to the currents during wave development in the range of the wind forcing conditions  $U_{10} / c_p = [0.83, 4.5]$ .

In other words, this data shows the relationship between the wave dissipation energy and the energy transferred from the wind to the waves. Hence, the dissipating fraction of the energy transferred from the wind to the waves can be described by the ratio:  $D/W$ . Therefore, a new parameter, the *dissipation rate*,  $R$ , was introduced as the ratio between the wave dissipation energy and the energy transferred from the wind to the waves:

$$R = \frac{\int S_{ds}(f)df}{\int S_{in}(f)df} \quad (\text{Eq. 4-29})$$

According to Donelan (1998), the dissipation rate takes values in the range  $R \sim [0.95, 1]$ . For fully developed waves ( $U_{10}/c_p = 0.83$ ), the dissipation rate is  $R = 1$ . According to Donelan's (1998) data, the dissipation rate  $R$  is a function of the inverse wave age  $U_{10}/c_p$ . In the present study, the experimental data obtained by Donelan (1998) was quantified and parameterised as a linear approximation function of the inverse wave age  $U_{10}/c_p$ .

According to this parameterisation the dissipation rate  $R$  is:

$$R_{linear} = \begin{cases} -0.12 U_{10}/c_p + 1.52, & 4.5 < U_{10}/c_p \leq 5.8 \\ 0.0031 U_{10}/c_p + 0.96, & 1.5 < U_{10}/c_p \leq 4.5 \\ -0.052 U_{10}/c_p + 1.043, & 0.83 < U_{10}/c_p \leq 1.5 \\ 1, & U_{10}/c_p = 0.83 \end{cases} \quad (\text{Eq. 4-30})$$

As noted previously, the upper limit for the wind forcing conditions  $U_{10}/c_p$  from Donelan's (1998) data was  $U_{10}/c_p = 4.5$ . The parameterisation (Eq. 4-30) includes the range of very young dominant waves  $U_{10}/c_p = [4.5, 5.8]$ . For this range of wind forcing conditions,

the dissipation rate  $R$  was determined on the basis of the significant level of consistency between the model results for the variance of the energy density spectra and the experimental data of Babanin and Soloviev (1998).

On the basis of the model computations, it was found that for very young waves the dissipation rates are small compared to the dissipation rates for mature waves. For very young waves with  $U_{10}/c_p = 5.8$ , the dissipation rate takes the value  $R_{linear} = 0.82$ . This topic will be discussed later in Section 4.3.

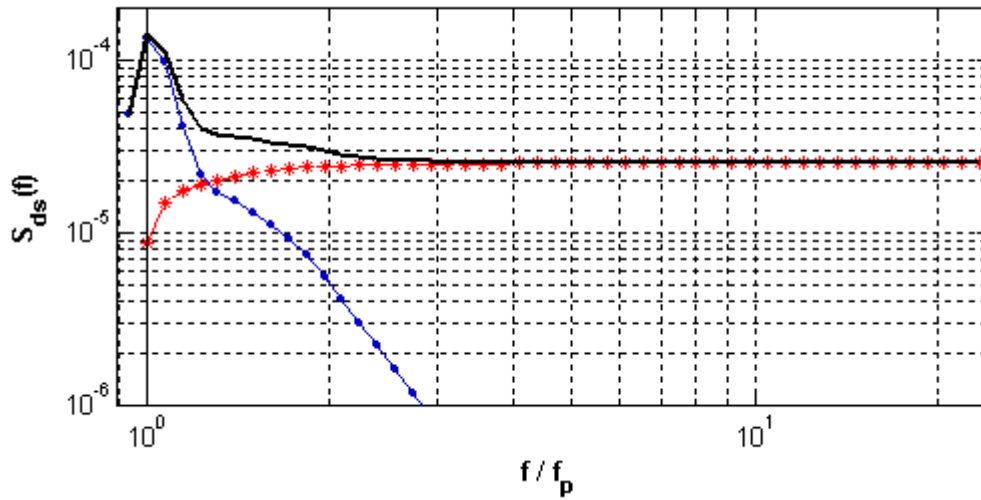


**Figure 4.43** The spectral dissipation function  $S_{ds}(f)$  (Eq. 2-29) (bold line) with the two terms  $T_1(f)$  (line with dots) and  $T_2(f)$  (line with asterisks) with coefficients  $a = b = 0.0065$ . The computations were performed for the Combi spectrum of the average-developed waves ( $f_p = 0.13\text{Hz}$ ) with  $U_{10}/c_p = 0.27$  for the wind speed  $U_{10} = 10\text{ m/s}$ .

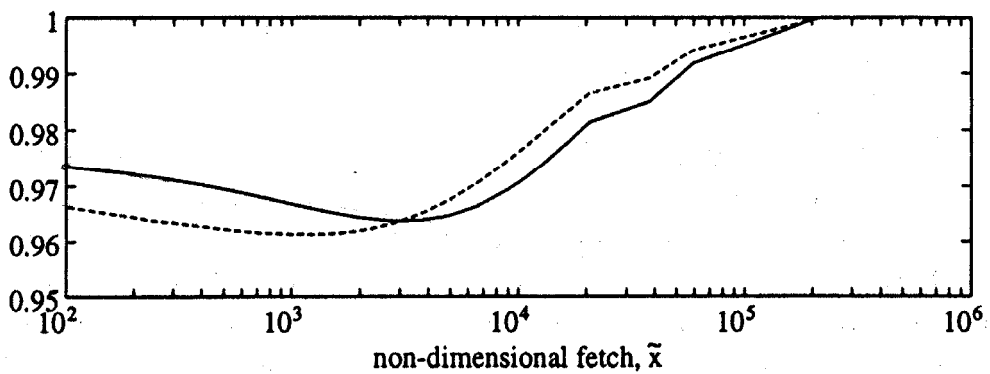


**Figure 4.44** Figure 6 from Donelan (1998) showing the fraction of momentum (dashed line) and of energy (plain line) from the wind is delivered to the surface waters.

The shown parameterisation form (Eq. 4-30) of the dissipation rate  $R$  is not a monotonic and smooth function. Application of this function in operational wave modelling is fraught with the numerical instabilities of some wave models. Therefore, for convenience in wave modelling, an alternative smoothed parameterisation form for the dissipation rate  $R$  was developed in this study:

$$R_{smooth} = \begin{cases} 0.97 - 0.07 \times (1 + \tanh[3(U_{10}/c_p - 5.2)]), & 2 < U_{10}/c_p \leq 5.8 \\ 0.97 + 0.015 \times (1 - \tanh[5(U_{10}/c_p - 1.1)]), & 0.9 < U_{10}/c_p \leq 2 \\ 1, & 0.83 \leq U_{10}/c_p \leq 0.9 \end{cases} \quad (\text{Eq. 4-31})$$

For the range  $2 < U_{10} / c_p < 5.8$ , the numerical parameters in Equation 4-31 can vary depending on the type of wave model. These parameters need to be tuned to achieve consistency between the results of the model computations and the observed data of wave growth (e.g. Babanin and Soloviev, 1998).

Figure 4.45 shows the dissipation rate  $R$  as a function of the inverse wave age  $U_{10} / c_p$  represented by different parameterisation forms as  $R_{linear}$  (plain line) and  $R_{smooth}$  (bold line) given by Equation 4- 30 and Equation 4-31, respectively. The dissipation rate  $R$  was defined on the basis of the existing observational data (Donelan, 1998) and has a strong physical background. As it can be observed in Figure 4.45, there were three distinct ranges of values for the dissipation rate during wave development. For very young and well-developed waves ( $U_{10} / c_p > 4.5$  and  $U_{10} / c_p < 1.5$ , respectively) the dissipation rate increases. However, for the range of the wind forcing conditions  $U_{10} / c_p = [1.5, 4.5]$ , the dissipation rate  $R_{linear}$  slightly decreases during wave development. The smooth approximation is constant  $R_{smooth} = 0.97$  for this range of wind forcing conditions.

Using Equation 4-29, the wave dissipation energy can be determined as follows:

$$\int S_{ds}(f)df = R \int S_{in}(f)df \quad (\text{Eq. 4-32})$$

Therefore, the right part of Equation 4-32 represents the physical constraint for the computations of the wave dissipation function. This physical constraint ensures that the total amount of energy dissipation corresponds to the energy transferred from the wind to the waves.

According to the defined physical constraint (Eq. 4-32), computations of the wave dissipation source term include the results of the computations of the corresponding wind input source term discussed in Section 4.1. Thus, the computations of the wave dissipation

source term, like the computations of the wind input source function, must be performed in the entire range of the spectral components. As it was mentioned in Section 4.1.1, the small-scale spectral components play a significant role in wave development processes. Therefore, the computations for the wave dissipation source term were performed in the spectral range up to  $f_{cut} = 10$  Hz in much the same way as the wind input computations described in Section 4.1.

As mentioned earlier, the two-phase behaviour of the wave dissipation source term creates additional complexity when estimating coefficients  $a$  and  $b$ . Prior to beginning the determination of these coefficients, it was reasonable to introduce temporary notations for these coefficients to differentiate their temporal operational forms from the final forms for Equation 2-29. Therefore, coefficients  $a$  and  $b$  were identified temporarily as  $a_0$  and  $b_0$ , respectively.

Before going on to determine coefficients  $a$  and  $b$ , the following notations were introduced to avoid the cumbersome mathematical expressions:

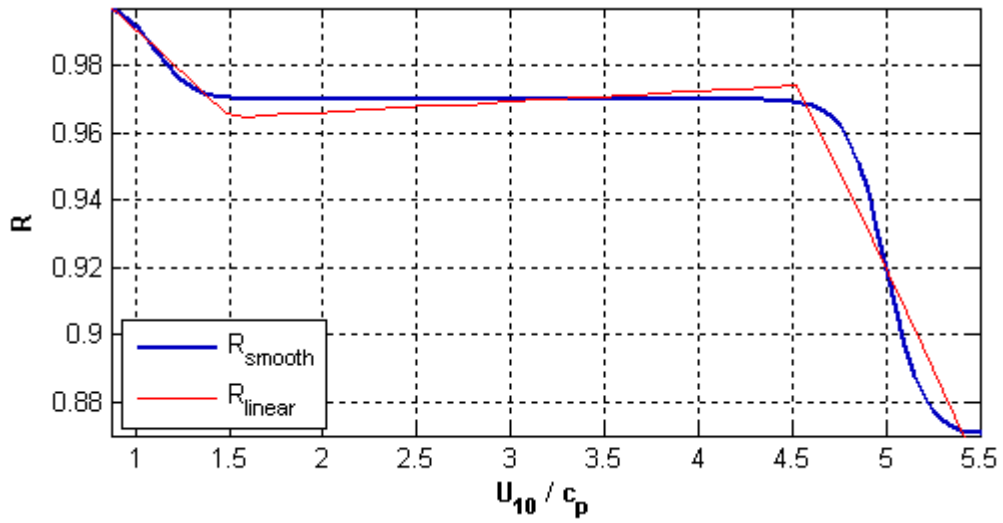
$$\begin{aligned}
 W &= \int S_{in}(f)df, W_1 = \int_{f_{min}}^{f_p} S_{in}(f)df, W_2 = \int_{f_p}^{f_{cut}} S_{in}(f)df \\
 D &= \int S_{ds}(f)df, S_1 = \int T_1(f)df, S_2 = \int T_2(f)df \quad (\text{Eq. 4-33}) \\
 S_{11} &= \int_{f_{min}}^{f_p} T_1(f)df, S_{12} = \int_{f_p}^{f_{cut}} T_1(f)df
 \end{aligned}$$

Figure 4.46 shows the schematic illustration of the above-mentioned notations introduced in Equation 4-33.

Knowledge of the total energy of the wave dissipation gleaned from Equation 4-32 does not provide a straightforward answer for these coefficients primarily due to the concurrent presence of the two terms. The solution lies in a distinct feature of the wave dissipation source function, which is the fact that the dissipation of waves longer than dominant waves is represented only by the inherent breaking term  $T_1(f)$  (i.e.  $T_2(f) = 0$ ) (refer to Figure 4.43).

Thus, for the waves in the spectral range  $f < f_p$ , the wave dissipation source term can be represented in the form:

$$S_{ds}(f) = a_0 \cdot T_1(f) \quad (\text{Eq. 4-34})$$



**Figure 4.45** Two parameterisation forms of the dissipation rate:  $R_{linear}$  (Eq. 4-30) and  $R_{smooth}$  (Eq. 4-31). The computations were performed for the Combi spectra at the different stages of the wave development for the wind speed  $U_{10} = 10$  m/s.

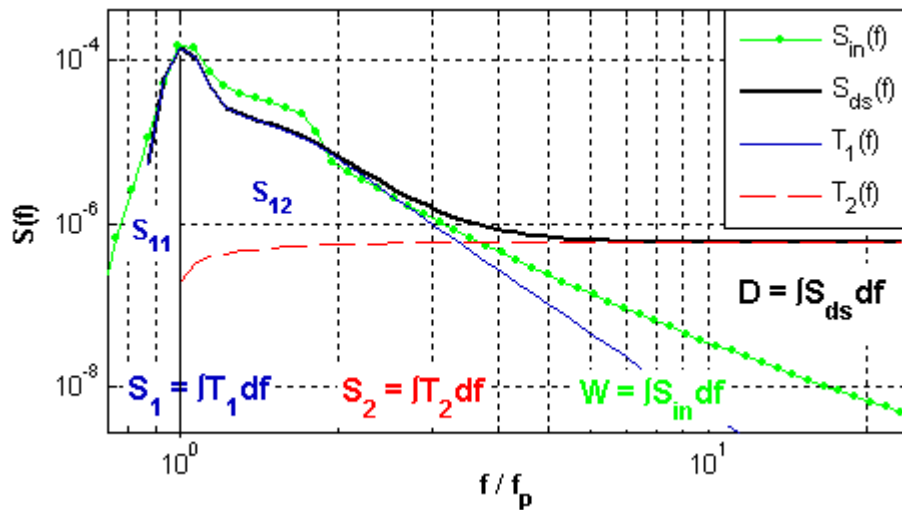


**Figure 4.46** Schematic illustration of the notations (4-33) for the computations of coefficients  $a$  and  $b$  of the spectral dissipation function  $S_{ds}(f)$  (bold line) with its two phase terms  $T_1(f)$  (dashed line) and  $T_2(f)$  (solid line). The wind input source function  $S_{in}(f)$  (line with dots) is also shown.

Subsequently, substituting the wave dissipation source term under the integral in Equation 4-32 by the expression from Equation 4-34, we have:

$$\int_{f_{\min}}^{f_p} a_0 \cdot T_1(f) df = R \int_{f_{\min}}^{f_p} S_{in}(f) df \quad (\text{Eq. 4-35})$$

where the integration was performed in the range of frequencies  $[f_{\min}, f_p]$ .

It should be noted that Equation 4-32 is true when integration includes the entire spectrum of waves. For a discrete spectral component, the energy fluxes due to the wave-wave nonlinear interactions must be considered. On the other hand, for young waves the spectral magnitudes of the wind input source term are significantly larger than the magnitudes of the nonlinear interaction source term, particularly at the spectral peak (Donelan 2001). Figure 4.47 compares the integral values of the wind input source term and the wave-wave nonlinear interaction source term in the spectral range of long waves  $[f_{\min}, f_p]$ . The computations were performed for the wind speed  $U_{10} = 10$  m/s.

According to Figure 4.47, for young waves ( $U_{10} / c_p > 4.5$ ) the difference between the integral values is in the order of magnitude of 2. Therefore, for young waves, the energy fluxes due to the wave-wave nonlinear interactions can be disregarded when compared to the energy exchange between the wind and the waves. Equation 4-35 is true for young waves, therefore. Thus, coefficient  $a_0$  may be assessed from Equation 4-35 and verified as consistent with the experimental findings of Young and Babanin (2006).

To determine coefficient  $a_0$ , it was assumed that coefficient  $a_0$  is constant for the entire range of spectral components and has no functional dependence on the spectral frequency. Hence, coefficient  $a_0$  can be taken out of the integral sign in the left part of Equation 4-35. Solving Equation 4-35 for coefficient  $a_0$  using the notations from Equation 4-33 looks like:

$$a_0 = \frac{RW_1}{S_{11}} = \frac{R \int_{f_{\min}}^{f_p} S_{in}(f) df}{\int_{f_{\min}}^{f_p} f \cdot A(f) \cdot (F(f) - F_T(f)) df} \quad (\text{Eq. 4-36})$$

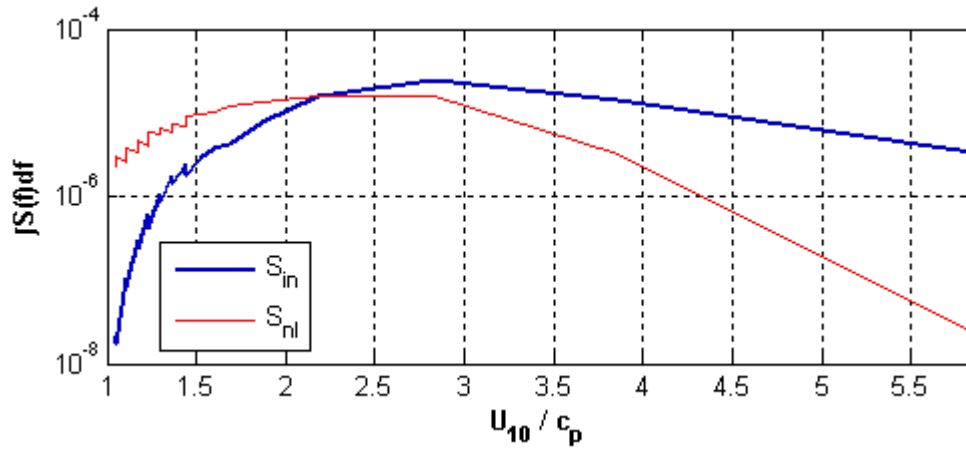


**Figure 4.47** Comparison of integral values of the wind input source function  $S_{in}(f)$  (bold line) with the wave-wave nonlinear interaction source term  $S_{nl}(f)$  (plain line) for long-scale spectral components. Integration was performed in the range  $[f_{min}, f_p]$ .

On the right hand side of Equation 4-36 all parameters are known to determine coefficient  $a_0$ . Furthermore, most of these parameters are dependent on the wind forcing conditions  $U_{10} / c_p$ . Subsequently, coefficient  $a_0$  is a function of the wind forcing conditions and changes its values during the wave development.

According to Equation 4-36, coefficient  $a_0$  has values in the spectral range where the spectral residual  $(F(f) - F_T(f))$  is a positive number. Otherwise, for  $(F(f) - F_T(f)) \leq 0$ , no wave breaking is occurring and coefficient  $a_0$  is assumed to be zero. Thus, coefficient  $a_0$  is always positive when wave breaking is occurring. As waves come close to their full development stage, wind transfers energy to the short scale waves and the integral in the numerator from Equation 4-36 becomes zero. Therefore, for mature waves ( $U_{10} / c_p \leq 1$ ), coefficient  $a_0 = 0$ . This implies that without wind energy input, dominant waves are not prone to breaking in deep-water conditions. This feature is completely consistent with the existing observational data. At this stage the dominant waves continue to develop due to the nonlinear energy transfer from the short scale waves to the longer waves known as the effect of the direct cascade (Pushkarev et al., 2002).

Subsequently, in this case, the wave dissipation source function is represented only by the forced dissipation term  $T_2(f)$  in the high frequency range of the wave spectrum. At this stage of wave development, short scale waves modulated by longer waves are experiencing increased breaking intensity due to the straining action of the longer waves (Donelan 2001). The average steepness of modulated short waves exceeds the threshold steepness, resulting in the breaking of the waves. Thus, for mature dominant waves the energy dissipation is mainly occurring in the high frequency domain of the wave spectrum.

Once one of coefficients was known, the task to determine the other coefficient became simpler. As with coefficient  $a_0$ , coefficient  $b_0$  was assumed scale independent. Integrating the new parameterisation form for the wave dissipation source term (Eq. 2-29) and combining with the physical constraint (Eq. 4-32), the following system of equations took place:

$$\begin{cases} D = RW \\ D = a_0 S_1 + b_0 S_2 \end{cases} \quad (\text{Eq. 4-37})$$

Solving this system regarding coefficient  $b_0$ , we have:

$$b_0 = \frac{RW - a_0 S_1}{S_2} \quad (\text{Eq. 4-38})$$

Using Equation 4-36 coefficient  $b_0$  proved to be a function of the inverse wave age  $U_{10}/c_p$  since the all parameters on the right hand sides of these equations are dependent on the inverse wave age.

Figure 4.48 shows coefficients  $a_0$  (Eq. 4-36) and  $b_0$  (Eq. 4-38) as functions of the wind forcing parameter  $U_{10}/c_p$ . The magnitudes of these coefficients are compared with the experimental value  $a_{exp} = 0.0065$  suggested by Young and Babanin (2006). As shown, the magnitudes of coefficients decrease with wave development. This trend indicates a reduction of the wave dissipation energy of the dominant waves as they develop.

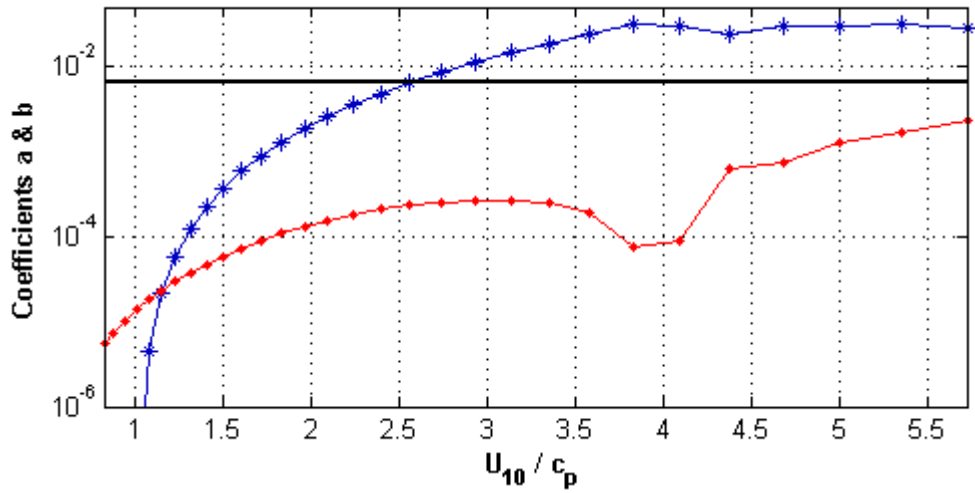
Figure 4.48 shows that coefficients  $a_0$  and  $b_0$  differ in order of magnitude for young and average-developed waves ( $U_{10}/c_p > 2$ ). However, this difference reduces with wave development until the wind forcing parameter becomes  $U_{10}/c_p \sim 1.2$ . At this stage coefficients are equal  $a_0 = b_0$ . Afterwards, coefficient  $a_0$  rapidly decreases towards zero and coefficient  $b_0$  gradually reduces its values compared to coefficient  $a_0$ . As was discussed earlier this trend shows a shift of the dissipation rates into the high frequency domain according to Donelan (2001).

Figure 4.48 demonstrates the domination of one of the two terms of the spectral dissipation source function (Eq. 2-29) over the other at different stages of wave development: from young waves to the fully developed. It shows that for young and average-developed waves, inherent wave breaking dominates forced dissipation. However, as the dominant waves approach their full development stage, the inherent breaking tends to vanish (coefficient  $a_0$  declines to zero) and the spectral dissipation function is mainly represented by the forced dissipation term  $T_2(f)$  of the short scale waves. The latter result is consistent with the existing observational data (Donelan, 2001).

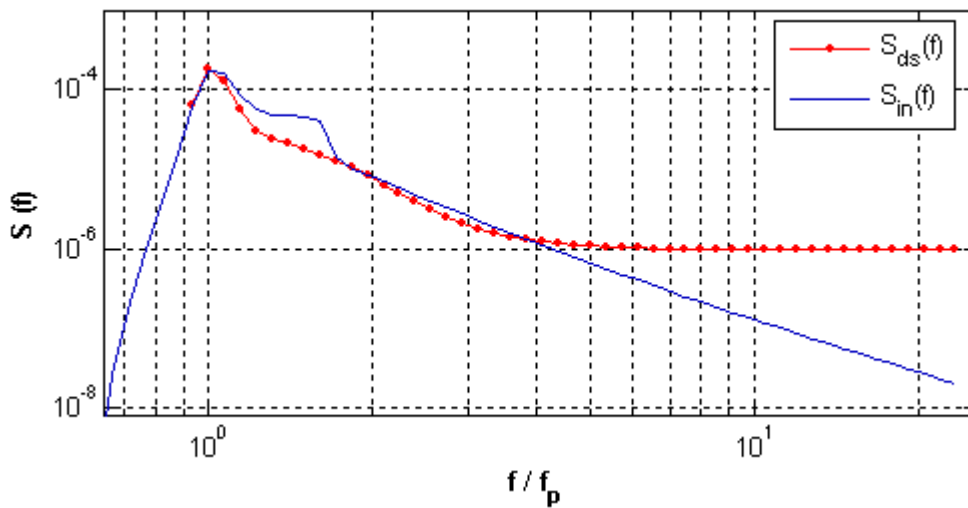
Figure 4.48 shows encouraging agreement between the computed coefficient  $a_0$  (Eq. 4-36) and the experimental value  $a_{exp}$  for the average-developed waves with the wind forcing  $U_{10} / c_p \sim 2.6$ . As shown, coefficient  $b_0$  is less than  $a_{exp}$  during all the time of wave development. The closest value of coefficient  $b_0$  to the experimental value  $a_{exp}$  was obtained only for very young waves with  $U_{10} / c_p \sim 5.8$ .

Figure 4.49 shows the resultant dissipation source function  $S_{ds}(f)$  (Eq. 2-29) with coefficients  $a_0$  (Eq. 4-36) and  $b_0$  (Eq. 4-38) computed for the Combi spectrum of the average-developed waves  $U_{10} / c_p = 2.7$  under the wind speed  $U_{10} = 10$  m/s. The figure shows the wave dissipation spectrum together with the corresponding wind energy input spectrum  $S_{in}(f)$  computed for the same wind forcing conditions. Although, according to the physical constraint (Eq. 4-32), the total dissipation energy is consistent with the wind energy input across the entire range of the spectral components. However, in the local spectral scale this consistency is not retained.

The wind energy input prevails for the dissipation of waves with the frequencies  $f_p < f < 2 f_p$ . For short scale waves ( $f > 4 f_p$ ), there is significant exceedance of wave dissipation spectral magnitudes over the wind energy input spectral levels. Furthermore, it should be noted that the shown spectra are integrated over the directional space. Therefore, taking into account the peculiarities of the directional distribution of these spectra, there is no direct answer regarding the spectral levels of the shown spectra. To the best of my knowledge, there has been no experimental evidence obtained regarding the relative spectral levels of the wind input and the wave dissipation source terms in the high frequency range of the wave spectrum. The credibility of such a spectral tail for the dissipation source term, as shown in Figure 4.49, was assessed by the performance of this spectral dissipation source function in the wave model. This topic will be discussed further in Section 4.3.



**Figure 4.48** Coefficients  $a_0$  (Eq. 4-36) (line with asterisks) and  $b_0$  (Eq. 4-38) (line with dots) as the functions of the wind forcing parameter  $U_{10} / c_p$  computed for the Combi spectra at the different stages of the wave development for the wind speed  $U_{10} = 10$  m/s. The experimental coefficient  $a_{exp} = 0.0065$  (bold line) is shown.



**Figure 4.49** The spectral dissipation function  $S_{ds}(f)$  (line with dots) with coefficients  $a_0$  (Eq. 4-36) and  $b_0$  (Eq. 4-38). The corresponding wind input source functions  $S_{in}(f)$  (plain line) is also shown. Computations were performed for the Combi spectrum of the average-developed waves with wind forcing  $U_{10} / c_p = 2.7$  for the wind speed  $U_{10} = 10$  m/s.

However, the exceedance of the wave dissipation spectral magnitudes over the wind energy input and nonlinear source terms may contradict the present understanding of the wind-wave coupling theory. As was mentioned in Section 2.3.2, in the discussion on wind-wave coupling, most of the energy fluxes from the wind to the waves occurred at the high frequency range of the wave spectrum in the main direction of wave propagation. The short scale waves in this range of the wave spectrum cannot maintain their growth. Furthermore, the so called direct cascade (Pushkarev et al., 2002) representing the energy transfer from the short waves to the long waves due to the nonlinear interactions between the waves, may not exist when the significant wave energy dissipates in the high frequency range of the wave spectrum.

In this case, due to the nonlinear interactions between the waves, the energy will be transferred from the longer waves to the short waves and the peak frequency will move towards the high frequencies during wave development, which totally contradicts the existing observational data (Hasselmann, 1973). On the other hand, the remarkable loss of the wave energy in the high frequency range is fraught with model instabilities. All the emerged issues, due to the enormous dissipation of wave energy in the high frequency spectral range, puts into doubt the credibility of such a dissipation spectral shape as that shown in Figure 4.49. Therefore, it may be necessary to apply a correction of the high frequency spectral tail for the dissipation source function.

As was shown in Figure 4.43, wave dissipation for the short scale waves is represented mostly by the forced dissipation term  $T_2(f)$ . Since the forced dissipation term is represented

in the integral form  $\int_{f_p}^{f_{cut}} A(f) \cdot (F(f) - F_T(f)) df$ , the spectral shape of the wave dissipation

function exhibits a distinct transition from the decreasing exponential curve to the flat spectral tail (see Figure 4.43). In its turn, this flat spectral tail remarkably exceeds the spectral magnitudes of the wave spectrum. This contrast raises questions about whether coefficient  $b_0$  is scale independent. It is more likely that coefficient  $b_0$  requires correction to maintain the spectral magnitudes of wave dissipation  $S_{ds}(f)$  in reasonable proximity to the spectral magnitudes of the wind input spectrum  $S_{in}(f)$  within the limits of the physical framework.

To find an alternative form for coefficient  $b$ , it was decided to apply to coefficient  $b_0$  an exponential function of the spectral frequency  $Z(f)$ . Furthermore, within the limits of the

physical framework, this functional dependence was required to meet the following specific requirements:

1. The function  $Z(f)$  is dimensionless
2. The magnitudes of the wave dissipation source function are in reasonable proximity to the magnitudes of the wind energy input and nonlinear source terms,  $S_{ds}(f) \sim S_{in}(f) + S_{nl}(f)$ .

After a series of attempts, the best suitable function was found to be the following form:

$$Z(f) = \left( \frac{f}{f_p} \right)^\mu \quad (\text{Eq. 4-39})$$

where  $\mu$  is the exponent of the high frequency spectral tail of the wind energy input source term  $S_{in}(f)$ . According to Equation 4-39, the exponential function  $Z(f)$  is the decreasing function, having a similar slope to the wind input source term  $S_{in}(f)$  in the high frequency spectral range. The resulting coefficient for the forced dissipation term  $T_2(f)$  can be presented as follows:

$$b = b_0 \cdot Z(f) \quad (\text{Eq. 4-40})$$

The functional dependence of coefficient  $b(U_{10}/c_p, f)$  on the spectral frequency strengthens the dependence of the wave dissipation on the wind energy input. The impact of wind energy transfer on wave dissipation is reflected not only in terms of total energy by the integration over the spectral range, but in terms of the spectral magnitudes of both functions. By applying the corrected coefficient  $b(U_{10}/c_p, f)$  to the forced dissipation term  $T_2(f)$ , the high frequency spectral tail of the wave dissipation source term adjusts to the wind input source function. As a result of this application, the magnitudes of coefficient  $b_0$ , shown in Figure 4.48, are changed. This alteration is determined by the fact that in the computation of coefficient  $b_0$  (Eq. 4-38) the value of the integral in the denominator (see Equation 4-38) is changed. Now instead of the integral  $S_2 = \int T_2(f)df$  in the denominator, it is  $S_{02} = \int Z(f)T_2(f)df$  due to the correcting function  $Z(f)$  retained under the sign of the integral. Therefore coefficient  $b_0$  (Eq. 4-38) is modified into the form:

$$b = \frac{RW - a_0 S_1}{S_{02}} \quad (\text{Eq. 4-41})$$

As the correcting function  $Z(f)$  (Eq. 4-39) is a decreasing exponential function along the frequency scale, the integral  $S_{02}$  is less than integral  $S_2$ . Since the integral  $S_{02} < S_2$ , the resulting magnitudes for coefficient  $b$  (Eq. 4-41) are expected to be larger than those shown in Figure 4.48.

Figure 4.50 shows the magnitudes of coefficient  $b$  (Eq. 4-41) computed at different stages of wave development. The magnitudes of coefficient  $a_0$  (line with asterisks) and  $b_0$  (dashed line) are also shown for comparison. The values of these coefficients are shown relative to the experimental value  $a_{exp} = 0.0065$  (bold line) suggested by Young and Babanin (2006).

Obviously, the magnitudes of coefficient  $a_0$  are not changed as the correction was applied in the high frequency range. Figure 4.50 shows that the magnitudes of coefficient  $b$  (Eq. 4-41) are remarkably larger than the magnitudes of coefficient  $b_0$  (Eq. 4-38). Moreover, for young waves ( $U_{10} / c_p = 4.3$ ) and average-developed waves in the range of the wind forcing  $U_{10} / c_p = [2.4, 2.7]$ , coefficient  $b$  is consistent with the experimental value  $a_{exp}$ .

Figure 4.50 shows that the magnitudes of coefficient  $b$  are close to coefficient  $a_0$ , particularly for very young waves with  $U_{10} / c_p = 5.7$  and average-developed waves ( $U_{10} / c_p = [2.4, 2.7]$ ). Figure 4.50 demonstrates a distinct agreement between the results of the computations for coefficients  $a_0$  and  $b$  and the value  $a_{exp}$  suggested by Young and Babanin (2006).

As it was mentioned earlier, for fully developed waves coefficient  $a_0 = 0$ . Therefore, considering Equation 4-41 for fully developed waves, coefficient  $b$  becomes the following form:

$$b = \frac{RW}{S_{02}} \quad (\text{Eq. 4-42})$$

Another distinct feature of coefficient  $b$  is the difference  $(RW - a_0 S_1)$  in the numerator from Equation 4-41. The question as to whether this difference becomes a negative number has been addressed in the present study.

To investigate the behaviour of the difference  $(RW - a_0 S_1)$ , coefficients  $a_0$  and  $b$  were computed for different types of wave spectra (JONSWAP, Donelan (1985) and Combi) at different stages of wave development and for different wind speeds  $U_{10} = \{7\text{m/s}, 10\text{m/s}, 15\text{m/s and } 20\text{m/s and } 30\text{m/s}\}$ .

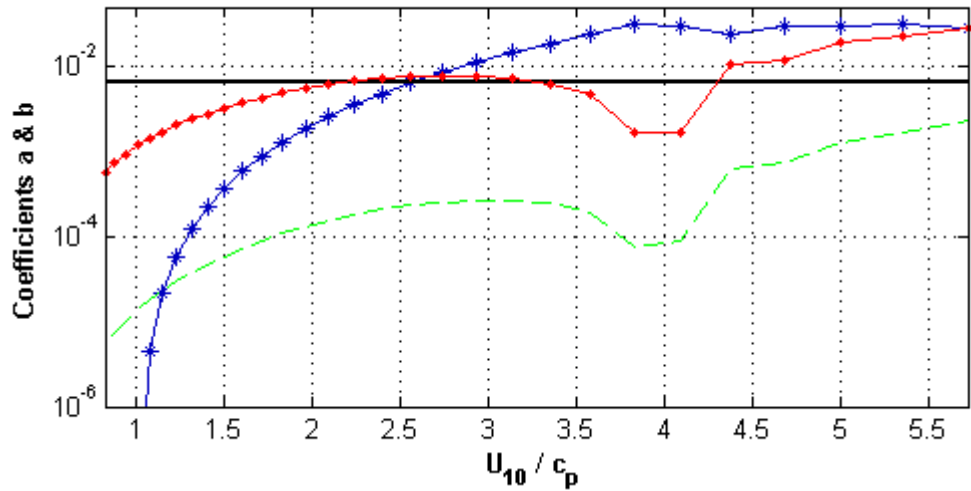


**Figure 4.50** Coefficients  $a_0$  (Eq. 4-36) (line with asterisks) and  $b_0$  before (Eq. 4-38) (dashed line) and after the correction in the high frequency spectral tail (Eq. 4-41) (line with dots) of the wave dissipation source term computed for the Combi spectra at different stages of the wave development for the wind speed  $U_{10} = 10$  m/s. The experimental coefficient  $a_{exp} = 0.0065$  (bold line) is also shown.

Figure 4.51 (a, b and c) shows the results of these computations, where subplot (a) shows the results of the computations for the JONSWAP spectra, subplot (b) shows the results for the Donelan (1985) spectra and subplot c shows the results for the Combi spectra for the above mentioned wind speeds.

Figure 4.51 demonstrates wind dependent behaviour for coefficient  $b$  in contrast to coefficient  $a_0$ , which is almost the same in all subplots. The dependence of coefficient  $b$  on the wind speed  $U_{10}$  is particularly high for young waves. As the waves approach their full development stage, this dependence becomes negligible, a situation clearly pronounced for the Donelan (1985) spectra (see subplot [b]).

As shown in Figure 4.51, coefficient  $b$  appears as a negative number for the light winds over the young waves, when the viscous drag is significantly high. Furthermore, the values of coefficient  $b$  computed for the Donelan (1985) spectra (see the subplot [b]) are remarkably lower than those are shown for the JONSWAP and Combi spectra.

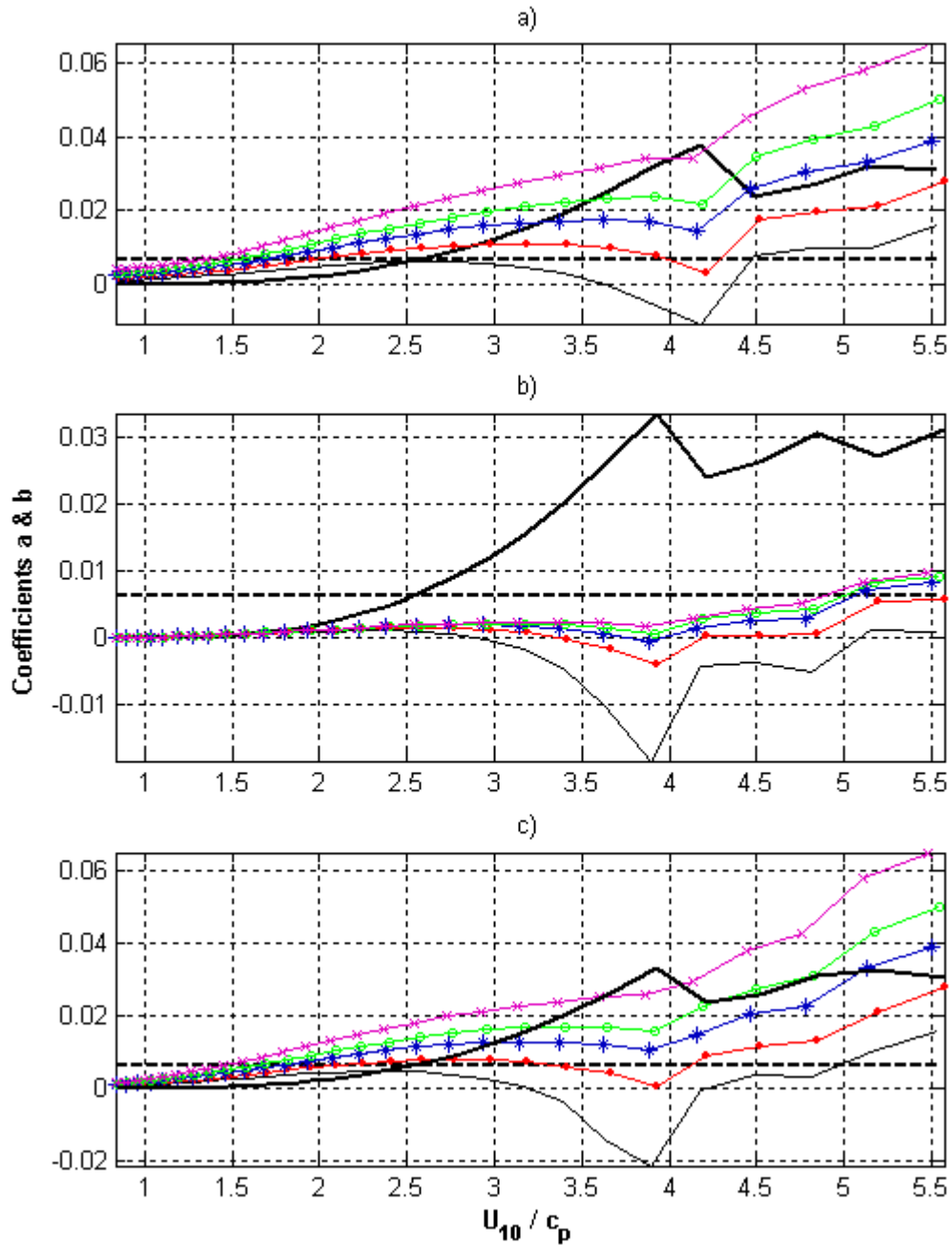


**Figure 4.51** Results of computations of coefficients  $a_0$  (bold line in all subplots) and  $b$  (Eq. 4-41) for the JONSWAP spectra (subplot [a]), the Donelan (1985) spectra (subplot [b]) and the Combi spectra (subplot [c]), at different stages of the wave development at different wind speeds  $U_{10} = \{7\text{m/s (plain line), } 10\text{m/s (line with dots), } 15\text{m/s (line with asterisks), } 20\text{m/s (line with circles) and } 30\text{m/s (line with crosses)}\}$ . The experimental coefficient  $a_{exp} = 0.0065$  (bold dashed line) is shown.

This indicates the effect of the spectral shape of the wave spectrum  $F(f)$  on the wave energy source functions  $S_{in}(f)$  and  $S_{ds}(f)$ , and will be addressed later in this section. For strong winds, when the wave breaking rates are high, this difference ( $RW - aS_I$ ) is a positive number during wave development. The results illustrated in Figure 4.51 lead to questions regarding the underlying physical processes in situations where coefficient  $b$  is a negative number, which corresponds to a positive flux of energy on short scale waves.

To explain the origin of the positive energy flux, we refer to the results of the recent experimental study at Lake George (Donelan et al., 2006). One of the important findings of the Lake George study was the influence of wave breaking on the energy transfer from the wind to the waves. The researchers reported that in terms of high breaking rates, the effect of wave breaking has the potential to double the energy transfer from the wind to the waves due to the increase in the roughness of the sea surface.

It is tempting, therefore, to speculate that the case when  $b < 0$  corresponds to the same process reported by Donelan et al. (2006). Additionally, this observation may indicate that the process of generating short scale waves is a result of wave breaking (Hwang and Wang, 2005) which leads to an increase in the roughness of the sea surface, which enhances the energy exchange between the wind and the waves. However, as shown in Figure 4.51, the incidence of  $b < 0$  appears only for a certain range of wind forcing conditions ( $3 < U_{10} / c_p < 5$ ), those corresponding to young waves under light winds only ( $U_{10} < 10$  m/s), when the breaking rates are lower relative to breaking rates in higher winds.

This observation contradicts the experimental findings of Donelan et al. (2006), according to whom the higher the breaking rates, the stronger the influence of wave breaking on wind-wave interaction. Due to limited related experimental data, this problem remains open for future investigations. Therefore, the incidence of  $b < 0$  is not relative to the effect of wave breaking on the energy exchange between the wind and the waves.

On the other hand, when  $b < 0$ , the forced dissipation term  $T_2(f)$  becomes a negative number. Since, dissipation source term has negative sign in Equation 2-21, the result will be an increased wave energy in the high frequency range of the wave spectrum. In this situation, the dissipation of short scale waves ceases. This result contradicts the experimental findings of Young and Babanin (2006). Therefore, the incidence when coefficient  $b$  is a negative number is groundless within the physical framework. Thus, coefficient  $b$  must be a positive number for any air-sea conditions.

To avoid the incidence when  $b < 0$ , it was decided to determine necessary conditions for coefficient  $b$  to be a positive number. In order for that, the forced dissipation term  $T_2(f)$  may contribute in the wave dissipation processes, the difference  $(RW - aS_1)$  must be a positive number:

$$RW - aS_1 > 0 \quad (\text{Eq. 4-43})$$

Substituting the integral  $S_1$  with the sum  $S_{11} + S_{12}$  and  $W$  with the sum  $W_1 + W_2$  using Equation 4-33 and performing a mathematical transformation with consideration of the Equation 4-36, the condition represented by Equation 4-43 can be presented as follows:

$$a < \frac{RW_2}{S_{12}} \quad (\text{Eq. 4-44})$$

The condition described by Equation 4-44 represents the limiting conditions for coefficient  $a$ , with the upper limit  $RW_2 / S_{12}$ . With regard to the condition described by Equation 4-44, the term  $RW_2$  is the upper limit for the spectral magnitudes of the inherent breaking term  $T_1(f)$  in the high frequency range of the wave spectrum. In terms of the physical processes occurring in nature, the same equation indicates that for inherent wave breaking the dissipation energy of the short scale waves must be less than the energy transferred from the wind to the waves. This fact is in excellent agreement with the existing observational data from Donelan (1998).

On the other hand, as described earlier in the current section, the term  $T_1(f)$  was adjusted to the wind input source function by coefficient  $a$  only in the long scale range of the wave spectrum (see Equation 4-36), while the high frequency range remained unadjusted. On this basis, it may be concluded that the unadjusted high frequency part of the term  $T_1(f)$  is the cause of the negative values for coefficient  $b$  shown in Figure 4.51. This interpretation is supported by the remarkable difference of the values of coefficient  $b$  for different types of the wave spectra, particularly for the Donelan (1985) spectra (see Figure 4.51).

As shown in Figure 4.51 the wind input source term computed for the Donelan (1985) spectra requires the highest rates of the suppression parameter  $\eta$  in order to comply with the physical constraint (Eq. 4-5). On the other hand, the inherent breaking term  $T_1(f)$  computed for the same wave spectrum remains unadjusted to the wind input source function in the high frequency range of the wave spectrum. This inconsistency between the wind input source function  $S_{in}(f)$  and the inherent breaking term  $T_1(f)$  generates the negative values of the difference  $(RW - aS_1)$  in computations for coefficient  $b$  (Eq. 4-41).

In the present study, it was decided to maintain only the positive values for coefficient  $b$  by applying the correction to coefficient  $a_0$  for the inherent breaking term  $T_I(f)$  in the high frequency range of the wave spectrum. In terms of spectral modelling, Equation 4-44 describes the disposition between the high frequency spectral tails of the wind input  $S_{in}(f)$  and the inherent breaking dissipation source term  $T_I(f)$ .

In order to meet the conditions implied by the equation, for any air-sea state, it is necessary to reduce the integral value  $S_{I2}$  by decreasing the spectral magnitudes of the inherent breaking term  $T_I(f)$  in the high frequency range. For this purpose, the correction function  $Z(f)$  (Eq. 4-39) was applied to coefficient  $a_0$  only in the high frequency range ( $f > f_p$ ),  $a = a_0 \cdot Z(f)$ . Therefore, the final form for coefficient  $a$  is:

$$a = \begin{cases} a_0, & f \leq f_p \\ a_0 \cdot Z(f), & f > f_p \end{cases} \quad (\text{Eq. 4-45})$$

As noted above (see Equation 4-39), the function  $Z(f)$  is the decreasing exponential function. Therefore, the magnitudes of coefficient  $a$  are less than  $a_0$  in the high frequency range of the wave spectrum. The correction function  $Z(f)$  (Eq. 4-39) was preferred among the other exponential functions on the basis of the fact that it includes the exponent  $\mu$  which allows the high frequency spectral magnitudes of the inherent breaking term  $T_I(f)$  to remain sensitive to the wind input source function. As a result of this correction, for the dominant waves coefficient  $b$  became larger than before the correction of coefficient  $a$  due to the reduction of the integral value of  $S_I$  in Equation 4-38. On the other hand, coefficient  $a$  remained unaffected in terms of peak frequency, since the correction was applied only in the high frequency range of the wave spectrum.

Figure 4.52 (a, b and c) shows the results of the computations of coefficients  $a$  and  $b$  for dominant waves with the correction (Eq. 4-39) applied in the high frequency spectral range of the inherent wave breaking term  $T_I(f)$ . As is clearly shown, coefficient  $b$  has positive number values for different types of wave spectra for any air-sea conditions. As noted previously, the correction (Eq. 4-39) of the inherent breaking term  $T_I(f)$  resulted in the increase of the magnitudes of coefficient  $b$ , which is shown in Figure 4.52. This increase is significant, particularly for the Donelan (1985) spectra (subplot [b]) of young waves.

Figure 4.52. demonstrates the relationship between coefficient  $b$  and wind speed  $U_{10}$ . For young waves, as wind speed increases, coefficient  $b$  is remarkably increased, while for well-developed waves there is no significant difference in its values.

This result leads to the conclusion that as the wind becomes stronger, the forced dissipation rates move higher. This conclusion is in excellent agreement with the existing observational data (Melville and Matusov, 2002; Young and Babanin, 2006; and Gemmrich, 2005). Remarkably, coefficient  $a$  is almost the same for each type of wave spectra, as shown in Figure 4.52. This fact demonstrates that the inherent breaking of waves relates only to their steepness.

In all three subplots, the pronounced steplike increase of coefficient  $a$  at the early stages of wave development ( $U_{10}/c_p = [4, 4.5]$ ) is clearly shown. A similar feature at the same stage of wave development was found for the wave growth rate in Section 4.1, in the discussion on growth rate. As discussed previously, the origin of this feature is the transition of the wind flow over the dominant waves from fully separated to non-separated. It seems that the effect of the change of the type of wind flow over the waves is pronounced for inherent wave breaking.

Figure 4.53 shows the sequential increase of the magnitudes of coefficient  $b$  as a result of the corrections applied to the wave dissipation function as described earlier in the current section. As is shown in Figure 4.53, the correction resulted in reducing the difference between coefficients  $a$  and  $b$  for young waves  $U_{10}/c_p > 3$ .

Furthermore, coefficient  $b$  (noted as  $b'_{corr}$  - bold line with dots see Figure 4.53) becomes less sensitive to the step-like increase of coefficient  $a$ , in contrast to that,  $b_{corr}$ , previously computed (see Figure 4.53 – line with dots and dashed line with dots) before the correction of the inherent breaking term  $T_1(f)$ . Before,  $b_{corr}$  had a pronounced drop of its values at  $U_{10}/c_p \sim 4$  corresponding to the increase of coefficient  $a$ .

Figure 4.54 shows the wave dissipation source function  $S_{ds}(f)$  with the corrected coefficients  $a$  and  $b$  in the high frequency range of the wave spectrum at different stages of wave development. The figure clearly shows the correspondence of the spectral slopes of the high frequency tail between the wave dissipation source term and the wind energy input spectrum in the high frequency range of wave spectra. For average-developed waves, the spectral magnitudes of the wave dissipation dominate the magnitudes of the wind energy input in the high frequency range. This issue can be understood in terms of the peculiarities of the directional spreading of the wave dissipation source function revealed in the experimental studies at Lake George (Young and Babanin, 2006). This topic will be discussed further in Section 4.2.4.

Figure 4.55 shows the wave spectral dissipation source functions computed for the average-developed waves for different wind speeds  $U_{10} = \{7, 10, 15, 20, 30\}$  m/s. The figure clearly demonstrates the increase in the spectral level of the wave dissipation with increasing wind speed.

Furthermore, the contribution of the forced wave breaking into the total wave dissipation slightly increases with increasing wind speed, as shown by the small reduction of the high frequency spectral slope of the wave dissipation spectra with the increasing wind speed.

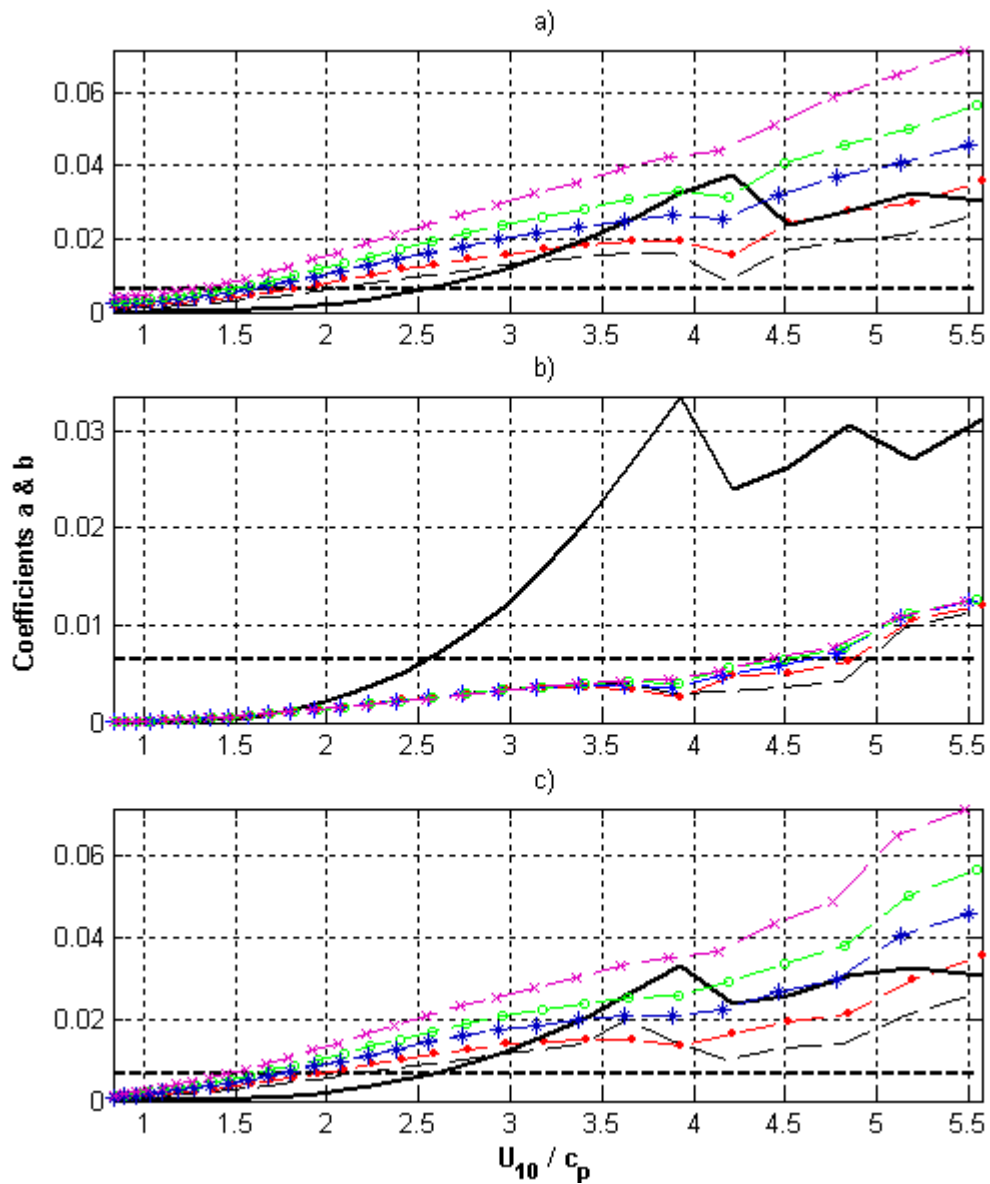
The higher the spectral magnitudes in the high frequency range relative to the magnitudes for the dominant waves, the greater is the contribution of the forced dissipation term  $T_2(f)$  to the total wave dissipation. This trend is clearly shown in the comparison between the wave dissipation source terms computed for  $U_{10} = 7$  m/s and  $U_{10} = 10$  m/s.

According to the data for the average developed waves ( $U_{10} / c_p = 2.7$ ) illustrated in Figure 4.55, the stronger the wind, the higher the rates of inherently breaking waves and the forced dissipation of short scale waves under the influence of long waves. This observation agrees with the present understanding of wave dissipation processes and the existing experimental data (Babanin et al., 2001; Melville and Matusov, 2002; Young and Babanin, 2006; Gemmrich, 2005).

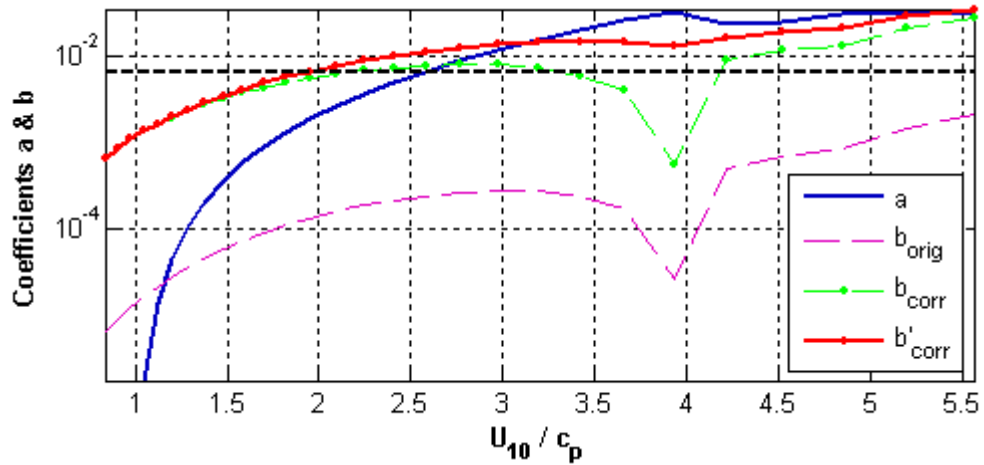
Wave dissipation energy relates to the wind input energy from the wind to the waves by means of the dissipation rate  $R$  (see Equation 4-32). This relationship was described in terms of the integral values of the spectral functions  $S_{ds}$  and  $S_{in}$ . Therefore, the selection of the threshold steepness  $\sqrt{B_{nT}}(f)$  cannot affect the integral value of the wave dissipation source term. However, the threshold value  $\sqrt{B_{nT}}(f)$  may affect the magnitudes of coefficients  $a$  (Eq. 4-45) and  $b$  (Eq. 4-41). Therefore, different values for threshold steepness were examined to determine the effect of various measures of threshold steepness  $\sqrt{B_{nT}}(f)$  on the magnitudes of coefficients  $a$  (Eq. 4-45) and  $b$  (Eq. 4-41).

Figure 4.56 shows the magnitudes of coefficients  $a$  and  $b$  that result from applying different values for the threshold steepness  $\sqrt{B_{nT}}(f)$ . It is clear from the results that with increasing values of threshold steepness the values of both coefficients increase.

This trend is determined by the response of the residual  $\Delta F = F(f) - F_T(f)$  on the change of the threshold magnitudes. As the threshold value increases, the residual  $\Delta F$  decreases, resulting in a decrease of the spectral magnitudes of the dissipation function.



**Figure 4.52** Results of computations of the coefficients  $a$  (Eq. 4-45) (bold line in all subplots) and  $b$  (Eq. 4-41) after the correction with the function  $Z(f)$  (Eq. 4-39) for the JONSWAP spectra (subplot [a]), the Donelan (1985) spectra (subplot [b]) and the Combi spectra (subplot [c]), at different stages of the wave development at different wind speeds  $U_{10} = \{7\text{m/s (dashed line), } 10\text{m/s (line with dots), } 15\text{m/s (line with asterisks), } 20\text{m/s (line with circles) and } 30\text{m/s (line with crosses)}\}$ . The experimental coefficient  $a_{exp} = 0.0065$  (bold dashed line) is also shown.



**Figure 4.53** Coefficients  $a$  (Eq. 4-45) and  $b$  (Eq. 4-41) after the applied correction using the exponential function  $Z(f)$  (Eq. 4-39). Coefficient  $b$  before the correction is also shown as  $b_{orig}$  (Eq. 4-38) (dashed line). Coefficient  $b$  after the correction of the inherent breaking term  $T_I(f)$  (Eq. 4-45) is noted as  $b'_{corr}$ . Computations were performed for the Combi spectra at different stages of the wave development for the wind speed  $U_{10} = 10$  m/s. The experimental coefficient  $a_{exp} = 0.0065$  (bold dashed line) is also shown.

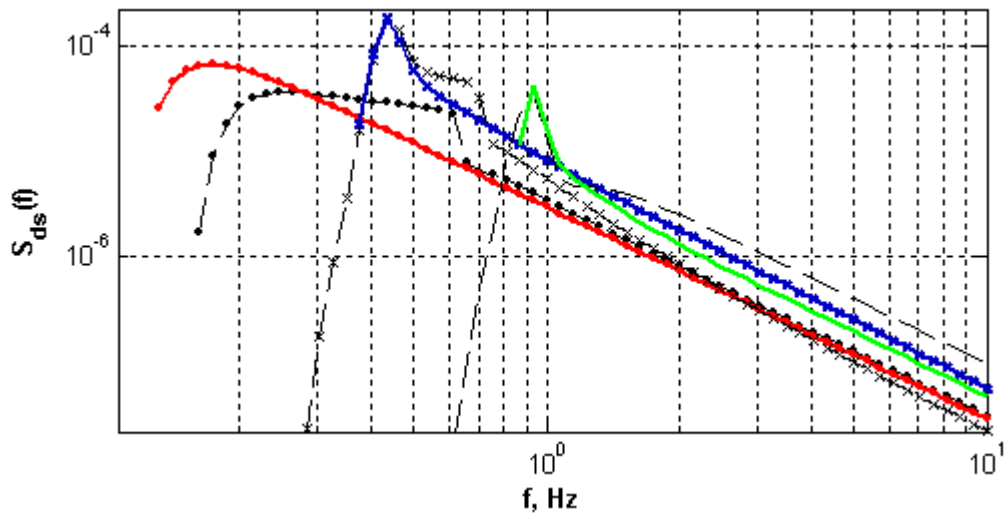


**Figure 4.54** The spectral dissipation source function  $S_{ds}(f)$  (Eq. 2-29) computed with coefficients  $a$  (Eq. 4-45) and  $b$  (Eq. 4-41). The corresponding wind input source functions  $S_{in}(f)$  are also shown. Computations were performed for the Combi spectra at different stages of the wave development with the wind forcing conditions:  $U_{10} / c_p = \{5.7$  (bold line),  $2.7$  (bold line with crosses),  $0.83$  (bold line with dots) $\}$ , for the wind speed  $U_{10} = 10$  m/s.

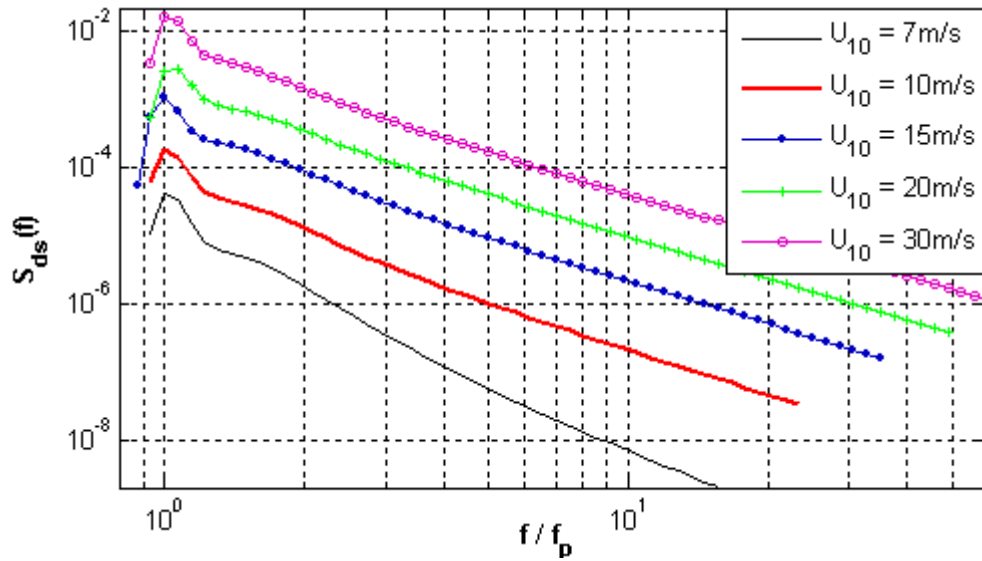


**Figure 4.55** Dissipation source term  $S_{ds}(f)$  (Eq. 2-29) computed with coefficients  $a$  (Eq. 4-45) and  $b$  (Eq. 4-41) for the Combi spectra of the average-developed waves ( $U_{10} / c_p = 2.7$ ) for the different wind speeds  $U_{10} = \{7\text{m/s (plain line), } 10\text{m/s (bold line), } 15\text{m/s (line with dots), } 20\text{m/s (line with crosses) and } 30\text{m/s (line with circles)}\}$  and wind forcing parameter,  $U_{10}/c_p = 2.7$ .

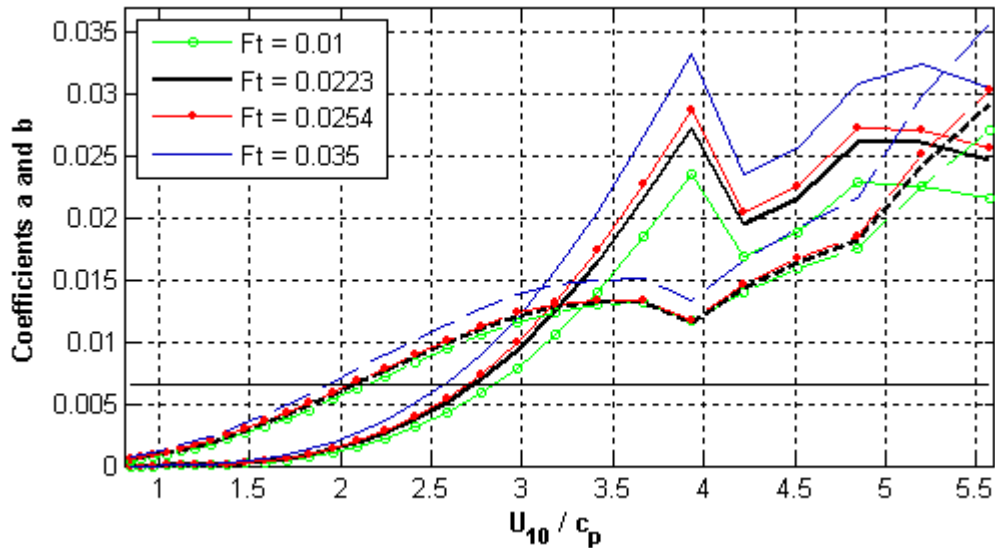


**Figure 4.56** Coefficient  $a$  (Eq. 4-45) (continuous lines) and  $b$  (Eq. 4-41) (dashed lines) computed for different values of the threshold steepness  $\sqrt{B_{nT}(f)}$  as a function of the wind forcing parameter  $U_{10} / c_p$ . Computations were performed for the Combi spectra at different stage of the wave development for the wind speed  $U_{10} = 10 \text{ m/s}$ .

On the other hand, the spectral dissipation function must meet the physical constraint (Eq. 4-32). Therefore, coefficients  $a$  and  $b$  adopt the corresponding magnitudes to maintain this constraint (Eq. 4-32).

Figure 4.56 shows that, the differences for both coefficients are significant for the young waves rather than the well developed ones. Furthermore, the effect of the changing threshold steepness is more pronounced for coefficient  $a$  than for coefficient  $b$ . The different values of threshold spectral steepness do not significantly affect the consistency of the corresponding values of coefficients  $a$  and  $b$  with the experimental value  $a_{exp} = 0.0065$  (Young and Babanin, 2006).

### 4.2.3 DIRECTIONAL SPREADING

In the present study an attempt has been made to model the least known feature of the spectral dissipation function, which is its directional behaviour. Previously, the unimodal directional shape was assumed for the dissipation source term. However, the recent experiment at the Lake George (Young and Babanin, 2006) revealed that the major dissipation of the wave energy occurs at angles oblique to the main wave propagation direction.

In terms of spectral modelling, this fact can be interpreted as the bimodal shape of the directional spreading for the spectral dissipation function (Eq. 2-29). Therefore, it was decided to develop a new directional spectral function which had a distinct bimodal shape in the angular space.

After a number of attempts, a new directional spreading function was developed as a superposition of two Gaussian functions. According to the experimental results of Young and Babanin (2006), there is no clear indication of the angles where the maximum directional dissipation rates were observed. Therefore, to investigate this issue, the new directional spreading function was provided with certain features giving the function the flexibility to modify the spectral shape in both spectral spaces, directional and frequency. The new directional spreading function includes the ability to:

- symmetrically shift the locations of the peaks along the directional scale
- vary with the height of its middle trough
- vary the cross-sectional shapes along the spectral frequency scale
- vary with different wind forcing conditions

Taking into account listed above features, the new directional spreading function  $V(\theta, f, U_{10}/c_p)$  has the following general form:

$$V(\theta, f, U_{10}/c_p) = \begin{cases} V_1(\theta, f, U_{10}/c_p) = A(f) \cdot \exp(-p(\theta + \theta_p)^2), & \theta < 0 \\ V_2(\theta, f, U_{10}/c_p) = A(f) \cdot \exp(-p(\theta - \theta_p)^2), & \theta \geq 0 \end{cases} \quad (\text{Eq. 4-46})$$

where  $p = p(f, U_{10}/c_p)$  is the trough parameter, which determines the depth of the middle trough

$\theta_p = \theta_p(f, U_{10}/c_p)$  is the angle (in radians) of the maximum dissipation rates relative to the main propagation direction of the waves, and

$\theta$  is the angle (in radians) relative to the main propagation direction of the waves.

The  $A(f)$  is the spectral width defined as  $A(f)^{-1} = \int_{-\pi}^{\pi} K(f, \theta) d\theta$  (Babanin and Soloviev,

1998), where  $K(f, \theta) = \exp(-p(\theta \pm \theta_p)^2)$ , satisfying the normalisation

condition:  $\int_{-\pi}^{\pi} V(f, \theta) d\theta = 1$ . If the angle is  $\theta_p = 0$ , the directional spreading has a unimodal shape.

As mentioned before, the directional spreading function  $V(\theta, f, U_{10}/c_p)$  was determined as the cross-section of the spectrum  $F(f, \theta)$  at a particular frequency and in a particular wind forcing condition. Therefore, the parameters  $p(f, U_{10}/c_p)$  and  $\theta_p(f, U_{10}/c_p)$  can linearly vary along the frequency scale and with the changing wind forcing conditions. Their functional dependencies can be determined on the basis of the correlation of the wave model results to the experimental data, to be discussed later in Section 4.3.

Initially, the parameter  $p$  was assumed as the constant value  $p = 0.5$ . This value was determined on the basis of the performance of the wave model. For the angle  $\theta_p(f, U_{10}/c_p)$ , initially, the linear dependence was assumed to be:

$$\begin{cases} \theta_p(f) = \theta_p(f_p) + \Delta\theta_f \frac{(f - f_s)}{(f_{cut} - f_s)} \\ \theta_p(U_{10}/c_p) = \theta_p(f_p) + \Delta\theta_{ucp} \frac{(5.7 - U_{10}/c_p)}{(5.7 - 0.83)} \end{cases} \quad (\text{Eq. 4-47})$$

where  $\Delta\theta_f$  is the total increment of the peak angle along the frequency scale  
 $\Delta\theta_{ucp}$  is the total increment during the wave evolution  
 $f_s$  is the frequency where spreading is started.

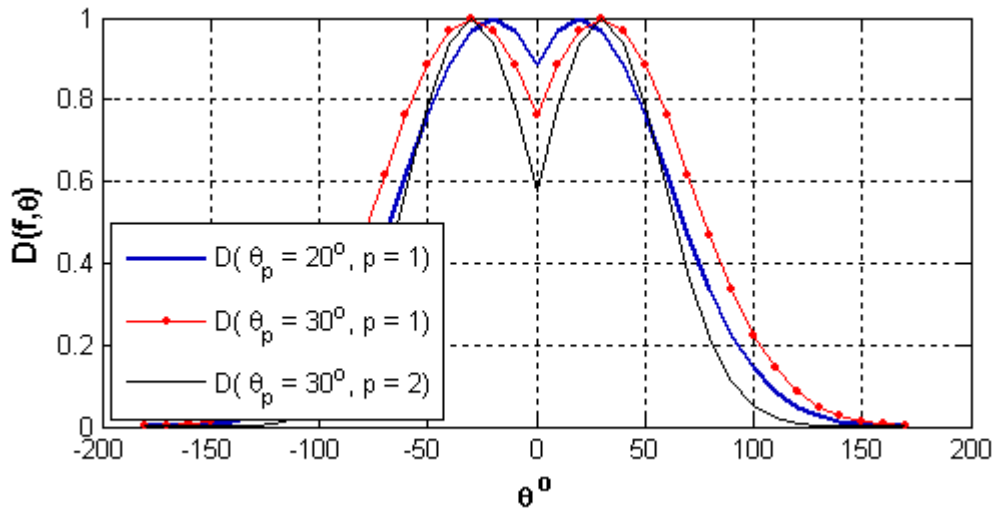
The total increments  $\Delta\theta_f$  and  $\Delta\theta_{ucp}$  can be positive as well as negative, corresponding to the increase or decrease of the angle  $\theta_p$ , respectively. It is worth mentioning that, based on the experimental findings of Young and Babanin (2006),  $\theta_p$  cannot be a large angle and the reasonable limits are  $-90^\circ < \theta_p \pm (\Delta\theta_f, \Delta\theta_{ucp}) < 90^\circ$  relative to the main propagation direction of the waves.

Figure 4.57 shows the resulting directional spreading function  $V(\theta, f, U_{10}/c_p)$  (Eq. 4-46) with different values for the parameters  $p$  and  $\theta_p$ . For the convenience of the comparisons, all the directional spreading functions are normalized by the maximum value at the angle  $\theta_p$ , i.e.  $V(\theta_p, f, U_{10}/c_p) = 1$ . Figure 4.57 shows that as the angle  $\theta_p$  increases, the lobes of the directional spreading function are moving apart, increasing the depth of the trough between them.

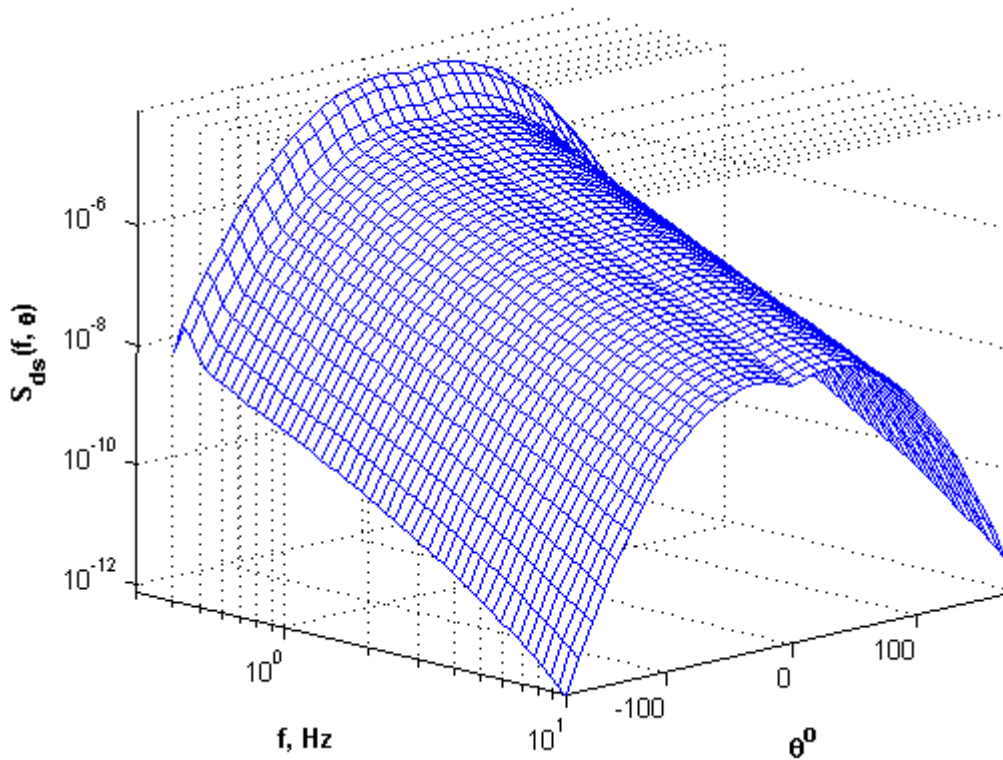
The increase of the parameter  $p$  reduces the widths of the lobes, increasing the depth of the trough between them. As is shown, the variation of the parameters  $p$  and  $\theta_p$  results in different directional spreading. These parameters provide the necessary flexibility to conduct further research of the wave spectral dissipation function.

Figure 4.58 shows the two-dimensional spectral dissipation function  $S_{ds}(f, \theta)$  with the bimodal directional spreading function  $V(\theta, f, U_{10}/c_p)$  (Eq. 4-46), with  $\theta_p = 20^\circ$ ,  $p = 1$  and  $\Delta\theta_f = 10^\circ$  with  $f_s = 3f_p$ . The computations were performed for the Combi spectrum of the average-developed waves ( $U_{10}/c_p = 2.7$ ) for the wind speed  $U_{10} = 10$  m/s.

Figure 4.58 shows the distinct trough of the dissipation spectrum  $S_{ds}(f, \theta)$  at the main direction of the wave propagation at  $\theta = 0^\circ$ . At the upper frequency  $f_{cut}$  the spectral peaks are located symmetrically to the main propagation direction at the angle  $\theta_p = 30^\circ$ . Thus, the parameters of the newly developed directional function (Eq. 4-46) together with Equation 4-47 can vary the spectral shape of the two-dimensional dissipation function  $S_{ds}(f, \theta)$ .



**Figure 4.57** Directional spreading function  $V(f, \theta_p)$  (Eq. 4-46) with different values of the parameters  $\theta_p$  and  $p$ .



**Figure 4.58** Two-dimensional dissipation spectrum  $S_{ds}(f, \theta)$  with the bimodal directional spreading  $V(f, \theta_p)$  (Eq. 4-46) ( $\theta_p = 20^\circ, p = 1$  and  $\Delta\theta_f = 10^\circ$  with  $f_s = 3f_p$ ) computed for the Combi spectrum of the average-developed waves with the inverse wave age  $U_{10} / c_p = 2.7$  for the wind speed  $U_{10} = 10$  m/s.

As it was mentioned in Section 4.2.2, the directionally integrated one-dimensional dissipation spectrum  $S_{ds}(f)$  exceeded the spectral levels of the wind energy input spectrum  $S_{in}(f)$ . However, the bimodal directional spreading of the dissipation spectrum reduces the probability of the exceedance over the spectral magnitudes of the directionally unimodal wind energy input spectrum at the main propagation direction.

Thus, the application of the bimodal directional spreading to the dissipation source function reduces singularities in the operational wave modelling caused by the exceedance of spectral magnitudes of the wave dissipation source term over the wind input spectral level in the high frequency range.

#### 4.2.4 COMPARING TO THE EXPERIMENTAL DATA

Performance of the corrected new wave dissipation source function  $S_{ds}$  (Eq. 2-29) was examined against the observed wave breaking data of Melville and Matusov (2002) and Gemmrich (2005). The observed wave breaking data relates to the energy dissipation due to wave breaking only,  $S_{br}$ , which is a constituent of the total wave energy dissipation. In the open ocean, the wave energy dissipates due to the turbulent viscosity of the fluid (Babanin and Young, 2005). It is believed, however, that turbulent viscosity dissipation is minimal for dominant waves and significant for short scale waves, where the induced dissipation phenomenon was observed by Young and Babanin (2006) and Manasseh et al., (2005).

One of the origins of induced dissipation can be enhanced turbulent viscosity due to the breaking of the dominant waves. Therefore, consistence between the computational results of the new spectral dissipation function  $S_{ds}$  (Eq. 2-29) and the observational data,  $S_{br}$ , was expected only for the dominant waves. Thus, the main purpose of these comparisons was to determine whether the new spectral dissipation function (Eq. 2-29) could reconcile computational results with the observed wave breaking data for the dominant waves.

The average length of breaking crests per unit area per unit speed interval  $A(v)$  (Phillips, 1985) was the main criterion used for any comparisons, where  $v$  is the crest propagation speed which is different from the phase speed of the breaking wave. The field measurements (Phillips et al., 2001; Melville and Matusov, 2002) suggest that  $v = 0.8c$ , where  $c$  is the phase speed of the wave.

Towed hydrofoil experiments (Duncan, 1981) have established that the rate of energy dissipation per unit length of breaking crest is proportional to  $v^5$ . Therefore, the spectral energy dissipation function due only to wave breaking is:

$$S_{br}(v) = b_{br} \rho_w g^{-1} v^5 \Lambda(v) \quad (\text{Eq. 4-48})$$

where  $b_{br}$  is a non-dimensional coefficient which reflects the strength of the wave breaking. The value of coefficient  $b_{br}$  is uncertain. The reported values of  $b_{br}$ , applicable to the ocean waves ranged from  $b_{br} \sim b_{G05} = 2 \times 10^{-5}$  (Gemrich, 2006) to  $b_{br} \sim b_{MM02} = 8.5 \times 10^{-3}$  (Melville and Matusov, 2002) and were assumed to be independent of the wave scale. The reason for this discrepancy is not clear yet and requires further experimental investigation.

On the other hand, the breaking crest length spectrum can be computed from the dissipation source term  $S_{ds}$  using Equation 4-48 and substituting  $S_{br}$  with  $S_{ds}$ :

$$\Lambda_m(v) = b_{br}^{-1} \rho_w^{-1} g v^{-5} S_{ds}(v) \quad (\text{Eq. 4-49})$$

where  $\Lambda_m(v)$  is the model for computing the breaking crest length spectrum and the spectral dissipation source term  $S_{ds}(v)$  is given in the crest propagation speed domain ( $S_{ds}(v) = \frac{0.8g}{2\pi} v^{-2} S_{ds}(f)$ ). It is worth noting that in the current section, the wave dissipation spectra  $S_{ds}$  are considered dimensional (i.e.  $S_{ds}(f) = \rho_w g S_{ds}(f)$ ) for the dimensional consistency of the comparisons, particularly with the results of Melville and Matusov (2002). It is important to emphasize the fact that  $\Lambda_m(v)$  (Eq. 4-49) is not valid for short scale waves due to the dissipation function  $S_{ds}(v)$  in addition to the fact that the wave breaking encompasses other dissipative processes (turbulent viscosity) significant in the high frequency range of the wave spectrum.

As was shown, coefficient  $b_{br}$  was included in the computations for  $\Lambda_m(v)$  (Eq. 4-49) and the wave breaking spectrum  $S_{br}$  (Eq. 4-48). Since coefficient  $b_{br}$  is uncertain, it creates complexity for the comparison between the computed and observed data. Therefore, to reduce the degree of uncertainty caused by coefficient  $b_{br}$ , a novel approach was developed in the present study. It was decided to determine a value of coefficient  $b_{br}$ , which provides consistency between the model results for the  $\Lambda_m(v_p)$  and the observed data  $\Lambda(v_p)$  at the spectral peak ( $\Lambda_m(v_p) = \Lambda(v_p)$ ). The resultant value of coefficient  $b_{br}$  was compared to other values suggested by various authors (Phillips, 2001; Melville 1994; Melville and Matusov 2002 and Gemrich, 2006). Following this, coefficient  $b_{br}$  was computed from

Equation 4-48 using the observed data  $\Lambda(v_p) = \Lambda_{MM02}(v_p)$  (Melville and Matusov, 2002) or  $\Lambda_{G05}(v_p)$  (Gemrich, 2006), giving:

$$b_{br} = \frac{g}{\rho_w} \frac{S_{ds}(v_p)}{v^5 \Lambda(v_p)} \quad (\text{Eq. 4-50})$$

The advantage of a novel approach was that no preferences were given to any previously reported values for coefficient  $b_{br}$ .

#### 4.2.4.1 Comparing to Melville and Matusov (2002)

In a field study Melville and Matusov (2002) investigated the breaking crest length spectra  $\Lambda(v)$  for well developed waves in various wind speeds  $U_{10} = \{7.2, 10, 13.6\}$  m/s. The authors experimentally obtained the spectral distribution of  $\Lambda(v)$  from the wave breaking data represented by the post-breaking signature of a visual signal of air entrainment (whitecapping).

They found a scaling factor of  $(10 / U_{10})^3$  to collapse their data sets approximately into the single exponential curve:

$$\Lambda_{MM02}(v) = \Lambda(v)(10 / U_{10})^3 = 3.3 \times 10^{-4} e^{-0.64v} \quad (\text{Eq. 4-51})$$

To compare the computed value for coefficient  $b_{br}$  (Eq. 4-50) with the experimental value  $b_{MM02} = 8.5 \times 10^{-3}$  of Melville and Matusov (2002), the spectral dissipation function  $S_{ds}(v)$  was weighted with the term  $(10 / U_{10})^3$  due to the weighted magnitudes of  $\Lambda_{MM02}(v_p)$ .

The observational data by Melville and Matusov (2002) were presented in terms of the wavenumber spectrum. Therefore, the comparisons to the results of Melville and Matusov (2002) were performed in the wavenumber domain  $k$ . Using transformation Jacobian

$j_{v2k} = \frac{0.8}{2} \sqrt{gk^{-3}}$  based on the relationship between the wavenumber and the crest propagation speed in the deep water:  $k = (0.8)^2 g v^{-2}$ , the breaking crest length spectrum  $\Lambda(v)$  can be converted into a wavenumber spectrum  $\Lambda(k)(10 / U_{10})^3 = \frac{0.8}{2} \sqrt{gk^{-3}} \Lambda(v)(10 / U_{10})^3$ .

To obtain a correct picture of the comparison, it is necessary to have the same wave spectrum as was observed experimentally. Therefore, for the computations of a corresponding wave dissipation source function (Eq. 2-29), the closest wave spectrum having a similar spectral level and spectral slope of the high wavenumber tail to the

observed spectrum by Melville and Matusov (2002) (their Figure 4.3a) was selected. The modelled spectrum is shown in Figure 4.59.

It was found that the Combi spectrum of well developed waves ( $U_{10} / c_p = 1.3$  for  $U_{10} = 13.6$  m/s) was the most appropriate for modelling the observed spectrum  $\Psi(k)$  (Melville and Matusov, 2002). The selection of the Combi spectrum was based on the distinct transition of the high wavenumber slope from  $k^{-5/2}$  to a  $k^{-3}$  mentioned by Melville and Matusov (2002). As noted, the Combi spectrum has a similar transition of its slope in the high wavenumber space, which is clearly shown in Figure 4.59. The spectral dissipation function  $S_{ds}(f)$  (Eq. 2-29) was computed for the modelled Combi spectrum (Figure 4.59) of mature waves with a wind forcing parameter  $U_{10} / c_p = 1.3$  at the various wind speeds of  $U_{10} = 7.2, 9.8$  and  $13.6$  m/s, correspondingly. The resulting dissipation source term was weighted according to Melville and Matusov (2002) with the term  $(10 / U_{10})^3$ . Coefficient  $b_{br}$  was computed by substituting the  $A(v_p)$  in Equation 4-50 by  $A_{MM02}(v_p)$  (Eq. 4-51) observed by Melville and Matusov (2002). The results of these computations showed that the consistency between the computed value  $A_m(v_p)$  and the observed value  $A_{MM02}(v_p)$  (Eq. 4-51) at the spectral peak was achieved when coefficient  $b_{br} = 0.001$ . The obtained value  $b_{br} = 0.001$  was close to the value  $b_{br} = 8.5 \times 10^{-3}$  used by Melville and Matusov (2002). Moreover, Melville (1994), based on the experiments, suggested the range of values for coefficient  $b_{br} \sim [3 \times 10^{-3}, 1.5 \times 10^{-2}]$ , which is close to the findings of the present study. The corresponding breaking crest length spectra  $A_m(k)$  were computed for the different wind speeds  $U_{10} = 7.2, 9.8$  and  $13.6$  m/s, using the value  $b_{br} = 0.001$ .

Figure 4.60 shows the comparison of the weighted breaking crest length spectra  $A_m(k)(10 / U_{10})^3$  computed by Equation 4-49 with the data observed by Melville and Matusov (2002)  $A_{MM02}(k_p)$  (Eq. 4-51). As it was expected, in the high wavenumber space, the model computations are remarkably greater than the observational results. This difference is determined by the fact that the observational data relate to dissipation due to wave breaking only whereas the computed dissipation function  $S_{ds}(f)$  (Eq. 2-29) includes other dissipation processes of wave energy.

Figure 4.61 compares the computed spectral dissipation function  $S_{ds}(k)$  (Eq. 2-29) and the dissipation function  $S_{br}(k)$  according to Melville and Matusov (2002). The comparison shows that both dissipation functions are close to agreement. The results of the computations of  $S_{br}(k)$  using  $b_{br} = 2 \times 10^{-5}$  (Gemmrich, 2005) are also shown in Figure 4.61 by the dashed line. The results indicate an encouraging agreement between the

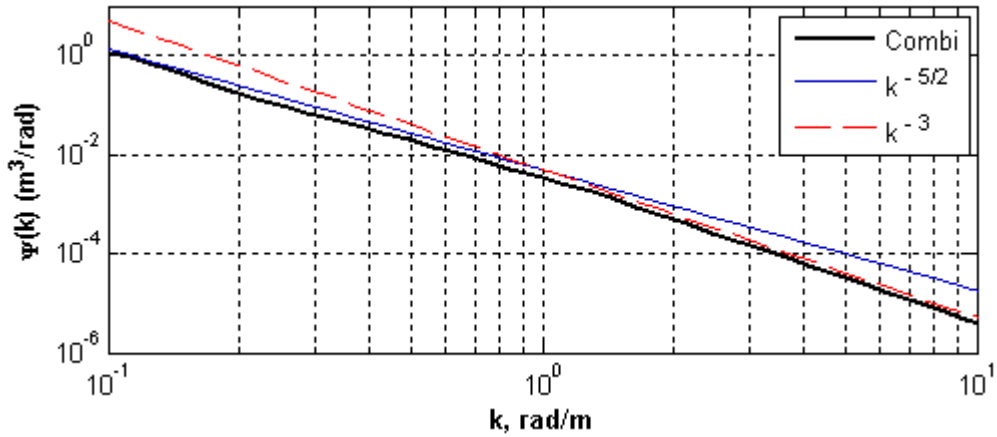
new spectral dissipation source term and the dissipation function according to Melville and Matusov (2002).

The question as to whether coefficient  $b_{br}$  has a constant value in different wind forcing conditions has been addressed in the present study. To investigate the behaviour of coefficient  $b_{br}$  in different wind forcing conditions, the coefficient was computed for the omnidirectional Combi spectra at different stages of wave development with different wind speeds  $U_{10} = 7.2, 9.8, 13.6, 15, 20, 30$  m/s. It should be emphasised that the observed breaking crest length spectrum  $A_{MM02}(k_p)$  was obtained for well developed waves and for wind speeds  $U_{10} = 7.2, 9.8$  and  $13.6$  m/s particularly.

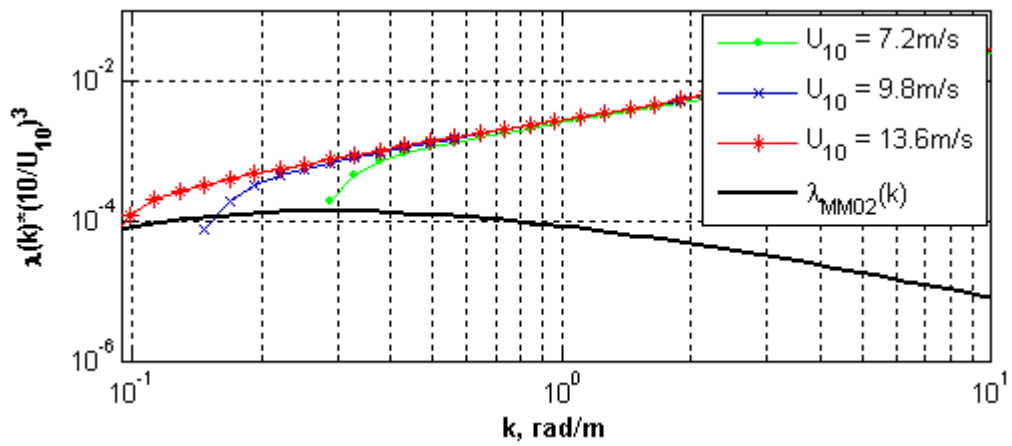
It has not been discovered whether the observed data would be applicable for different air-sea conditions (i.e. stronger winds and young waves). The present study applied the results obtained by Melville and Matusov (2002) to a wide range of the air-sea conditions. Furthermore, it is important to consider that the spectral dissipation source term  $S_{ds}(k)$  in Equation 4-52 includes the effect of different dissipative processes together with the wave breaking, while the breaking crest length spectrum  $A_{MM02}(k_p)$  relates only to wave breaking. Therefore, the results of computations for coefficient  $b_{br}$  were expected to be greater than  $b_{MM02} = 8.5 \times 10^{-3}$ . The results of these computations showed that for winds  $U_{10} \leq 20$  m/s the computed coefficient  $b_{br}$  was larger for the young and average-developed waves, while for the mature waves it had fewer values than  $b_{MM02}$ . However, for the stronger winds, coefficient  $b_{br}$  exhibited the inverse behaviour.

Figure 4.62 shows the results of computations of coefficient  $b_{br}$  for the omnidirectional Combi spectra for different wind speeds  $U_{10} = \{7.2, 9.8, 13.6, 15, 20, 30\}$  m/s at different stages of wave development.

In Figure 4.62, coefficient  $b_{br}$  demonstrates different behaviour for different ranges of wind speed. For wind speeds  $U_{10} \leq 20$  m/s, as waves are developing, coefficient  $b_{br}$  exhibits a reducing trend starting with the values  $b_{br} > b_{MM02}$  for young waves and reaching value  $\sim 10^{-3}$  at full development. However, for very strong winds  $U_{10} = 30$  m/s, coefficient  $b_{br}$  remains  $b_{br} \geq b_{MM02}$  throughout wave development.



**Figure 4.59** The wavenumber Combi spectrum similar to the wavenumber spectrum observed by Melville and Matusov (2002) for well developed waves with wind forcing  $U_{10} / c_p = 1.3$  and wind speed  $U_{10} = 13.6$  m/s. Transition from  $k^{-5/2}$  slope to a  $k^{-3}$  is shown.



**Figure 4.60** Comparing the average length of the breaking crests spectra  $A_m(k)(10 / U_{10})^3$ , computed by (Eq. 4-49) using  $b_{br} = 0.001$ , with the observed  $A_{MM02}(k)$  (Melville and Matusov, 2002). The computations were performed for the Combi spectrum for the mature waves with wind forcing  $U_{10} / c_p = 1.3$  and the wind speed  $U_{10} = 10$  m/s.

Figure 4.62 shows that for young waves with  $U_{10} / c_p > 4$ , coefficient  $b_{br}$  decreases with increasing wind speed. As waves are reaching a range of the wind forcing conditions  $1.5 < U_{10} / c_p < 2.5$ , coefficient  $b_{br}$  gradually becomes equal to  $b_{MM02} = 8.5 \times 10^{-3}$  (Melville and Matusov, 2002) for the winds  $U_{10} = 30$  m/s.

For well-developed waves (i.e.  $0.83 < U_{10} / c_p < 1.5$ ) including the waves observed by Melville and Matusov (2002), coefficient  $b_{br}$  takes values in the range  $[10^{-4}, 10^{-3}]$  for the winds  $U_{10} \leq 20$  m/s. Contrary to this, as the waves approach their full development under the very strong winds  $U_{10} = 30$  m/s, coefficient  $b_{br}$  increases remarkably.

These processes are not well understood yet and require further investigation. The results of computations for coefficient  $b_{br}$  shown in Figure 4.62 are consistent with the experimental value  $b_{MM02} = 8.5 \times 10^{-3}$  suggested by Melville (1994) in the range of the wind forcing conditions mentioned by Melville and Matusov (2002).

It was interesting to compare the spectral dissipation source term  $S_{ds}(k)$  computed for different wind forcing conditions with the wave breaking spectral function  $S_{br}(k)$  obtained by Melville and Matusov (2002). To address this question, the spectral dissipation function,  $S_{ds}(k)$ , was computed for the Combi spectra at different stages of wave development  $U_{10} / c_p = \{0.83, 1.6, 2.7, 4, 5.8\}$  for wind speed  $U_{10} = 10$  m/s. The results of these computations are shown in Figure 4.63. For young and average-developed waves the computed spectral dissipation function  $S_{ds}(k)$  exceeds wave breaking  $S_{br}(k)$  obtained by Melville and Matusov (2002).

This fact is consistent with the present understanding of wave dissipation processes. As mentioned above, the computed spectral dissipation source term,  $S_{ds}(k)$ , relates to different dissipative processes in the waves, while  $S_{br}(k)$  (Melville and Matusov, 2002) considers wave energy loss due to wave breaking only. For the young waves the effect of the turbulent viscosity on the wave development is more significant than for the mature waves due to the fact that more wave breaking occurred in this spectral range. Therefore, more energy loss occurred due to the turbulent viscosity besides to the wave breaking. Therefore, the total wave dissipation expressed by the spectral function  $S_{ds}(k)$  is larger than the dissipation due to wave breaking only,  $S_{br}(k)$ . This effect is clearly shown in Figure 4.63.

As waves are approaching their full development stage, the computed spectral dissipation is less than the experimental. One of the reasons for this discrepancy could be related to the fact that the experimental results (Melville and Matusov, 2002) are not applicable for this stage of wave development.

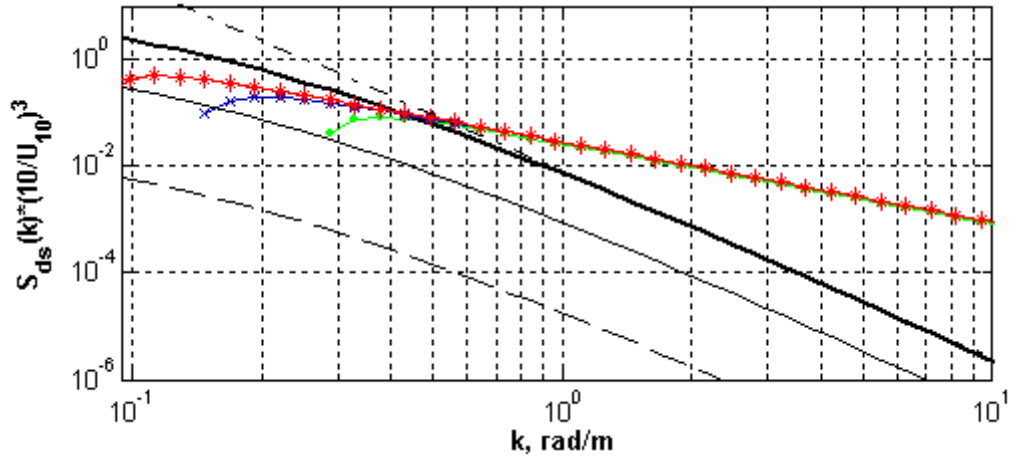


**Figure 4.61** Comparing a new dissipation function  $S_{ds}(k)$  (Eq. 2-29) with the dissipation due to the wave breaking  $S_{br}(k)$  (Eq. 4-48) (Melville and Matusov, 2002) using different values of coefficient  $b_{br} = \{2 \times 10^{-5}$  (dashed line),  $1 \times 10^{-3}$  (plain line) and  $8.5 \times 10^{-3}$  (bold line)}. Computations were performed for the Combi spectra of the well-developed waves with wind forcing  $U_{10} / c_p = 1.3$  and for the wind speeds  $U_{10} = \{7.2\text{m/s}$  (line with dots),  $9.8\text{m/s}$  (line with crosses),  $13.6\text{m/s}$  (line with asterisks)}. The computed dissipation functions  $S_{ds}(f)$  (Eq. 2-29) are weighted by the term  $(10 / U_{10})^3$ .

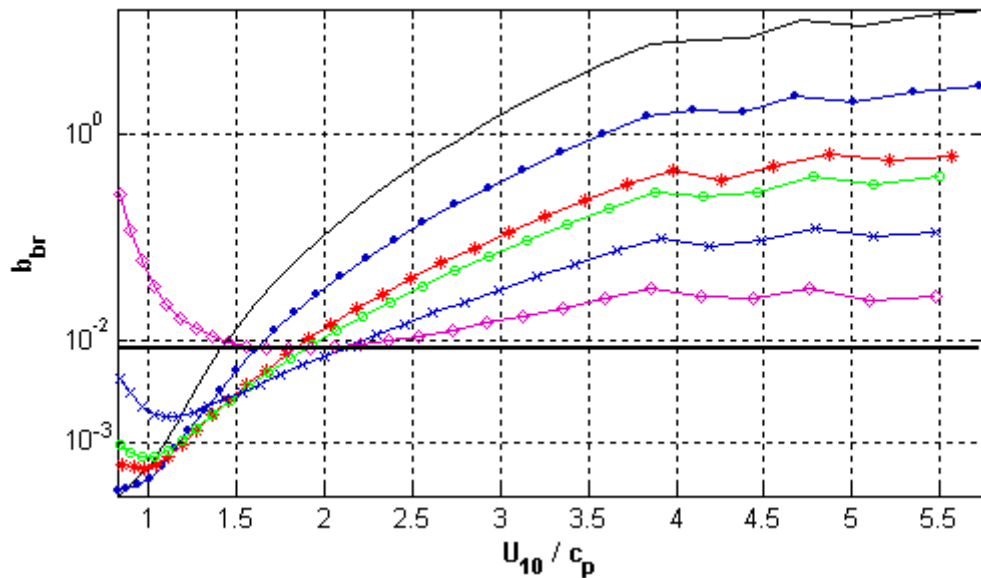


**Figure 4.62** Coefficient  $b_{br}$  (Eq. 4-50) as a function of the wind forcing parameter  $U_{10} / c_p$  computed at the spectral peak of the Combi spectra at different stages of the wave development for the different wind speeds:  $U_{10} = \{7.2\text{m/s}$  (plain line),  $9.8\text{m/s}$  (line with dots),  $13.6\text{m/s}$  (line with asterisks),  $15\text{m/s}$  (line with circles),  $20\text{m/s}$  (line with crosses) and  $30\text{m/s}$  (line with diamonds)}.

As the researchers have noted, the data in the low wavenumber range are not considered accurate due to the noise. Therefore, the topic still remains open for further experimental investigations.

For the dominant waves with  $U_{10}/c_p = 1.6$ , Figure 4.63 shows excellent agreement between the model computations and the experimental results (Melville and Matusov, 2002) at the spectral peak frequency. It worth mentioning that Melville and Matusov (2002) observed the waves with the wind forcing  $U_{10}/c_p = 1.3$ . The value  $U_{10}/c_p = 1.6$  corresponds to the point where the computed coefficient  $b_{br}$  coincides with the experimental value of  $b_{MM02} = 8.5 \times 10^{-3}$  (see Figure 4.62). This agreement led to an investigation of whether a similar agreement exists for different wind speeds. To address this question, the spectral dissipation source term  $S_{ds}(k)$  was computed for the dominant waves with  $U_{10}/c_p = 1.6$  at different wind speeds  $U_{10} = \{7.2, 9.8, 13.6, 20 \text{ and } 30\}$  m/s and compared with the experimental wave breaking function  $S_{br}(k)$  (Melville and Matusov, 2002). The results of the comparison are shown in Figure 4.64. In general, the results indicate close agreement between the compared spectral functions  $S_{ds}(k)$  and  $S_{br}(k)$  for the dominant waves.

As illustrated in Figure 4.64, the largest difference at the spectral peak is shown for the wind speed  $U_{10} = 7.2$  m/s. The reasons for this discrepancy are determined by different scopes of the dissipation processes considered by the spectral dissipation source term  $S_{ds}(k)$  and the wave breaking function,  $S_{br}(k)$  (Melville and Matusov, 2002).

Since the impact of the viscosity of the fluid on wave development is more significant in light winds (e.g.  $U_{10} = 7.2$  m/s) than in strong winds (Banner and Pierson, 1998), more wave energy dissipates through viscous drag rather than through wave breaking. Moreover, at such winds there may be no breaking of the dominant waves. Therefore, for light winds, the dissipation source term  $S_{ds}(k)$  is greater than the wave breaking term  $S_{br}(k)$ .

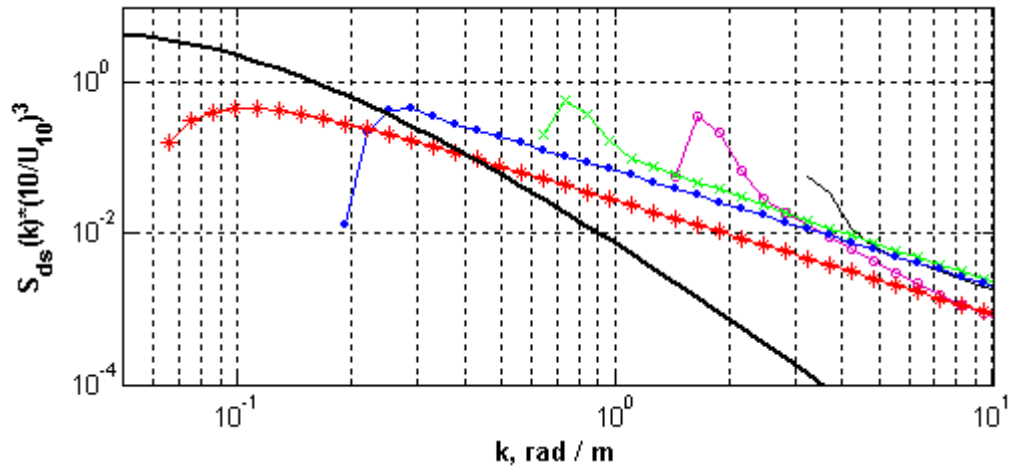


**Figure 4.63** Comparing the wave spectral dissipation source functions  $S_{ds}(f)$  computed for the Combi spectra at different stages of the wave development with the wind forcing conditions:  $U_{10} / c_p = \{5.7$  (plain line),  $4.5$  (line with circles),  $2.7$  (line with crosses),  $1.6$  (line with dots) and  $0.83$  (line with asterisks)}, for the wind speed  $U_{10} = 10$  m/s. The dissipation due to the wave breaking  $S_{br}(k)$  (Eq. 4-48) (Melville and Matusov, 2002) is represented by bold line. The dissipation functions are weighted by the term  $(10 / U_{10})^3$ .

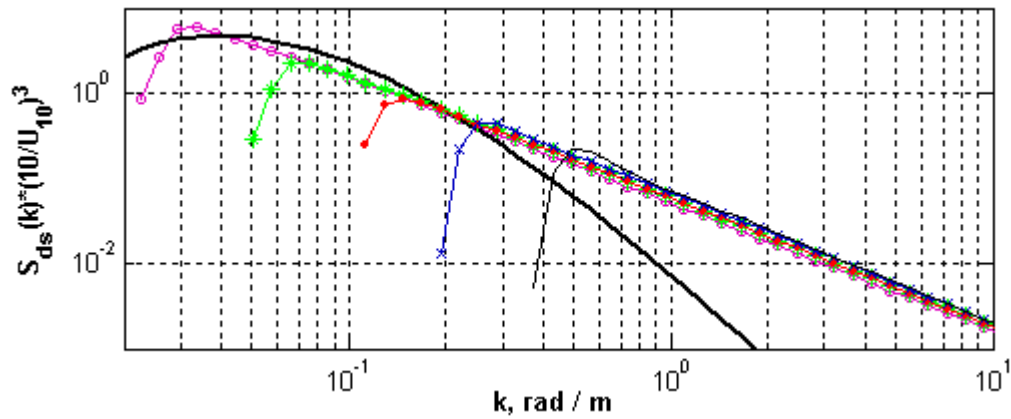


**Figure 4.64** Comparing the wave spectral dissipation source functions  $S_{ds}(f)$  (2-29) computed for the Combi spectrum of the mature waves with the spectrum of the mature waves with the wind forcing parameter:  $U_{10} / c_p = 1.6$  for the different wind speeds  $U_{10} = \{7.2\text{m/s}$  (plain line),  $9.8\text{m/s}$  (line with crosses),  $13.6\text{m/s}$  (line with dots),  $20\text{m/s}$  (line with asterisks) and  $30\text{m/s}$  (line with circles)}. The dissipation due to the wave breaking  $S_{br}(k)$  (Eq. 4-48) (Melville and Matusov, 2002) is represented by bold line. The computed dissipation functions are weighted by the term  $(10 / U_{10})^3$ .

#### 4.2.4.2 Comparing to Gemmrich (2005)

The results of computations for the breaking crest length spectrum  $A(\nu)$  were compared to the measured wave breaking data obtained by Gemmrich (2005) during the FAIRS experiments. In contrast to Melville and Matusov (2002), the observed wave breaking data from the FAIRS experiment (Gemmrich and Farmer, 2004; Gemmrich, 2005; Gemmrich, 2006) relates to developing wind sea conditions, as well as conditions for mature seas. Wave breaking data were not previously available for growing wind seas. According to Gemmrich (2005), the four data sets used offered corresponding measurements of  $A(\nu)$ . From these data sets only two were selected for comparison with the results of the model computations using Equation 4-51: data 1 ( $U_{10} = 12$  m/s with  $f_p = 0.156$  and  $U_{10} / c_p = 1.2$ ) and data 3 ( $U_{10} = 12$  m/s with  $f_p = 0.125$  and  $U_{10} / c_p = 0.98$ ).

The selection of the two datasets was made similar to Banner et al., (2006) in order to compare the results of the present study with the experimental data of Gemmrich (2005) and the results of other model computations (Banner et al., 2006). Coefficient  $b_{br} = 2 \times 10^{-5}$  (Gemmrich, 2006) was used in computations for the breaking crest length spectrum  $A(\nu)$  in Equation 4-52. The results of these comparisons are shown in Figure 4.65. The figure illustrates the excellent agreement of  $A(\nu)$  (Gemmrich, 2005) with the available data for the dominant waves with the wind forcing  $U_{10} / c_p = 1.2$ . However, for mature waves with  $U_{10} / c_p = 0.98$ , the computed results using the same value  $b_{br} = 2 \times 10^{-5}$  are  $A(\nu_p) = 4 \times 10^{-5}$  which is higher than the results of other authors (Gemmrich, 2005 and Banner et al., 2006). This difference could be caused by the uncertainty of coefficient  $b_{br}$ .

The results of the computations indicate that to match the experimental data  $A(\nu_p) = 8 \times 10^{-6}$  (Gemmrich, 2005) coefficient  $b_{br}$  must be  $b_{br} = 9.5 \times 10^{-5}$  which is comparable with open ocean estimates reported in recent field studies. Moreover, this value is consistent with the range  $[8 \times 10^{-5}, 1.2 \times 10^{-3}]$  reported by Banner and Song (2002) from their laboratory experiments. In general, Figure 4.65 shows an encouraging agreement between the results of the present study and the results of Gemmrich (2005) and Banner et al. (2006).

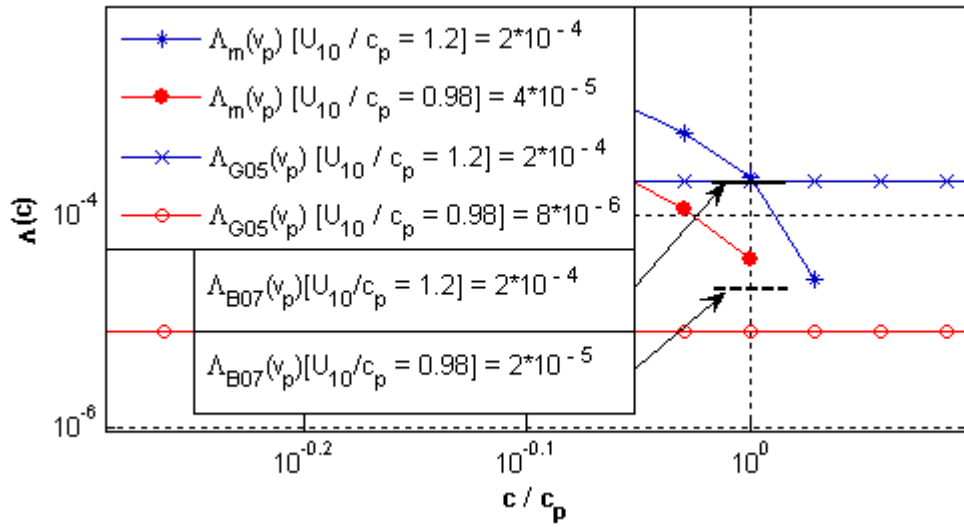


**Figure 4.65** Comparing the results of computations of  $A_m(v_p)$  computed for the Combi spectra of the waves with wind forcing  $U_{10} / c_p = 1.2$  and  $0.98$ , for the wind speed  $U_{10} = 12$  m/s to the corresponding wave breaking data according to Gemmrich (2005) ( $A_{G05}(v_p)$ ) and model computations by Banner et al. (2006) ( $A_{B07}(v_p)$ ).

As noted earlier, previous observational studies reported various values for coefficient  $b_{br}$  ranging from  $b_{br} \sim 2 \times 10^{-5}$  (Gemmrich, 2006) to  $b_{br} = 8.5 \times 10^{-3}$  (Melville, 1994 and Melville and Matusov, 2002). The present study supports the values suggested by Melville (1994) and Melville and Matusov (2002), even though questions still remain regarding the reasons for the remarkable discrepancy between the experimental results reported by Melville and Matusov (2002) and Gemmrich (2006).

To address the question of this disparity in the results, it was decided to carry out an alternative computation of coefficient  $b_{br}$  to match the experimental value obtained by Gemmrich (2006). As described in Section 4.2.5 the computations of coefficient  $b_{br}$  were performed using Equation 4-50. Therefore, this equation was analysed with regard to the nature of the possible variations in the computations that resulted in the remarkable discrepancy of coefficient  $b_{br}$ . The dimensional consistency of both sides of this equation was analysed. Taking into account that  $b_{br}$  is a non-dimensional coefficient, the right hand side of Equation 4-50 must be non-dimensional:

$$[b_{br}] = \frac{\left[ \frac{m}{s^2} \right] \left[ \frac{kg}{m^3} \frac{m}{s^2} m^2 \frac{m}{s \cdot rad} \right]}{\left[ \frac{kg}{m^3} \right] \left[ \frac{m}{s} \right]^5 \left[ \frac{1}{rad} \right]} = [1] \quad (\text{Eq. 4-52})$$

It should be noted that the weight parameter  $(10 / U_{10})^3$  (Melville and Matusov, 2002) was omitted from Equation 4-51 as  $A_{MM02}(k_p)$  is already weighted by  $(10 / U_{10})^3$ . Equation 4-52 shows that the computations for coefficient  $b_{br}$  were performed correctly. However, if coefficient  $b_{br}$  (assigned as  $b_{alt}$ ) is computed using the non-dimensional wave dissipation spectrum in the frequency scale, then  $A_{MM02}(v)$  (Eq. 4-49) can be represented as follows:

$$b_{alt} = \frac{g}{\rho_w} \frac{S_{ds}(f)(10/U_{10})^3}{v^5 \Lambda_{MM02}(v)} \quad (\text{Eq. 4-53})$$

Computations using Equation 4-53 showed that coefficient  $b_{alt}$  correlated with the values reported by Gemmrich (2006) and it is dimensional:

$$\left( [b_{br}] = \frac{\left[ \frac{m}{s^2} \right] [m^2]}{\left[ \frac{kg}{m^3} \right] \left[ \frac{m}{s} \right]^5 \left[ \frac{s}{m^2} \right]} = \left[ \frac{m^3 s^2}{kg} \right] \right).$$

This result is a contradiction to the definition of the non-dimensional coefficient  $b_{br}$ . Therefore, it can be concluded that the computations using Equation 4-53 are erroneous.

Figure 4.66 shows the comparison of the results of computations for coefficient  $b_{br}$  using Equations 4-50 and 4-53 with the experimental values according to Melville and Matusov (2002) and Gemmrich (2006). The computations were performed for the Combi spectra at different stages of wave development under the wind  $U_{10} = 10$  m/s.

Figure 4.66 shows that the results of both computations (see  $b_{br}$  for [Eq. 4-50]) and  $b_{alt}$  for [Eq. 4-53]) are consistent with both reported experimental values (see  $b_{MM02}$  and  $b_{G06}$ ) for well-developed waves with  $U_{10} / c_p = 1.6$  (see arrows), respectively. Moreover, Figure 4.66 shows the similar behavioural pattern of two differently computed results ( $b_{br}$  and  $b_{alt}$ ) for wave development. Furthermore, Figure 4.66 demonstrates convincing coincidence between the results of two different computations (Eqs. 4-50 and 4-53) with the two experimentally obtained discrepant values for coefficient  $b_{br}$  (Melville and Matusov, 2002; Gemmrich, 2006).

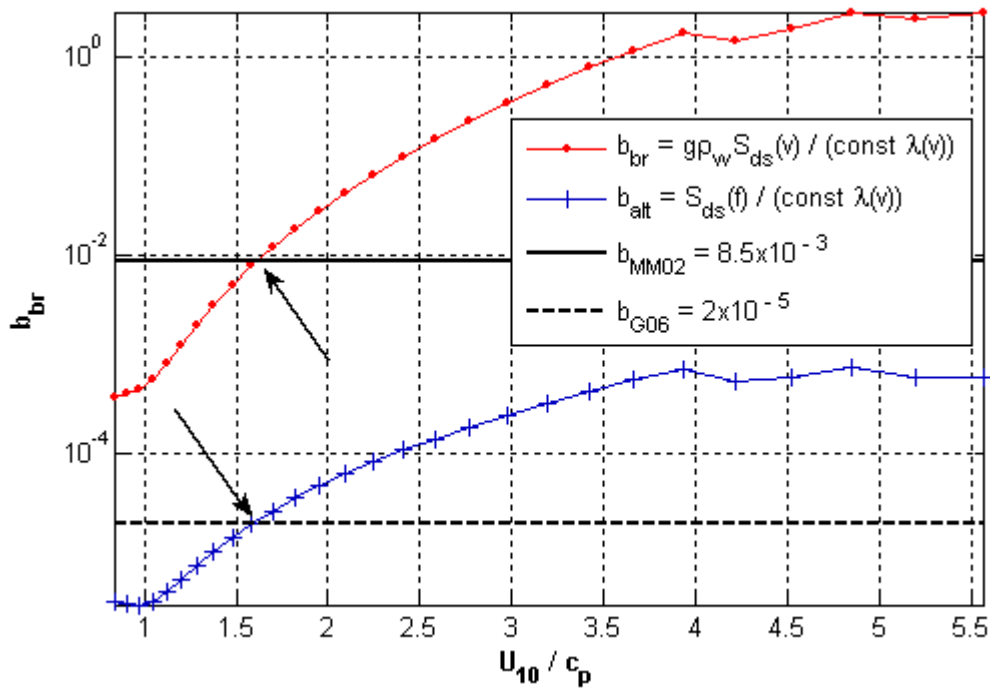


**Figure 4.66** Comparing coefficient  $b_{br}$  (Eq. 4-50) with coefficient  $b_{alt}$  for (Eq. 4-53) computed for the Combi spectra at different stages of the wave development for the wind speed  $U_{10} = 10$  m/s. The experimental values  $b_{MM02}$  for (Melville and Matusov, 2002) and  $b_{G06}$  for (Gemrich, 2006) are also shown.

### 4.2.5 CONCLUSIONS

Recently a suggested new parameterisation form for the wave dissipation source term  $S_{ds}(f)$  (Eq. 2-29) (Young and Babanin, 2005) was investigated as it related to a wide range of air-sea conditions. Since the spectral level of a wave dissipation source term depends on the level of the threshold spectrum  $F_T(f)$ , the suggested dissipation source function was investigated in terms of the threshold wave steepness presented by the newly proposed function called the saturation transformer  $T(f)$  which is an analogue of the spectral saturation  $B(f)$ . The threshold level  $\sqrt{B_{nT}(f)} = 0.035$  was determined as the optimal value based on the observational data of Babanin and Young (2005), since breaking can hardly be observed for the fully developed waves used as the criterion for selection of the threshold value of  $\sqrt{B_{nT}(f)}$ .

In the current study a new approach was developed within the strong physical framework based on recent observations of Donelan (2001) and Young and Babanin (2005). One of the important physical constraints was the consistency between the wave dissipation and the wind energy input to the waves. Since the wind input source term varies depending on wave-induced stress, the wave dissipation source function changes correspondingly. Hence, wind stress becomes the main physical constraint in operational wave modelling. The new relational parameter between the wind input and wave dissipation source terms was introduced in this study as a dissipation rate  $R$ . The parameterisation form of the dissipation rate was presented as a function of the inverse wave age  $U_{10} / c_p$ .

The dissipation rate can be widely applied in operational wave modelling to maintain the correct level of wave dissipation energy in wave models. This approach led to the recording of a new balance scheme between the energy source terms in the wave models, referred to as the split balance scheme. The basis of this scheme is the fact that the integral of the wind input source term is balanced by the corresponding integral of the dissipation source term while the nonlinear energy transfer between the waves is self-balanced. This is in agreement with the findings of Badulin et al. (2006).

The two-phase behaviour of the spectral dissipation function was investigated in terms of the functional dependency of coefficients  $a$  for the inherent wave breaking term and  $b$  for the forced dissipation term (Eq. 2-29). The present study found that both coefficients have functional dependence on the inverse wave age  $U_{10} / c_p$  and the spectral frequency. The dependence on the inverse wave age is mostly determined by the relationship between the wind energy input and the wave dissipation source terms. Both coefficients are decreasing with wave development. For well developed waves ( $U_{10} / c_p < 1$ ) coefficient  $a$  becomes zero, which means that no breaking of the dominant waves occurs. For this stage of wave development, the dissipation occurs only in the high frequency range of the wave spectrum. The spectral scale dependence of coefficient  $a$  and  $b$  is determined by applying the correction function  $Z(f)$  (Eq. 4-39), which ensures that  $b$  will be positive at all times. Moreover it provides the correspondence of the spectral slopes between the wind input source term and the wave dissipation in the high frequency spectral range. The correspondence of the slopes is determined by the fact that the exponent in the function  $Z(f)$  (see Equation 4-40) is equal to the exponent of the high frequency spectral tail of the wind energy input source term  $S_{in}(f)$ . This feature is very important, particularly in achieving the numerical stability of the wave model in the high frequency spectral range.

According to the observations of Young and Babanin (2006), wave dissipation was maximal at oblique angles relative to the main propagation direction of the waves. Therefore, in the present study, a new directional spreading function of a bimodal shape was developed for the wave dissipation source term. This function includes features that allow the variations of the directional spectral shape for further research purposes.

The performance of the corrected new spectral dissipation source term was examined to ascertain whether the new dissipation source term (Eq. 2-29) was able to reconcile computed breaking crest length spectral magnitudes for dominant waves  $\Lambda(v_p)$  with the experimental data (Melville and Matusov, 2002; Gemmrich, 2005). The findings of the present study indicate encouraging agreement with the results of both independent studies (see Figure 4.64). However, a remarkable discrepancy of values for coefficient  $b_{br}$ , which is used in computations of the breaking crest length spectrum, was observed. This issue was investigated by computing coefficient  $b_{br}$  using observed  $\Lambda(v_p)$  and analysing the results of these computations against the reported values for coefficient  $b_{br}$  from previous studies (Duncan, 1981; Melville, 1994; Phillips 2001; Melville and Matusov, 2002; Gemmrich 2006). The results of these computations varied depending on the values of the observed  $\Lambda(v_p)$  used.

In addition, the behaviour of coefficient  $b_{br}$  in terms of wave development and for a wide range of the wind speeds was investigated using  $\Lambda_{MM02}(v_p)$ , as suggested by Melville and Matusov (2002). The results obtained shed light on the physical properties of coefficient  $b_{br}$  in a wide range of air-sea conditions. The results show that for well-developed seas ( $U_{10} / c_p < 1.5$ ) coefficient  $b_{br}$  as a function of the inverse wave age becomes very sensitive to the wave age (see the steep decrease in the range of values  $b_{br} \sim [10^{-4}, 10^{-3}]$  (see Figure 4.62) for wind speeds  $U_{10} < 20$  m/s. Moreover, for average-developed waves ( $U_{10} / c_p \sim 2.7$ ), good agreement was shown with the value  $b_{br} = 3 \times 10^{-2}$  reported by Duncan (1981) from a laboratory experiment.

The findings lead to the conclusion that the observed discrepancy of the values of coefficient  $b_{br}$  is caused by its sensitivity to the changing wind forcing conditions during the wave observations. Summarising the results of the comparisons, it is important to emphasise that the new spectral dissipation source function demonstrates the ability to predict wave energy losses consistent with the experimental data.

It can be concluded that the wave dissipation source function according to Young and Babanin (2006) is an advanced form composed of the new features of the wave dissipation processes revealed during recent observations (Young and Babanin, 2006) and can be widely adopted in operational wave modelling. The performance of the corrected wave dissipation source function (Young and Babanin, 2006) in evolution runs based on the wave model WAVETIME-1 is discussed further in Section 4.3.

### 4.3 MODELLING SPECTRAL EVOLUTION

This section presents the results of the numerical experiments designed to validate the newly proposed parameterisation forms for the wind energy input  $S_{in}$  (Donelan et al., 2006) and the wave dissipation  $S_{ds}$  (Young and Babanin, 2006) source terms discussed in Sections 4.1 and 4.2. These experiments consisted of simulations of duration-limited evolution of wind-waves, computed using the wind-wave model WAVETIME-1 (Van Vledder, 2004) with modifications applied in the present study. These modifications included a novel balance scheme required for the new forms of the source terms  $S_{in}$  and  $S_{ds}$ . The model validation was made against the non-dimensional evolution curves proposed by Babanin and Soloviev (1998) with asymptotic limits based on Pierson and Moskowitz (1964). The validation strategy aimed to achieve an optimal agreement with the observed experimental curves.

Section 4.3.1 outlines the setup and preliminary validation of the wind-wave model. The new balance scheme of the wave model is discussed in Section 4.3.2. Results of the numerical experiments are reported subsequently in three sections. Section 4.3.3 includes comparative analyses of the model results against the non-dimensional evolution curves observed by Babanin and Soloviev (1998). Section 4.3.4 presents the results of assessment of the model performance in terms of the set of empirical parameters (Banner and Young, 1994) described in Section 4.3.5. Section 4.3.5 provides evaluation of the model results in terms of the width of the directional spreading of the wave frequency spectrum.

#### 4.3.1 MODEL SETUP

The performance of the new spectral functions of the wind input  $S_{in}(f)$  and the wave dissipation  $S_{ds}(f)$  source terms was assessed using a third generation one dimensional

research wave model WAVETIME-1 developed by Van Vledder (Alkyon, 2002, personal communication).

This model includes the EXACT-NL model of Hasselmann and Hasselmann (1985a) using the WRT method (Webb, 1978; Tracy and Resio, 1982) for computations of nonlinear wave interactions incorporated by Van Vledder (2005) for the finite depth conditions.

A detailed description of the wave model WAVETIME-1 was provided in Chapter 3. The model essentially solves the radiative transfer Equation 2-20 either for fetch limited or duration limited conditions. For the present study only duration limited conditions were considered: a uniform and steady wind blown over homogeneous deep water waves for a length of time after a sudden onset. The advection term in Equation 2-20 was excluded. The time dependent term  $\partial F / \partial t$  allows better convergence of model results towards an equilibrium state. Furthermore, the model showed best performance in the duration-limited mode during the preliminary validation tests to match the experimental wave growth curves observed by Babanin and Soloviev (1998).

#### 4.3.1.1 Initial Conditions

The initial conditions for all numerical experiments were represented using the JONSWAP spectrum with directional spreading as recommended by Babanin and Soloviev (1998). Parameters for the JONSWAP spectrum were specified according to Babanin and Soloviev's (1998) relationships of wave growth. In order to investigate the performance of the new source functions in the wave model, four different wind speeds ( $U_{10} = 7, 10, 15$  and  $20$  m/s) with initial dominant waves with wind forcing conditions  $U_{10} / c_p = 5.8$  were considered in the experiments. The results of computations discussed in Section 4.3.2 were obtained for the wind speed  $U_{10} = 10$  m/s with an initial peak frequency  $f_p = 0.9$  Hz corresponding to very young waves in wind forcing conditions  $U_{10} / c_p = 5.8$ .

#### 4.3.1.2 Output Parameters

The model WAVETIME-1 produced four separate output data files for the one dimensional wave spectrum  $F(f, \theta)$  and for associated source terms  $S_{nl}(f)$ ,  $S_{in}(f)$  and  $S_{ds}(f)$ . Other output files contained test reports of the model computations as a form of quality assurance for the operation of the model. The numerical data from the output files were processed using a specifically developed MATLAB subroutine that was computed using the following parameters:

- the non-dimensional energy  $\varepsilon = \sigma^2 g^2 / U_{10}^4$ , where  $\sigma$  is the variance of the wave spectrum
- the non-dimensional frequency  $\nu = f_p U_{10} / g$
- the non-dimensional duration  $\zeta = gT / U_{10}$ , where  $T$  is the duration of the wave development
- the lobe ratio  $\lambda(f) = F(f, \theta)_{max} / F(f, \theta_w)$ , where  $F(f, \theta_w)$  is the slice of the spectrum in the wind direction
- the Phillips coefficient  $\alpha$  - the level of the equilibrium interval computed according to Bandou et al. (1986)
- the average level of the spectral tail  $\alpha_{BY}$  and the exponent of the spectral tail slope  $n$  for the directional slice of the wave spectrum in the direction of the main propagation of the waves
- the similarity parameter  $\zeta$  which is the ratio of the wind direction energy at a given frequency and wave age to that predicted by Banner (1990)
- the spectral spreading parameter  $A(f)$  (Babanin and Soloviev, 1998)
- the mean spectral width  $\bar{\theta}$

### 4.3.2 SELF-CORRECTING WAVE MODEL

On the basis of new insight into the physical processes associated with wave development, a new computational routine was implemented in the WAVETIME-1 model. This routine was identified as self-correcting and suggested for the operational wave modelling. The self-correcting routine involves the dynamic correction of the computations of the source terms in order to ensure consistency with the physical constraints during the model operation.

Wave-induced stress (Eq. 4-6) was selected as the main physical criterion for the model computations. According to recent experimental results (Ancil and Donelan, 1996; Drennan et al. 2003 and Donelan et al. 2004) more evidence is currently emerging in support of wave-age-dependent, wave-induced stress. Therefore, wave-age-dependent wind stress was considered to be the physical constraint in the present study.

As was mentioned earlier, the integral relationship (Eq. 4-32) between the wave dissipation and wind input source functions represents the physical constraint for the dissipation spectral function. According to this, the wind input and wave dissipation source terms are coupled separately from the nonlinear interaction source term  $S_{nl}$ . Thus, this coupling between the source terms of radiative transfer Equation 2-20 determines the split balance scheme. The split balance scheme was integrated into the self-correcting routine of the wave model shown in Figure 4.67. As can be seen from the figure, for each stage of model computation, wave-induced stress  $\tau_w$  was computed for the wave spectrum that had resulted from the previous stage of wave development.

The model computed the wave-induced stress using the bulk formula by Guan and Xie (2004). This wave-induced stress was then used as a physical criterion for the correction of the wind input source term  $S_{in}$  in order to be consistent with the physical reality. The consistency was achieved by the correction routine for the wind input source term introduced in Section 4.1. After that, the spectral dissipation source term  $S_{ds}$  was computed on the basis of the integral relationship (Eq. 4-32) shown in Figure 4.67 (on the low right hand side).

### 4.3.3 VALIDATION STRATEGY

Traditionally in wave modelling the main objective of the validation of a source term is to reproduce the observational results by manually tuning the parameters for the investigating source term. In most numerical investigations, the validation strategy consists of a series of experiments applying different values for tuning parameters to improve the performance of the model. In the present study, this task was complicated by the fact that two new source terms had to be investigated concurrently. This issue was overcome by a novel self-correcting computational routine (see Section 4.3.2) applied to the WAVETIME-1 model.

In this way, the wind input source term was corrected by the model during the investigation of the source terms  $S_{in}$  and  $S_{ds}$ , and only the wave dissipation source function needed to be adjusted to achieve the optimal fit of the model results to the spectral parameters associated with the observational data from the Black Sea experiments (Babanin and Soloviev, 1998).

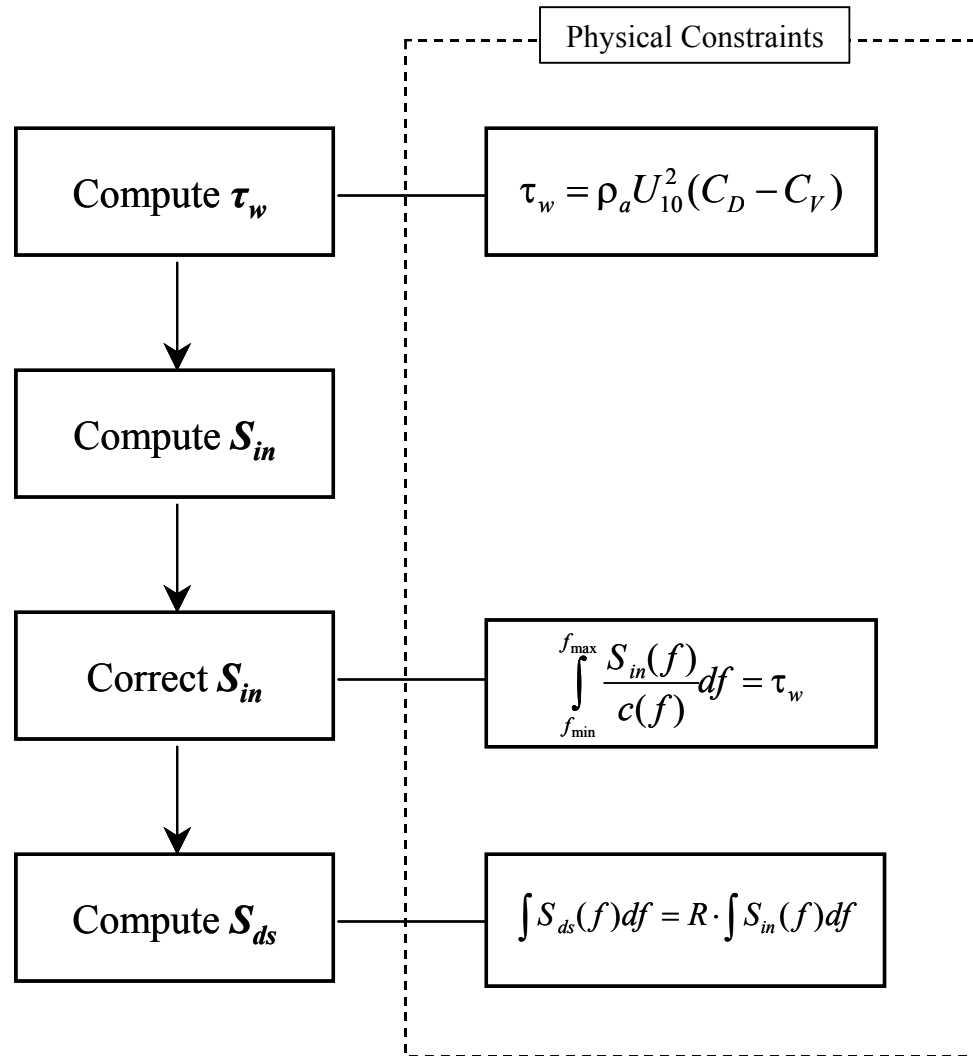


**Figure 4.67** Split-balance scheme integrated with the self-correcting routine of the wave model WAVETIME-1.

The adjustment of the dissipation source term was performed using a number of tuning parameters, including the directional spreading parameters  $p$ ,  $\theta_p$ ,  $\Delta\theta_f$  and  $\Delta\theta_{ucp}$  altering bimodal shape along the directions.

The main objective was to reproduce the observed power-law evolution of non-dimensional energy  $\varepsilon$  and non-dimensional frequency  $\nu$  with non-dimensional duration  $\zeta$  within 10% of approximation range. In addition, the supplementary goal was to obtain wave spectra with spectral shape properties consistent with the existing observational data including directional spreading. The performance of the new forms of wind input and wave dissipation source terms was investigated by the diagnostic method developed in the present study on the basis of that suggested by Banner and Young (1994).

Assessment of the model results was made on the basis of the following test comparisons of:

- the growth curves  $\varepsilon(\nu)$ ,  $\nu(\zeta)$  and  $\varepsilon(\zeta)$  against observational data from the Black Sea experiments of Babanin and Soloviev (1998)
- the spectral shape parameters  $\alpha_{BY}$  and  $n$  as diagnostic for the behaviour of the wind direction slice of the wavenumber spectrum  $F(k, \theta_w)$
- the Phillips coefficient  $\alpha$  against the values reported from wave observations
- the lobe-ratio  $\lambda$  as a diagnostic parameter for bimodality of the directional shape of wave spectrum
- the spectral spreading function  $A_{fp}(U_{10}/c_p)$ ,  $A_{2fp}(U_{10}/c_p)$  and  $A_{3fp}(U_{10}/c_p)$  against the results obtained by Babanin and Soloviev (1998)
- the mean spectral width  $\bar{\theta}$  against the observational data obtained by Hwang (2000)
- the parameter called the similarity parameter  $\zeta$  as a diagnostic tool for the spectral energy level.

As was discussed in Section 4.2.2 there is no experimental evidence regarding the relative spectral levels of the wind input and the wave dissipation source terms in the high frequency range of the wave spectrum. Therefore, in this study, two types of high frequency spectral tails for the wave dissipation source terms were considered: one described coefficient  $b$  as constant along the frequency scale ( $b = b_0(U_{10}/c_p)$ ) and the other described coefficient  $b$  as the frequency dependent function ( $b = b(f, U_{10}/c_p)$ ). In the second case, the slope of the dissipation spectrum in the high frequency range was bound with the slope of the wind input source term.

The first coefficient  $b$  was termed the unconstrained dissipation spectrum and the second coefficient  $b$  was referred to as the constrained dissipation spectrum. The performance of each type of dissipation spectrum in the wave model was assessed by the diagnostic scheme already outlined, and the results are discussed in Section 4.3.3.

#### 4.3.4 RESULTS

This section outlines the results of computations of wave development in deep water conditions carried out on the model WAVETIME-1. The computations were performed on AMD Athlon(tm) MP 1800+ server with a dual processor running at 1.5 GHz and RAM 1GB. The average computational time for the model run with 10000 cycles was 24 hours. The computations were stopped as the trend of the wave growth became apparent.

All computations were carried out for the wind speeds  $U_{10} = 7, 10, 15$  and  $20\text{m/s}$ . The model runs were assigned on the basis of a selected set of the tuning parameters for the dissipation source term as follows:

CP0.5A20W10,

where C / U means the model run for the constrained / unconstrained  
dissipation source term  
P is a notation for the trough parameter  $p$   
A is a notation for the angle parameter  $\theta_p$   
W is a notation for the wind speed.

Initially the parameters  $\Delta\theta_f$  and  $\Delta\theta_{ucp}$  were set to zero maintaining the  $\theta_p$  constant along the frequency scale and throughout the wave development. The reported results are outlined according to the diagnostic scheme mentioned earlier for each type of dissipation spectrum.

##### 4.3.4.1 Results for the Unconstrained $S_{ds}(f)$

Primarily, computations were performed for the unconstrained dissipation spectrum (when the coefficient  $b = b_0 (U_{10} / c_p)$ ). The computations were performed for the model run UP0.5A20W10. The results of the computations showed numerical instabilities during the model runs.

It was determined that the significant exceedance of the absolute values of the dissipation function over the magnitudes of the wind input source term in the high frequency range of wave spectra was the cause of these instabilities. The resulting integral values for the total source term  $S_{tot}$  are shown in Figure 4.68. Moreover, coefficient  $b$  of the dissipation source term takes negative values during wave development.

Figure 4.69 shows coefficients  $a$  and  $b$  as functions of the inverse wave age during the model run UP0.5A20W10. As was discussed earlier, coefficient  $b$  cannot be a negative number. As the result of these factors, the wave spectra were taking shapes inconsistent with the experimental data. The results lead to the conclusion that the unconstrained spectral tail for the dissipation source function does not produce desirable outcomes during the model runs. Therefore, the new form of the spectral dissipation source term was henceforth considered only in terms of the constrained high frequency spectral tail.

#### 4.3.4.2 Results for the Constrained $S_{ds}(f)$

The main results of the current study are presented in this section. All computations were performed for the new form of the dissipation source term with the constrained high frequency spectral tail (bound with the  $S_{in}(f)$  spectral tail). Initially, model validation was performed for the wind speed  $U_{10} = 10$  m/s applying different values to the functional parameters of the dissipation source term mentioned earlier in Section 4.3.1.

After a number of attempts, the best performing set of the parameters was determined and these values were tested for the other wind speeds mentioned in Section 4.3.1. The model results were grouped and presented according to the list of output parameters outlined in Section 4.3.2.

Seeking an optimal fit to the target evolution curves (Babanin and Soloviev, 1998), the dissipation rate  $R$  was adjusted in the range of very young waves  $U_{10} / c_p = [4.5, 5.5]$  by obtaining the variance of the wave spectra within 10% of the range of the target experimental values. To the best of the researcher's knowledge, there exists no experimental evidence relating to the dissipation rates of very young waves. Therefore, the dissipation rate of the short scale waves was selected by fitting the variance to the target experimental data (Babanin and Soloviev, 1998).

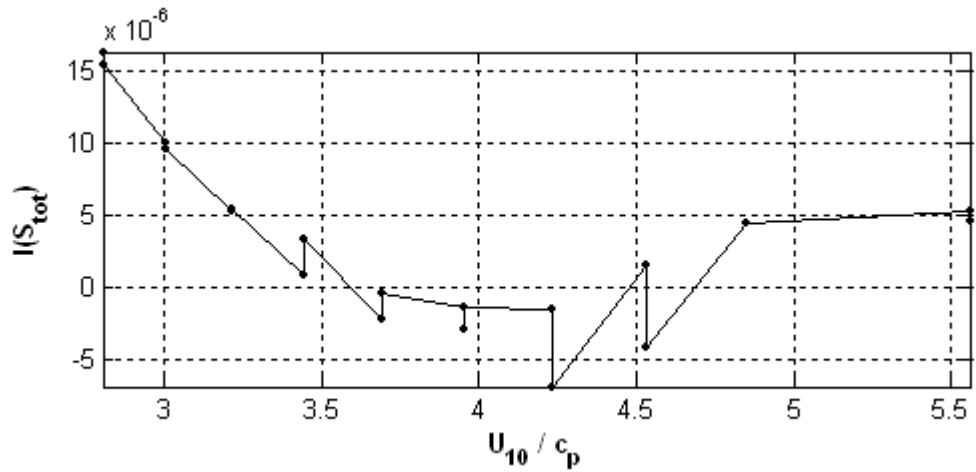


**Figure 4.68** The integral of  $S_{tot}$  as function of the inverse wave age produced by the model during the run UP0.5A20W10.

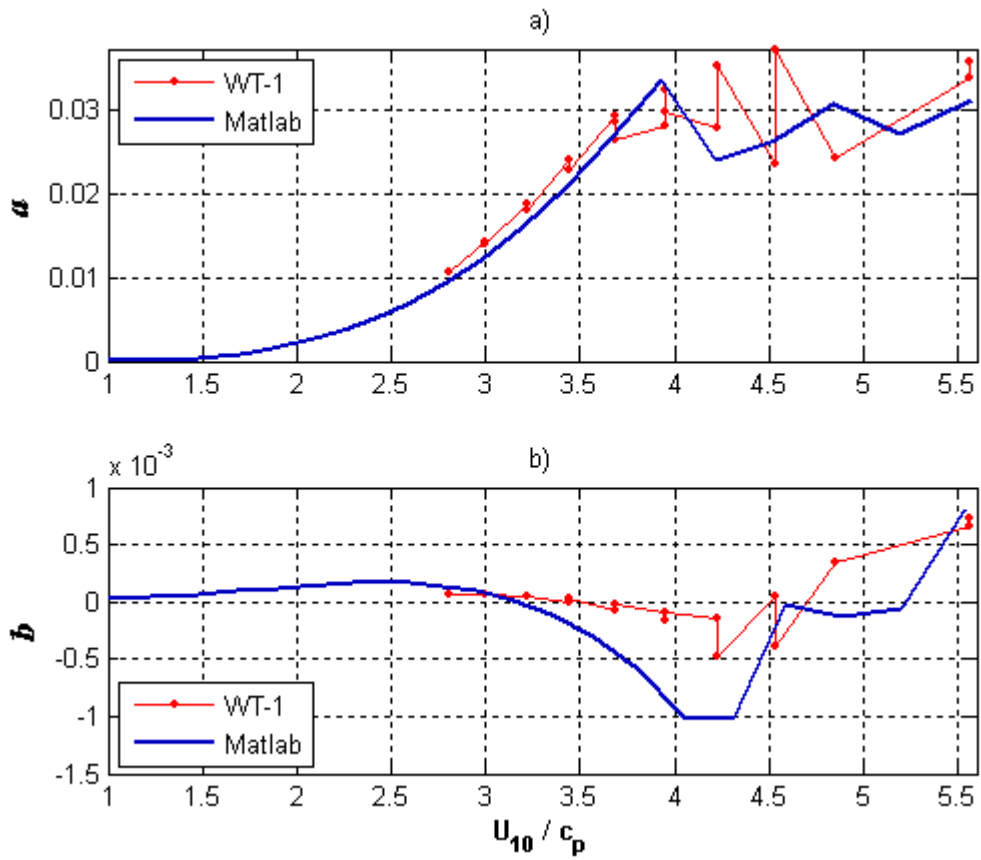


**Figure 4.69** Coefficient  $a$  and  $b$  during the model run UP0.5A20W10.

**Growth Curves.** Figure 4.70 shows the growth curves of the model run CP0.5A20W10 compared to the experimental curves of Babanin and Soloviev (1998). The dashed lines correspond to the 10% approximation of the experimental curve (plain line). The growth of non-dimensional energy as a function of non-dimensional frequency space  $\varepsilon$  ( $\nu$ ) is presented in Figure 4.70, subplot (a). Subplot (b) shows the non-dimensional energy growth as a function of inverse wave age  $\varepsilon$  ( $U_{10}/c_p$ ).

Figure 4.70b shows the intense growth of wave energy at the early stages of wave development  $U_{10}/c_p = [4.7, 3.8]$ . The maximum difference between the model results and the observational data relating to the spectral energy was noticed for average developed waves with  $U_{10}/c_p = [3.5, 2]$ . As wave development approaches the full development stage, wave growth slows. This trend is shown by the gradual change of the slope of the growth curve towards the lower frequencies (see Figure 4.70a). This trend is consistent with the wave observations.

The slowing of wave growth is clearly illustrated in Figure 4.71 in subplots (a) and (b) which show non-dimensional frequency and non-dimensional energy as functions of non-dimensional duration  $\nu$  ( $\zeta$ ) and  $\varepsilon$  ( $\zeta$ ), respectively. In subplots (a) and (b) this trend is shown as a transition of the slope into a plateau. The growth curves  $\nu$  ( $\zeta$ ) and  $\varepsilon$  ( $\zeta$ ), presented in Figure 4.71, are compared with the experimental data obtained by other authors, such as Kahma (1981), Donelan et al. (1985) and Babanin and Soloviev (1998). The comparison shows an encouraging agreement between the model results and the presented observational data for young dominant waves.

For intermediate dominant waves, the model results are close to the experimental data of Kahma (1981). For well-developed waves, the model produces wave spectra close to the data reported by Donelan (1985). Only for fully developed waves do the model results approach the experimental data of Babanin and Soloviev (1998). The trend of energy growth in the waves is determined by two factors. First, at  $U_{10}/c_p = 4.7$  the wave spectrum is transformed from a  $f^{-5}$  to  $f^{-4}$  slope spectral tail and the second is the effect of the transition of fully separated wind flow to non-separated flow over the dominant waves (see Figure 4.3, the step-form behaviour of the growth rate of dominant waves.)

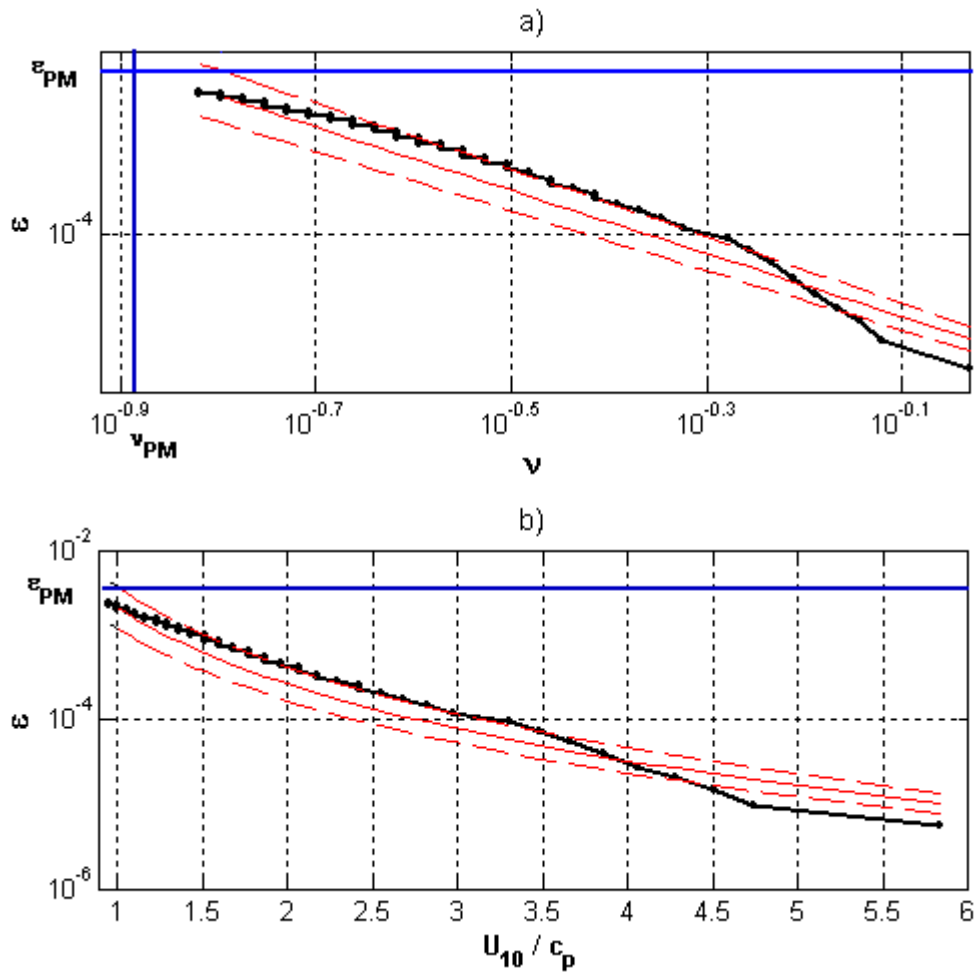


**Figure 4.70** Growth curves of the model run CL1P0.5A20W10. The subplot (a) shows the growth of non-dimensional energy  $\varepsilon$  as a function of non-dimensional frequency  $\nu$ ; and subplot (b) shows the growth of non-dimensional energy  $\varepsilon$  as a function of the inverse wave age  $U_{10}/c_p$ . The model results are compared with the experimental data of Babanin and Soloviev (1998) (plain line) with 10% approximation limits (dashed lines). The  $\varepsilon_{PM} = 3.64 \cdot 10^{-3}$  and  $\nu_{PM} = 0.13$ , the magnitudes of the Pierson-Moskowitz limit are also shown.

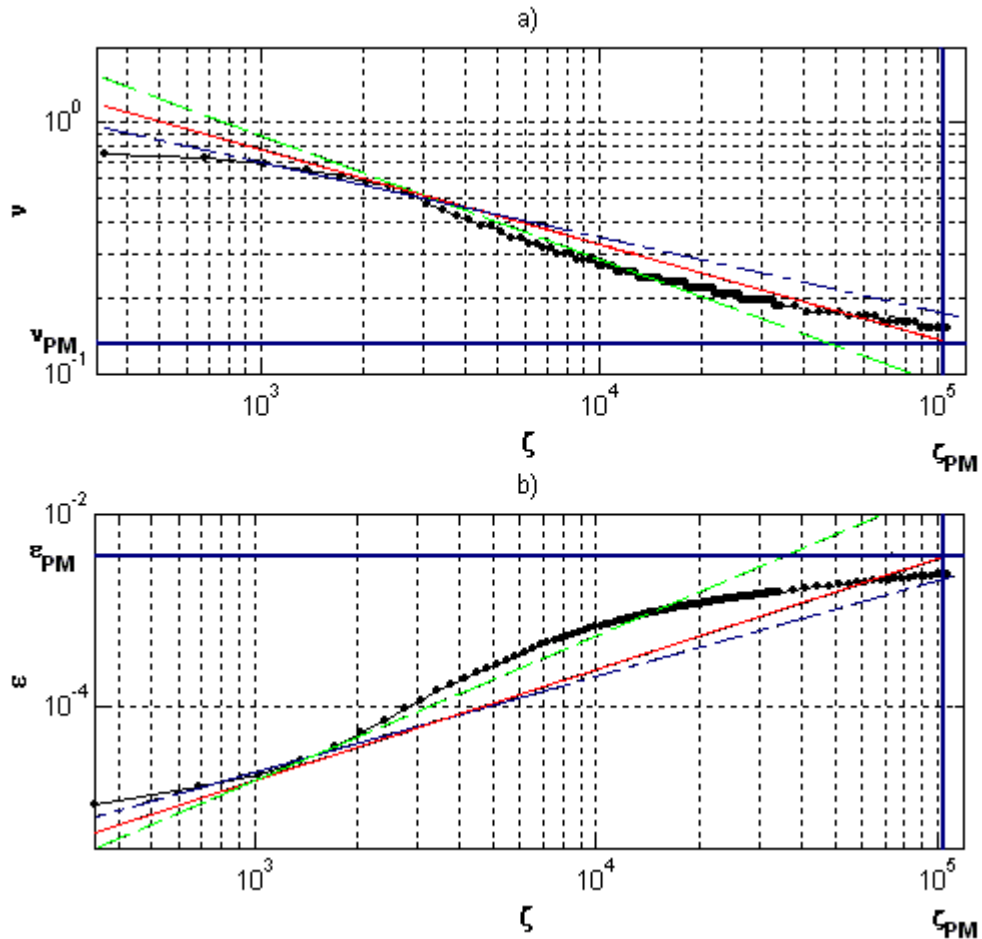


**Figure 4.71** Growth curves of the model run CL1P0.5A20W10. The subplot (a) shows the growth of non-dimensional frequency  $\nu$  as a function of non-dimensional time  $\zeta$ ; and subplot (b) shows the growth of non-dimensional energy  $\varepsilon$  as a function of non-dimensional time  $\zeta$ . The model results are compared with the experimental data of Kahma (1981) (dashed line), Donelan et al. (1985) (dash-dotted line) and, Babanin and Soloviev (1998) (plane line). The magnitudes of Pierson-Moskowitz limit are also shown as  $\varepsilon_{PM}$ ,  $\nu_{PM}$ , and  $\zeta_{PM}$ .

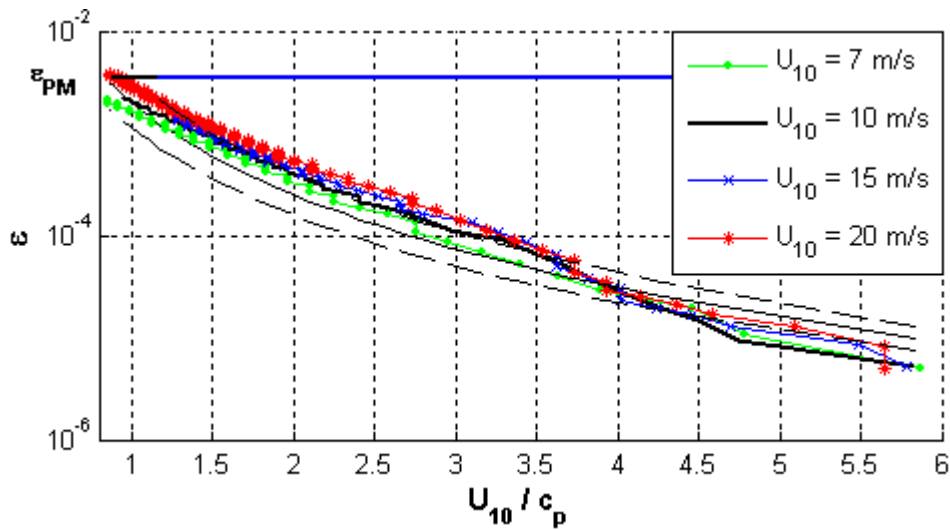


**Figure 4.72** Comparing the growth curves computed for the different wind speeds  $U_{10} = 7\text{m/s}$ ,  $10\text{m/s}$ ,  $15\text{m/s}$  and  $20\text{m/s}$ . with the experimental data of Babanin and Soloviev (1998) (plain line) with 10% approximation limits (dashed lines). The magnitude of energy for the Pierson-Moskowitz limit is also shown as  $\varepsilon_{PM}$ .

In general, the results show that the trend of spectral level  $\alpha$  is to decrease. However, the stepwise increase of the spectral level is clearly shown in the range of average developed waves  $U_{10} / c_p = [3, 4.5]$ . This distinct stepwise increase traces the flow separation effect included in the new form of the wind input source term. This effect becomes apparent with the lag due to the delay of the model response in reflecting the stepwise increase in the growth rate at  $U_{10} / c_p = [4, 4.5]$  (see Figure 4.3).

The present study found that the magnitudes of spectral level  $\alpha$  relate to the magnitudes of wave-induced stress. The results indicate that the larger the wind stress, the higher the spectral level of the resulting wave spectrum. This relationship is due to the selection of wind stress as a determining factor of the new form of the wind input source term, which defines the increment of the spectral energy and consequently the spectral level of the resulting wave spectra. Based on this fact, it can be concluded that in WAVETIME-1 the magnitude of the wind stress determines the spectral level of the wave spectra which have been generated.

Figure 4.72 compares the growth curves of wave development under different wind speeds  $U_{10} = 7, 10, 15$  and  $20\text{m/s}$  with the experimental data of Babanin and Soloviev (1998). This comparison shows encouraging agreement between the model results and observations of Babanin and Soloviev (1998) for all selected wind speeds. The results of computations indicate that the model is able to reproduce growth curves that are consistent with the existing observational data, even for very strong winds.

**Level of the Equilibrium Interval  $\alpha$ .** Figure 4.73 presents the values of spectral level  $\alpha$  of the equilibrium interval of wave spectra produced during the model run CL1P0.5A20W10. The model results were compared with the experimental values of spectral level  $\alpha$  obtained by other authors (Hasselmann, 1973; Donelan, 1985; Bandou, 1986; Evans, 1990 and, Babanin and Soloviev, 1998). The comparisons show an encouraging consistency of the model results with the experimental values. The general trend of the spectral level is shown by the linear approximation of the values of  $\alpha$  (bold line). The spectral level can be regulated by other factors which also affect dissipation rates, including the dissipation rate  $R$ , including the directional spreading parameters  $p$ ,  $\theta_p$ ,  $\Delta\theta_f$  and  $\Delta\theta_{ucp}$ , all of which influence the bimodal shape in all directions.

**The Average Level  $\alpha_{BY}$  and the Exponent  $n$ .** Figure 4.74 shows the values of the non-dimensional spectral parameters  $\alpha_{BY}$  and  $n$  for the wind direction slice of the wavenumber spectra as functions of the inverse wave age  $U_{10}/c_p$ . The parameters  $\alpha_{BY}$  and  $n$  were computed by applying the least square method to data from the model in the high frequency range  $f > 2.5f_p$ .

The model results were compared with the results of Banner (1990) (see the bold lines in both subplots). Subplot (a) shows encouraging agreement between the model results (line with dots) and the values suggested by Banner (1990) (bold line). Subplot (b) shows that in general the modelled spectra have less slope exponent than suggested by Banner (1990).

Similar results reported by Banner and Young (1994) showed less rapid decay of the modelled wavenumber spectra than the results of Banner (1990). In general, the results indicate that the model can produce wave spectra with a spectral level matching the experimental spectra in high wavenumber regions.

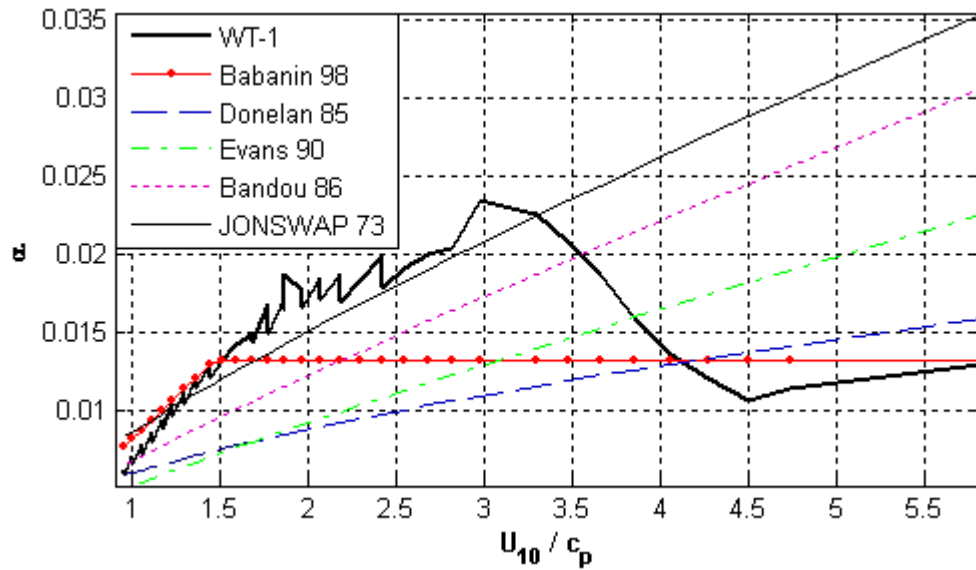


**Figure 4.73** Values of  $\alpha$  during the model run CL1P0.5A20W10. The results of computations are compared with the experimental values obtained by different studies.

**The Similarity Parameter  $\zeta$ .** Figure 4.75 shows the similarity parameter  $\zeta$  as a function of the inverse wave age  $U_{10}/c_p$  for the model run CL1P0.5A20W10. Figure 4.75 shows the value of  $\zeta = 0.78$  evaluated for the wave spectrum at the given wavenumber  $k = 0.5\text{cpm}$  for the inverse wave age  $U_{10}/c_p = 1.64$  corresponding to the value  $c_p/u^* = 16$  from Banner and Young (1994). The obtained value of  $\zeta = 0.78$  indicates that for this stage of wave development the wind direction slice of the wavenumber spectrum has a wavenumber tail close to that suggested by Banner (1990).

Moreover, the results of computations presented in Figure 4.75 show that the model produces the wavenumber spectrum suggested by Banner (1990) (when  $\zeta = 1$ ) for the inverse wave age  $U_{10}/c_p = 1.2$  (see Figure 4.75 the intersection of horizontal bold line with the curvy line with dots). Furthermore, Figure 4.77 shows that  $\zeta$  takes values close to 1 several times at different stages of wave development: the first for young waves with  $U_{10}/c_p = 4.75$ ; the second for average developed waves with  $U_{10}/c_p = 2.5$ ; and the third for well developed waves with  $U_{10}/c_p = 1.2$ . For fully developed waves the values of  $\zeta$  are retained within 20% of the similarity value  $\zeta = 1$ .

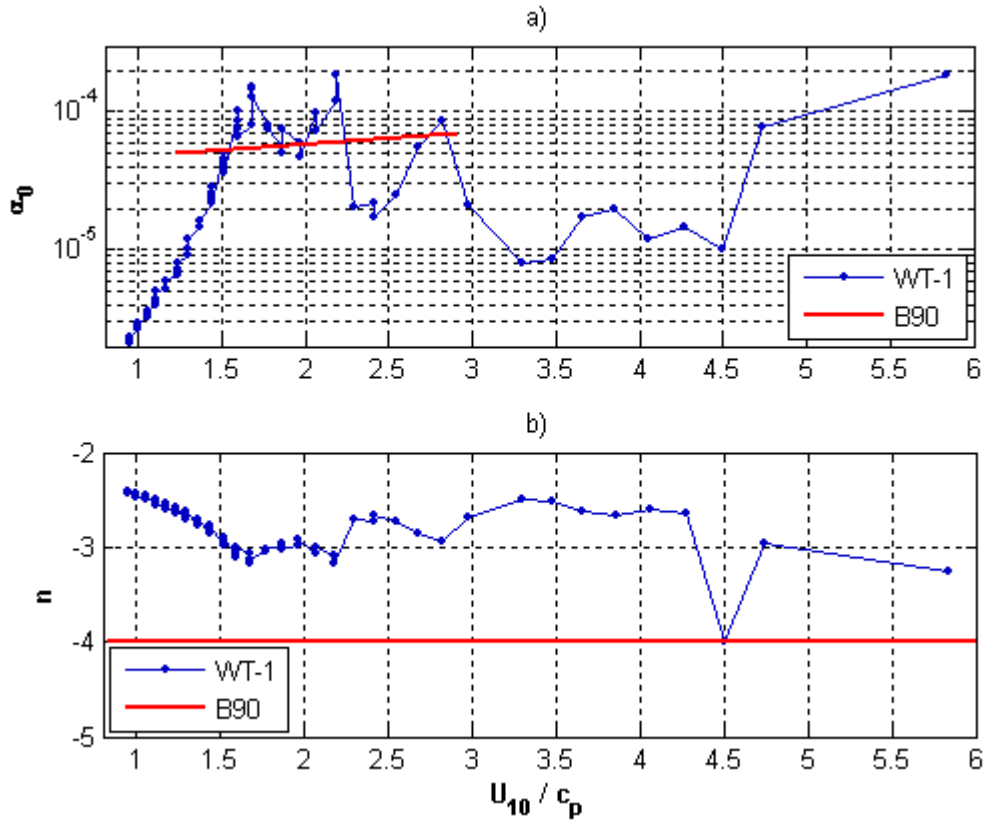


**Figure 4.74** Values of nondimensional spectral parameters  $\alpha_{BY}$  (subplot [a]) and  $n$  (subplot [b]) for wind direction slice of the wavenumber spectra as functions of the inverse wave age  $U_{10} / c_p$  for the model run CL1P0.5A20W10. The parameters  $\alpha_{BY}$  and  $n$  were computed by means of the least square method for the model data in the high-frequency range  $f > 2.5f_p$ . The model results (lines with dots) are compared to the results of Banner and Young (1994) (bold lines).

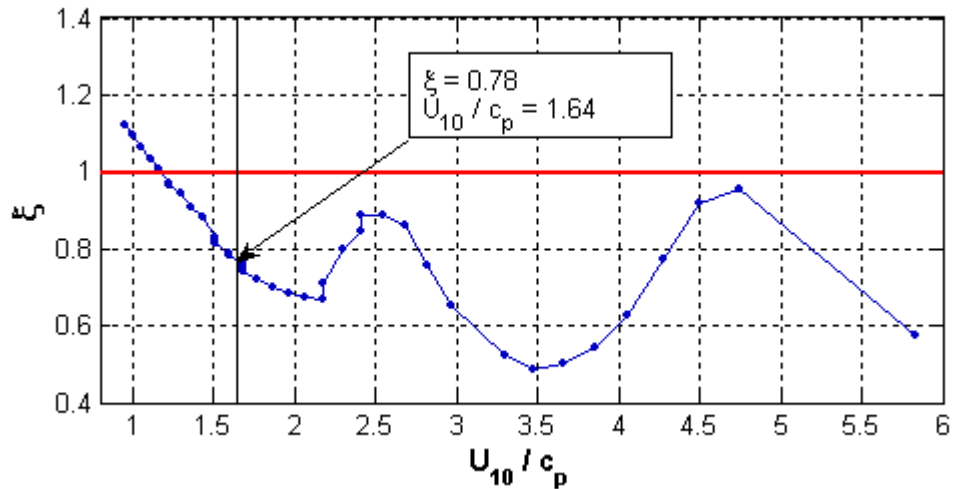


**Figure 4.75** The similarity parameter  $\zeta$  as a function of the inverse wave age  $U_{10}/c_p$  computed from the results of the model run CL1P0.5A20W10.

It is worth noting that the values of the similarity parameter  $\zeta$  are determined by the magnitudes of the equilibrium spectral level  $\alpha$  (see Figure 4.73). It is clearly shown that for the range of the wind forcing  $U_{10}/c_p = [2.8, 4.8]$ , the similarity parameter  $\zeta$  shows the maximum difference between the spectra produced by the model and that suggested by Banner (1990). For the same range of wind forcing conditions, the shape parameter  $\alpha$  shows an intensive growing trend in its values which demonstrate a step-like jump (see Figure 4.73). As was mentioned in the previous section, the step-like jump is related to the sudden increase of growth rates marking the transition of the wind flow from fully separated to non-separated from the water surface. On this basis, it can be concluded that the difference indicated by the similarity parameter  $\zeta$  in the range  $U_{10}/c_p = [2.8, 4.8]$  may be related to the change of wind flow conditions over dominant waves. This topic will be discussed further in Chapter 5.

**Directional Spreading Function  $D(f, \theta)$ .** Figure 4.76 shows the directional spreading function at frequencies  $f_p$ ,  $2f_p$  and  $3f_p$  for intermediate dominant waves with  $U_{10}/c_p = 2.7$  from the model run CL1P0.5A20W10. This directional function has a unimodal shape for the dominant waves. In the high frequency range of the spectrum, it has

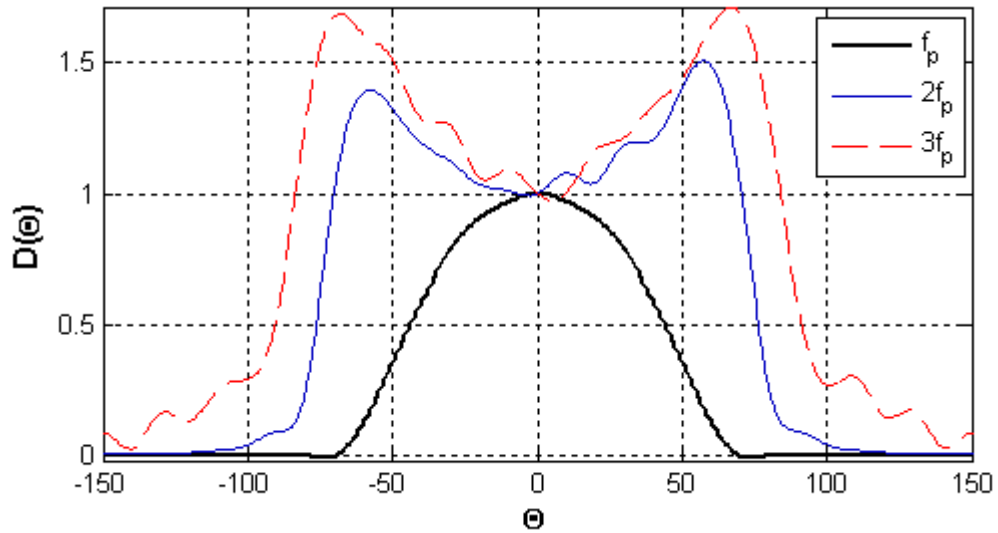
a clearly pronounced bimodal shape with its width increasing towards the short scale waves. More energy is contained in the off-wind direction than in the wind direction. The bimodal structure was maintained by the directional transfer of energy through nonlinear wave-wave interactions.

Figure 4.77 shows the directional spreading function at frequencies  $f_p$ ,  $0.9f_p$ ,  $0.8f_p$  and  $0.7f_p$  for intermediate dominant waves with  $U_{10}/c_p = 2.7$  from the model run CL1P0.5A20W10. The results indicate that directional spreading broadens in the range of frequencies below peak frequency. The bimodality of the spreading is pronounced below  $0.8f_p$ . In the range  $[0.9f_p, f_p]$  the wave spectrum shows unimodal directional spreading. These results are completely consistent with the observations of directional spreading reported by various authors (Young et al., 1995; Babanin et al., 1997; Hwang et al., 2000, and, Wang and Hwang, 2001).

According to the observations, the spreading broadens for frequencies just above and below the spectral peak frequency. At frequencies of approximately twice the peak frequency, however, the unimodal spreading becomes bimodal, and more wave energy propagates at an angle to the wind than in the direction of the wind. The bimodal sidelobes continue to separate with increasing frequency and become larger in magnitude. The results of the current study indicate that the model can reproduce wave spectra with directional spreading shapes that match the observational data.

**Sidelobe Ratio  $\lambda$ .** Figure 4.78 shows the sidelobe ratio  $\lambda$  at the frequencies  $2f_p$  and  $3f_p$  as a function of inverse wave age  $U_{10}/c_p$  during the model run CL1P0.5A10W10. The results indicate the presence of sidelobes as part of the directional spectra ( $\lambda > 1$ ). The bimodality is clearly pronounced starting from young waves where  $U_{10}/c_p = 4.7$ . Furthermore, the results show that the bimodal shape is more pronounced for short scale waves at the frequency  $3f_p$  (dashed line). The results computed for waves with this frequency are consistent with the results of Banner and Young (1994) for their constraint tail run K10CT (their Figure 6).

This match of the results is very interesting in light of the fact that in the present study all model runs were performed for wave spectra with an unconstrained high frequency tail. This indicates that the model is able to reproduce a spectral tail matching the prescribed constrained tail in both shape and spectral level, and even in directional distribution. The latter attribute is discussed in the next section.



**Figure 4.76** Directional spreading function of the wave spectrum at the average stage of wave development ( $U_{10} / c_p = 2.7$ ) from the model run CL1P0.5A20W10. The computations were performed for the directional spectral slices at the frequencies  $f_p$ ,  $2f_p$  and  $3f_p$ . An angle  $\theta = 0$  corresponds to the wind direction.

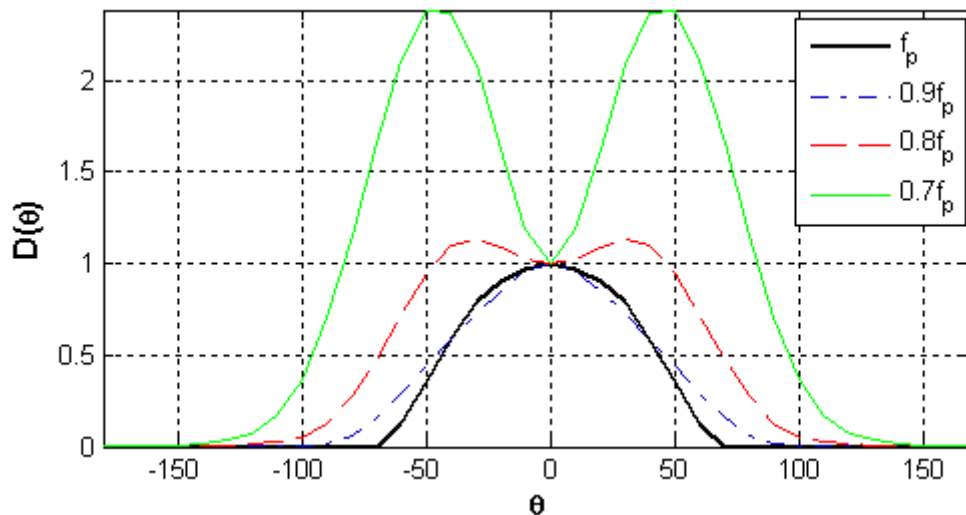


**Figure 4.77** Directional spreading function of the wave spectrum at the average stage of wave development ( $U_{10} / c_p = 2.7$ ) from the model run CL1P0.5A20W10. The computations were performed for the directional spectral slices at the frequencies  $f_p$ ,  $0.9f_p$ ,  $0.8f_p$  and  $0.7f_p$ . An angle  $\theta = 0$  corresponds to the wind direction.

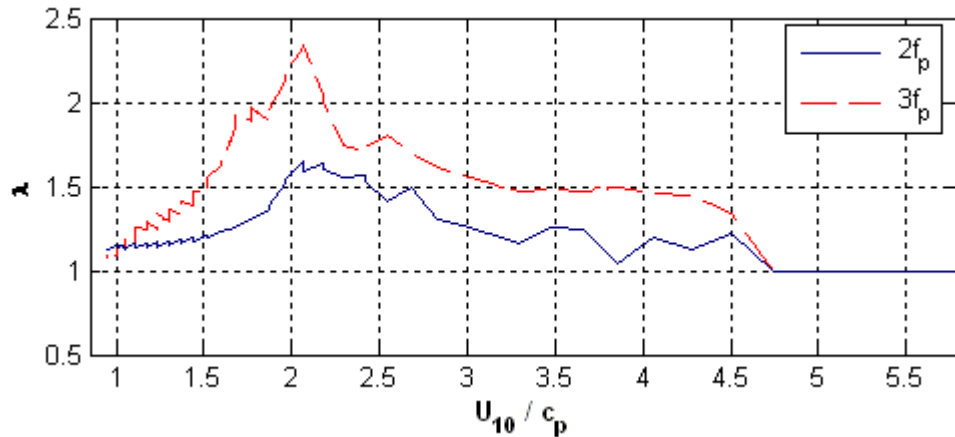


**Figure 4.78** The sidelobe ratio  $\lambda$  at the frequencies  $2f_p$  and  $3f_p$  as a function of inverse wave age  $U_{10}/c_p$  during the model run CL1P0.5A10W10.

**Directional Spreading Width  $A(f)$ .** Figure 4.79a shows the values of the directional spreading parameter  $A$  as a function of the inverse wave age computed for the directional spectra at the frequencies  $f_p$ ,  $2f_p$  and  $3f_p$  during the model run CL1P0.5A20W10, and compared with the experimental dependences of Babanin and Soloviev (1998a). The results show a broadening of the wave spectra above the peak frequency ( $A(f_p) > A(2f_p) > A(3f_p)$ ). Behavior of the angular spread at the spectral peak is reproduced well. Figure 4.79a shows the narrowing of the directional spectral width at the spectral peak of wave development (see increasing trend of the  $A(U_{10}/c_p)$  with the decreasing  $U_{10}/c_p$ ). For higher frequencies and younger waves, agreement is achieved. However, for later wave development stages some limitations are still to be addressed. As is illustrated, the model produces wider spectra in the range of short scale waves than the experimentally obtained data (see comparisons for  $A(2f_p)$  and  $A(3f_p)$ ).

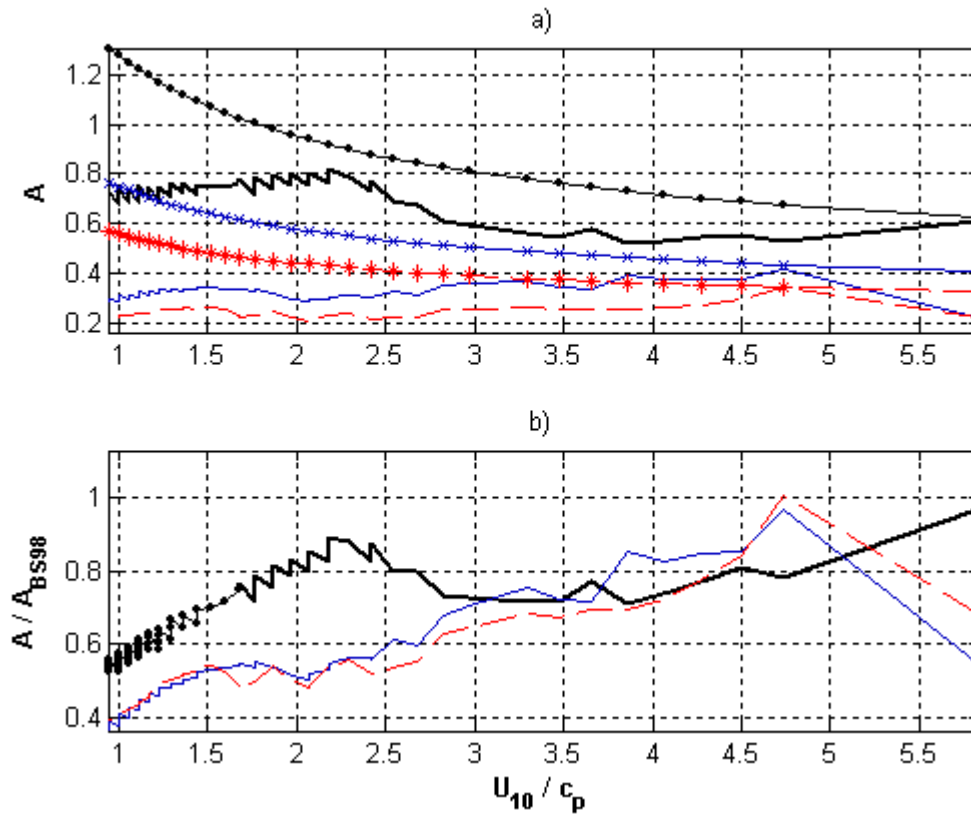


**Figure 4.79** Subplot (a) shows comparisons of the model results for the directional spreading parameter  $A$  (lines with dots, crosses and asterisks) with the experimental data of Babanin and Soloviev (1998a) (bold, plain and dashed lines). The computations were performed for the directional spectral slices at the frequencies  $f_p$ ,  $2f_p$  and  $3f_p$ . Subplot (b) shows the relative magnitudes of the directional width computed for the model spectra compared to the experimental values  $A_{BS98}$ .

The comparison between the model results and the experimental data can be clearly demonstrated using the ratio of the compared values. Figure 4.79b shows the relative magnitudes of the directional width computed for the model spectra compared to the experimental values  $A_{BS98}$ .

It is clearly shown that for young waves where  $U_{10}/c_p > 3$ , the directional width is close to the experimental data (line with dots). However, for well-developed waves ( $U_{10}/c_p < 2.5$ ), the wave spectra are broader than experimentally observed. Further investigation was required to achieve agreement between the modelled directional spectra and the observed spectra.

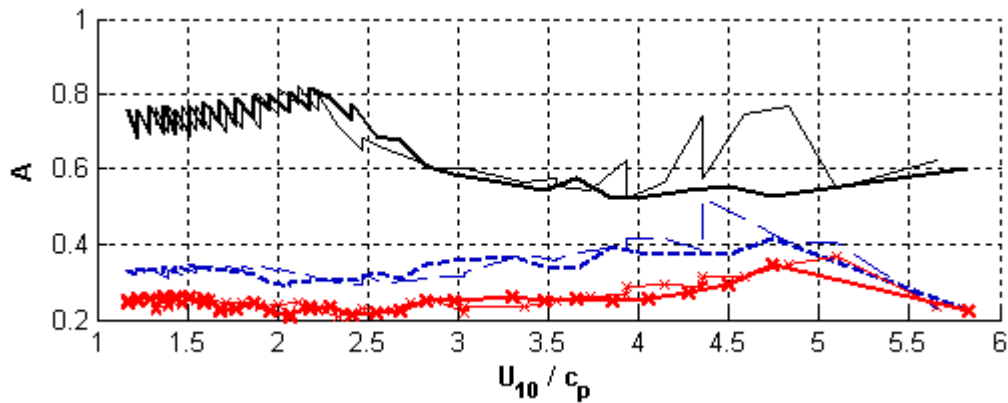


**Figure 4.80** Comparisons of the directional spreading parameter  $A$  computed for different wind speeds  $U_{10} = 10$  (bold lines),  $20$  (plain lines) m/s. The computations were performed for the directional spectral slices at the frequencies  $f_p$  (plain line),  $2f_p$  (dashed lines) and  $3f_p$  (lines with crosses).

The effect of broadening the wave spectrum was to influence the directional redistribution of energy by the nonlinear term  $S_{nl}$ . Energy from components in the spectral tail close to the wind direction is transferred to the larger angles. Such redistribution occurs because the sum of  $S_{in} + S_{ds}$  is negative at such angles.

The magnitudes of the sum of  $S_{in} + S_{ds}$  at oblique angles are controlled by the parameters of the directional spreading function (Equation 4-48) of the dissipation source term  $S_{ds}$  ( $p$ ,  $\theta_p$ ,  $\Delta\theta_f$  and  $\Delta\theta_{ucp}$ ). Variation of these parameters results in the alteration of the directional width of the wave spectra. When the trough parameter  $p$  is decreased, the width of the directional lobes is increased. Consequently the magnitudes of the dissipation source term are increasing in all directions excluding the directions of the spectral lobes (Figure 4.57). By increasing the peak angle  $\theta_p$  the dissipation source term is decreased in the direction of the wind and increased at angles larger than  $\theta_p$ .

Figure 4.80 shows a comparison of the values of the angular width parameter  $A(f_p)$  computed from model runs with different wind speeds  $U_{10} = 10$  m/s and  $20$  m/s. The results indicate that with increasing wind speed the angular width of the wave spectra does not change significantly.

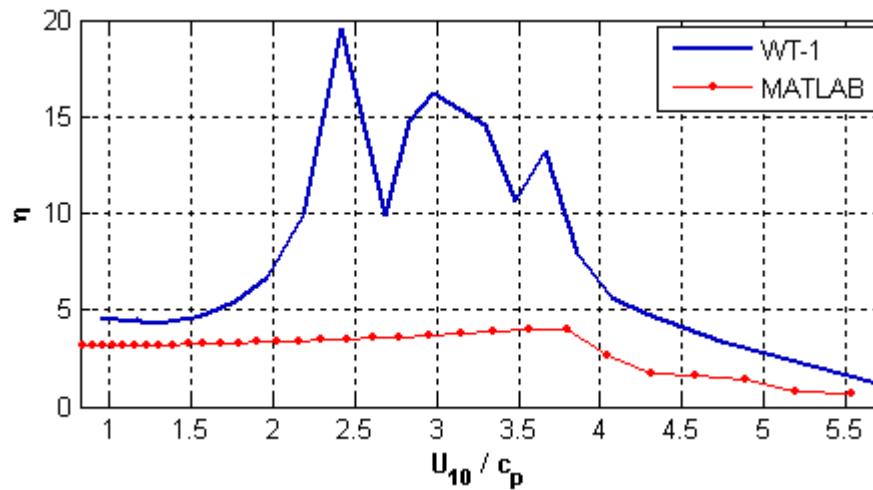


**Figure 4.81** Comparison of the correction rates  $\eta$  as functions of the inverse wave age  $U_{10}/c_p$  computed for the model run CP0.5A20W10 (shown as WT-1) and for the MATLAB modeled wave evolution for the wind speed  $U_{10} = 10\text{m/s}$ .

**Model Results for  $S_{IN}$  Source Function.** The method developed to correct the new wind input source function allowed the degree of adjustment of the function to be estimated in order to achieve correspondence with the correct value of the wave-induced stress in terms of the correction rate  $\eta$  introduced in Section 4.1.3.

Figure 4.81 shows the correction rate  $\eta$  as a function of the inverse wave age  $U_{10}/c_p$  for the model run CP0.5A20W10 (shown as WT-1) and for the MATLAB modelled wave evolution for the wind speed  $U_{10} = 10\text{m/s}$ . Using MATLAB, for each stage of wave development the wind input source term was computed for the Combi-type wave spectrum, with the spectral parameters corresponding to the observations of Hasselmann et al. (1973), Donelan (1985), and Babanin and Soloviev (1998) for this stage of wave development.

Therefore, in MATLAB, source functions at each previous stage did not contribute to the subsequent wave spectrum. This type of modelling of wave development can be called pseudo-evolution of waves. In contrast to this behaviour, in real-time wave models each following spectrum is a result of the contribution of the activated source functions computed for the wave spectrum at the previous stage.

Therefore, in real-time wave models there is interdependence between the wave spectra and the source functions. The difference between the results of these two modelling approaches allows the performance of the real-time wave model to be estimated relative to the observational data and establishes the source of bias. This method proved very helpful during the present research.

The correction rate for the model run CP0.5A20W10 shows higher suppression rates than those for the wind input source term computed for the spectra modeled in MATLAB. The maximal difference was obtained for average developed waves where  $U_{10} / c_p = [2, 4]$ . In particular, in the same range, the spectral level  $\alpha$  has an increasing trend as shown in Figure 4.73. This indicates that the wind input source function exhibits higher growth rates than can actually be observed in nature. It's quite possible, that the higher growth rates are related to the transition of the wind flow from fully-separated to non-separated. In Figure 4.3 (see Section 4.1), the growth rate  $\gamma$  reaches its maximum at  $U_{10} / c_p = 4$ . Based on this observation, it can be concluded that this feature may relate to that shown in Figure 4.81 difference of correction rates. This difference between the model run CP0.5A20W10 and the MATLAB results indicates that probably the magnitude of the step-like jump of the growth rate (see Figure 4.3) needs further experimental evaluation. Moreover, the magnitude of this jump may relate to the magnitude of the wind speed (discussed later in this chapter).

Figure 4.82 shows the correction rate  $\eta$  as a function of the inverse wave age  $U_{10} / c_p$  computed for the model runs with different wind speeds  $U_{10} = 7, 10, 15$  and  $20$  m/s. The results indicate that light winds require higher suppression rates for  $S_m(f)$  than strong winds. The differences are significant in the same range of  $U_{10} / c_p = [2, 4]$  as mentioned above. This indicates that one of the reasons for this difference could be that the magnitude of the step-like jump of the growth rate may relate to the magnitude of the wind speed. As was shown in Figure 4.3, the magnitude of this jump was the same for all the wind speeds. Further experimental study is recommended to determine the relationship between the magnitude of the sudden increase of the growth rate and wind speed.

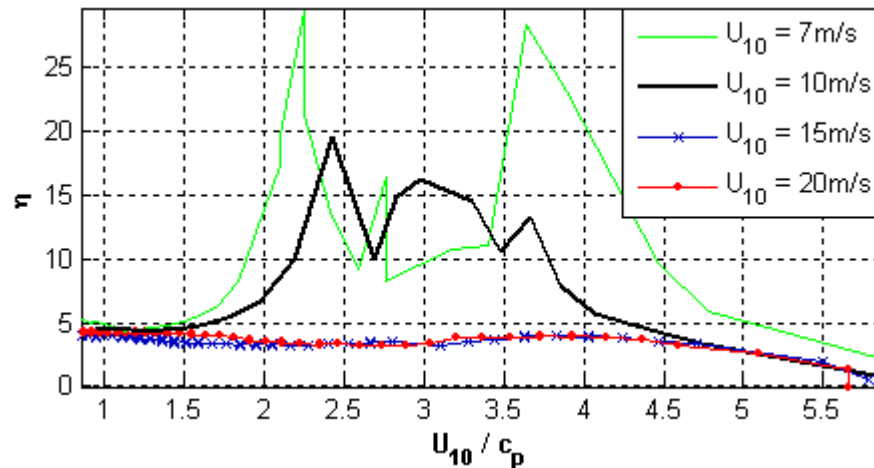


**Figure 4.82** Comparisons of the correction rate  $\eta$  as a function of the inverse wave age  $U_{10}/c_p$  computed for model runs with various wind speeds  $U_{10} = 7\text{m/s}$ ,  $10\text{m/s}$ ,  $15\text{m/s}$  and  $20\text{m/s}$ .

### **Model Results for the $S_{DS}$ Source Function.**

Figure 4.83 shows coefficients  $a$  and  $b$  of the new dissipation source term  $S_{ds}(f)$  as functions of the inverse wave age  $U_{10}/c_p$  for the model run CP0.5A20W10 (assigned as WT-1) in both subplots (a) and (b). The experimental value of  $a_{exp} = b_{exp} = 0.0065$  is shown in both subplots. Coefficients  $a$  and  $b$  from the model run CP0.5A20W10 were compared with coefficients of the dissipation source term computed from the MATLAB pseudo-evolution of the Combi spectra for wind speed  $U_{10} = 10\text{m/s}$  (assigned as MATLAB). Subplot (a) shows an encouraging agreement between the model run CP0.5A20W10 and the results obtained from MATLAB. Moreover, coefficient  $a$  obtained from the model run CP0.5A20W10 takes the experimental value  $a_{exp} = 0.0065$  in the range of average developed waves where  $U_{10}/c_p \sim 2.5$ . The results shown in subplot (a) indicate the excellent performance of the new dissipation source function in the range of dominant waves. Subplot (b) shows an encouraging agreement for coefficient  $b$  between the results of the model run CP0.5A20W10 and the experimental value  $b_{exp} = 0.0065$ . The agreement between these results was obtained in the range of  $U_{10}/c_p = [2.3, 4.3]$ .

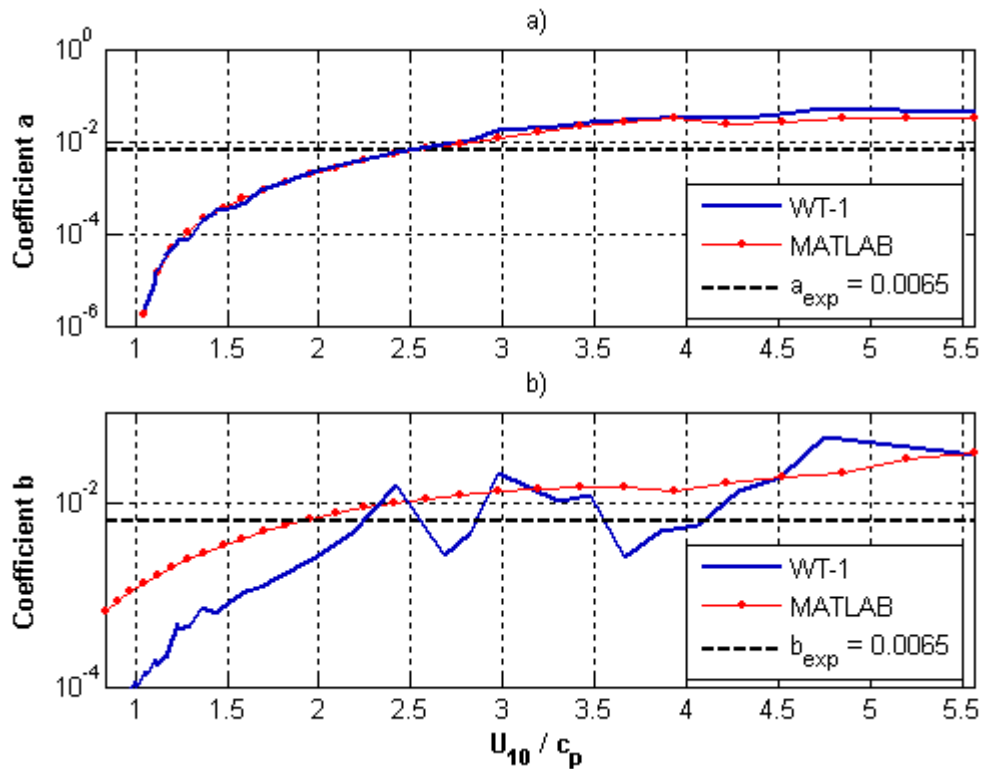


**Figure 4.83** Coefficients  $a$  and  $b$  of the new dissipation source term  $S_{ds}(f)$  as functions of the inverse wave age  $U_{10}/c_p$  for the model run CP0.5A20W10 (assigned as WT-1) in the both subplots (a) and (b). The experimental value of  $a_{exp} = b_{exp} = 0.0065$  is shown in both subplots. The coefficients  $a$  and  $b$  from the model run CP0.5A20W10 are compared with coefficients of the dissipation source term computed from the MATLAB pseudo-evolution of the Combi spectra for the wind speed  $U_{10} = 10\text{m/s}$  (assigned by MATLAB).

Comparing coefficient  $b$  from the model run CP0.5A20W10 with the results of the MATLAB computations, the discrepancies are pronounced, particularly for well-developed waves. Identification if the source of this discrepancy is a complex task. The complexity is based on the specific construction of the model which was discussed in Section 4.3.2. Based on the model structure, the dissipation source term is computed in such a way as to correspond to the wind input source term, which is, in turn, corrected to satisfy the current value of the wave-induced stress.

As was discussed in Section 4.1, the correction of the wind input source function was applied in the high frequency range of the wave spectrum. In this range of the wave spectrum the magnitudes of the dissipation rates are determined by coefficient  $b$ . Therefore, any correction applied to the wind input source term significantly affects the values of coefficient  $b$ .

Since the correction of the wind input source term was described in terms of correction rates  $\eta$ , coefficient  $b$  may exhibit relational dependence on the correction rate. Consequently, the high level of suppression of the wind input source term results in lower magnitudes of coefficient  $b$ . This relationship is pronounced in the range  $U_{10}/c_p = [2, 4]$ , where coefficient  $b$  exhibits uneven behavior. For the range of fully developed waves, the reduced values of coefficient  $b$  may be produced by low spectral values, since the dissipation source term depends on the wave spectrum.

Figure 4.84 shows coefficients  $a$  and  $b$  as functions of the inverse wave age  $U_{10}/c_p$  for the model runs computed with different wind speeds  $U_{10} = 7, 10, 15$  and  $20$  m/s. Subplot (a) shows that coefficient  $a$  remains the same for all winds. This result indicates the magnitude of the relation between wind energy transfer to the waves and the dissipation energy present independent of wind speed. The inherent breaking of waves is increased with increasing wind speed. This increase is due to the increase of the residual between the values of the wave spectrum and the threshold spectrum  $\Delta F = F(f) - F_T(f)$  corresponding to an increase of wave steepness at higher wind speeds. Due to this increase of the  $\Delta F$ , coefficient  $a$  remains the same. This result shows that the dissipation rates relate to the hydrodynamic properties of the waves.

Figure 4.84b shows that coefficient  $b$  for young waves did not exhibit a relationship to the wind speed similar to the MATLAB results for the Donelan (1985) spectra (see Figure 4.52b). However, for the Combi spectra (see Figure 4.52c) the MATLAB pseudo-evolution runs, showed that the values of coefficient  $b$  for young waves were increasing in correspondence with the wind speed. However, both Figure 4.52b and Figure 4.52c show that these differences are not significant at later stages of wave development, which supports the WAVETIME-1 results.

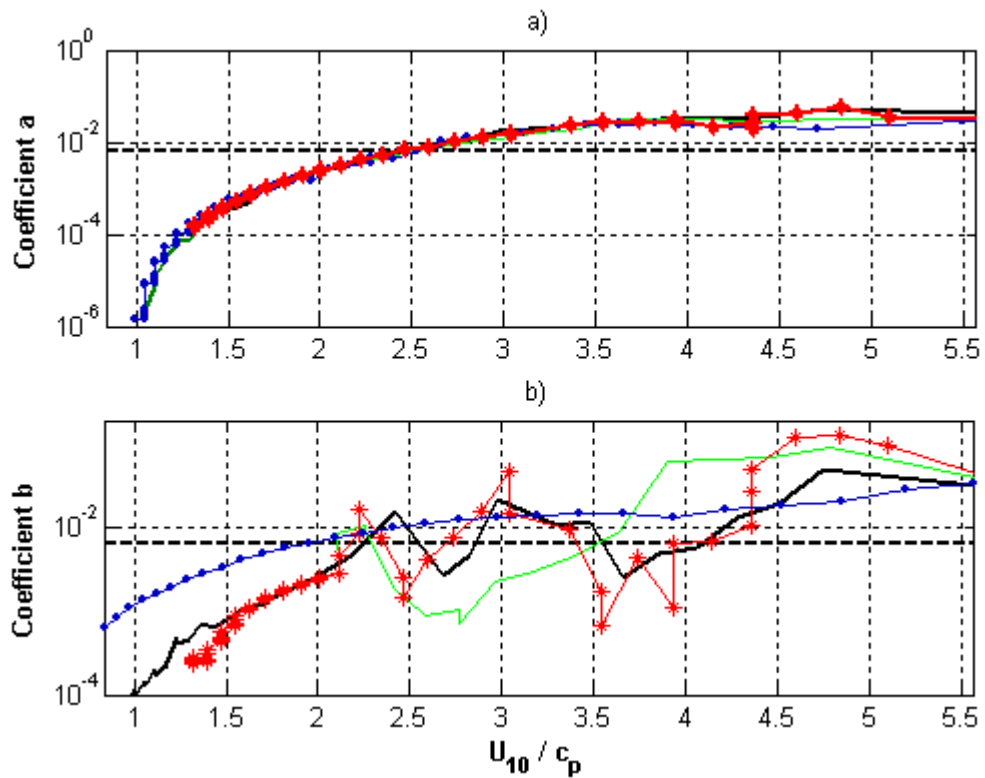


**Figure 4.84** Coefficients  $a$  and  $b$  as functions of the inverse wave age  $U_{10} / c_p$  computed for the model runs for different wind speeds  $U_{10} = 7\text{m/s}$  (plain line),  $10\text{m/s}$  (bold line),  $15\text{m/s}$  (line with dots) and  $20\text{m/s}$  (line with asterisk).

In conducting the MATLAB computations, it was agreed that all constraints had to be satisfied, and the model was basically a verification of how the new parameterisations worked, even though the dependence was not so distinct as it was in the case of the rectified modelling with MATLAB. Therefore, it was concluded that the forced breaking term of the dissipation source function (Eq. 2-29) exhibits a nonlinear relationship to the wind speed of young waves, whereas the inherent breaking term exhibits linear dependence. For the later stages of wave development both terms of the dissipation source function (Eq. 2-29) exhibit linear dependence on the wind speed. Furthermore, Figure 4.84 shows that the model results for both coefficients are in agreement with the experimental value  $a_{exp} = 0.0065$ .

**Exponents of the Spectral Tail of  $S_{in}(f)$  and  $S_{ds}(f)$ .**

One of the outcomes of the novel approach to the interdependence of the wave dissipation and the wind input source terms was the correlation between their slope exponents  $\mu$  in the high frequency range of the spectral tail. Figure 4.85 shows the slope exponent  $\mu$  computed for both source terms  $S_{in}(f)$  and  $S_{ds}(f)$  as a function of the inverse wave age  $U_{10} / c_p$  for the model runs testing different wind speeds  $U_{10} = 7, 10, 15$  and  $20$  m/s shown in the subplots (a), (b), (c) and (d), respectively. Figure 4.85 shows the correlation between the slope exponents of  $S_{in}(f)$  and  $S_{ds}(f)$  for all winds. For young dominant waves where  $U_{10} / c_p > 4$ , the high frequency spectral slopes of  $S_{in}(f)$  and  $S_{ds}(f)$  differ. However, as the waves develop, these exponents converge. Figure 4.85 clearly shows that the slope  $\mu$  decreases during wave development for all wind speeds.

Moreover, as wind speed increases, the range of variation of the slope exponent decreases. This trend correlates with the variation in the correction rates of the increasing wind speed (Figure 4.82). This correlation is determined by the degree to which the wind input source term is suppressed as a result of the correction routine applied at each stage of wave development. Once again, the correction rate significantly influences the spectral shape formation of both source functions  $S_{in}(f)$  and  $S_{ds}(f)$ .

Since the total energy of wave dissipation across the entire wave spectrum is close to the wind energy input to the waves (see Equation 4-32) which is described by the integral relationship between the source functions  $S_{in}(f)$  and  $S_{ds}(f)$ , the spectral magnitudes of these source functions in the short scale range are comparable. This is an important factor to consider when attempting to achieve stability in the operational wave model.

**Comparing to Melville and Matusov (2002).**

The performance of the wave model in reproducing the observed data related to wave breaking was estimated in terms of coefficient  $b_{br}$  computed from the results of the model runs. The objectives of this approach were discussed earlier in Section 4.2.5. The computed coefficient  $b_{br}$  was compared with experimental values  $b_{MM02} = 8.5 \times 10^{-3}$  (Melville and Matusov, 2002) and  $b_{G05} = 2 \times 10^{-5}$  (Gemrich, 2006) and the results of pseudo-evolution performed in MATLAB.

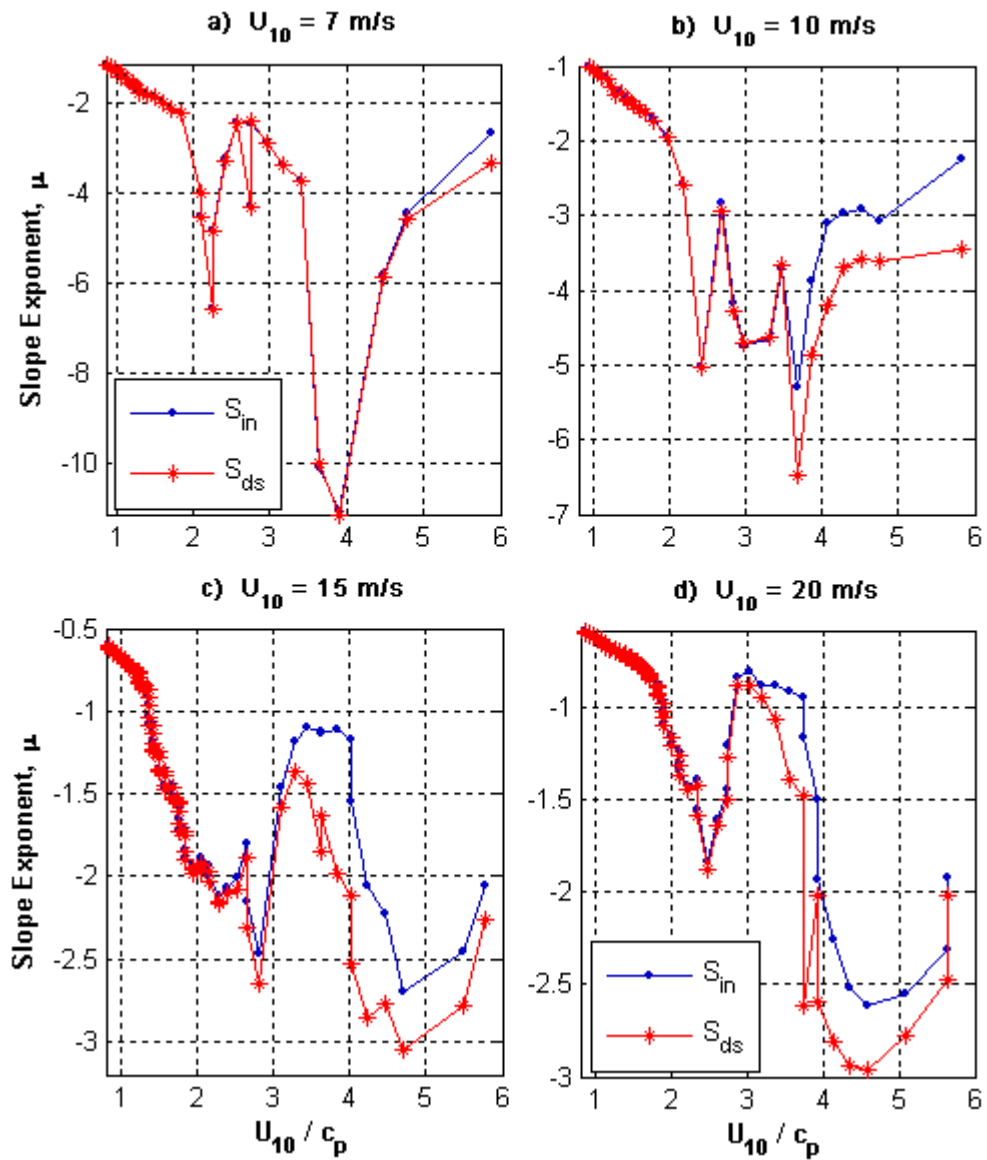
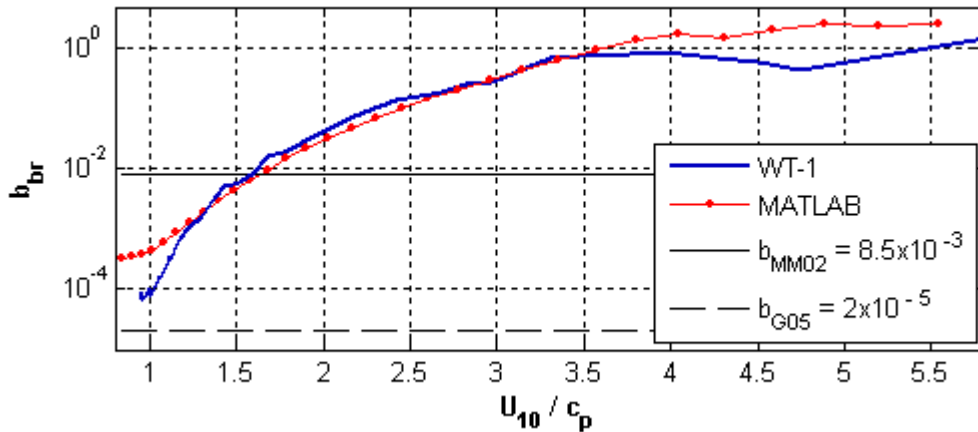


**Figure 4.85** Slope exponent  $\mu$  computed for both source terms  $S_{in}(f)$  (line with dots) and  $S_{ds}(f)$  (line with asterisk) as a function of the inverse wave age  $U_{10} / c_p$  for the model runs with different wind speeds  $U_{10} = 7\text{m/s}$ ,  $10\text{m/s}$ ,  $15\text{m/s}$  and  $20\text{m/s}$  shown in the subplots (a), (b), (c) and (d), respectively.

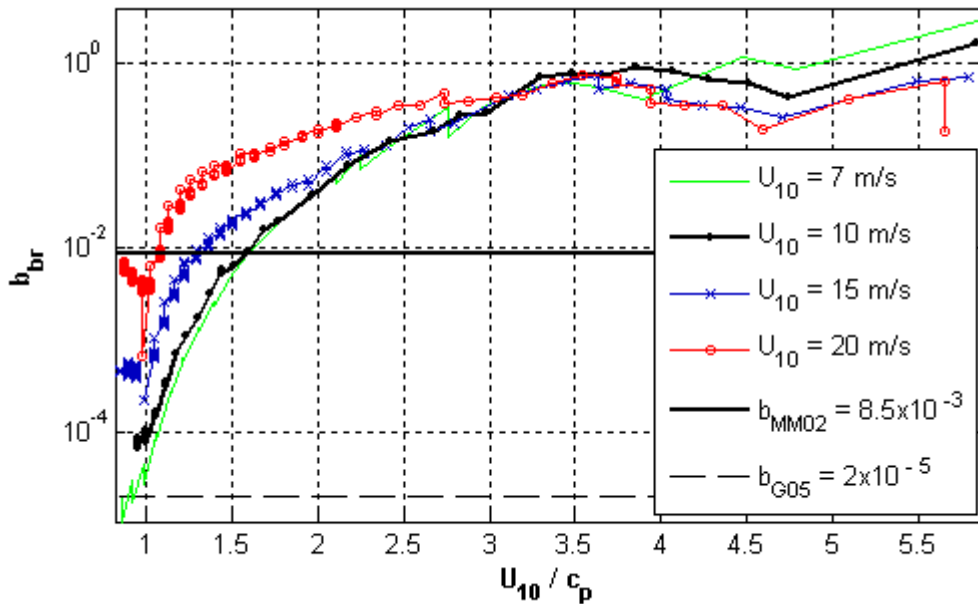
Figure 4.86 shows an encouraging agreement between the results from the model run CP0.5A20W10 and the experimental value of Melville and Matusov (2002) for well-developed dominant waves where  $U_{10} / c_p = 1.55$ . Moreover, the model reproduced the values of coefficient  $b_{br}$  close to the results computed from the MATLAB pseudo-evolution.

Figure 4.87 shows coefficient  $b_{br}$  as a function of the inverse wave age  $U_{10} / c_p$  computed for the model runs with different wind speeds  $U_{10} = 7, 10, 15$  and  $20$  m/s. The results computed from the model data indicate similar behaviour on the part of coefficient  $b_{br}$  as was presented in Figure 4.62. However, in Figure 4.87 the model results are more converged those shown in Figure 4.62. This difference may be the result of the difference in correction rates of the wind input source function shown in Figure 4.82. As waves reach their full development under wind forcing conditions  $0.83 < U_{10} / c_p < 1.5$ , coefficient  $b_{br}$  gradually becomes equal to  $b_{MM02} = 8.5 \times 10^{-3}$ . In particular, for fully developed waves associated with wind speed  $U_{10} = 20$  m/s, coefficient  $b_{br}$  is very close to the experimental value  $b_{MM02}$ . Figure 4.87 shows that in light winds ( $U_{10} < 10$  m/s) and for well developed waves ( $U_{10} / c_p < 1$ ) the model results are close to the results of Gemmrich (2006).

Figure 4.88 compares the dissipation source function computed from model run CP0.5A20W10 for dominant waves with inverse wave age  $U_{10} / c_p = 1.55$  with the dissipation function computed by Melville and Matusov (2002) on the basis of their experimental data. The dissipation of the dominant waves from the model run matches the experimental magnitude of the dissipation function of Melville and Matusov (2002). However, in the range of short scale waves there is remarkable difference. This difference is to be expected due to the fact that the dissipation function of Melville and Matusov (2002) relates only to breaking waves, while the dissipation source function of Babanin and Young (2006) includes all dissipation processes occurring in the waves. Therefore, it is consistent that the model results are greater than the experimental data. However, the magnitudes of difference in the range of short scale waves still require more experimental verification.



**Figure 4.86** Coefficient  $b_{br}$  as a function of the inverse wave age  $U_{10} / c_p$  computed from the model run CP0.5A20W10 (assigned as WT-1) (bold line). The model results were compared with the experimental values  $b_{MM02} = 8.5 \times 10^{-3}$  (Melville and Matusov, 2002) (plain line) and  $b_{G05} = 2 \times 10^{-5}$  (Gemrich, 2006) (dashed line) and the results of pseudo-evolution performed in MATLAB (line with dots).



**Figure 4.87** The coefficient  $b_{br}$  as a function of the inverse wave age  $U_{10} / c_p$  computed for the model runs with different wind speed  $U_{10} = 7\text{m/s}$ ,  $10\text{m/s}$ ,  $15\text{m/s}$  and  $20\text{m/s}$ .

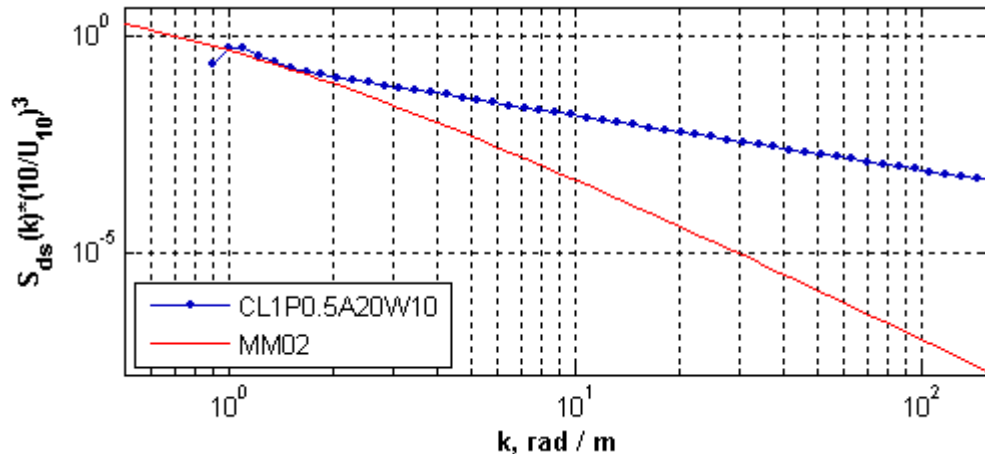


**Figure 4.88** Comparison of the dissipation source function produced by model run CP0.5A20W10 for dominant waves with inverse wave age  $U_{10} / c_p = 1.55$  with the dissipation function computed by Melville and Matusov (2002) on the basis of their experimental data.

#### 4.3.5 CONCLUSIONS

The performance of the new wind input and wave dissipation source functions was investigated using the wave model WAVETIME-1. The investigation of new source functions with unknown parameters in a radiative transfer equation is a complex task. Additional complexity was introduced, however, through the concurrent investigation of two new source functions  $S_m(f)$  and  $S_{ds}(f)$  which interrelated to one another. Moreover, it was necessary that these functions reflected the constraints that dictated the physical framework of the model.

Uniquely, this study developed a unique approach that addressed all aspects of the physical framework of the wave model. Wave induced stress was selected as the main physical constraint for the model, which describes the strength of the interaction between the wind and the waves. Using this approach, the computational routine of the model was changed to a new one, which was introduced as the *split-balance self-correcting routine*, which most closely describes the physical processes of wind-wave interactions known in current wave modelling. One of the significant advantages of this routine is the dynamic correction of the wind input source function, which ensures consistency with the existing value of wind stress

during a model run. Furthermore, the split-balance self-correcting routine can be easily implemented in other wave models with different forms of the wind input source functions.

The results of the model runs were intensively tested against the observed experimental data in terms of various spectral parameters (listed in Section 4.3.3). The results of the tests showed that the model was able to reproduce the experimental data in terms of wave growth curves and spectral magnitudes of the wave spectra. The model results fit the experimental growth curves of Babanin and Soloviev (1998) within a 10% range. Furthermore, the model exhibits an energy saturation level approaching the Pierson-Moskowitz limit at the full development stage of wave evolution. This feature was clearly shown in time dependent growth curves in Figure 4.71.

It was found that there was very intense growth during the early stages of wave development  $U_{10}/c_p = [4.7, 3.8]$  due to the transformation from  $f^{-5}$  to  $f^{-4}$  of the slope of the spectral tail and the transition from a fully separated wind flow to a non-separated flow over the dominant waves. This last mentioned feature was the result of the step-form behaviour of the growth rate of dominant waves revealed in the observed data of Donelan et al. (2006).

The spectral level of the model spectra was verified in terms of the spectral parameter  $\alpha$  and the average level  $\alpha_{BY}$ . The model results for  $\alpha$  were compared to the experimental data obtained by different researchers (Hasselmann, 1973; Donelan, 1985; Bandou, 1986; Evans, 1990; and Babanin and Soloviev, 1998). The comparisons showed an encouraging correlation between the model results and the established experimental values. The previously mentioned step-form behaviour of the growth rate was traced in the increase of the magnitudes of  $\alpha$  in the range  $U_{10}/c_p = [3, 4.5]$ . However, the increased magnitudes of  $\alpha$  remained consistent with the experimental data (see Figure 4.71). The average levels  $\alpha_{BY}$  of the model spectra were compared with the results of Banner (1990). The comparisons also showed agreement between the compared values.

The spectral slope of the model spectra was examined in terms of the exponent slope  $n$  in order to determine the directional slice of the wave spectrum at the point of the main propagation of the waves. The model results showed that the wave spectra had less slope exponent than suggested by Banner (1990). Similar results were reported by Banner and Young (1994) whose research showed less rapid decay of the modelled wavenumber spectra than the results of Banner (1990).

The present study showed that the model was able to replicate the observed directional spreading of the wave spectra. Particularly, the directional slice of the wave spectrum of the dominant waves had a unimodal shape, while in the low and the high frequency range it had a bimodal shape. This bimodality of the directional spreading in the high frequency range of the wave spectrum was clearly confirmed by the sidelobe ratio parameter  $\lambda$ . The model results for  $\lambda$  were consistent with the results of Banner and Young (1994), even though the model computations were performed for an unconstrained spectral tail in contrast to the Banner and Young's (1994) model setup.

The directional spreading of the model spectra was verified in terms of the spreading width  $A(f)$  (Babanin and Soloviev, 1998). The results showed broadening of the wave spectra above the peak frequency, which indicates that the model is able to reproduce the observed behavior of the angular spread. For the high frequency range, the model results were consistent with the observations at the early stages of wave development. However, for the later wave development stages the model produced broader directional spectra than the observed ones and some limitations are still to be addressed.

The behavior of the new source terms  $S_{in}$  and  $S_{ds}$  was investigated on the basis of the model results obtained for different wind speeds. The wind input source function was examined in terms of the correction rate  $\eta$ . The results indicated that the correction rates are high in the range  $U_{10} / c_p = [2, 4]$  where the transition of the wind flow from fully-separated to non-separated was occurring. Moreover, the model results showed that light winds required higher suppression rates than strong winds. Further experimental study was recommended in order to determine the relationship between the magnitude of the sudden increase in growth rate and wind speed during the transition of the wind flow from fully-separated to non-separated.

The behavior of the new dissipation source term was examined in terms of the behavior of coefficients  $a$  and  $b$  as the functions of the inverse wave age and wind speed. It was found that coefficient  $a$  for inherent wave breaking does not relate to wind speed, whereas coefficient  $b$  was dependent on the wind speed of young waves only. It was concluded, therefore, that the forced breaking term of the dissipation source function (Equation 2-29) exhibits a nonlinear relationship to the wind speed for young waves, whereas the inherent breaking term possesses linear dependence. For the later stages of wave development both terms of the dissipation source function (Equation 2-29) exhibit linear dependence on wind

speed. Furthermore, the model results show that both coefficients are in agreement with the experimental value  $a_{exp} = 0.0065$ .

In general, it was found that both terms of wave dissipation decrease with wave development. Moreover, the inherent breaking term decreases more rapidly than the forced breaking term. When the waves approach full development stage, their phase speed is high enough that the wind cannot transfer more energy to the dominant waves. On this basis, the dominant waves have zero wave-induced stress. Since coefficient  $a$  relates to wave-induced stress, it becomes zero as well. Consequently, for fully developed waves, the inherent breaking term vanishes and wave dissipation is represented only by the forced breaking term, which always exists (Young and Babanin, 2006). These results are consistent with the observations of Young and Babanin (2005) and Gemmrich (2005).

On the basis of the model results it was found that the major dissipation of wave energy occurs at oblique angles  $\theta = [20^\circ, 30^\circ]$  to the main wave propagation direction. Model stability was achieved when the angle  $\theta$  broadened from  $\theta_p = 20^\circ$  for the dominant waves towards  $\theta_p = 30^\circ$  for the short scale waves.

One of the important findings of the present study was the interrelationship between the new source terms  $S_{in}$  and  $S_{ds}$  in terms of the spectral magnitudes and their slope exponents particularly in the high frequency range. It was found that for short scale waves, the spectral magnitudes of  $S_{in}$  should be comparable to the magnitudes of  $S_{ds}$ . In the high frequency range, wave dissipation cannot exceed the other source terms, which implies a very fast decay of wave energy.

It was shown that the model produced stable results when the spectral tail of the wave dissipation source term was constrained by the slope exponent of the wind input source term. Furthermore, their slope exponents were computed from the model results at different stages of the model run. It was found that during wave development, slope exponents converge.

The performance of the new dissipation source term in reproducing the observed wave breaking data (Melville and Matusov, 2002 and Gemmrich, 2005) was evaluated in terms of coefficient  $b_{br}$ . Coefficient  $b_{br}$  computed from the results of the model runs was compared with the experimental values  $b_{MM02} = 8.5 \times 10^{-3}$  (Melville and Matusov, 2002) and  $b_{G05} = 2 \times 10^{-5}$  (Gemmrich, 2006) from wave observations. The comparison showed an encouraging agreement between the model results and the experimental value of coefficient

$b_{br}$  (see the Figure 4.86) computed for dominant waves with experimental values from Melville and Matusov (2002).

On the other hand, the present study found that in light winds ( $U_{10} < 10$  m/s) for well developed waves ( $U_{10} / c_p < 1$ ) the model results are close to the results of Gemmrich (2006). Furthermore, model results for the dissipation of dominant waves matched observed wave breaking. In the high frequency range, as expected, the model dissipation was larger than that observed due to the different scope of the dissipation processes considered in the compared functions. The dissipation function of Melville and Matusov (2002) was defined only for breaking waves, while the dissipation source function of Young and Babanin (2006) includes all dissipation processes occurring in the waves. However, the magnitudes of difference in the range of short scale waves still requires more experimental investigation.

In general it can be concluded that the model incorporating the corrected forms of the new source functions  $S_{in}(f)$  (Donelan et al. 2006) and  $S_{ds}(f)$  (Young and Babanin, 2006) was able to reproduce the existing experimental data. Therefore, the new forms of the wind input  $S_{in}$  (Donelan et al. 2006) and wave dissipation  $S_{ds}$  (Young and Babanin, 2006) are suggested as advanced source terms in wave modeling.

# CHAPTER 5 CONCLUSIONS AND RECOMMENDATIONS

---

The present study investigated new parameterisation forms for the wind input source term from Donelan et al. (2006) and the wave dissipation term from Young and Babanin (2006). Simulations of the duration-limited evolution of wind-waves were conducted using a modified third-generation two-dimensional research wave model, WAVETIME-1 (Van Vledder, 2004), incorporating the exact nonlinear wave model of Tracy and Resio (1982). The novel approach, developed in this study was based on a strong physical framework. The model results showed an encouraging agreement with the existing experimental data. The important findings and conclusions of this study are listed below.

## 5.1 THE WIND INPUT SOURCE FUNCTION $S_{IN}$

1. The physical framework of the present study was built on one of the important physical characteristics of wind-wave interactions – wave-induced stress  $\tau_w$  – which is directly measured using wave observations. Wave-induced stress  $\tau'_w$  computed via a frequency integration of  $S_{in}(f)$  should not exceed the  $\tau_w$  computed from the balance of stresses at the water surface. Noted during the present study, this condition was termed the *stress consistency criterion* and was used as the main criterion for verifying the consistency of a wind input parameterisation form in terms of its relationship to the physical processes occurring in the open ocean.
2. Previously suggested parameterisation forms (Snyder 1981; Hsiao and Shemdin 1983; Donelan 1990) were tested using the stress consistency criterion. The results show a remarkable inconsistency on the part of the parameterisation forms for the wind input source term in relation to the physics of wind-wave interactions.

3. A new parameterisation form (Eq. 4-7) for viscous drag was introduced as a function of wind speed  $U_{10}$  on the basis of the reported data of Banner and Peirson (1998).
4. A new method of representing a dynamic self-correction routine, where wave-induced stress is defined as the main physical constraint determining the momentum transfer from wind to waves, was developed. According to this model, the self-correction routine amends the investigated parameterisation form of the wind input source term in order to achieve consistency in terms of the physical processes involved in wave development. One of the advantages of this method is that the correction is applicable in the high frequency range, where measurements are currently not certain.

This approach does not interfere with the range of applicability of the experimental results. The high frequency range of wave spectra is suggested as a domain appropriate for numerical studies of wave processes. In the present study, the upper limit for the frequency scale was set at  $f_{cut} = 10\text{Hz}$ , taking into account the range of capillary waves.

Another advantage of the dynamic self-correction routine is that it is applicable to any parameterisation form of the wind input source term in operational wave modelling.

5. It was found that the correction routine changes the dependency law of the growth rate  $\gamma(f)$  on the frequency thus reducing a spectral slope. This trend is consistent with the results obtained by Chalikov (personal communication) on the basis of numerical simulations of air-sea interaction.
6. The wind input source function was examined in terms of the correction rate  $\eta$ . The model results show that light winds require higher suppression rates than strong winds. Furthermore, the results indicate that the correction rates are high, in the range  $U_{10} / c_p = [2, 4]$ , where transition of the wind flow from the fully-separated to the non-separated type was occurring.
7. Further experimental study is recommended to determine the relationship between the magnitude of a sudden increase in growth rate and the wind speed

during the transition of wind flow from the fully-separated to the non-separated type. In nature a smoother transition may be expected than was obtained experimentally for wave growth rate.

## 5.2 THE WAVE DISSIPATION SOURCE FUNCTION $S_{DS}$

1. The parameterisation form of the threshold spectrum  $F_T(f)$  was introduced on the basis of the threshold wave steepness in terms of the saturation transformer  $T_T(f)$ , introduced in the present study, which is an analogue of the spectral saturation  $B_T(f)$  (Section 4.2.1).
2. The threshold level  $\sqrt{B_{nT}(f)} = 0.035$  was determined from the experimental data of Babanin and Young (2005) on the basis of model simulations. The main criterion for the selection of the threshold value  $\sqrt{B_{nT}(f)}$  was that the breaking probability of the fully developed dominant waves ( $U_{10} / c_p \sim 0.83$ ) was significantly small (Section 4.2.1).
3. The present study shows that dissipation rates are highest for intermediate-scale waves  $f / f_p \sim 6$ . This fact is in good agreement with the results of the FAIRS experiment (Gemrich 2005) (Section 4.2.1).
4. Since the wave dissipation source function relates to the wind input source term, which in its turn relates to wave-induced stress, the latter becomes the governing physical constraint in modelling deep-sea conditions (Section 4.2.2).
5. The fractional relationship between the energy transferred from wind to waves and wave dissipation energy is described by the new relational parameter – the dissipation rate  $R$  – introduced in the present study as a ratio between the wave dissipation energy and the energy transferred from the wind to the waves. Based on existing experimental data, the dissipation rate takes values in the range  $R \sim [0.9, 1]$  (Section 4.2.2).
6. Based on the experimental data of Donelan (2001), the parameterisation form of the dissipation rate  $R$  was determined as a function of the inverse wave age  $U_{10} / c_p$ . The dissipation rate  $R(U_{10} / c_p)$  can be widely used in operational wave modelling to maintain the correct level of wave dissipation energy in wave models (Section 4.2.2).

7. The two phase behaviour of the new dissipation function was investigated in terms of the functional dependency of the coefficients  $a$  for the inherent wave breaking term and  $b$  for the forced dissipation term (Eq. 2-29). The findings of this study show that both coefficients have functional dependence on the inverse wave age  $U_{10} / c_p$  and the spectral frequency. The dependence on the inverse wave age was mostly determined by the relationship between the wind energy input and the wave dissipation source terms. It was found that both coefficients decrease with the development. This points to a nonlinear relationship between the dissipation source function and the wave spectrum. The functional dependence of coefficients  $a$  and  $b$  on the spectral frequency was determined using the correspondence between the spectral slopes of the wind input source term and wave dissipation in the high frequency spectral range (Section 4.2.2).
8. The present study indicates that for short scale waves the spectral magnitudes of the wave dissipation source function  $S_{ds}(f)$  the wind input source term  $S_{in}(f)$  and nonlinear source term  $S_{nl}(f)$  must be comparable. This feature is very important, particularly when attempting to achieve numerical stability for the wave model in the high frequency spectral range (Section 4.2.2).
9. This study demonstrates that in deep water conditions and in the absence of current shear, the dominant waves do not break if there is no energy input from the wind. In this case, the inherent breaking term of the dissipation source function (Eq. 2-29) vanishes and the dissipation of the waves is presented only by the forced breaking term (Section 4.2.2).
10. The behavior of the new dissipation source term was examined in terms of the behavior of coefficients  $a$  and  $b$  as the functions of the inverse wave age and wind speed. It was found that coefficient  $a$ , representing inherent wave breaking, does not relate to wind speed, whereas coefficient  $b$  is dependent on wind speed only for young waves. It was therefore concluded that the forced breaking term of the dissipation source function (Eq. 2-29) exhibits a nonlinear relationship to the wind speed for young waves, whereas the inherent breaking term has linear dependence. For the later stages of wave development both terms of the dissipation source function (Eq. 2-29) exhibit linear dependence on wind speed (Section 4.2.2).

11. The model results show that both coefficients are in agreement with the experimental value  $a_{exp} = 0.0065$  (Section 4.2.2).
12. In general, it was found that both terms of wave dissipation decrease with wave development. The model results indicate that the inherent breaking term decreases more rapidly than the forced breaking term (Section 4.2.2).
13. The present study shows that for waves approaching their full development stage the inherent wave breaking is small, and the wave dissipation is predominantly represented by the forced breaking of short-scale waves ( $f > 4 f_p$ ). It was shown that forced wave breaking should always exist ( $T_2(f) \neq 0$ ) during wave development (Section 4.2.2).
14. Experiments with different wind speeds indicated that for young waves the forced breaking rate is higher as wind speed increases. For medium wave age ( $U_{10} / c_p = [2, 3]$ ) stronger wind speeds mean a higher rate of inherent breaking and higher forced breaking for short waves. However, for well-developed waves there is not much difference in forced breaking rates. These findings are consistent with the experimental data of Melville and Matusov (2002), Young and Babanin (2005), and Gemmrich (2005) (Section 4.2.2).
15. It was found that turbulent viscosity dissipation is more significant in light winds. With increasing wind speed the dissipation processes due the turbulent viscosity give place to increasing events of wave breaking (Section 4.2.2).
16. According to the observations of Young and Babanin (2006) wave dissipation is maximal at oblique angles relative to the main propagation direction of the waves. In the present study, a new directional spreading function of a bimodal shape was developed for the wave dissipation source term. For further research purposes this function includes features allowing transformations of the directional spectral shape during wave development and along the frequency scale (Section 4.2.3).
17. Results obtained from the model indicate that the major dissipation of wave energy occurs at oblique angles  $\theta = [20^\circ, 30^\circ]$  to the main wave propagation direction. Stability of the model was achieved when the angle  $\theta$  was broadened from  $\theta_p = 20^\circ$  for the dominant waves, and to  $30^\circ$  towards the short scale waves (Section 4.2.3).

18. The performance of the corrected new spectral dissipation source term was examined to determine whether the new dissipation source term (Eq. 2-29) was able to reconcile computed breaking crest length spectral magnitudes for the dominant waves  $A(v_p)$  with the experimental data (Melville and Matusov, 2002; Gemmrich, 2005). The findings of the present study indicate an encouraging agreement with the results of both these independent studies (Section 4.2.4).

It is worth mentioning that both Melville and Matusov (2002) and Gemmrich (2005) report a remarkable discrepancy of values for the coefficient  $b_{br}$  used in computations of the breaking crest length spectrum. This issue was addressed in the present study by computing the coefficient  $b_{br}$  using the observed data of  $A(v_p)$  and analysing the results of this computation against the reported values for the coefficient  $b_{br}$  from different studies (Duncan, 1981; Melville, 1994; Phillips 2001; Melville and Matusov, 2002 and Gemmrich 2006). The results of these computations varied depending on what values of the observed  $A(v_p)$  were used. The results provided insight into the physical properties of  $A(v_p)$  in a wide range of air-sea conditions.

The behaviour of the coefficient  $b_{br}$  in terms of wave development and for a wide range of wind speeds was investigated using observations by Melville and Matusov (2002)  $A_{MM02}(v_p)$ . The results showed that for well-developed seas ( $U_{10} / c_p < 1.5$ ) the coefficient  $b_{br}$  exhibits a highly sensitive relationship to the inverse wave age (see the steep decrease in the range of values  $b_{br} \sim [10^{-4}, 10^{-3}]$ , for winds  $U_{10} < 20$  m/s. Moreover, for average-developed waves ( $U_{10} / c_p \sim 2.7$ ), good agreement was shown with the value  $b_{br} = 3 \times 10^{-2}$  reported by Duncan (1981) from a laboratory experiment.

On the other hand, the present study found that in light winds ( $U_{10} < 10$  m/s) the model results are close to the results of Gemmrich (2006) for well-developed waves ( $U_{10} / c_p < 1$ ). These findings lead to the conclusion that the discrepancy of the values of the coefficient  $b_{br}$  is caused by its sensitivity to changing wind forcing conditions during wave observations. Furthermore, the spectral levels of the modelled dissipation function (Young and Babanin, 2006) for dominant waves match those computed by Melville and Matusov (2002) for the wave breaking function. In the high frequency range, as expected, the modelled dissipation rates are higher than the observed rates due to the different scope of the dissipation processes considered in the compared functions. The dissipation function of Melville and Matusov (2002) is defined only for breaking

waves, while the dissipation source function of Young and Babanin (2006) includes all dissipation processes occurring in the waves.

The comparisons demonstrate that the magnitudes of difference in the range of short-scale waves still require more experimental investigation. Summarising the results of the comparisons, it is important to emphasise that the new spectral dissipation source function demonstrates the ability to predict wave energy losses consistent with the experimental data.

### 5.3 MODEL PERFORMANCE

1. The model validation strategy addressed all aspects of the physical framework selected for the present study. The main physical constraint for the model was wave-induced stress, which describes the strength of interaction between the wind and the waves. The novel *split-balance self-correcting routine* was introduced as computational routine of the model. This routine most closely describes the physical processes of known wind wave interactions used in wave modelling. The term ‘split balance’ was used due to the coupling of wind input and wave dissipation source terms in the energy balance equation. One of the significant advantages of the routine is the dynamic correction of the wind input and wave dissipation source functions so that they become consistent to the physical constraints introduced during the model run. It is suggested that the split-balance self-correcting routine could be implemented in other wave models with other forms of wind input and wave dissipation source terms.
2. The results of the model runs were intensively tested against the observed experimental data in terms of the various spectral parameters listed in Section 4.3.3. The results of the tests show that the model was able to reproduce the experimental data in terms of wave growth curves and spectral magnitudes of the wave spectra. The model results fit the experimental growth curves of Babanin and Soloviev (1998) within the 10% range of approximation. Furthermore, the model exhibits an energy saturation level approaching the Pierson-Moskowitz limit at the full development stage of wave evolution. This feature was clearly shown in time dependent growth curves in Figure 4.71.

3. It was found that very intense wave growth at the early stages of wave development  $U_{10} / c_p = [4.7, 3.8]$  is due to the transformation of the slope spectral tail from  $f^{-5}$  to  $f^{-4}$  and the transition from fully-separated wind flow to non-separated flow over the dominant waves. This last mentioned feature is the result of the step-form behaviour of the growth rate of dominant waves revealed in the observed data of Donelan et al. (2006).
4. The spectral level of the model spectra was verified in terms of the spectral parameter  $\alpha$  and the average level  $\alpha_{BY}$ . The model results for  $\alpha$  were compared to the experimental data obtained by different authors (Hasselmann, 1973; Donelan, 1985; Bandou, 1986; Evans, 1990 and, Babanin and Soloviev, 1998). The comparisons indicate an encouraging consistency in the model results in relation to the experimental values.
5. The previously mentioned step-form behaviour of the growth rate was furthermore traced in the increase of the magnitudes of  $\alpha$  in the range  $U_{10} / c_p = [3, 4.5]$ . However, the increased magnitudes of  $\alpha$  are still consistent with the experimental data (see Figure 4.72). The average level  $\alpha_{BY}$  of the model spectra were compared with the results of Banner (1990). The comparisons show agreement between the compared values.
6. The spectral slope of the model spectra was examined in terms of the exponent slope  $n$  using a directional slice of the wave spectrum at the point of the main propagation of the waves. The results showed that the wave spectra had less exponent slope than suggested by Banner (1990). Similar results later reported by Banner and Young (1994) showed less rapid decay of the modelled wavenumber spectra.
7. The present study confirmed that the model developed for the study is able to replicate the observed directional spreading of the wave spectra. In particular, the directional slice of the wave spectrum of the dominant waves demonstrated unimodal shape, while in the low and the high frequency ranges demonstrated bimodal shape.

8. This bimodality of the directional spreading in the high frequency range of the wave spectrum was also clearly confirmed by the sidelobe ratio parameter  $\lambda$ . The model results for  $\lambda$  are consistent with the results of Banner and Young (1994), even though the model computations were performed for an unconstrained spectral tail, in contrast to Banner and Young's 1994 model setup.
9. The directional spreading of the model spectra was verified in terms of the spreading width  $A(f)$  (Babanin and Soloviev, 1998). The results demonstrate a broadening of the wave spectra above peak frequency, which indicates that the model is able to reproduce the observed behaviour of the angular spread. In the high frequency range, the model results are consistent with the observations of the early stages of wave development. However, for the later wave development stages, the model produced broader directional spectra than the observed ones and some limitations are still to be addressed.

## 5.4 THE WAVE SPECTRUM

The present study resolved an important issue of spectral modelling regarding the shape of the wave spectrum. The Combi spectrum was introduced as a probable shape for the wave spectrum. Based on the analysis of experimental data and the model results, the Combi spectrum can be interpreted as a correction to the Donelan et al. (1985) spectrum, which has a  $f^{-4}$  spectral slope in the high frequency range. The Combi spectrum, on the other hand, provides for the transition of the spectral slope from  $f^{-4}$  to  $f^{-5}$  occurring at  $f_T \sim 3f_p$ . The parameterisation form (Eq. 4-23) of the Combi spectrum, introduced in this study, is recommended for wider use in operational wave modelling.

## 5.5 WAVE STEEPNESS

1. The present study revised the parameterisation form of spectral saturation  $B(f)$ . The new function – the saturation transformer  $T(f)$  – is suggested as an advanced and alternative form analogous to spectral saturation  $B(f)$ . One of the advantages of this function is that it maintains the saturation level in the high frequency range for both types of frequency spectrum, JONSWAP and Donelan's (1985). The saturation transformer includes the influence of long scale waves on the steepness of short scale waves. These attributes are advantageous when applying this form to spectral wave modelling.

2. The investigation presented in this work was based on intensive tests of the new source functions  $S_{in}$  (Donelan et al 2006) and  $S_{ds}$  (Young and Babanin, 2006) for a wide range of air-sea conditions in deep water. In general, it can be concluded that the model incorporating the corrected source functions was able to reproduce the existing experimental data. This result indicates that the new forms of the wind input  $S_{in}$  (Donelan et al 2006) and wave dissipation  $S_{ds}$  (Young and Babanin, 2006) source terms are able to be used as advanced parameterisation forms for operational wave modeling.

## BIBLIOGRAPHY

---

- Al-Zanaidi, M.A., and Hui, W.H., 1984, “Turbulent air flow over water waves – a numerical study”, *Journal of Fluid Mechanics*, Vol. 148, P. 225 – 246.
- Anctil, F., Donelan, M.A., 1996, “Air-water momentum flux observations over shoaling waves”, *Journal of Physical Oceanography*, Vol. 26, P. 1344–1353.
- Ardhuin, F., Herbers, T.H.C. and O’Reilly, W.C., 2001, “A hybrid Eulerian–Lagrangian model for spectral wave evolution with application to bottom friction on the continental shelf”, *Journal of Physical Oceanography*, Vol. 31 (6), P. 1498–1516.
- Babanin A.V., Soloviev Y.P., 1998a, “Variability of directional spectra of wind-generated waves, studied by means of wave staff arrays”, *Marine Freshwater Research*, Vol. 49, P. 89 – 101.
- Babanin A.V., Soloviev Y.P., 1998b, “Field investigation of transformation of the wind wave frequency spectrum with fetch and the stage of development”, *Journal of Physical Oceanography*, Vol. 28, P. 563 – 576.
- Babanin, A.V., I.R. Young, and M.L. Banner, 1999, “An observational investigation of bimodal directional spreading of fetch limited waves”, In *Proceedings of the Symposium on the Wind-Driven Air-Sea Interface. Electromagnetic and Acoustic Sensing, Wave Dynamics and Turbulent Fluxes. Sydney, Australia, 11-15 January 1999*, Ed. M.L. Banner, ADFA Document Production Centre, Canberra, Australia
- Babanin A.V., Young I.R., Banner M.L., 2001, “Breaking probabilities for dominant surface waves on water of finite constant depth”, *Journal of Geophysical Research*, Vol. 106, C6, P. 11659 – 11676.
- Babanin, A.V., and Young I.R., 2005, “Two-phase behaviour of the spectral dissipation of wind waves”, in *Proceedings Ocean Waves Measurement and Analysis, Fifth International Symposium WAVES2005, 3-7 July, 2005, Madrid, Spain*, Eds. B. Edge and J.C. Santas, paper no.51, 11p.
- Babanin, A.V., and Young I.R., 2007, “Modelling wind-generated waves at moderate-to-extreme conditions”, *Proceedings of the 18th Australasian Coastal and Ocean Engineering Conference and the 11th Australasian Port and Harbour Conference, 17-20 July 2007, Melbourne, Victoria*, accepted on the 2nd of May, 2007.

- Babanin, A.V., Banner, M.L., Young, I.R., and Donelan, M.A., 2007, “Wave follower measurements of the wind input spectral function. Part 3. Parameterisation of the wind input enhancement due to wave breaking”, *Journal of Physical Oceanography*, in press.
- Babanin, A.V. and Van der Westhuysen, A.J., 2008, “Physics of ”Saturation-Based” Dissipation Functions Proposed for wave forecast models”, *Journal of Physical Oceanography*, accepted on the 15th of December, 2007.
- Babanin A.V., Chalikov, D. Young I.R. and Saveliev, I., 2008, “Breaking of nonlinear two-dimensional waves in deep water”, submitted to *Journal of Fluid Mechanics*, (June 2008).
- Badulin S., Babanin A.V., Zakharov V.E. and Resio D., 2006, “Self-similarity laws of wind-wave growth” *Proceedings of The Waves In Shallow Environments (WISE)*, April 23 - 27, 2006, Venice, Italy.
- Banner M.L., 1990, “Equilibrium spectra of wind waves *Journal of Physical Oceanography*, Vol. 20, P. 966 – 984.
- Banner M.L., Young I.R., 1994, “Modelling spectral dissipation in the evolution of wind waves - Part 1 Assessment of existing model performance”, *Journal of Physical Oceanography*, Vol. 24, P. 1550 – 1571.
- Banner M.L., Babanin A.V., Young I.R., 2000, “Breaking probabilities for dominant waves on the sea surface”, *Journal of Physical Oceanography*, Vol. 30, P. 3145 – 3160.
- Banner, M.L. and Song, J., 2002, “On determining the onset and strength of breaking for deep water waves. Part 2: Influence of wind forcing and surface shear”, *Journal of Physical Oceanography*, Vol. 32, P. 2559-2570.
- Banner M.L., Gemmrich J.R. and Farmer D.M., 2002, “Multiscale measurements of ocean wave breaking probability”, *Journal of Physical Oceanography*, Vol. 32, P. 3364 – 3375.
- Banner M.L. and Peirson W.L., 2006, “Wave breaking onset and strength for two-dimensional deep water waves”, submitted to *Journal of Fluid Mechanics*, (June 2006).
- Banner M.L. and Morison R.P., 2006, “On modelling spectral dissipation due to wave breaking for ocean wind waves”, *9th Int’l Workshop on Wave Hindcasting and Forecasting*, Victoria, B.C., Canada, Sept. 24-29, 2006

- Barnett, T. P., 1968, "On the generation, dissipation and prediction of ocean wind waves", *Journal of Geophysical Research*, Vol. 73, P. 513 – 529.
- Battjes J.A., Zitman T.F. and Holthuijsen L.H., 1987, "A reanalysis of the spectra observed in JONSWAP", *Journal of Physical Oceanography*, Vol. 17, P. 1288 – 1295.
- Booij, N., Holthuijsen, L.H. and Ris, R.C., 1996, "The SWAN wave model for shallow water", *International Conference in Coastal Engineering*, ASCE, Orlando, P. 668 – 676.
- Booij, N., Ris, R.C. and Holthuijsen, L.H., 1999, "A third generation wave model for coastal regions: Part I. Model description and validation", *Journal of Geophysical Research*, Vol. 104 (C4), P. 7649–7666.
- Booij, N., Haagsma, I.J.G., Holthuijsen, L.H., Kieftenburg, A.T.M.M., Ris, R.C., Van der Westhuysen, A.J., Zijlema, M., 2004, "SWAN User Manual, SWAN Cycle III, Version 40.41", *Delft University of Technology*.
- Bretschneider, C.L., 1952a, "Revised wave forecasting relationship", *Proc. 2nd Conf. on Coastal Engineering*, Houston, TX, ASCE, Council on Wave Research.
- Bretschneider, C.L., 1952b, "The generation and decay of wind waves in deep water", *Trans. Amer. Geophys. Union*, Vol. 33, P. 381–389.
- Cavaleri et al. (The WISE Group), 2007, "Wave modeling – The state of the art", *Progr. Oceanogr.*, doi:10.1016/j.pocean.2007.05.005, 72p., in press.
- Chalikov, D. and Makin, V.K., 1991, "Models of the wave boundary layer", *Boundary Layer Meteorology*, Vol. 56, P. 83 – 89.
- Chalikov, D. and Belevich, M.Yu., 1993, "One-dimensional theory of the wave boundary layer", *Boundary Layer Meteorology*, Vol. 63, P. 65 – 96.
- Dean, R.G. and Dalrymple, R.A., 1991, "Water wave mechanics for engineers and scientists", *World Scientific*, 353pp.
- Dobson, F., Perrie, W. and Toulany, B., 1989, "On the deep-water fetch laws for wind-generated surface gravity waves", *Atmosphere–Ocean*, Vol. 27, P. 210–236.
- Donelan M.A., Hamilton J., Hui W.H., 1985, "Directional spectra of wind-generated waves", *Philos.Trans.R.Soc.Lond.*, A 315.

- Donelan, M.A., and Pierson, W.J., 1987, "Radar scattering and equilibrium ranges in wind-generated waves with application to scatterometry", *Journal of Geophysical Research*, Vol. 92, P. 4971 – 5029.
- Donelan, M. A., 1990, "Air-sea interaction, in the sea", *Ocean Engineering Science*, edited by B. LeMehaute and D. M. Hanes, Vol. 9, P. 239–292, Wiley-Interscience, Hoboken, N. J.
- Donelan, M.A., Skafel, M., Graber, H.C., Liu, P., Schwab, D. and Venkatesh, S., 1992, "On the growth rate of wind-generated waves", *Atmosphere–Ocean*, Vol. 30, P. 457–478.
- Donelan M.A., 1998, "Air-water exchange processes", *Physical Processes in Lakes and Oceans*, ed. J. Imberger, Coastal and Estuarine Studies Volume 54, P. 19-36, American Geophysical Union.
- Donelan M.A., 1999, "Wave-induced growth and attenuation of laboratory waves", *Wind-over-Wave Couplings. Perspective and Prospects*, S.G. Sajadi, N.H. Thomas and J.C.R. Hunt, Eds., Clarendon Press, Oxford, P. 183 – 194.
- Donelan M.A., 2001, "A Nonlinear Dissipation Function due to Wave Breaking", *Proceedings of the European Centre for Medium-Range Weather Forecasts Workshop on Ocean Wave Forecasting, July 2-4, 2001*, Reading, England.
- Donelan, M.A., Haus, B.K., Reul, N., Plant, W.J., Stiassne, M., Graber, H.C., Brown, O.B., Saltzman, E.S., 2004, "On the limiting aerodynamic roughness in very strong winds", *Geophysical Research Letters*, Vol. 31, No. 18, L18306, doi:10.1029/2004GL019460.
- Donelan M.A., Babanin A.V., Young I.R., Banner M.L., 2006, "Wave follower field measurements of the wind input spectral function. Part II. Parameterization of the wind input", *Journal of Physical Oceanography*, Vol. 36, P. 1672-1688.
- Drennan, W.M., Graber, H.C., Hauser, D. and Quentin, C., 2003, "On the wave age dependence of wind stress over pure wind seas", *Journal Geophysical Research*, Vol. 108(C3), P. 8062, doi:10.1029/2000JC000715.
- Duncan J.D., 1981, "An experimental investigation of breaking waves produced by an airfoil", *Proc. R. Soc, Lond. A*, 377, P. 331-348.
- Ewing J.A., 1983, "Wind waves: a review of research during the last twenty-five years", *Geophys. J.R.astr.Soc.*, Vol.74, P. 313 – 329.

- Ewing J.A., 1971, "A numerical wave prediction method for the North Atlantic Ocean", *Dtsch. Hydrog. Z.*, Vol.24, P. 241 – 329.
- Forristall G.Z., 1981, "Measurements of a saturation range in ocean wave spectra", *Journal of Geophysical Research*, Vol. 86, P. 8075 – 8084.
- Gelci, R., Cazalé, J. and Vassal, J., 1957, "Prévision de la houle. La méthode des densités spectroangulaires", *Bull. Inform. Comité Central Oceanogr., D'Etude Côtes*, Vol. 9, P. 416 – 435.
- Gemmrich, J.G. and Farmer D. M., 2004, "Near-surface turbulence in the presence of breaking waves", *Journal of Physical Oceanography*, Vol. 34, P. 1067-1086.
- Gemmrich J.G., 2005, "On the occurrence of wave breaking", *14th 'Aha Huliko'a Hawaiian Winter Workshop, January 2005*, Proceedings, P. 123-130.
- Gemmrich J.G, 2006, "Spectral properties of breaking surface waves", *9th Workshop on Wave Forecasting*.
- Gent P.R., and Taylor P.A., 1976, "A numerical model of air-flow above water waves", *Journal of Fluid Mechanics*, Vol. 77, P. 105 – 128.
- Graber H., Madsen O., 1988, "A finite-depth wind-wave model, 1. Model description", *Journal of Physical Oceanography*, Vol. 18, P. 1465 – 1483.
- Guan, C.L., and Xie, L., 2004, "On the linear parameterisation of drag coefficient over sea surface", *Journal of Physical Oceanography*, Vol. 32, P. 2847–2851.
- Hasselmann K., 1960, "Grundleichugen der Seegangsvorhsage", *Schifftechnik*, Vol. 7, P. 191-195.
- Hasselmann K., 1962, "On the non-linear energy transfer in a gravity-wave spectrum, Part 1. General Theory", *Journal of Fluid Mechanics*, Vol. 12, P. 481 – 500.
- Hasselmann K., 1963a, "On the non-linear energy transfer in a gravity-wave spectrum, Part 2. Conservation theorems; wave-particle analogy; irreversibility", *Journal of Fluid Mechanics*, Vol. 15, P. 273 – 281.
- Hasselmann K., 1963b, "On the non-linear energy transfer in a gravity-wave spectrum, Part 3. Evaluation of energy flux and swell-sea interaction for Neumann spectrum", *Journal of Fluid Mechanics*, Vol. 15, P. 385 – 398.
- Hasselmann S., Collins J., 1968, "Spectral dissipation of finite-depth gravity waves due to turbulent bottom friction", *Journal of Marine Research*, Vol. 26, P. 1-12.

- Hasselmann K. et al., 1973, “Measurements of wind-wave growth and swell decay during the Joint North Sea Wave Project (JONSWAP)”, *Dtsch. Hydrog. Z.*, Suppl. A, 8, 12, P. 95.
- Hasselmann K., 1974, “On the spectral dissipation of ocean waves due to white-capping”, *Boundary Layer Meteorology*, Vol. 6, P. 107 – 127.
- Hasselmann K., Ross D.B., Muller P., Sell W., 1976, “A parametric wave prediction model”, *Journal of Physical Oceanography*, Vol. 6, P. 200 – 228.
- Hasselmann S., Hasselmann K., 1981, “A symmetrical method of computing the nonlinear transfer in a gravity wave spectrum”, *Hamburger Geophys. Einzelschriften*, A 52.
- Hasselmann, S., Hasselmann, K., 1985a. The wave model EXACT-NL”, *Ocean Wave Modelling*, The SWAMP group. Plenum Press, New York, P. 256.
- Hasselmann, S., Hasselmann, K., 1985b, ”Computation and parameterisations of the nonlinear energy transfer in a gravity-wave spectrum: Part 1. A new method for efficient computations of the exact nonlinear transfer integral”, *Journal of Physical Oceanography*, 15, P. 1369–1377.
- Hasselmann K., Bösenberg J., 1991, “Field measurements of wave-induced pressure over wind-sea and swell”, *Journal of Fluid Mechanics*, Vol. 230, P. 391 – 428.
- Hsiao S.V., Shemdin O.H., 1983, “Measurements of wind velocity and pressure with wave follower during MARSEN”, *Journal of Geophysical Research*, Vol. 88, P. 9841 – 9849.
- Hwang, P. A., Wang D., Walsh E., Krabill W. and Swift R., 2000, “Airborne measurements of the wavenumber spectra of ocean surface waves. Part II: Directional distribution”, *Journal of Physical Oceanography*, Vol. 30, P. 2768 – 2787.
- Hwang, P. A., and Wang D. W., 2004a, “Field measurements of duration limited growth of wind-generated ocean surface waves at young stage of development”, *Journal of Physical Oceanography*, Vol. 34, P. 2316–2326.
- Hwang, P. A., and Wang D. W., 2004b, “An empirical investigation of source term balance of small scale surface waves”, *Geophysical Research Letters*, Vol. 31, L15301.
- Hwang, P. A. and Wang D. W. 2005, “Analysis of the spectral signature of breaking waves”, *NRL Review*, P. 186-188.

- Hwang, P. A. and Sletten M. A., 2007, “Dissipation function of wind seas and wave parameterization of whitecap coverage”, The 15th Conference on Air-Sea Interaction and the 14th Conference on Middle Atmosphere, August 2007, Portland, OR.
- Hwang, P. A. 2007, “Spectral signature of wave breaking in surface wave components of intermediate-length scale”, *Journal of Marine Systems*, Vol. 66, Issues 1-4, P. 28-37.
- Jeffreys H., 1925, “On the formation of waves by wind. II”, *Proc. Roy. Soc. A*, 110, P. 341 – 347.
- Janssen P.A.E.M., 1991, “Quasi-linear theory of wind-wave generation applied to wave forecasting”, *Journal of Physical Oceanography*, Vol. 21, P. 1631 – 1642.
- Kahma K.K., 1981, “A study of the growth of the wave spectrum with fetch”, *Journal of Physical Oceanography*, Vol. 11, P. 1503 – 1515.
- Kahma K.K. and Calkoen C.J., 1992, “Reconciling discrepancies in the observed growth of wind-generated waves”, *Journal of Physical Oceanography*, Vol. 22, P. 1389 – 1405.
- Kawai S., Okada K. and Toba Y., 1977, “Field data support of three-seconds law and  $gU_*\sigma^{-4}$  spectral form for growing wind waves”, *Journal of Oceanography, Soc. Japan*, Vol. 33, P. 137 – 150.
- Khatri S.K., 1999, “A numerical investigation of the physical processes active in the evolution of finite depth wind waves”, *PhD Thesis*, University of New South Wales.
- Kitaigorodskii S.A., 1962, “Applications of the theory of similarity to the analysis of wind-generated wave motion as a stochastic process”, *Bull. Acad. Sci. USSR, Geophys. Ser.*, 1, P. 105 – 117.
- Kitaigorodskii, S.A., 1970, “The physics of air-sea interaction”, translated from Russian, *Israel Program for Scientific Translations*, Jerusalem, 273 pp.
- Kitaigorodskii S.A., 1983, “On the theory of the equilibrium range in the spectrum of wind-generated gravity waves”, *Journal of Physical Oceanography*, Vol. 13, P. 816 – 827.
- Komen G.J., Hasselmann S. and Hasselmann K., 1983, “On the existence of a fully developed wind-sea spectrum”, *Journal of Physical Oceanography*, Vol. 14, P. 1271 – 1285.

- Komen G.J., Cavaleri L., Donelan M., Hasselmann K., Hasselmann S. and Janssen P.A.E.M., 1994, “Dynamics and modelling of ocean waves”, *Cambridge Univ. Press*, P. 532.
- Lavrenov I.V., 1998, “Mathematical modelling of wind waves in a non-isotropic ocean”, *Hydrometeoisdat*, Sanct-Petersburg, (in russian).
- Lavrenov I.V. and Polnikov V.G., 2001, “Properties of time-dependent solutions of the Hasselmann kinetic equation”, *Izvestiya, Atmospheric and Oceanic Physics*, Vol.37, N5, P. 661 – 670.
- Lavrenov I.V., 2003, “A numerical study of a nonstationary solution of the Hasselmann equation”, *American Meteorological Society*, P. 499 – 511.
- Lin R.Q. and Huang, N.E., 1998, “The Goddard coastal wave model. Part III: Nonlinear interactions”, *Journal of Physical Oceanography*, Vol. 27, P. 1813 – 1826.
- Liu P.C., 1989, “On the slope of the equilibrium range in the frequency spectrum of wind waves”, *Journal of Geophysical Research*, Vol. 94, P. 5017 – 5023.
- Longuet-Higgins, M.S., Cartwright, D.E. and Smith, N.D., 1963, “Observations of the directional spectrum of sea waves using the motions of a floating buoy”, *Ocean Wave Spectra*, Prentice Hall, P. 111–136.
- Makin V.K., and Chalikov D.V., 1979, “Numerical modelling of air structure above waves”, *Izvestiya, Atmospheric and Oceanic Physics*, Vol.15, P. 199 – 204.
- Manasseh, R., Babanin, A., Forbes, C., Rickards, K., Bobevski, I. & Ooi, A. 2006, “Passive acoustic determination of wave-breaking events and their severity across the spectrum”, *Journal of Atmospheric and Ocean Technology*, Vol. 23 (4), P. 599–618.
- Melville W.K., 1994, “Energy dissipation by breaking waves”, *Journal of Physical Oceanography*, Vol. 24, P. 2041 – 2049.
- Melville W.K. and Matusov P., 2002, “Distribution of breaking waves at the ocean surface”, *Nature*, 417, P. 58 – 63.
- Miles J.W., 1957, “On the generation of surface waves by shear flows”, *Journal of Fluid Mechanics*, Vol. 3, P. 185 – 204.
- Mitsuyasu, H., Tasai, F., Suhara, T., Mizuno, S., Onkusu, M., Honda, T. and Rukiishi K., 1975, “Observations of the power spectrum of waves using a cloverleaf buoy”, *Journal of Physical Oceanography*, Vol. 10, P. 286 – 296.

- Mitsuyasu, H., 1977, "Measurements of the high frequency spectrum of ocean surface waves *Journal of Physical Oceanography*, Vol. 7, P. 882 – 891.
- Mitsuyasu, H., and K. Rikiishi, 1978, "The growth of duration-limited wind waves", *Journal of Fluid Mechanics*, Vol. 85, P. 705–730; Corrigendum, Vol. 87, P. 796–797.
- Monbaliu, J., Hargreaves, J.C., Carretero, J.C., Gerritsen, H. and Flather, R., 1999, "Wave modelling in the PROMISE project", *Coastal. Engineering*, Vol. 37, P. 379– 407.
- Motzfeld H., 1937, "Die turbelence Strömung an welligen Wänden", *Z. Math. Mech.*, 17, P. 193 – 212.
- Pierson, W.J. and Moskowitz, L., 1964, "A proposed spectral form for fully developed wind seas based on the similarity theory of S.A.Kitaigorodskii", *Journal of Geophysical Research*, Vol. 69, P. 5181 – 5190.
- Phillips O.M., 1958, "The equilibrium range in the spectrum of wind-generated waves", *Journal of Fluid Mechanics*, Vol. 4, P. 426 – 434.
- Phillips O.M., 1977, "The dynamics of the upper ocean", *Cambridge Univ. Press*, 336pp.
- Phillips O.M., 1985, "Spectral and statistical properties of the equilibrium range in wind-generated waves", *Journal of Fluid Mechanics*, Vol. 156, P. 505 – 531.
- Phillips, O.M., Posner F. L. and Hansen, J. P., 2001,"High range resolution radar measurements of the speed distribution of breaking events in wind-generated ocean waves: Surface impulse and wave energy dissipation rates", *Journal of Physical Oceanography*, Vol. 31, 450-460.
- Polnikov V.G., Farina L., 2002, "On the problem of optimal approximation of the four-wave kinetic integral", *Nonlinear Processes in Geophysics*, Vol.20, P.1 – 16.
- Pushkarev A., Resio D., Zakharov V., 2003, "Weak turbulent approach to the wind-generated gravity sea waves", *Physica D* 184, (1-4), P. 29-63.
- Resio, D.T., and Perrie, W., 1991, "A numerical study of nonlinear energy fluxes due to wave-wave interactions. Part 1: Methodology and basic results", *Journal of Fluid Mechanics*, Vol. 223, P. 609– 629.
- Resio, D.T., Pihl, J.H., Tracy, B.A. and Vincent, C.L., 2001, "Non-linear energy fluxes and the finite depth equilibrium range wave spectra", *Journal of Geophysical Research*, Vol. 106 (C4), P. 6985– 7000.

- Snyder, R.L., Dobson, F.W., Elliot, J.A. and Long, R.B., 1981, "A field study of wind generation of ocean waves", *Journal of Fluid Mechanics*, Vol. 102, P. 1– 59.
- Song, J. and Banner, M.L. 2002, "On determining the onset and strength of breaking for deep water waves. Part 1: Unforced irrotational wave groups", *Journal of Physical Oceanography*, Vol. 32, P. 2541-2558.
- Stanton T.E., Marshall D and Houghton R., 1932, "The growth of waves on water due to the action of the wind", *Proc. Roy. Soc., A*, 137, P. 283 – 293.
- Stolte S., 1984, "Modulation of short waves by long wind waves and wind", *PhD Thesis, University of Hamburg*, P.199.
- Sverdrup, H.U. and Munk, W.H., 1947, "Wind, Sea, and Swell: Theory of Relations for Forecasting", *U.S. Navy Dept., Hydrographic Office, H.O.*, Pub. No. 601, 44 pp.
- Thijssse J.T., 1951, "Growth of wind-generated waves and energy transfer", *Gravity Waves, Nat. Bur. Stand. Washington Circular*, 521, P. 281 – 287.
- Toba Y., 1973, "Local balance in the air-sea boundary process", *Journal of Oceanography Soc. Japan*, 29, P. 209 – 220.
- Tolman H.L., Chalikov D., 1996, "Source terms in a third-generation wind wave model", *Journal of Physical Oceanography*, Vol.26, N11, P. 2497 – 2518.
- Tolman H.L., 1992, "Effect of numerics on the physics in a third-generation wind wave model", *Journal of Physical Oceanography*, Vol. 22, P. 1095 – 1111.
- Tolman, H.L., 1999, "User manual and system documentation of WAVEWATCH-III, version 1.18", *NCEP/NOAA Tech. Note*, Vol. 116, 110 pp.
- Tolman H.L., 2002, "Limiters in Third-Generation Wind Wave Models", *The Global Atmosphere and Ocean System*, 200, Vol.8, N1, P. 67 – 83.
- Tolman H.L., 2003 "Inverse modeling of Discrete Interaction Approximations for nonlinear interactions in wind waves", *Ocean Modelling*.
- Tracy B.A., Resio D.T., 1982, "Theory and calculation of the nonlinear energy transfer between sea waves in deep water", *U.S. Army Engineer Waterways Experiment Station, Rep. N11*, Vicksburg, U.S.A.

- Van der Westhuysen, A.J., Zijlema, M. and Battjes, J.A., 2007, “Nonlinear saturation-based whitecapping dissipation in SWAN for deep and shallow water”, *Coastal Engineering*, Vol. 54, P. 151-170.
- Van Vledder, G.Ph., Herbers, T.H.C., Jensen, R.E., Resio, D.T., Tracy, B.A., 2000, “Modelling of non-linear quadruplet wave–wave interactions in operational wave models”, *Proc. 27th Int. Conf. on Coastal Engineering*, Sydney, pp. 797– 811.
- Van Vledder, G.Ph., 2000, “Improved method for obtaining the integration space for the computation of non-linear quadruplet wave–wave interactions”, *Proc. 6th Int. Conf. on Wave Forecasting and Hindcasting*, Monterey, California, USA.
- Van Vledder, G.Ph., 2002, “A subroutine version of the Webb/Resio/Tracy method for the computation of nonlinear quadruplet wave-wave interactions in deep and shallow water”, *Alkyon Report 151b*, The Netherlands.
- Van Vledder, G.Ph., Bottema, M., 2002, “Improved modelling of nonlinear fourwave interactions in shallow water”, *Proc. 28th Int. Conf. on Coastal Eng.*, Cardiff, pp. 459– 471.
- Van Vledder, G.Ph., 2005, “The WRT method for the computation of non-linear four-wave interactions in discrete spectral wave models”, *Coastal Engineering*, Vol. 53, P. 223-242.
- The WAMDI Group (Hasselmann, S., Hasselmann, K., Bauer, E., Janssen, P.A.E.M., Komen, G.J., Bertotti, L., Lionello, P., Guillaume, A., Cardone, V.C., Greenwood, J.A., Reistad, M., Zambresky, L. and Ewing, J.A.), 1988, “The WAM model – a third generation ocean wave prediction model”, *Journal of Physical Oceanography*, Vol. 18, P. 1775–1810.
- Waseda, T. and Tulin, M. P. 1999, “Experimental study of the stability of deep-water wave trains including wind effects”, *Journal of Fluid Mechanics*, Vol. 401, P. 55-84.
- Webb, D.J., 1978, “Nonlinear transfer between sea waves”, *Deep-Sea Res.*, Vol. 25, P. 279– 298.
- Yefimov, V.V. and Babanin, A.V., 1991, “Dispersion relation for the envelope of groups of wind waves”, *Izv. Acad. Sci. USSR, Atmos. Oceanic Phys.* 27, P. 599.
- Young, I. R., 1988a, “A Shallow Water Spectral Wave Model”, *Journal of Geophysical Research*, Vol. 95, P. 5113 – 5129.

- Young, I. R., 1988b, "A parametric hurricane wave prediction model", *Journal Waterw. Port Coastal Ocean Engineering*, Vol.114, P. 637 – 652.
- Young, I.R., and van Vledder, G.Ph., 1993, "A review of the central role of nonlinear interactions in wind-wave evolution", *Philos. Trans. R. Soc. London*, Vol. A342, P. 505-524.
- Young, I. R., L. A. Verhagen, and M. L. Banner, 1995, "A note on bimodal directional spreading of fetch-limited wind waves", *Journal of Geophysical Research*, Vol. 100(C1), P. 773 – 778.
- Young I.R., Verhagen L.A., 1996, "The growth of fetch limited waves in water of finite depth. Part 1. Total energy and peak frequency", *Coastal Engineering*, Vol.28, P. 47 – 78.
- Young I.R., Verhagen L.A., 1996, "The growth of fetch limited waves in water of finite depth. Part 2. Spectral evolution", *Coastal Engineering*, Vol.29, P. 79 – 99.
- Young I.R., Verhagen L.A., Khatri S.K., 1996, "The growth of fetch limited waves in water of finite depth. Part 3. Directional spectra", *Coastal Engineering*, Vol.29, P. 101 - 121.
- Young I.R., 1999 "Wind generated ocean waves", Elsevier.
- Young I.R., Banner M.L., Donelan M.A., Babanin A.V., Melville K.W, Veron F., McCormick C., 2005 "An Integrated Study of the wind wave source term balance in finite depth water", submitted to *Journal of Atmospheric and Oceanic Technology*, Vol. 22, P. 814–828.
- Young, I.R., and Babanin A.V., 2006: Spectral distribution of energy dissipation of wind-generated waves due to dominant wave breaking, *Journal of Physical Oceanography*, Vol. 36, N3, P. 376–394.
- Yuan, Y., Tung, C.C. and Huang, N.E, 1986, "Statistical characteristics of breaking waves", *Wave Dynamics and Radio Probing of the Sea Surface*, O.M. Phillips and K. Hasselmann, (eds.), Plenum, New-York, P. 262–272.
- Zakharov, V.E., 1968, "Stability of periodic waves of finite amplitude on the surface of a deep fluid", *Zhurnal Prikladnoi Mekhaniki Tekhnicheskoi Fiziki*, (U.S.S.R.), Vol. 3, P. 86–94.

\* \* \*